Title

CATALYTIC REACTIONS OF HYDROCARBONS ON PLATINUM SINGLE CRYSTAL STEPPED SURFACES: THE EFFECT OF SURFACE STRUCTURE ON REACTIVITY

Author

Blakely, Donald William.

Publication Date

1976-05-01

LBL-6064

CATALYTIC REACTIONS OF HYDROCARBONS ON PLATINUM SINGLE CRYSTAL STEPPED SURFACES: THE EFFECT OF SURFACE STRUCTURE ON REACTIVITY

Donald William Blakely
(Ph. D. thesis)

May 1976

Prepared for the U. S. Energy Research and
Development Administration under Contract W-7405-ENG-48

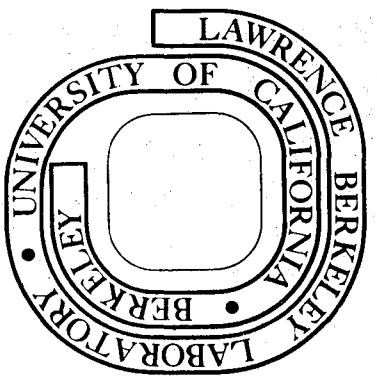

LBL-6064

DISCLAIMER

Catalytic Reactions of Hydrocarbons on Platinum Single Crystal Stepped Surfaces: The Effect of Surface Structure on Reactivity

Contents

Catalytic Reactions of Hydrocarbons on Platinum Single Crystal Stepped Surfaces: The Effect of Surface Structure on Reactivity

Donald William Blakely

Materials and Molecular Research Division, Lawrence Berkeley Laboratory
and Department of Chemistry, University of California,
Berkeley, California 94720

ABSTRACT

The structure, stability, adsorption and reaction characteristics of a large number of platinum single crystal surfaces were studied. The techniques of low-energy electron diffraction and Auger electron spectroscopy were used to determine the surface structure and stability and adsorption characteristics of the crystals. Quadrapole mass spectrometer was used to measure the reaction rates of hydrocarbons on the various crystals.

The dehydrogenation and hydrogenolysis of cyclohexane and cyclohexene were studied on platinum single crystal surfaces of varying atomic surface structure at low pressures (10^{-6} Torr) in the temperature range of 300-723°K. Atomic steps have been identified as the active sites for C-H and H-H bond breaking processes. The dependence of the dehydrogenation and hydrogenolysis rates on the platinum surface structure revealed kinks in the steps as active sites for C-C bond scission in addition to their ability for breaking C-H and H-H bonds. The active catalyst surface was covered with a carbonaceous overlayer, which was ordered or disordered. The properties of this overlayer influence significantly both, the rate and the product distribution of the catalytic reactions. An expanded classification of structure-sensitive reactions is suggested.

The adsorption of carbon monoxide was studied by flash desorption mass spectroscopy. On a series of stepped surfaces cut between the (111) and (001) planes ([110] zone), three distinct adsorption sites were found. One is associated with each type of low Miller Index terrace, (111) and (001), and a third stronger binding site is associated with the monatomic height steps separating the terraces. The heat of desorption from these sites is 23.5, 24 and 29.6 kcal/mole, respectively. The amount of CO which adsorbed in the high binding energy site is proportional to the number of step sites on the surface, confirming the assignment to the step atom-CO interaction and not CO-CO interactions. The adsorbed CO is highly mobile on the Pt-(111) terraces.

The equilibrium structure and stability of high Miller Index platinum has been studied on atomically clean surfaces. The stability has also been determined on crystals with known impurities, oxygen or carbon, on their surfaces. The equilibrium structure of the crystal surface is directly related to the surface free energy, or surface tension, of the crystal. The atomically clean surfaces of Pt exhibit the largest region of stability of the monatomic height step configuration. The surfaces vicinal to the (111) plane and between the (111) and (001) planes are stable in a monatomic height step structure. Near the (011) plane and between the (011) and (001) planes either a hill and valley structure or double height steps are stable. When heated in an oxygen ambient, the surfaces become unstable. Near the (001) plane, as little as 0.01 monolayers of oxygen cause the formation of a hill and valley structure composed of (001) and (113) and/or (012) planes, and near the (111) plane, the steps become multiple height. Near the (011)

plane, the steps are already unstable and no further changes result from either oxygen or carbon adsorption. Graphitic carbon of the (001) vicinal surfaces induces the formation of a similar hill and valley structure to that formed by oxygen. On (111) vicinal surfaces between the (112) and (445) surfaces (between Pt(S)-[3(111)×(001)] and Pt(S)-[9(111)×(001)]), a monolayer of graphitic carbon causes the formation of a hill and valley structure consisting of the (112) and (445) planes and not the low Miller Index plane, (111). The (445) plane is stabilized from the coincidence of the Pt and graphite lattices at a nine Pt atom terrace width.

1. INTRODUCTION

The catalytic processing of hydrocarbons is very important industrially, particularly in the petroleum refining industry. In petroleum refining, there are three main catalytic processes, cracking, hydrocracking and reforming. There are also several minor catalytic processes such as hydrodesulferization and dimerization. Cracking and hydrocracking use highly acidic catalysts to break large hydrocarbon molecules into smaller, more useful molecules through carbonium ion mechanisms. In the industrial reforming catalysts, there is a metal dispersed on a mildly acidic support, a high surface area alumina.[1] The acidic component promotes isomerization of parafinnic molecules into higher octane branched hydrocarbons. The metal component of the catalyst dehydrogenates and dehydrocyclizes the hydrocarbons to higher octane forms. The metal used in reforming catalysts is almost exclusively Pt. Alloying of two or more metals is coming into use, but long term stability of the small alloy particles is difficult to achieve.[2] Alloys will be advantageous industrially because it may be possible to tailor the catalyst for selectivity to the desired products to a greater degree than now possible.[3,14] However, why Pt is better as a reforming catalyst and how it works is really not known in any detail.

In an industrial catalyst, both the metal and the support are active catalytically. Their is a synergistic relationship between the components which makes the composite catalyst more active than its components.[1,5] There is one function, that of dehydrogenation, which is solely performed by the metal, and is the main subject of this

thesis. The pure metal component has been studied in its highly dispersed state by supporting it on an acidically neutral support such as silica,[6,7] making it into a very fine powder[8] and by forming thin films of the metal on smooth substrates.[9] Csicsery and Burnett[6] showed that the Pt metal component can perform isomerization and cyclization as well as dehydrogenation. They found the mechanism of isoalkane formation on Pt on silica not to be a methyl shift type of mechanism as found with acid catalysts but a ring opening reaction involving simple bond scission. Their proposed scheme is shown in Fig. 1-1. The n-heptane would cyclize into methylcyclohexane, 1,2-dimethylcyclopentane or ethylcyclopentane. When the ring was opened at the various positions shown in Fig. 1-1, the isomerization products were 2-methylhexane, 3-methylhexane, 2,3-dimethlypentane and 3-ethlypentane. They found the products were produced in a ratio corresponding to equal ring opening probabilities at each position and equal formation probabilities of the three ring compounds. The methylcyclohexane also dehydrogenated to form toluene. Others have found an unequal ring opening probability[8,10] for dimethlycyclopentanes. The ring opening of methlycyclopentane is also important in the isomerization of n-hexane.[9,11-15] Anderson and Avery[16-18] and others[8,19] have found a bond shift mechanism prominent on Pt catalysts. This mechanism may involve a multiple bond between two carbon atoms of the hydrocarbon and the metal surface as shown in Fig. 1-2a. If the n-heptane, in this case, is 1,3- (2,4-) diadsorbed, a bond shift can occur which forms 2- (3-)methylhexane. This mechanism also gives the possible path to the formation of the cyclic intermediates.[20] If the n-heptane is 2,6- (1,6- or 1,5-) diadsorbed as

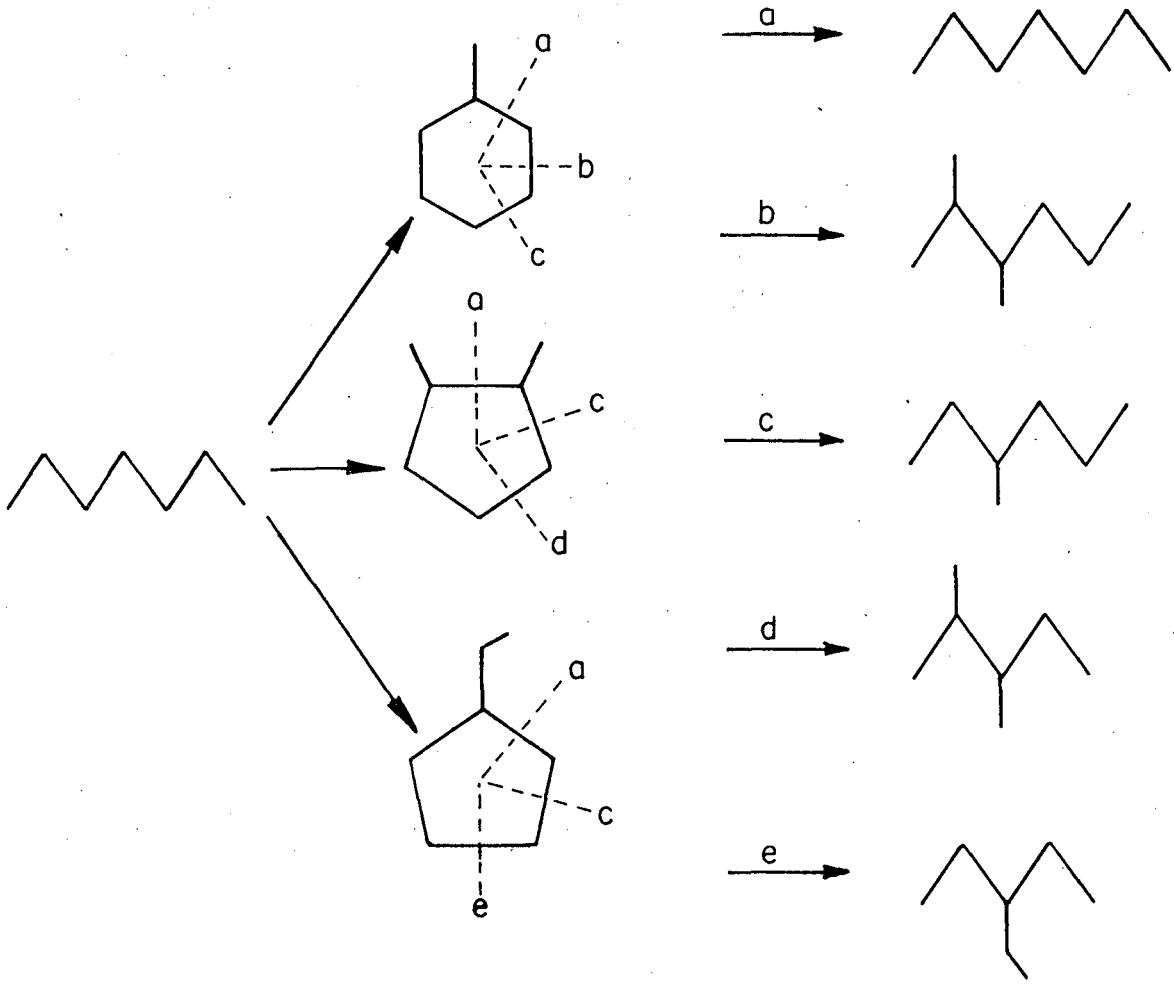

XBL 763-6618

Fig. 1-1. Possible path for the isomerization of n-heptane via a 5 or 6-member ring intermediate (from Csicsery and Burnett[6]).

shown in Fig. 1-2b, it can cyclize to form 1,2-dimethylcyclopentane (methylcyclohexane or ethylcyclopentane). These species then undergo the simple ring opening hydrogenolysis reactions discussed earlier.

It is interesting that some investigators found the predominance of the bond shift mechanism,[8] while others found the cyclic ring opening mechanism exclusively.[6] This type of behavior was classified by Boudart[19,21-24] and recently more elaborately by Manogue and Katzer[25] and Blakely and Somorjai.[26] Boudart's classification separates reactions into two groups: in the first, the specific reaction rate depends on the mean metal particle size of the catalyst, and in the second, the specific reaction rate is independent of the mean particle size of the catalyst. Changes in the mean metal particle size are generally accomplished by sintering the catalyst, and imply changes in the surface structure of the metal particle, although how the surface structure changes is unknown. A number of other reactions besides the isomerization reactions just described have been catagorized. The dehydrogenation of cyclohexane[26-31] and the hydrogenation of benzene[28,32,33] are independent of the metal particle size on supported catalysts and polycrystalline foils. The dehydrogenation of cyclohexane is investigated on controlled surface structures in this thesis. The hydrogenation of cyclopropane to propane is structure insensitive[23,34] on both supported catalysts and single crystal catalysts. The hydrogen-deuterium exchange has been found structure insensitive on supported catalysts[28,35] at high pressures, but Bernasek and Somorjai[36] found the reaction to be structure sensitive on single crystal catalysts at low pressure. Possibly all the structure insensitive reactions proceed through a structure sensitive step, but

the sensitive step is not rate limiting at the conditions of the experiment. This thesis demonstrates this for the dehydrogenation of cyclohexane.

There are many structure sensitive reactions, and this catagory has been separated into three classes by Monogue and Katzer.[25] Primary structure sensitivity is the effect of changing the metal particle size on the specific reaction rate. Neopentane hydrogenolysis,[17,19] deuterium exchange of benzene[37] and cyclopentanes,[38] isomerizations of n-hexanes,[9] dehydrocyclization of n-heptane,[29,39] hydrogenolysis of ethane[40,41] and hydrogenolysis of methylcyclopentane[42] among others have been shown to be structure sensitive to changes in the mean particle size. This thesis also presents data that the dehydrogenation of cyclohexane, dehydrocyclization of n-heptane and the hydrogenolysis of cyclohexane are structure sensitive on single crystal catalysts. The above studies were performed on catalysts which were thoroughly reduced in H_2. The catalytic surface should be clean. Their surface structure should be the equilibrium shape for the H_2 or vacuum reduction atmosphere. When the catalyst is treated in O_2 reactions which do not exhibit primary structure sensitive can show quite marked particle size dependences, such as cyclopropane hydrogenation,[23] cyclohexane dehydrogenation and ethylene hydrogenation.[43] This has been classified as "secondary structure sensitivity",[25] along with the effect of particle size on the self poisoning reactions of hydrocarbons. Cyclohexane dehydrogenation,[27] ethlyene hydrogenation,[46,47] n-heptane dehydrocyclization[48,49] and oxidation reactions on Pt,[50-53] as well as data in this thesis, show self poisoning which is dependent on the surface structure of the

catalyst. A third kind of particle size sensitivity is the effect of very small particles (<10Å) on adsorption[54] and reactions.[55]

This thesis uses the surface sensitive techniques of low-energy electron diffraction (LEED) and Auger electron spectroscopy (AES) to assess the structure and cleanliness of the surface of single crystals of Pt. The overall orientation of the surface and, therefore, its structure can be readily varied simply by changing the angle of cut from the single crystal rod. Twenty-one samples of different surface orientation have been studied to determine the stability and structure of their surface. This has been studied for clean surfaces as determined by AES, for graphite covered surfaces and for surfaces heated in an oxygen ambient. There are marked differences in the stability and structure of the surfaces under the different conditions; these differences and their possible relationship to catalysis and structure sensitivity are discussed in Chapter 4.

The effect of surface structure on the adsorption of small molecules, carbon monoxide and hydrogen, is considered in Chapter 5. The heat of adsorption and the overlayer structure are dependent on the surface structure of the catalyst, although the amount adsorbed is, within a factor of two, independent of the surface structure. On supported catalysts, the adsorption decreases on the larger particles.[56] Flash desorption mass spectroscopy and LEED have been used to characterize the adsorbates.

The specific reaction rates of several hydrocarbon reactions have been studied at low pressures using a quadrapole mass spectrometer as a detector on the various single crystal catalyst surfaces and are reported

in Chapter 6. The use of single crystal catalysts allows the unambiguous determination of the surface structure sensitivity of the reactions. The structure may be readily varied and characterized, and all orientations of surfaces may be studied (although practically only a small sampling has been studied). The main reactions studied were the dehydrogenation and hydrogenolysis (ring opening) of cyclohexane and the dehydrogenation of cyclohexene. The dehydrocyclization reactions of n-heptane were also studied, along with the isomerization of isobutane. From these studies came a significant discovery: the identification of active sites for the C-H and H-H and the C-C, C-H and H-H bond breaking reactions.[26,57] These sites are at a monatomic height step in the metal surface and at a kink in a monatomic height step, respectively. This confirms previous speculations that low coordination number metal atoms are the site of catalytic reactions, and, in particular, that a corner atom or kink atom, is necessary for the ring opening hydrogenolysis reaction. The self poisoning of the cyclohexane dehydrogenation reaction is found to be dependent on both metal surface structure and carbonaceous residue. An ordered residue does not deactivate the catalyst, while a disordered, amorphous deposit causes deactivation. This is related to the expanded classification of structure sensitivity. A model is proposed which relates the carbonaceous residues formed at low pressures and the necessity of high hydrogen pressure to the maintenance catalytic activity on a metal surface.

2. EXPERIMENTAL PROCEDURES

2.1. Surface Characterization

2.1.1. Experimental Apparatus

The experimental apparatus used in this investigation was a standard early model Varian LEED chamber. It is pictured in Fig. 2.1 and shown schematically in Fig. 2.2. A 4-grid Varian LEED optics with a bariated nickel Phillips cold-cathode electron source is mounted opposite the viewing port. The experimental operating problems of LEED have been described by Taylor[58] and Lyon.[59] Chesters and Somorjai[60] recently reviewed experimental results; theoretical problems have been reviewed by Farrell and Somorjai[61] and recently by Kesmodel and Somorjai.[62]

Briefly, as depicted in Fig. 2.3, a well collimated beam of monochromatic energy electrons in the energy range of 10 to 450 eV is incident on the single crystal sample. The back scattering diffraction beams are displayed on post-acceleration phosphorized (P-11[63]) screen where the diffraction spots may be viewed or photographed. A Crown Graphic camera with a f3.5 lens and Polaroid type 57 (ASA 3000) sheet film with an exposure time of 45 sec are used to photograph the diffraction pattern. Low Energy Electron Diffraction is a surface sensitive technique because of the strong interaction of the electrons with the solid as compared to X-ray diffraction; this is depicted in Fig. 2-4. In the range of electron energies used the mean free path of an electron (mean distance between inelastic collisions) varies from approximately 3 to 10Å (see the universal curve in Fig. 2-5).[64]

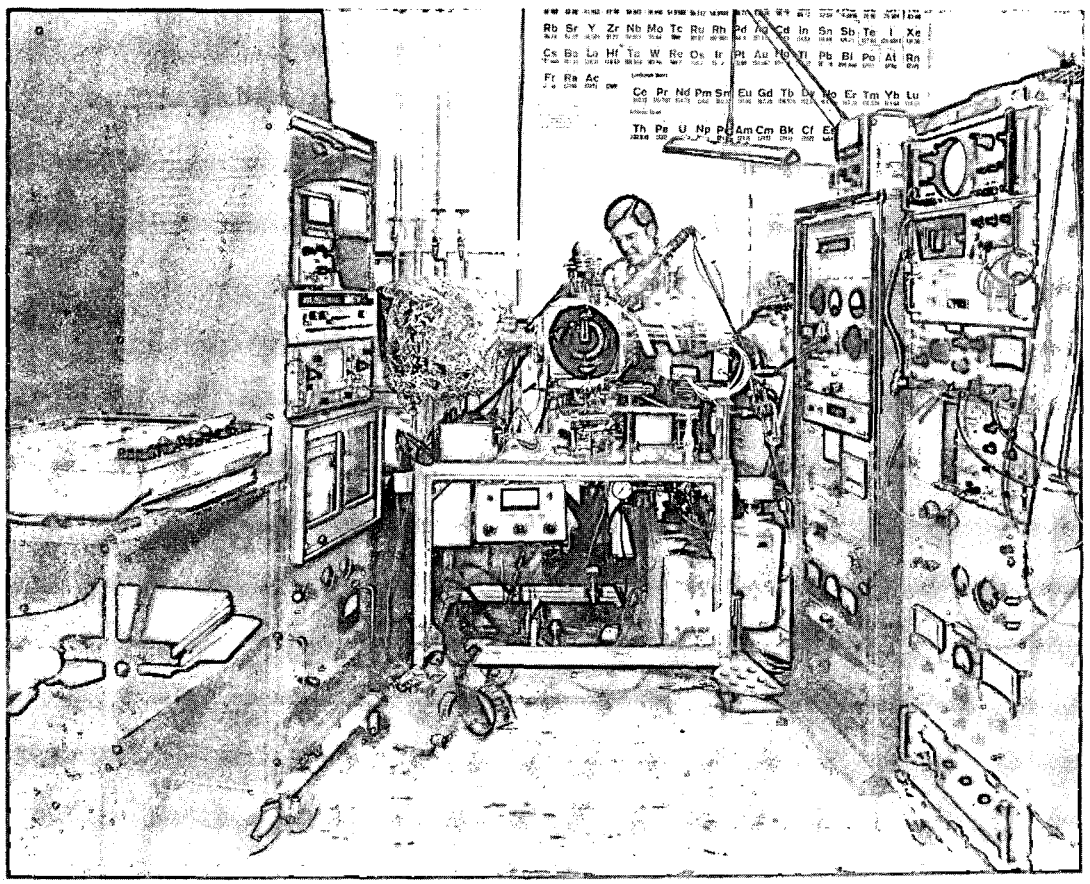

XBB 754-3287

Fig. 2-1. Photograph of experimental apparatus used in this investigation showing vacuum system and associated electronics.

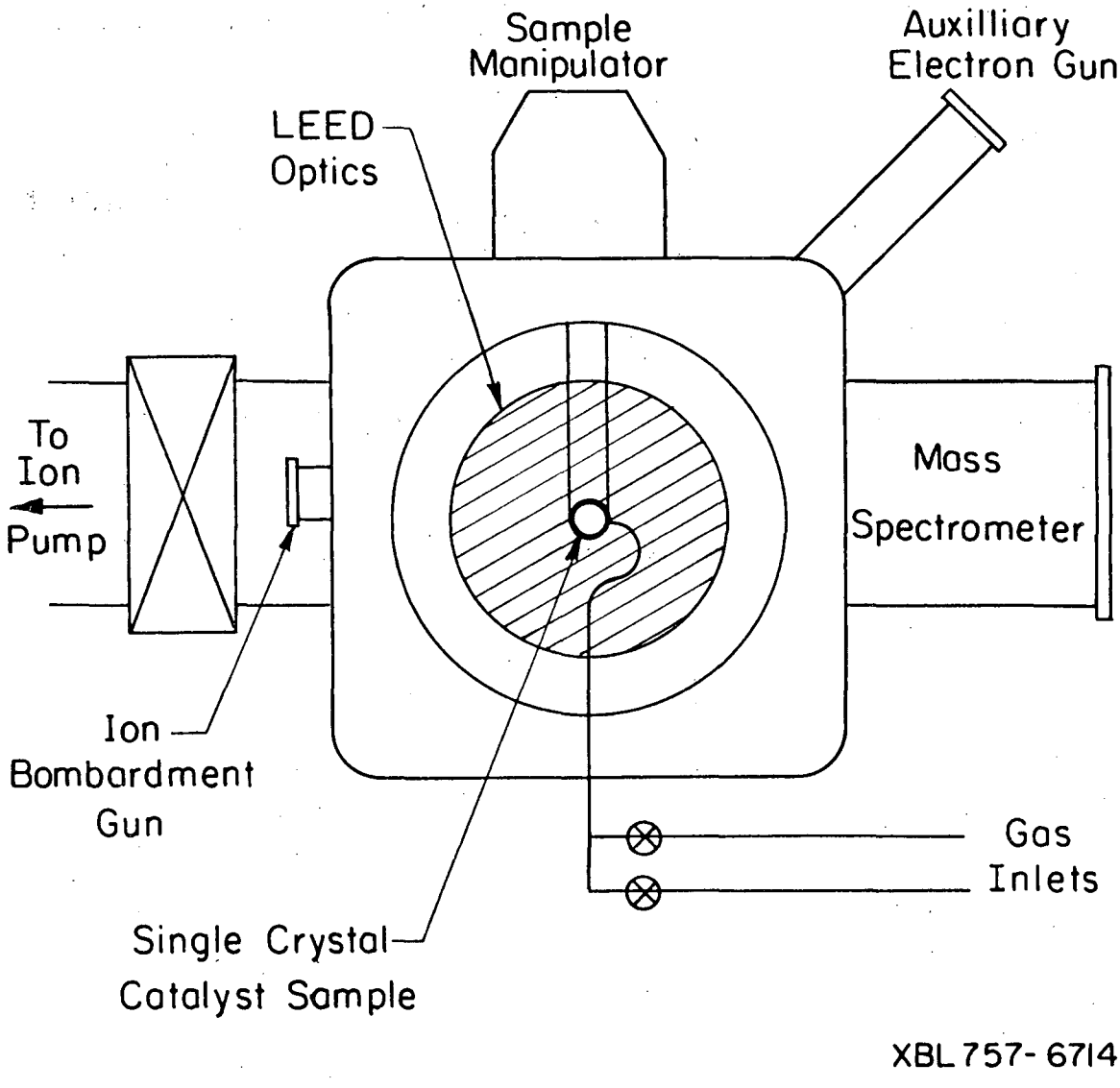

Fig. 2-2. Schematic diagram of experimental apparatus showing LEED optics, quadrapole mass spectrometry gas handling and pumping system.

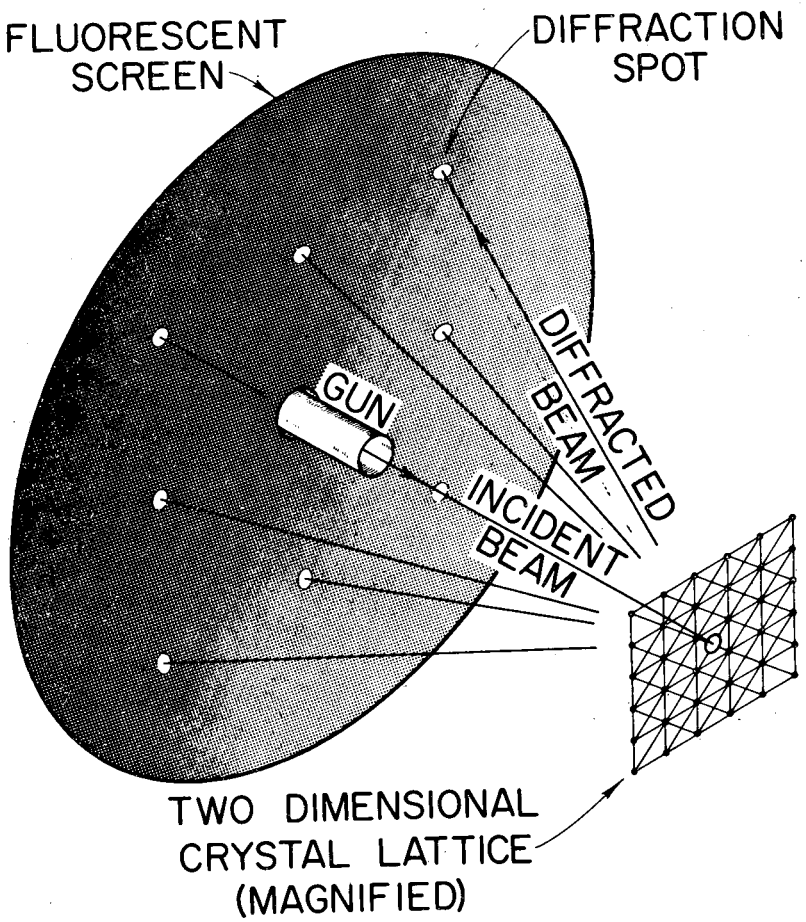

XBB 708-3583

Fig. 2-3. Idealized schematic diagram of LEED optics demonstrating diffraction of low energy electrons.

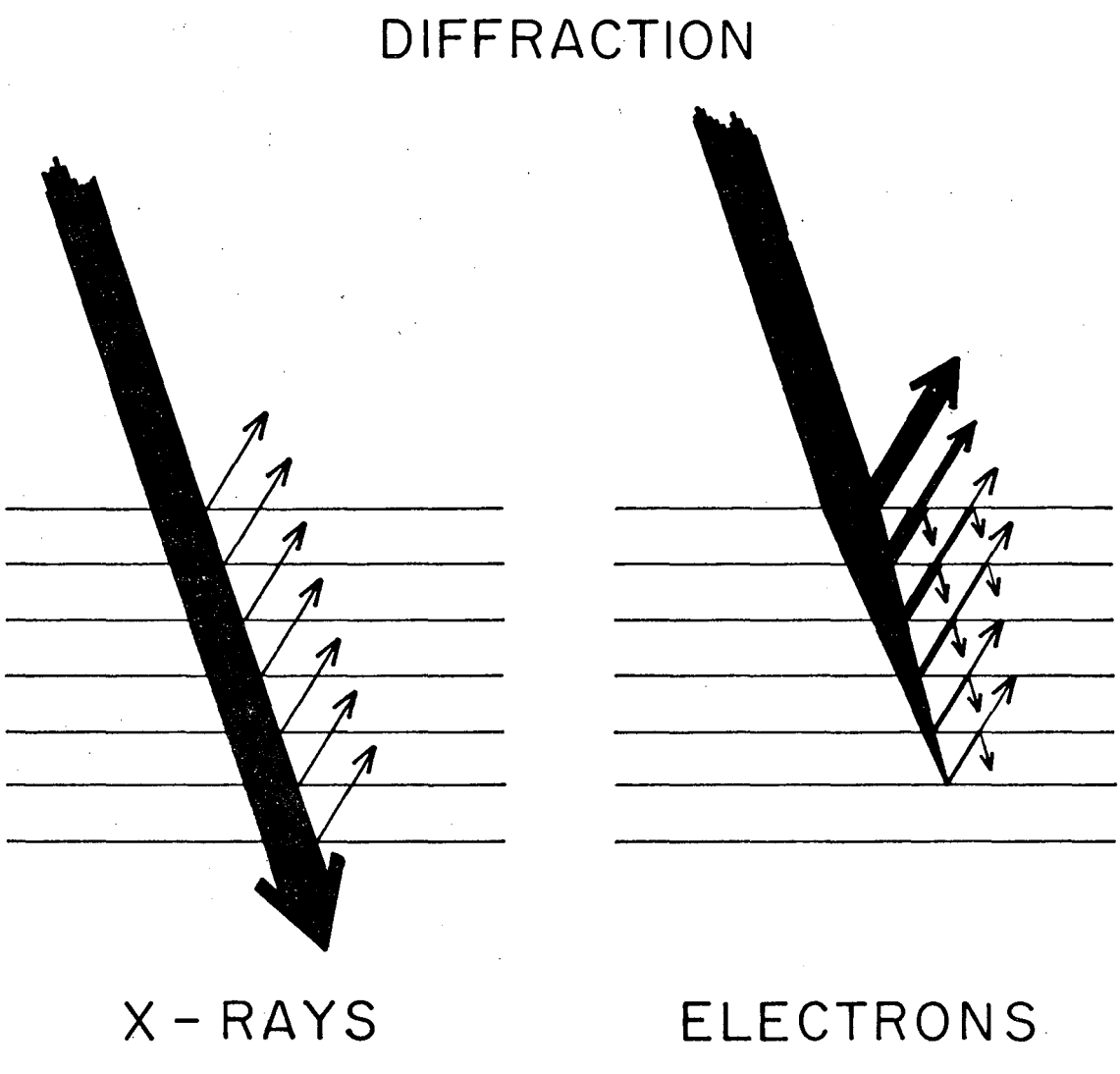

XBL 7012-7436

Fig. 2-4. Comparison of scattering abilities of X-rays and low energy electrons. X-rays penetrate 10^4A or more into a solid while low energy electrons penetrate ~10A.

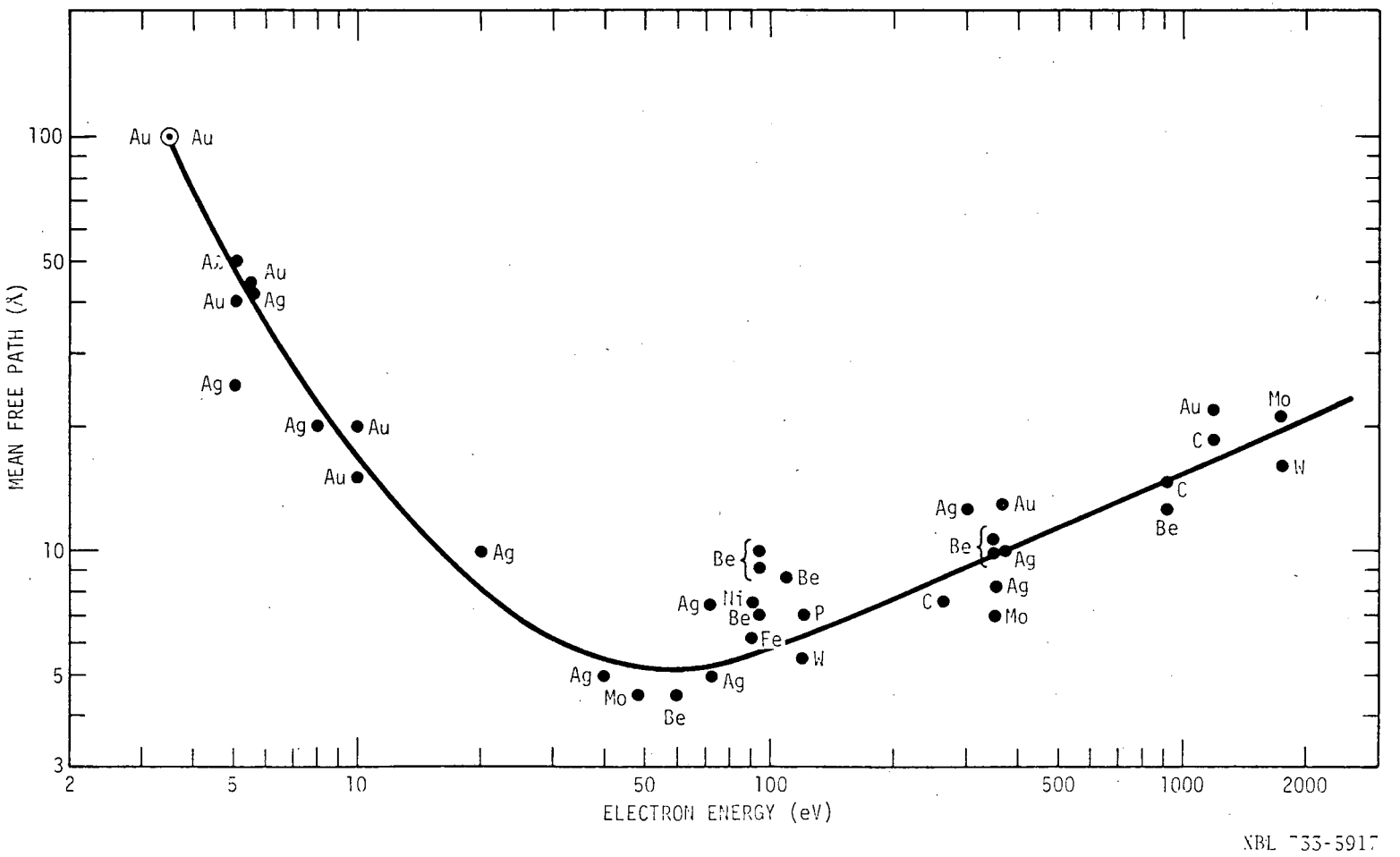

XBL 733-5917

Fig. 2-5. Universal curve for the mean free path of an electron before it undergoes an inelastic collision.

Because of the strong interaction, all the diffraction information comes from the top 3 to 5 atomic layers of the solid,[65] as opposed to X-ray diffraction where typical penetrations are 10^4 Å or greater.

The LEED optics is also used as a retarding field Auger electron spectrometer. Auger Electron Spectroscopy (AES) has been reviewed by C. C. Chang,[66] Szalkowski and Somorjai,[67] Szalkowski,[64] and recently by Palmberg.[68] The AES electronics were designed and built in the LBL electronic shops.[69] A 12B cathode ray tube electron gun fitted with a 0.030×0.001×0.670 in. tungsten ribbon was used as the primary source of electrons for the AES spectra. The primary used in practically all spectra was 2 keV.

A representation of the physics of the Auger process is shown in Fig. 2-6. A vacancy is created in a low lying electron shell of energy E_z by the primary incident electrons. Another electron from a higher shell of energy E_y drops down and fills the lower vacancy releasing energy $E_z - E_y$. This energy can be dissipated by the release of a photon as in fluorescence or by ejecting another electron as in the Auger process. This third electron (second ionization of the atom) from a shell of energy E_x is ejected from the solid with kinetic energy: $E_k = E_z - E_y - E_x + \Delta E$. The kinetic energy of the electron is measured in the retarding field spectrometer as shown in Fig. 2-7. The ΔE term must be included since there is some shifting or relaxation of energy levels with the two ionizations of the atom. The small mean free path of the useful Auger electrons (kinetic energy of 20 to 1000 eV) makes the surface sensitivity of AES similar to LEED.

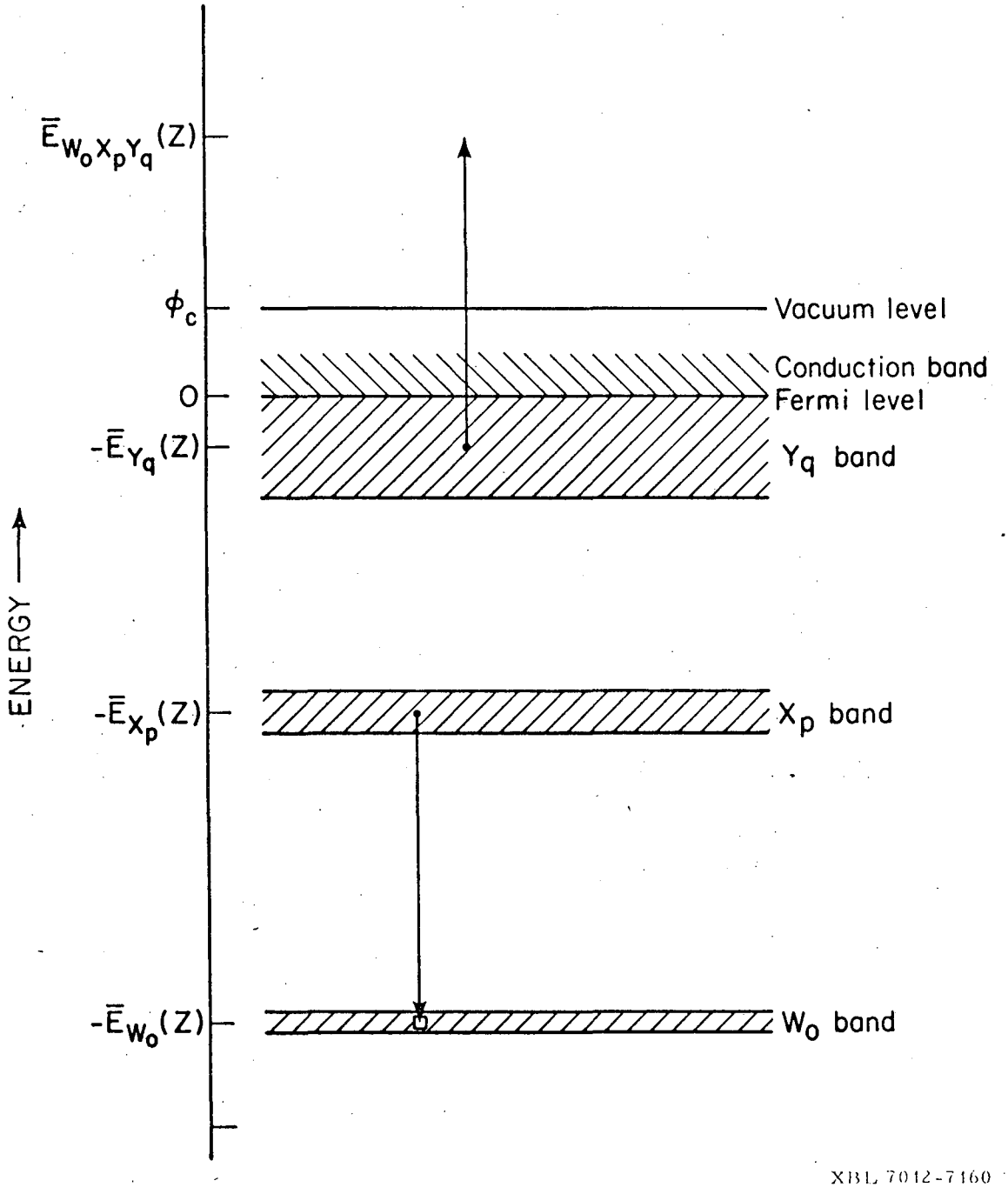

Fig. 2-6. Schematic diagram of physics of Auger process. A hole is created in W_o band which is filled by an electron from the X_p band; the energy released ejects a second electron from the solid. Its kinetic energy is measured, allowing elemental characterization.

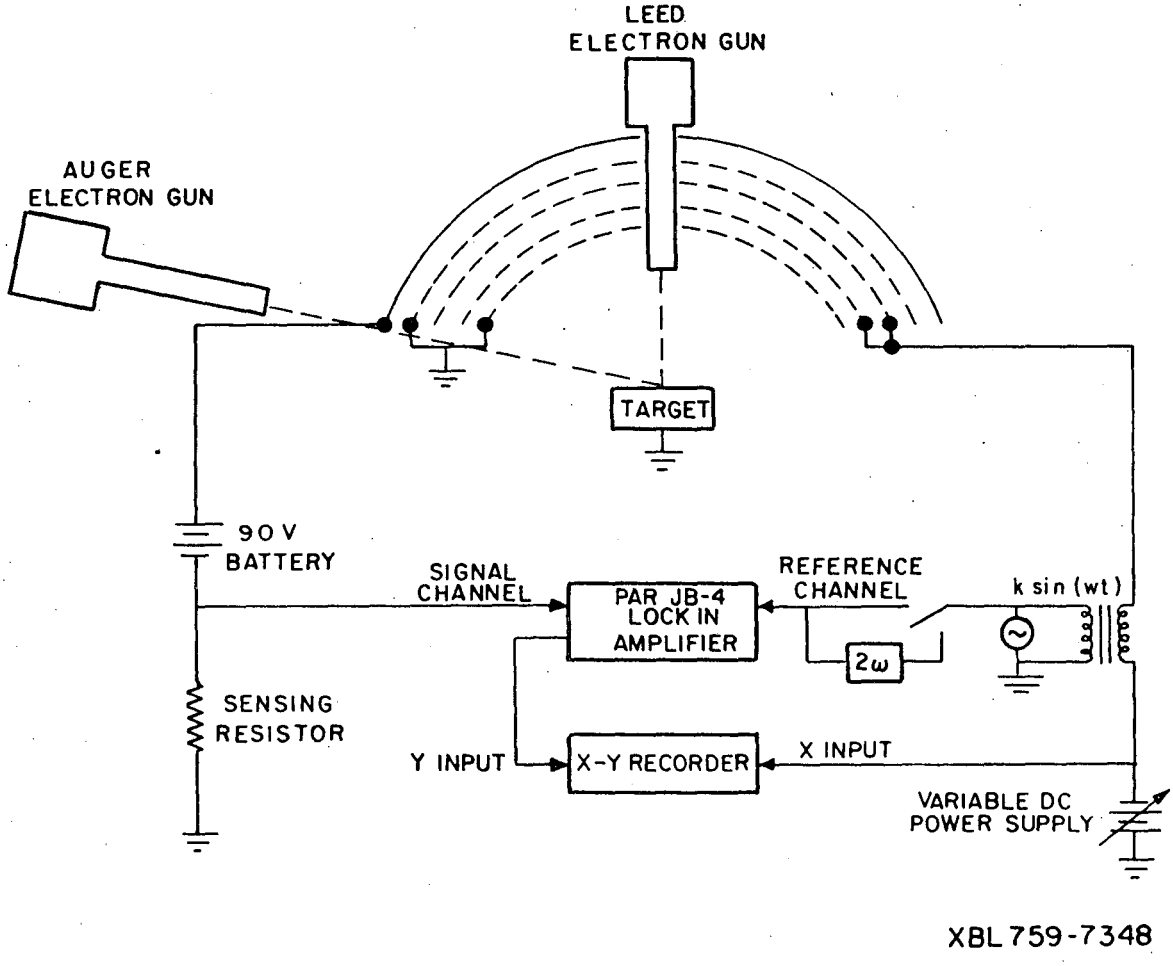

Fig. 2-7. Schematic diagram of the retarding field spectrometer used to measure the Auger electron spectra.

A UTI, model 100C quadrapole mass spectrometer was mounted in direct line of site with the samples. The dual tungsten filaments were replaced with a single thoriated iridium filament to reduce the background reaction rate. A Physical Electronics Industries, Edina, MN, ion bombardment gun model PHI-2000 was mounted opposite the mass spectrometer. Gases were admitted to the chamber through two Varian bakeable leak valves directly onto the sample via an 026 gauge hypodermic needle for the hydrogen and an 014 gauge needle for the condensable vapors. The 15 liter stainless steel vacuum chamber was pumped by a 140 ℓ/S Vac-Ion pump separated from the chamber by a Thermionics stainless steel bellows sealed gate valve. The chamber could be rough pumped to 2×10^{-4} Torr by two liquid nitrogen cooled molecular sieve adsorption pumps, and could be baked at 250°C using heating tapes and wrapping in aluminum foil. An overpressure-timer bakeout control was built in the LBL electronics shops.[70] The gas inlet manifold was bakeable with heating tapes. The liquid hydrocarbons were purified by vacuum distillation retaining only the middle third of the distillate. Gases (H_2, O_2, CO, Ar, etc) were research grade and used directly from the bottles. The liquid hydrocarbons were obtained from Chemistry Stores or Van-Waters-Rogers Co., San Francisco, CA and gases from Mattheson Corp. The crystal samples were mounted on a Varian Sample Manipulator refitted with mini-conflat flange mounted, electrical feedthroughs. The two single crystal samples were mounted as shown in Fig. 2-8 on 0.010 in. platinum thermocouple wire. The thick supports for the wires are platinum and the upper supports are 304 stainless steel. On the top

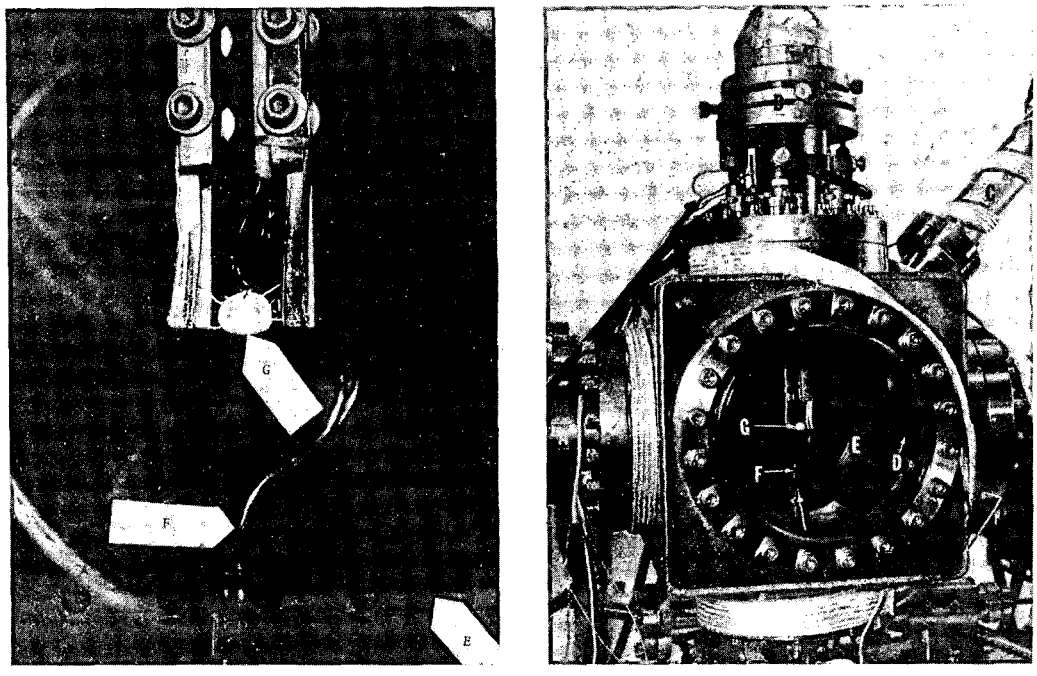

XBB 7510-7341

Fig. 2-8. Photograph of LEED chamber and close up of a mounted single crystal. (a) Ion bombardment gun, (b) sample manipulator, (c) Auger electron gun, (d) quadrupole mass spectrometer ionizer, (e) LEED optics, (f) gas inlet lines and (g) Pt single crystal mounted on 0.010 in Pt wire.

edge of each crystal a 0.005 in. dia wire Pt-Pt-10% Rh thermocouple is spot welded. This arrangement allows the samples to be independently heated by conduction from the resistively heated wires to approximately 1400°C and keeps the amount of heated polycrystalline Pt to a minimum.

2.1.2. Platinum Single Crystal Surface Preparation

The platinum single crystals used in these studies were prepared from several different single crystal rods. All but one of the 7 mm diameter single crystal rods were purchased from Materials Research Corp. Materials Research Corporation claims a purity of 99.99% before the metal is triply zone refined; the third slow pass produces the single crystal. The claimed impurity levels are found in Table 2-1. The other supplier was Research Organic/Inorganic Corp., Sunnyvale, CA, whose crystal was also of similar origin and professed purity.

The crystallographic orientation of the single crystal samples used was determined by a Laue back-reflection X-ray camera. The orientation of the crystal could be determined to within approximately 1/4 to 1/3° while in the camera. Slices 0.5 to 1.2 mm thick were cut from the single crystal rods by a Metals Research, Cambridge, England spark erosion saw at a rate of 7 mm/45 min with a non-rotating brass blade. The spark saw was only accurate to approximately 1°. The slices were mounted in "Koldmount" an eposy resin soluble in methyl-ethylketone manufactured by Vernon-Benshoff Co., Albany, NY for the polishing process. The crystals were polished on four successively finer grades of emery paper from 20μ to 10μ, then 1μ diamond paste on a rotating wheel and the final step of 0.05μ

Table 2-1. Typical mass spectrographic analysis of "Marz" grade platinum.

Element	Content (ppm)	Element	Content (ppm)
Li	<0.0002	Rh	15.0
Be	<0.02	Pd	0.6
B	0.0003	Ag	0.012
C	10.0	Cd	<0.025
H_2	1.5	In	0.03
O_2	10.0	Sb	<0.004
N_2	3.0	Sn	0.08
F	<0.003	Te	<0.008
Na	<0.06	I	<0.002
Mg	<0.06	Cs	<0.002
Al	7.0	Ba	<0.003
Si	7.0	La	<0.002
P	0.002	Ce	<0.002
S	0.2	Pr	<0.002
Cl	0.4	Nd	<0.01
K	0.1	Sm	<0.01
Ca	0.05	Eu	<0.005
Sc	<0.03	Gd	<0.01
Ti	2.5	Tb	<0.003
V	0.25	Dy	<0.01
Cr	2.5	Ho	<0.003
Mn	0.6	Er	<0.008
Fe	30.0	Tm	<0.003
Co	0.3	Yb	<0.06
Ni	2.5	Lu	<0.003
Cu	0.05	Hf	0.05
Zn	0.05	Ta	< 5.0
Ga	0.01	W	5.0
Ge	<0.004	Re	< 0.02
As	0.01	Os	<0.08
Se	<0.003	Ir	0.3
Br	0.008	Au	< 0.3
Rb	<0.01	Hg	<0.15
Sr	<0.003	Tl	<0.15
Y	<0.01	Pb	<0.6
Zr	2.5	Bi	<0.06
Nb	1.0	Th	<0.07
Mo	<0.3	U	<0.07
Ru	0.3		

alumina powder in a water slurry on a vibrator. The orientation was then rechecked in the Laue camera before removing from the Koldmount. If the orientation was not satisfactory (within 1/2° of desired orientation), the crystal was ground with emery paper on a facing wheel in the camera gonimeter to the proper orientation and the polishing procedure repeated. The crystal was removed from the Koldmount and the back face paralleled to the front face with a metal rod and snug fitting concentric sleeve. The back face is then polished. The Koldmount must be carefully and completely removed from the crystal with both boiling methyl-ethyl ketone and final rinse with reagent grade acetone. The Koldmount appears to contain Ca and S and contaminates the platinum if not completely removed.

2.1.3. Stepped Surface Nomenclature

The Laue back reflection X-ray pattern only gives information on the macroscopic normal to the surface, the crystallographic orientation of the bulk crystal. This is the Miller Index of the crystal orientation, which is the same whether the surface configuration is monatomic height steps, multiple height steps or large facets of low index planes. To overcome this disadvantage, a surface nomenclature was proposed by Lang, Joyner and Somorjai[71] which uses pairs of adjacent low index planes to describe the surface atomic configuration. A Pt-(976) surface which is depicted in Fig. 2-9 is more readily visualized as a Pt(S)-[7(111)×(310)]. Briefly, Pt(S) means a platinum stepped surface, 7(111) refers to the 7 atom wide terrace of (111) orientation and x1(310) is the orientation of the monatomic height steps which separate the (111) orientation terraces. The {310}

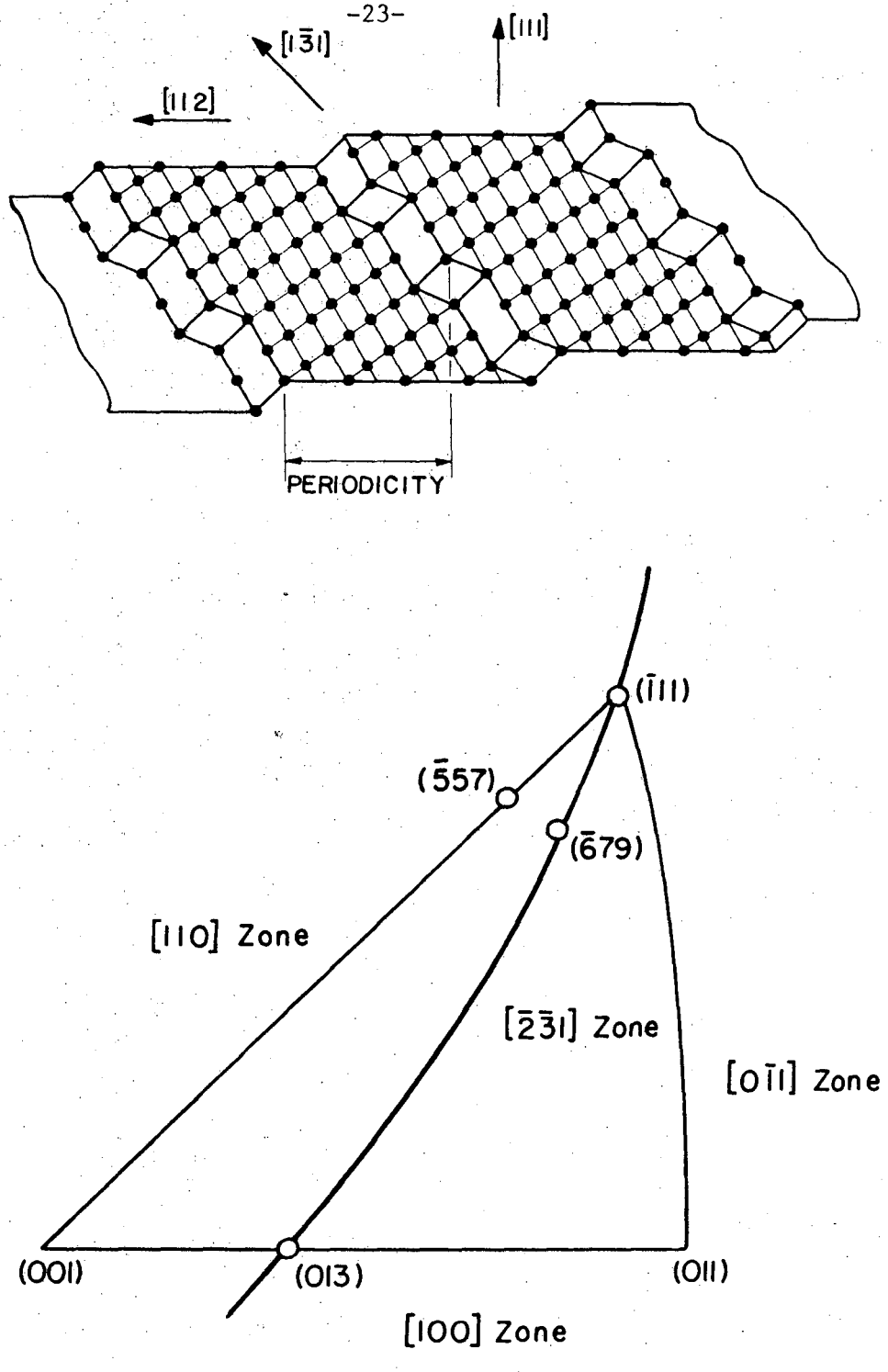

Fig. 2-9. (a) Schematic drawing of the Pt(s)-[7(111) (310)] surface showing 7 atom wide terraces and kink every third atom along the step. (b) Stereographic projection triangle showing method for determination of kink step orientation.

is a pole direction normal to the plane on the opposite boundary of the stereographic triangle from the low index pole. As shown on the stereographic triangle in Fig. 2-9b, it is the pole at the intersection of the zone line, $[\bar{2}\bar{3}1]$ in this case, through the terrace pole, $(\bar{1}11)$, and the surface pole, $(\bar{6}79)$, with the boundary zone line [100] of the stereographic triangle. This procedure can be applied to determine the step orientation from any surface.

2.1.4. Removal of Bulk Impurities from the Pt Samples

The major impurities in the zone refined Pt single crystal rods vary greatly from rod to rod. The rods all contained greater amounts of Ca than the specification of 0.05 ppm. (One rod which was not used in this investigation when returned to manufacturer was admitted to have over specification Ca.) In a 1 mm thick crystal, 1.0 ppm corresponds approximately 10 monolayers or 10^{16} atoms of Ca. The other major impurities were C, present in all rods, and S and P present in one rod each. No other impurities could be found in any samples. The Auger electron spectra in Fig. 2-10 are from a clean Pt surface and a Pt crystal with the impurities segregated to the surface.

The removal of the C, S and P impurities could readily be accomplished by oxidation at low oxygen pressure, 5×10^{-8} Torr. The rate limiting step in the removal of impurities was their diffusion to the surface; sulfur and phosphorous were particularly slow around 850°C where C diffuses readily and is easily removed. Around 1100°C, the rates of S and P diffusion are about the same as their oxidation rate. If the surface is free of S and P after an O_2 treatment at

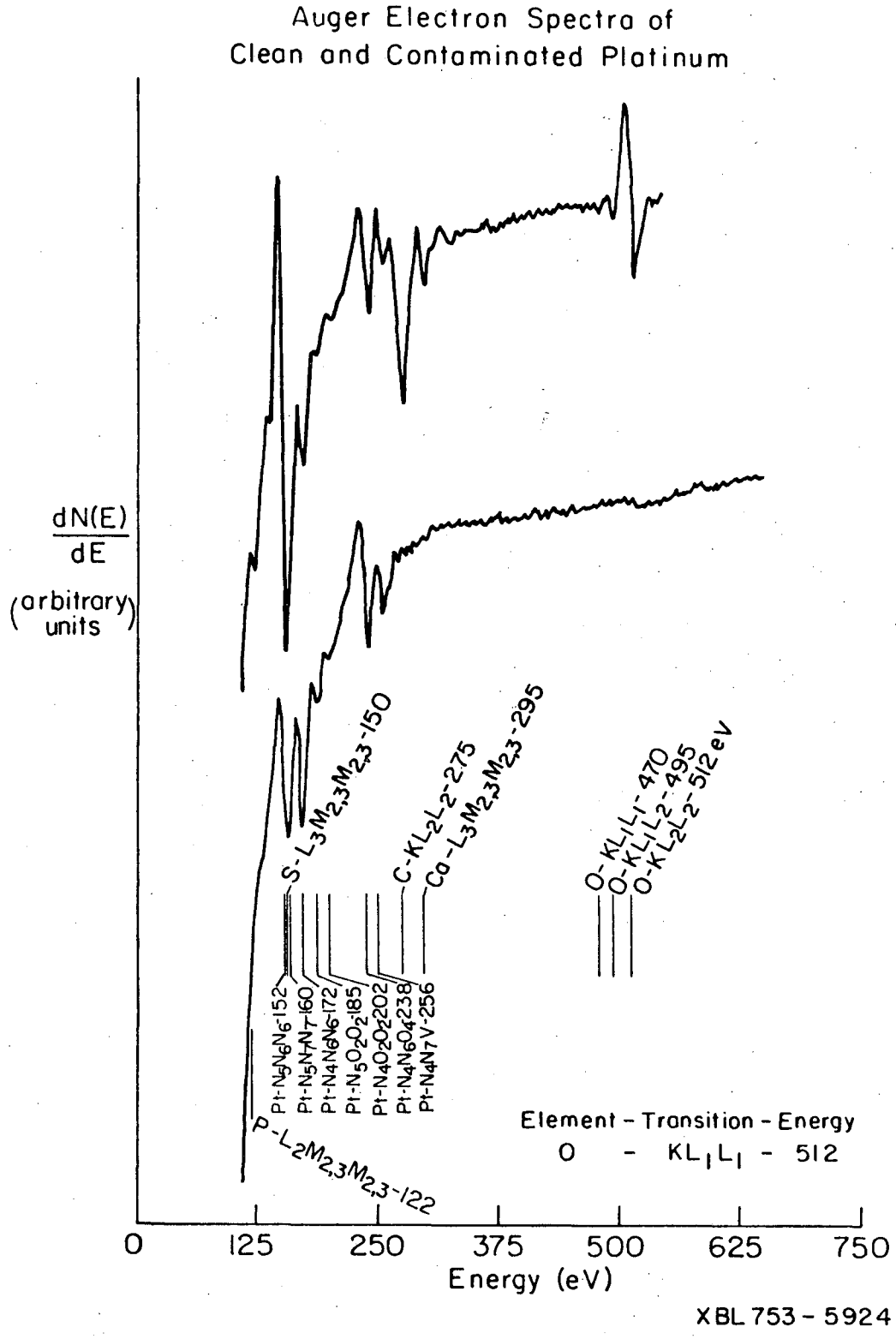

Fig. 2-10. Auger spectrum of contaminated (upper curve) and clean (lower curve) Pt single crystal surfaces. Contaminates shown are P, S, C, Ca and O.

1100°C, the bulk has been cleaned.

Calcium represents a much greater problem in that the oxide is not volitale. There were two methods used to remove the Ca from the bulk. A high concentration of calcium impurity, which possibly remained in the sample from the reduction of the platinum ore, could only be removed by extensive oxidative heat treatments. The sample was oxidized at 1500°K in 10^{-5} Torr of oxygen for 24-48 hr. This treatment fixes the calcium on the surface in the form of a stable oxide which will decompose with calcium vaporization from the surface with brief heating to 1900°K. A small calcium impurity may be removed also by argon ion bombardment and 1100°K anneal cycles.

2.1.5. Calcium Solubility in Pt

Calcium has an interesting distribution within the Pt single crystal rod. The solubility of Ca in Pt appears to be endothermic, similar to that of C.[72] Figure 2-11 shows the ratio of the Ca 295 eV Auger peak height to the Pt 240 eV peak height on an unoxidized (O Auger peak in noise) Pt(S)-[6(111)×(100)] surface after 2 min anneals at the given temperature. The highest coverage of Ca observed on an unoxidized surface on any sample is Ca(295 eV)/Pt(240 eV) ≈ 1.0. The corresponding LEED pattern was $a\begin{vmatrix} 3 & 2 \\ -2 & 5 \end{vmatrix}$. A hexagonal close packed layer of Ca with its metallic radius fits 9 atoms into this unit cell with a coverage of 0.473. The initial rise is caused by insufficient time to reach equilibrium at the lower temperatures (<1000°C). Above 1100°C, the Ca goes back into solution in the bulk Pt. The spatial distribution of Ca in the Pt rods cross-section is depicted in Fig. 2-11b. On highly contaminated crystals which were oxidized, the Ca-Pt-Oxide

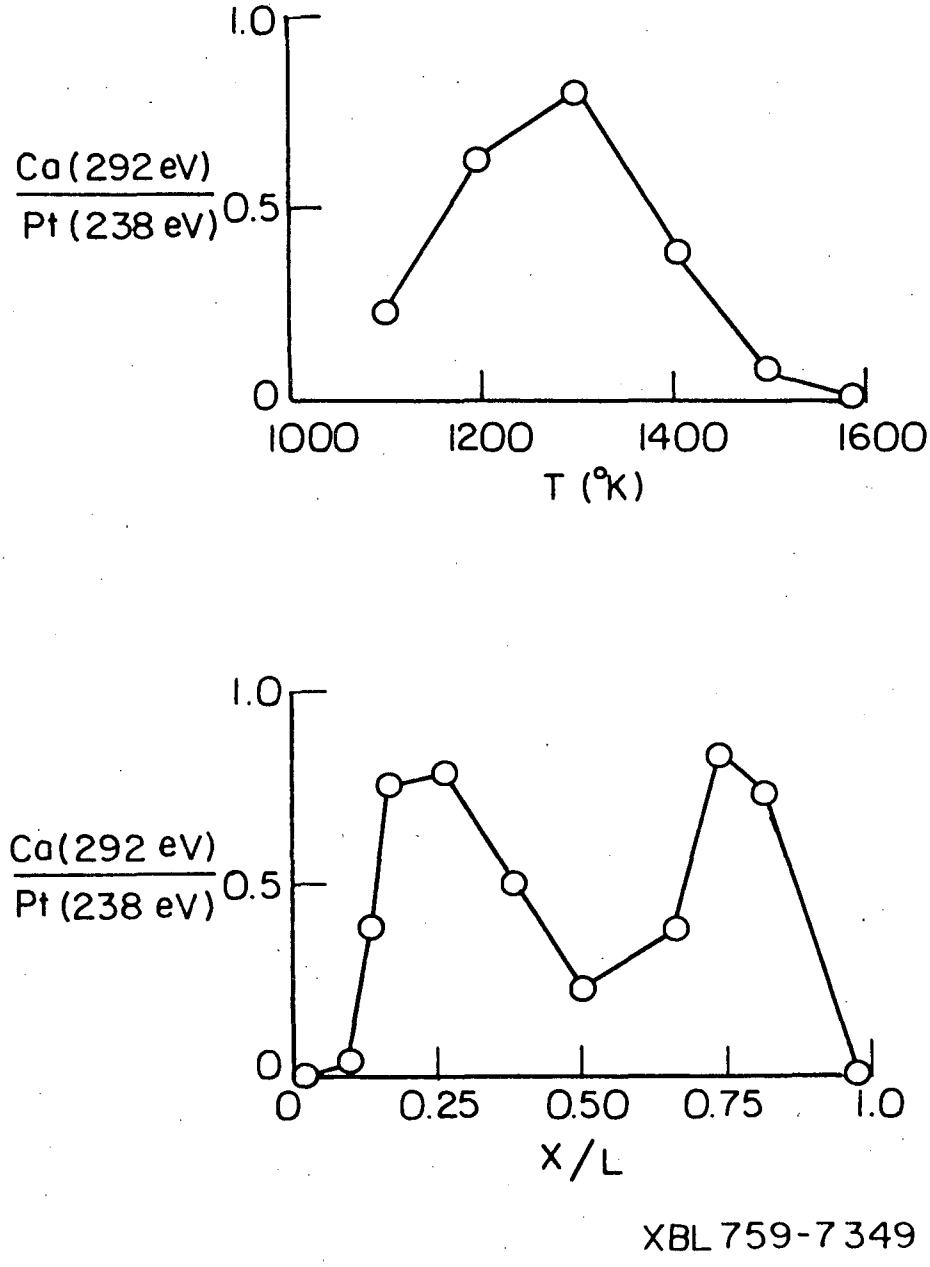

Fig. 2-11. Ratio of Auger single from Ca-292 eV to Pt-238 eV peaks as (a) function of temperature for 1 min anneals at each temperature and (b) as a function of position cross single crystal sample after 1300°K anneal. This pattern is typical of all crystals.

could be seen as a grayish discoloration. Since the cut sample heated uniformly and the oxygen flux was uniform, the oxide distribution should represent the Ca distribution in the Pt.

2.2. Mass Spectrometer Calibrations

2.2.1. The Mass Spectrometer Characteristics

There are many variables which can effect the observed mass spectrum of a given molecule. The ionizing energy of the electrons affects the fragmentation of the organic molecules studied; the higher the energy of the electrons the greater the fragmentation. The geometry of the ionizer, along with the applied potentials, affects the collection and injection efficiency of the ionized fragments into the filtering section. The type of filtering, quadrapole or magnetic sector, together with the resolution setting, affects the transmission of the ions to the catcher. Faraday cups and electron multipliers have different responses to various mass ions; the Faraday cup signal is proportional to the number ions and independent of mass and the electron multiplier signal is theoretically proportional to the momentum of the ion ($P_i = \sqrt{2m_i E_i}$) striking the first dynode times the gain through the dynode chain (10^3-10^7) and dependent on the square root of the mass. In actuality there is a mass dependence between 1 amu and about 25 amu which is approximately proportional to $\sqrt{m_i}$. Between 25 amu and 100 amu there is no mass dependence on the gain of the electron multiplier. For these reasons, it was necessary to determine the cracking pattern of each molecule of interest under the same spectrometer condition used during the experiments.

The mass spectrometer used is a UTI 100C quadrapole residual gas analyzer (RGA). In a space charge effect ionizer each electron emitted from the filament makes more than one pass through the ionization zone and can increase the number of ions created per molecule by an order of magnitude over the normal arrangements. The ionizer potentials used in all the experiments and calibrations are shown in Table 2-2. The ion energy and focus values are adjusted to nonoptimum[74] values to allow for the measurement of mass 2 ions $\left(H_2^+\right)$ with the Faraday cup. With the higher E_I and lower E_f, a large number of electrons (approximately equivalent to a 1×10^{-7} Torr negative current) reach the Faraday cup and make the positive ion current difficult to measure. This is not a problem at higher masses because the filtering potentials on the rods are sufficient to exclude electrons. The electron energy is reduced to decrease fragmentation and the emission current is reduced to decrease filament temperature and which in turn reduces reactions of hydrocarbons on the filaments. The resolution control is set for the resolution of $\frac{M}{\Delta M} \approx 2M$ where M is the ion mass the ΔM is the full width at half maximum of the mass peak which maintains maximum signal. The resolution is determined by the ratio of the rf to dc voltages on the filtering rods. The instrument has both an electron multiplier and a Faraday cup, although the Faraday cup was used for all the calibrations and most of the reactions.

Table 2-2. Detuning of ionizer to allow measurement of H_2 with Faraday cup.

	Optimum Settings	Values Used
Ion Energy	15	10
Electron Energy	70	50
Focus	-20	-40

2.2.2. Calibration Procedure

A nude ion gauge with tungsten filaments was used as the standard for the calibrations. Since the geometry was not changed between calibrations of the various gases, rough estimates could be made of the actual pressures of the gases using the calibrations given by various groups for nude ionization gauges.[75-84] Table 2-3 presents a summary of these values. All pressures given in this text are uncorrected ionization gauge pressures unless specifically noted; all reaction rates are determined using uncorrected ionization gauge pressures.

The calibrations were performed with the ion pump gate value partially closed. The reduced pumping speed from the chamber to the ion pump, about 1-2 ℓ/s, was much lower than the pumping speed of the ion pump. This reduction minimized backstreaming of hydrogen[85] and small hydrocarbons such as CH_4 or C_2H_4. The background was allowed increase up to a factor pressure of two upon partially closing the gate valve, but the pressure was kept under 2×10^{-9} Torr. A mass spectra was taken of the mass range of interest to determine the background gases' contribution to each mass peak.

The mass spectrometer calibrations were made at several different pressures. This was done by increasing the flow of the gas into the chamber at a constant gate valve closure. The background contribution of each mass peak was subtracted from the spectra of the gas. The resultant mass spectrometer signal for the parent peak (mass peak at molecular weight of molecule) was plotted against the recorded ionization gauge pressure corrected for the background pressure. The slope of this line through the origin gives the calibration factor shown in column

Table 2-3. Ionization gauge sensitivities for Bayard-Alpert gauge.

	References									
	75	76	77	78	79	80	81	82	83	84
	Accelerating Voltage									
			260	150		145	130	150	150	190
	Ionization Gauge Sensitivity									
Common	S/S_{N_2}	S/S_{N_2}	S/S_{Ar}	S/S_{Ar}	S/S_{N_2}	S/S_{N_2}	S/S_{N_2}	S/S_{N_2}	S/S_{N_2}	S/S_{N_2}
He	0.15	---	0.17	0.13	0.27	0.18	0.22	0.22	0.18	0.17
Ne	---	---	0.26	0.22	---	0.31	0.38	0.40	0.32	---
Ar	1.30	---	1.00	1.00	1.79	1.42	1.35	1.49	1.42	1.42
Kr	---	---	1.53	1.40	---	1.97	1.81	2.04	1.94	---
Xe	---	2.72	2.22	2.02	---	2.86	2.50	2.80	2.81	---
N_2	1.00	1.00	---	---	1.00	1.00	1.00	1.00	1.00	1.00
H_2	---	---	---	---	---	0.42	0.38	0.36	0.41	0.42
O_2	1.25	---	---	---	---	0.87	0.85	1.15	0.78	0.88
CO	---	1.09	---	---	---	1.11	0.85	0.87	1.01	0.99
CO_2	---	---	---	---	---	1.43	1.45	1.54	1.39	1.45
Air	1.05	---	---	---	---	---	---	---	0.91	---
SF_6	---	---	---	---	---	---	---	---	2.20	---
Cl_2	---	---	---	---	1.14	---	---	---	---	---
CH_4	---	---	---	---	---	---	---	---	---	1.6
C_2H_4	---	---	---	---	---	---	---	---	---	2.1
C_2H_6	---	---	---	---	---	---	---	---	---	2.6
C_6H_6	---	---	---	---	---	---	---	---	---	3.75
$C_6H_5CH_3$	---	---	---	---	---	---	---	---	---	6.8

3 of Table 2-4. The peak heights of the various mass fragments relative to either the parent peak or primary peak (mass peak with largest signal) of the gas were found, after subtracting the background contribution, by taking the mean of the relative values from each pressure.

2.2.3. Comparison with API Tables

Table 2-4 shows the values of the relative peak heights for all the fragments of the hydrocarbon molecules studied for both the UTI 100C and the National Bureau of Standards (NBS) contribution to the API Project 44.[86] As can be seen from Table 2-4, there is general agreement between the relative peak heights of the two types of instruments. The agreement between two laboratories, who contributed to the API Project 44 and used equivalent instruments, is slightly better. This is demonstrated for benzene with contributions by the NBS and the Atlantic Refining Co. using Consolidated Mass Spectrometers. There is better agreement within a group of peaks where the variances, which are a function of mass, are diminished than between two separated groups where variances are more important. Most of the data was taken with the Faraday cup; however, the electron multiplier was also used. Interestingly, this changes the relative cracking patterns of the hydrocarbons only a few percent. The gain of the electron multiplier changes reasonably linearly from 1.72×10^3 at 84 amu to 1.89×10^3 at 28 amu. The data from the UTI RGA is used for the reduction of reaction rate data when accuracy is desired. On preliminary experiments where only trends are desired, the API data was used.

Table 2-4. Relative intensities and calibration factor for various hydrocarbons.

Hydrocarbon	Mass Spec.	Calibration Torr Volts on 10^{-12} A m.f.c.	15	16	26	27	28	29	30	42	43	44	56	57	58	70	71	72	78	82	84	85	86	91	98	100	18	API Serial No.
Methane (CH_4)	UTI	$1.2\cdot10^{-5}$	0.78	1.00																								
	API	on 16	0.85	1.00																								
Ethylene (C_2H_4)	UTI	$1.1\cdot10^{-5}$	0.0069	--	1.00	0.986	1.86	0.039	0.001																			
	API	on 26	0.009	--	1.00	1.02	1.61	0.037	--																			
Ethane (C_2H_6)	UTI	$3.0\cdot10^{-5}$	0.114	--			4.10		1.00																			
	API	on 30	0.168	0.001	0.845	1.27	3.42	0.822	1.00																			
Propylene (C_3H_6)	UTI	$1.9\cdot10^{-5}$	0.0524	--	0.138	0.521				1.00	0.0366	0.0089																
	API	on 42	0.0787	0.0023	0.150	0.551	0.020			1.00	0.0327	0.0004																
Cyclopropane (C_3H_6)	UTI	$2.3\cdot10^{-5}$	0.0326	--					--	1.00		0.0028																
	API	on 42	0.054	0.0019	0.127	0.350	0.025	--	--	1.00	0.033	0.0004																
Propane (C_3H_8)	UTI	$7.5\cdot10^{-5}$	0.090	--	ND	ND	ND	3.00	0.0600	1.49	0.842	1.00																
	API	on 44	0.202	0.0055	0.282	1.38	2.04	3.42	0.0752	0.291	0.792	1.00																
n-Butane (C_4H_{10})	UTI	$1.6\cdot10^{-5}$	0.0177	--				0.405	0.0092		1.00	0.0340	0.0063	0.0220	0.144													4
	API	on 58	0.0483	0.0011	0.0536	0.379	0.333	0.448	0.0098	0.124	1.00	0.0336	0.0075	0.0256	0.126													
2-Methylpropane (i-C_4H_{10})	API		0.0555	0.0016	0.0195	0.279	0.0251	0.0637	0.0014	0.319	1.00	0.0332	0.0037	0.0301	0.0275													5
n-Pentane (n-C_5H_{12})	API	$(1.3\cdot10^{-5})$ on 72	0.0392	0.0009	0.0262	0.361	0.0580	0.247	0.0055	0.590	1.00	0.0333	0.0221	0.127	0.0055	0.0011	0.0050	0.0884										6
2-Methyl Butane (i-C_5H_{12})	API		0.0700	0.0025	0.0305	0.408	0.0607	0.460	0.0102	0.866	1.00	0.0337	0.171	0.545	0.0244	0.0010	0.0180	0.0686										7
Benzene (C_6H_6)	UTI	$1.2\cdot10^{-5}$	--	--	0.0298	0.0326		0.005	0.004	--	--	--	--	--	--	--	0.0014	0.0007	1.00									
	NBS		0.0089	0.0001	0.0322	0.0306	0.0019	0.0001	--	--	--	--	--	--	--	--	0.0001	0.0011	1.00									250
	ARCo	on 78	0.0073	--	0.0318	0.0318	0.0087	0.0004	--	--	--	--	--	--	--	--	--	0.0014	1.00									175
Cyclohexene (c-C_6H_{10})	UTI	$6.75\cdot10^{-5}$	0.0116	--	0.132	0.795		0.125	0.24	0.096	0.017	--	0.024	--	--	--	--	--	0.108	1.00								209
	API	on 82	0.108	0.0020	0.113	0.718	0.204	0.0865	0.0020	0.0761	0.0107	--	0.0109	0.0010	--	--	--	--	0.0384	1.00	0.0018							
Cyclohexane (c-C_6H_{12})	UTI	$5\cdot10^{-5}$	0.0542	0.001	0.065	ND	ND	ND	0.0054	0.642	0.283	ND	ND	ND	0.0010	ND	ND	--	0.00224	0.00272	1.00	0.0600	0.00188					216
	API	on 84	0.0589	0.0012	0.0429	0.371	0.181	0.164	0.0079	0.399	0.181	0.0058	1.325	0.0653	0.0009	0.0160	0.0006	--	0.0028	0.0029	1.00	0.0652	0.0017					
n Hexane (n-C_6H_{14})	API	$(1\cdot10^{-5})$ on 86	0.567	0.0023	0.0381	0.505	0.133	0.632	0.0136	0.410	0.813	0.277	0.447	1.00	0.0445	0.0068	0.0502	0.0027	--	--	0.0004	0.0041	0.141					9
Toluene (C_7H_8)	API	$2\cdot10^{-5}$ on 91	0.0117	0.0001	0.0154	0.0029	0.0005	--	0.0014	0.0069	0.0078	--	--	--	--	--	--	--	0.0019	--	0.0009	0.0042	0.0082	1.000				251
Methylcyclohexane (CH_3-c-C_6H_{11})	API		0.0492	0.0015	0.0198	0.287	0.0880	0.195	0.0051	0.354	0.0876	0.0026	0.299	0.0593	0.0018	0.216	0.0138	--	0.0023	0.142	0.0654	0.0019	--	0.0023	0.440	0.0011		217
n-Heptane (n-C_7H_{16})	API	$2\cdot10^{-5}$ on 100	0.0393	0.0011	0.0229	0.365	0.0747	0.464	0.0095	0.247	1.00	0.0320	0.265	0.480	0.0200	0.174	0.444	0.0233	0.0003	--	0.0017	0.0194	0.0028	0.0001	0.0003	0.130		14
2-Methylhexane	API		0.0395	0.0016	0.0125	0.250	0.0514	0.241	0.0050	0.382	1.00	0.0135	0.204	0.260	0.0115	0.0135	0.0176	0.0009	0.0002	--	0.0428	0.323	0.0269	--	--	0.0186		15
3-Methylhexane	API		0.0413	0.0012	0.0196	0.321	0.0501	0.431	0.0091	0.424	1.00	0.0136	0.341	0.471	0.0210	0.178	0.473	0.0260	0.0001	--	0.0094	0.0450	0.0024	--	--	0.0367		16
2,3-Dimethylpentane	API		0.0643	0.0022	0.0183	0.362	0.0645	0.481	0.0102	0.261	1.00	0.0135	1.00	0.714	0.0306	0.0962	0.348	0.0190	0.0002	0.0002	0.0020	0.0586	0.0048	--	0.0001	0.0222		19
2,4-Dimethylpentane	API		0.0651	0.0050	0.0141	0.240	0.0358	0.202	0.0045	0.261	1.00	0.0135	0.462	0.676	0.0294	0.0029	0.0092	0.0005	0.0001	0.0002	0.0029	0.174	0.0113	0.0002	--	0.0114		20
1-trans, 2-Dimethylcyclopentane			0.0582	0.0013	0.0202	0.292	0.108	0.199	0.0050	0.275	0.117	0.0036	1.00	0.136	0.0049	0.525	0.0305	0.0007	0.0018	0.0058	0.0082	0.0004	--	0.0011	0.257	0.0006		187
1-cis, 2-Dimethylcyclopentane	API		0.0582	0.0015	0.0239	0.349	0.124	0.219	0.0063	0.337	0.117	0.0046	1.00	0.127	0.0055	0.923	0.0498	0.0012	0.0020	0.0044	0.0092	0.0005	--	0.0013	0.224	0.0004		188
1-trans, 3-Dimethylcyclopentane	API		0.0701	0.0022	0.0227	0.330	0.120	0.229	0.0060	0.279	0.116	0.0031	1.00	0.143	0.0063	0.565	0.029	0.0008	0.0021	0.0254	0.0160	0.0004	--	0.0008	0.160	0.0003		189
1-cis, 3-Dimethylcyclopentane	API		0.0691	0.0019	0.0231	0.332	0.122	0.236	0.0064	0.294	0.119	0.0042	1.00	0.145	0.0054	0.988	0.0527	0.0012	0.0023	0.0205	0.0167	0.0005	--	0.0011	0.145	0.0004		190
Ethylpentane	API		0.0527	0.0008	0.0157	0.228	0.0810	0.260	0.0058	0.0842	1.00	0.0135	0.367	0.0357	0.0017	0.441	0.041	0.0236	0.0001	--	0.0008	0.0031	0.0001	--	--	0.0178		17
CO	UTI		--	ND	--	--	1.00	0.0127	0.0022																			179
	API		--	0.0267	--	--	1.00	0.0116	0.0022																			
H_2O	API		--	0.024																						1.00		

2.2.4. Linearity of Mass Spectrometer Signal

The linearity of the mass spectrometer for H_2 and N_2 is shown in Fig. 2-12. This is highly dependent on the geometry of the ionizer and in particular the filament placement. The instrument signal is linearly proportional to the ion gauge pressure up to 1×10^{-4} Torr and recommended in the UTI operating manual. The spectrometer signal is linear proportional to the ion gauge pressure up to 1×10^{-4} Torr and then bends over quite sharply and decreases with pressure above 5×10^{-4} Torr. It appears that ion-molecule reactions occur since the 3 amu peak for H_2 becomes prevalent above 5×10^{-4} Torr. The ion gauge pressure reading itself is non-linear in this region but maintains a positive slope. The older EAI quadrapoles mass spectrometers are linear at higher pressures, between 5×10^{-4} and 1×10^{-3} Torr, because of the different ionizer and smaller diameter filtering rods (shorter flight path in quadrapole section).

2.3. LEED Chamber as a Low Pressure Reactor

2.3.1. General Types of Reactors

There are several types of reactor configurations which can be used to measure kinetics of reactions on small area crystal surfaces. The reactors vary mainly by the method in which reactants are introduced and products removed. In a batch reactor, the reactants are introduced all at once at time (t) = zero and are consumed without replacement while being continually mixed. In a flow reactor, products are continuously withdrawn and reactants continuously feed. A semi-bath reactor is a combination of the batch and flow, using features of both types which are best suited for control of particular reaction studied.

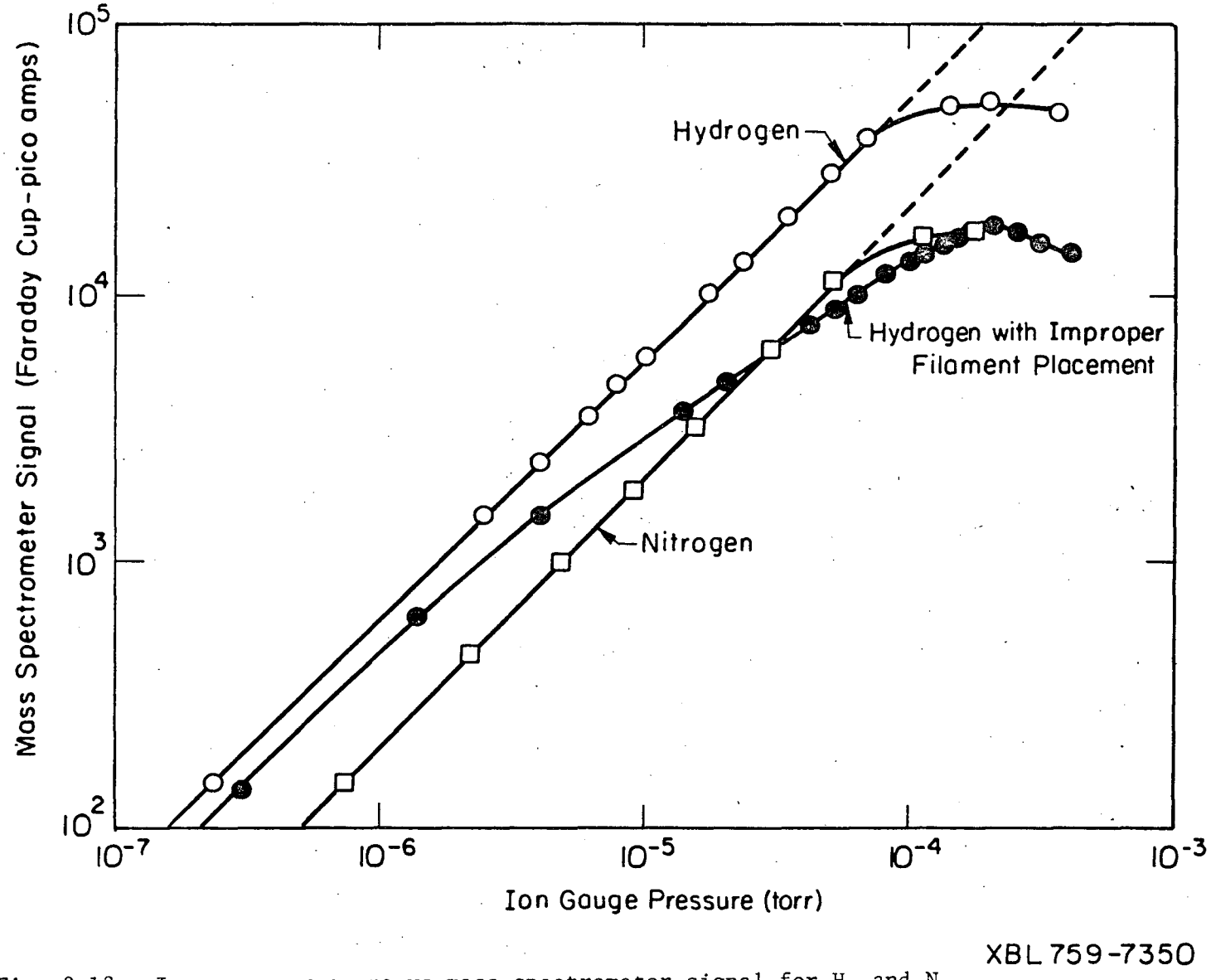

Fig. 2-12. Ion gauge pressure vs mass spectrometer signal for H_2 and N_2 demonstrating non-linearity above 1×10^{-4} Torr.

The various types of reactors are illustrated in Fig. 2-13 along with conversion profiles. The batch reactor configuration which was used in the n-heptane dehydrocyclization experiments is discussed in detail in Section 2.3.3. A semibatch reactor usually starts with one reactant in the reactor with the other reactant added slowly; the reaction mixture containing the product and reactant is either withdrawn slowly to maintain constant volume or allowed to accumulate. Several alternatives are depicted in Fig. 2-13b. Kinetic data are more difficult to obtain from these reactors as a result of the varying composition of the reactants with time; however, they offer good control of reaction rate. This method of reaction was not used in this investigation because of the difficulty in analyzing the kinetic data. There are two types of flow reactors as seen in Figs 2-13c and d, the back-mix reactor and the plug-flow reactor. The back mix reactor was used in the cyclohexane and cyclohexene dehydrogenation study and is described in Section 2.3.4. In a plug-flow reactor, which is the idealized fixed bed industrial catalytic reactor, the concept is that each volume element proceeds down the reactor with perfect radial mixing but no axial mixing. The geometry of the single crystal catalyst and the LEED chamber prevent this configuration from being used in the low pressure experimental studies. The plug-flow reactor depicted in Fig. 2-13d is called an integral reactor since the rate equation must be integrated to predict the reactor effluent composition. Another form has only a small volume of catalyst and very small differential conversions are achieved per pass of reactent through the catalyst. In the differential reactor, the rate equation need not be integrated for

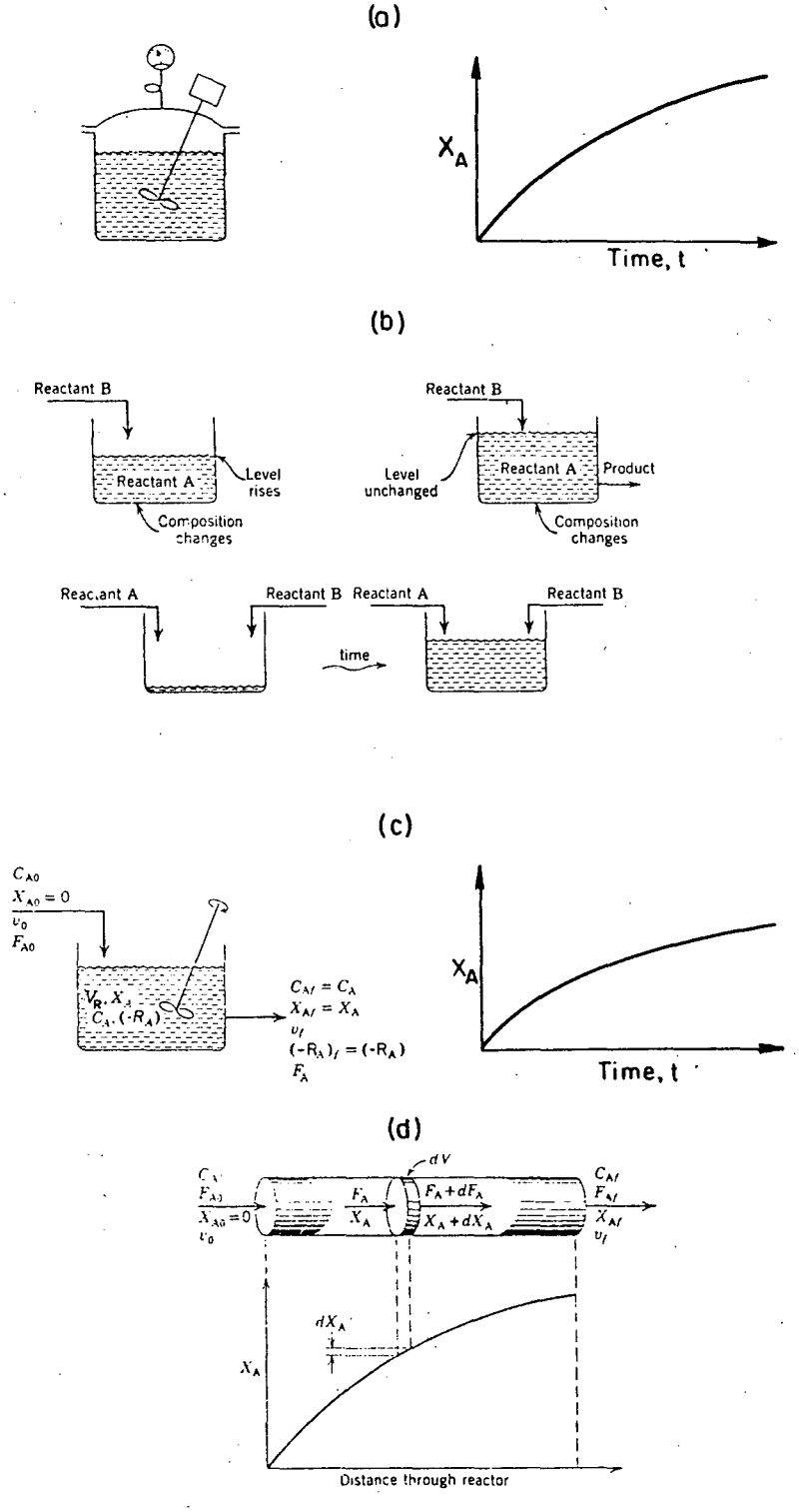

XBL 759 7346

Fig. 2-13. Illustration of various types of reactors and conversion curves for each. (a) Batch reactor, (b) several versions of a semibatch reactor, (c) back-mix flow reactor and (d) plug-flow reactor.

the idfferential conversion achieved in one pass. For examples of a differential reactor not plug flow reactor configuration, used in single crystal catalytic work at high pressures see Kahn[88] and Appendix B.

2.3.2. The Mass Balance

To analyze data from a reactor an accounting system for the reactant and product molecules is needed. This done with the material balance equation[89]

$$\begin{pmatrix}\text{rate of species}\\ \text{i flow into an}\\ \text{element of}\\ \text{volume}\end{pmatrix}-\begin{pmatrix}\text{rate of species}\\ \text{i flow out of an}\\ \text{element of volume}\end{pmatrix}-\begin{pmatrix}\text{rate of species}\\ \text{i removal by}\\ \text{chemical reaction}\\ \text{from element of}\\ \text{volume}\end{pmatrix}=\begin{pmatrix}\text{rate of species}\\ \text{accumulation in}\\ \text{an element of}\\ \text{volume}\end{pmatrix} \qquad (2\text{-}1)$$

This equation is entirely general and can be used for any system with any number of components.

A batch reactor is assumed well mixed throughout its entire volume and the element of volume in Eq. (2-1) becomes the reactor volume V_R. The rates of flow in and out of all species are zero; so Eq. (2-1) reduces into the familiar form for the removal of reactant i and a batch reactor

$$-R_i = \frac{dc_i}{dt} \qquad (2\text{-}2)$$

where R_i is the rate of reaction of species i. For example, in a second order irreversible bimolecular reaction $A + B \rightarrow C + D$, the conversion of A,

$$X_A(t) \equiv [C_A(t = 0) - C_A(t)]/C_A(t = 0) \quad ,$$

assuming $C_{A_o} = C_{B_o}$, is

$$C_{A_o} \frac{dX_A}{dt} = -R_A = -kC_{A_o}^2 (1 - X_A)^2$$

which integrates to

$$X_A = \frac{kC_{A_o} t}{1 - kC_{A_o} t} \quad . \tag{2-3}$$

This is the curve in Fig. 2-13a.

A back-mix reactor is assumed to be well mixed throughout (the element of volume is the entire reactor volume V_R); there is of course no accumulation of reactant in the reactor at steady state. Therefore, Eq. (2-1) becomes for the back-mix reactor configuration

$$v_o C_{i,in} - C_{i,out} v_o - R_i V_R = 0 \tag{2-4}$$

where v_o is the volumetric flow rate through the reactor and $c_{i,in}$ and $C_{i,out}$ are the concentrations of species i in the input and outflow streams of the reactor. For the example used above, $A + B \rightarrow C + D$ the conversion of A is obtained by algerbraic manipulations only,

$$X_A = \left(\frac{V_R}{v_o}\right) \frac{R_A}{C_{A,in}} = \left(\frac{V_R}{v_o}\right) kC_{A,in}(1 - X_A)^2 \quad . \tag{2-5}$$

The quantity $\tau \equiv (V_R/v_o)$ is the mean residence time of a molecule in the reactor and is used to control the extent of conversion. Equation (2-5) represents the curve plotted in Fig. 2-13c. Equations (2-2) and (2-4) will be specialized to a low pressure catalytic reactor like a LEED chamber in the next sections.

the idfferential conversion achieved in one pass. For examples of a differential reactor not plug flow reactor configuration, used in single crystal catalytic work at high pressures see Kahn[88] and Appendix B.

2.3.2. The Mass Balance

To analyze data from a reactor an accounting system for the reactant and product molecules is needed. This done with the material balance equation[89]

$$\begin{pmatrix}\text{rate of species}\\ \text{i flow into an}\\ \text{element of}\\ \text{volume}\end{pmatrix}-\begin{pmatrix}\text{rate of species}\\ \text{i flow out of an}\\ \text{element of volume}\end{pmatrix}-\begin{pmatrix}\text{rate of species}\\ \text{i removal by}\\ \text{chemical reaction}\\ \text{from element of}\\ \text{volume}\end{pmatrix}=\begin{pmatrix}\text{rate of species}\\ \text{accumulation in}\\ \text{an element of}\\ \text{volume}\end{pmatrix} \qquad (2\text{-}1)$$

This equation is entirely general and can be used for any system with any number of components.

A batch reactor is assumed well mixed throughout its entire volume and the element of volume in Eq. (2-1) becomes the reactor volume V_R. The rates of flow in and out of all species are zero; so Eq. (2-1) reduces into the familiar form for the removal of reactant i and a batch reactor

$$-R_i = \frac{dc_i}{dt} \qquad (2\text{-}2)$$

where R_i is the rate of reaction of species i. For example, in a second order irreversible bimolecular reaction $A + B \rightarrow C + D$, the conversion of A,

$$X_A(t) \equiv [C_A(t = 0) - C_A(t)]/C_A(t = 0) \quad ,$$

assuming $C_{A_o} = C_{B_o}$, is

$$C_{A_o} \frac{dX_A}{dt} = -R_A = -kC_{A_o}^2 (1 - X_A)^2$$

which integrates to

$$X_A = \frac{kC_{A_o} t}{1 - kC_{A_o} t} \quad . \tag{2-3}$$

This is the curve in Fig. 2-13a.

A back-mix reactor is assumed to be well mixed throughout (the element of volume is the entire reactor volume V_R); there is of course no accumulation of reactant in the reactor at steady state. Therefore, Eq. (2-1) becomes for the back-mix reactor configuration

$$v_o C_{i,in} - C_{i,out} v_o - R_i V_R = 0 \tag{2-4}$$

where v_o is the volumetric flow rate through the reactor and $c_{i,in}$ and $C_{i,out}$ are the concentrations of species i in the input and outflow streams of the reactor. For the example used above, $A + B \rightarrow C + D$ the conversion of A is obtained by algerbraic manipulations only,

$$X_A = \left(\frac{V_R}{v_o}\right) \frac{R_A}{C_{A,in}} = \left(\frac{V_R}{v_o}\right) kC_{A,in}(1 - X_A)^2 \quad . \tag{2-5}$$

The quantity $\tau \equiv (V_R/v_o)$ is the mean residence time of a molecule in the reactor and is used to control the extent of conversion. Equation (2-5) represents the curve plotted in Fig. 2-13c. Equations (2-2) and (2-4) will be specialized to a low pressure catalytic reactor like a LEED chamber in the next sections.

the idfferential conversion achieved in one pass. For examples of a differential reactor not plug flow reactor configuration, used in single crystal catalytic work at high pressures see Kahn[88] and Appendix B.

2.3.2. The Mass Balance

To analyze data from a reactor an accounting system for the reactant and product molecules is needed. This done with the material balance equation[89]

$$\begin{pmatrix}\text{rate of species}\\ \text{i flow into an}\\ \text{element of}\\ \text{volume}\end{pmatrix}-\begin{pmatrix}\text{rate of species}\\ \text{i flow out of an}\\ \text{element of volume}\end{pmatrix}-\begin{pmatrix}\text{rate of species}\\ \text{i removal by}\\ \text{chemical reaction}\\ \text{from element of}\\ \text{volume}\end{pmatrix}=\begin{pmatrix}\text{rate of species}\\ \text{accumulation in}\\ \text{an element of}\\ \text{volume}\end{pmatrix} \qquad (2\text{-}1)$$

This equation is entirely general and can be used for any system with any number of components.

A batch reactor is assumed well mixed throughout its entire volume and the element of volume in Eq. (2-1) becomes the reactor volume V_R. The rates of flow in and out of all species are zero; so Eq. (2-1) reduces into the familiar form for the removal of reactant i and a batch reactor

$$-R_i = \frac{dc_i}{dt} \qquad (2\text{-}2)$$

where R_i is the rate of reaction of species i. For example, in a second order irreversible bimolecular reaction A + B → C + D, the conversion of A,

$$X_A(t) \equiv [C_A(t = 0) - C_A(t)]/C_A(t = 0) \quad ,$$

assuming $C_{A_o} = C_{B_o}$, is

$$C_{A_o} \frac{dX_A}{dt} = -R_A = -kC_{A_o}^2 (1 - X_A)^2$$

which integrates to

$$X_A = \frac{kC_{A_o} t}{1 - kC_{A_o} t} \quad . \tag{2-3}$$

This is the curve in Fig. 2-13a.

A back-mix reactor is assumed to be well mixed throughout (the element of volume is the entire reactor volume V_R); there is of course no accumulation of reactant in the reactor at steady state. Therefore, Eq. (2-1) becomes for the back-mix reactor configuration

$$v_o C_{i,in} - C_{i,out} v_o - R_i V_R = 0 \tag{2-4}$$

where v_o is the volumetric flow rate through the reactor and $c_{i,in}$ and $C_{i,out}$ are the concentrations of species i in the input and outflow streams of the reactor. For the example used above, $A + B \rightarrow C + D$ the conversion of A is obtained by algerbraic manipulations only,

$$X_A = \left(\frac{V_R}{v_o}\right) \frac{R_A}{C_{A,in}} = \left(\frac{V_R}{v_o}\right) kC_{A,in}(1 - X_A)^2 \quad . \tag{2-5}$$

The quantity $\tau \equiv (V_R/v_o)$ is the mean residence time of a molecule in the reactor and is used to control the extent of conversion. Equation (2-5) represents the curve plotted in Fig. 2-13c. Equations (2-2) and (2-4) will be specialized to a low pressure catalytic reactor like a LEED chamber in the next sections.

the idfferential conversion achieved in one pass. For examples of a differential reactor not plug flow reactor configuration, used in single crystal catalytic work at high pressures see Kahn[88] and Appendix B.

2.3.2. The Mass Balance

To analyze data from a reactor an accounting system for the reactant and product molecules is needed. This done with the material balance equation[89]

$$\begin{pmatrix}\text{rate of species}\\ \text{i flow into an}\\ \text{element of}\\ \text{volume}\end{pmatrix}-\begin{pmatrix}\text{rate of species}\\ \text{i flow out of an}\\ \text{element of volume}\end{pmatrix}-\begin{pmatrix}\text{rate of species}\\ \text{i removal by}\\ \text{chemical reaction}\\ \text{from element of}\\ \text{volume}\end{pmatrix}=\begin{pmatrix}\text{rate of species}\\ \text{accumulation in}\\ \text{an element of}\\ \text{volume}\end{pmatrix} \tag{2-1}$$

This equation is entirely general and can be used for any system with any number of components.

A batch reactor is assumed well mixed throughout its entire volume and the element of volume in Eq. (2-1) becomes the reactor volume V_R. The rates of flow in and out of all species are zero; so Eq. (2-1) reduces into the familiar form for the removal of reactant i and a batch reactor

$$-R_i = \frac{dc_i}{dt} \tag{2-2}$$

where R_i is the rate of reaction of species i. For example, in a second order irreversible bimolecular reaction A + B → C + D, the conversion of A,

$$X_A(t) \equiv [C_A(t = 0) - C_A(t)]/C_A(t = 0) \quad ,$$

assuming $C_{A_o} = C_{B_o}$, is

$$C_{A_o} \frac{dX_A}{dt} = -R_A = -kC_{A_o}^2 (1 - X_A)^2$$

which integrates to

$$X_A = \frac{kC_{A_o} t}{1 - kC_{A_o} t} \quad . \tag{2-3}$$

This is the curve in Fig. 2-13a.

A back-mix reactor is assumed to be well mixed throughout (the element of volume is the entire reactor volume V_R); there is of course no accumulation of reactant in the reactor at steady state. Therefore, Eq. (2-1) becomes for the back-mix reactor configuration

$$v_o C_{i,in} - C_{i,out} v_o - R_i V_R = 0 \tag{2-4}$$

where v_o is the volumetric flow rate through the reactor and $c_{i,in}$ and $C_{i,out}$ are the concentrations of species i in the input and outflow streams of the reactor. For the example used above, $A + B \rightarrow C + D$ the conversion of A is obtained by algerbraic manipulations only,

$$X_A = \left(\frac{V_R}{v_o}\right) \frac{R_A}{C_{A,in}} = \left(\frac{V_R}{v_o}\right) kC_{A,in}(1 - X_A)^2 \quad . \tag{2-5}$$

The quantity $\tau \equiv (V_R/v_o)$ is the mean residence time of a molecule in the reactor and is used to control the extent of conversion. Equation (2-5) represents the curve plotted in Fig. 2-13c. Equations (2-2) and (2-4) will be specialized to a low pressure catalytic reactor like a LEED chamber in the next sections.

the idfferential conversion achieved in one pass. For examples of a differential reactor not plug flow reactor configuration, used in single crystal catalytic work at high pressures see Kahn[88] and Appendix B.

2.3.2. The Mass Balance

To analyze data from a reactor an accounting system for the reactant and product molecules is needed. This done with the material balance equation[89]

$$\begin{pmatrix}\text{rate of species}\\ \text{i flow into an}\\ \text{element of}\\ \text{volume}\end{pmatrix}-\begin{pmatrix}\text{rate of species}\\ \text{i flow out of an}\\ \text{element of volume}\end{pmatrix}-\begin{pmatrix}\text{rate of species}\\ \text{i removal by}\\ \text{chemical reaction}\\ \text{from element of}\\ \text{volume}\end{pmatrix}=\begin{pmatrix}\text{rate of species}\\ \text{accumulation in}\\ \text{an element of}\\ \text{volume}\end{pmatrix} \qquad (2\text{-}1)$$

This equation is entirely general and can be used for any system with any number of components.

A batch reactor is assumed well mixed throughout its entire volume and the element of volume in Eq. (2-1) becomes the reactor volume V_R. The rates of flow in and out of all species are zero; so Eq. (2-1) reduces into the familiar form for the removal of reactant i and a batch reactor

$$-R_i = \frac{dc_i}{dt} \qquad (2\text{-}2)$$

where R_i is the rate of reaction of species i. For example, in a second order irreversible bimolecular reaction A + B → C + D, the conversion of A,

$$X_A(t) \equiv [C_A(t = 0) - C_A(t)]/C_A(t = 0) \quad ,$$

assuming $C_{A_o} = C_{B_o}$, is

$$C_{A_o} \frac{dX_A}{dt} = -R_A = -kC_{A_o}^2 (1 - X_A)^2$$

which integrates to

$$X_A = \frac{kC_{A_o} t}{1 - kC_{A_o} t} \quad . \tag{2-3}$$

This is the curve in Fig. 2-13a.

A back-mix reactor is assumed to be well mixed throughout (the element of volume is the entire reactor volume V_R); there is of course no accumulation of reactant in the reactor at steady state. Therefore, Eq. (2-1) becomes for the back-mix reactor configuration

$$v_o C_{i,in} - C_{i,out} v_o - R_i V_R = 0 \tag{2-4}$$

where v_o is the volumetric flow rate through the reactor and $c_{i,in}$ and $C_{i,out}$ are the concentrations of species i in the input and outflow streams of the reactor. For the example used above, A + B → C + D the conversion of A is obtained by algerbraic manipulations only,

$$X_A = \left(\frac{V_R}{v_o}\right) \frac{R_A}{C_{A,in}} = \left(\frac{V_R}{v_o}\right) kC_{A,in}(1 - X_A)^2 \quad . \tag{2-5}$$

The quantity $\tau \equiv (V_R/v_o)$ is the mean residence time of a molecule in the reactor and is used to control the extent of conversion. Equation (2-5) represents the curve plotted in Fig. 2-13c. Equations (2-2) and (2-4) will be specialized to a low pressure catalytic reactor like a LEED chamber in the next sections.

the idfferential conversion achieved in one pass. For examples of a differential reactor not plug flow reactor configuration, used in single crystal catalytic work at high pressures see Kahn[88] and Appendix B.

2.3.2. The Mass Balance

To analyze data from a reactor an accounting system for the reactant and product molecules is needed. This done with the material balance equation[89]

$$\begin{pmatrix}\text{rate of species}\\ \text{i flow into an}\\ \text{element of}\\ \text{volume}\end{pmatrix}-\begin{pmatrix}\text{rate of species}\\ \text{i flow out of an}\\ \text{element of volume}\end{pmatrix}-\begin{pmatrix}\text{rate of species}\\ \text{i removal by}\\ \text{chemical reaction}\\ \text{from element of}\\ \text{volume}\end{pmatrix}=\begin{pmatrix}\text{rate of species}\\ \text{accumulation in}\\ \text{an element of}\\ \text{volume}\end{pmatrix} \qquad (2\text{-}1)$$

This equation is entirely general and can be used for any system with any number of components.

A batch reactor is assumed well mixed throughout its entire volume and the element of volume in Eq. (2-1) becomes the reactor volume V_R. The rates of flow in and out of all species are zero; so Eq. (2-1) reduces into the familiar form for the removal of reactant i and a batch reactor

$$-R_i = \frac{dc_i}{dt} \qquad (2\text{-}2)$$

where R_i is the rate of reaction of species i. For example, in a second order irreversible bimolecular reaction $A + B \rightarrow C + D$, the conversion of A,

$$X_A(t) \equiv [C_A(t = 0) - C_A(t)]/C_A(t = 0) \quad ,$$

assuming $C_{A_o} = C_{B_o}$, is

$$C_{A_o} \frac{dX_A}{dt} = -R_A = -kC_{A_o}^2 (1 - X_A)^2$$

which integrates to

$$X_A = \frac{kC_{A_o} t}{1 - kC_{A_o} t} \quad . \tag{2-3}$$

This is the curve in Fig. 2-13a.

A back-mix reactor is assumed to be well mixed throughout (the element of volume is the entire reactor volume V_R); there is of course no accumulation of reactant in the reactor at steady state. Therefore, Eq. (2-1) becomes for the back-mix reactor configuration

$$v_o C_{i,in} - C_{i,out} v_o - R_i V_R = 0 \tag{2-4}$$

where v_o is the volumetric flow rate through the reactor and $c_{i,in}$ and $C_{i,out}$ are the concentrations of species i in the input and outflow streams of the reactor. For the example used above, A + B → C + D the conversion of A is obtained by algerbraic manipulations only,

$$X_A = \left(\frac{V_R}{v_o}\right) \frac{R_A}{C_{A,in}} = \left(\frac{V_R}{v_o}\right) kC_{A,in}(1 - X_A)^2 \quad . \tag{2-5}$$

The quantity $\tau \equiv (V_R/v_o)$ is the mean residence time of a molecule in the reactor and is used to control the extent of conversion. Equation (2-5) represents the curve plotted in Fig. 2-13c. Equations (2-2) and (2-4) will be specialized to a low pressure catalytic reactor like a LEED chamber in the next sections.

2.3.3. The Batch Reactor at Low Pressure

A batch reactor is good for measuring initial rates of reaction and determining reaction kinetics of a simple form. The changing reactant concentrations and the possible inhibiting effects of the products make analysis of the rate data difficult. However, since a complete kinetic description was not desired, the batch reactor was used in studies of the dehydrocyclization of n-heptane to toluene.

The batch reactor configuration is simple and straightforward. The two leak values are again used for accurate control of the amount of reactant introduced. The mass spectrometer monitors the reactant and product pressures.

Equation (2-2) is modified at low pressures in the single crystal catalytic reactor to

$$V_R \frac{dn_i}{dt} = -(TN_i)\ S \qquad (2\text{-}6)$$

where TN_i is the turnover number of species i in units of molecules of i removed/surface atom/second, S is the total number of surface atoms and n_i is the number density of molecules in the reactor. Since only initial rates were determined using the batch reactor, the initial slope was approximated by $\delta n_i/\delta t$. Typical values for the terms in Eq. (2-6) for the formation of toluene from n-heptane are: $V_R = 15{,}000\ cm^3$, $S = 10^{15}$ surface atoms (approximately 0.8 cm^2 of Pt), $\delta n_i/\delta t$ is 2×10^5 molecules/cm^2 in 30 sec (3×10^9 molecules of toluene produced in 30 sec by the catalyst), which gives a turnover number of 10^{-7} sec^{-1}.

The assumption of the reactor volume being well mixed is excellent. At the low pressures used in this investigation 10^{-5} Torr or below, there

is molecular flow in the reactor. The mean free path of nitrogen at 10^{-5} Torr and 25°C is 5.3 meters,[90] which is much larger than the largest dimension of the reactor, ~0.5 meter. This is good in that the reactor becomes mixed on the order of 5 milliseconds, the transit time of a molecule across the reactor.

2.3.4. The Back-Mix Reactor at Low Pressure

The back-mix flow reactor is good for measuring steady-state rates of reaction. The constant reactant concentrations ease the determination of kinetics and changing the conversion level will give information on the inhibiting effects of the products. This reactor configuration was used in the studies of the dehydrogenation of cyclohexane and cyclohexene to benzene.

The reactants enter the 15 liter well mixed vessel through two hypodermic needles aimed at the center of the chamber. These needles cause the "pressure" (flux) of reactant molecules to be higher in the region facing the LEED optics. This is good for adsorption studies where a low background pressure and high flux to the sample are desirable. However, in the reaction studies where the pumping speed is low, the chamber background pressure becomes equivalent to or higher than the entering pressure from the needle. Thus the effect of the needle is lower, and experimentally is has no affect on the rate of the cyclohexane dehydrogenation reaction which has a very low reaction probability, 10^{-4}. This was determined by rotating the active crystal away from the needle and blocking the flux with the "cold and dirty" crystal. For the cyclohexene dehydrogenation reaction, where the reaction probability is on the order of 0.1 to 1.0, rotating the crystal causes a 10% drop

in the reaction rate. Two separate leak valves are used for easy control of the hydrogen to hydrocarbon ratio during the reaction. If hydrogen and hydrocarbon are fed into one manifold, mixing takes place by gas diffusion which at the pressures used would have a time constant for mixing of $\tau = \ell^2/D \approx 30$ min; a wait of 1 to 2 hr would be required before the H_2:HC ratio changed the desired amount. This is an unreasonably long time since the surface will not stay clean that long.

The general equation for a back-mix reactor, Eq. (2-4), is modified for the low pressure back-mix reactor configuration to give

$$N_{i,in} - N_{i,out} = (TN_i)\ S \tag{2-7}$$

where $N_{i,in}$ and $N_{i,out}$ are the number of molecules of species i which flow in and out per second and $(TN_i)\ S$ the total rate of removal of species i. For the products such as benzene the influx is zero, and the outflow can be calculated from the equation for molecular flow through an orifice,[91] therefore Eq. (2-7) becomes

$$N_{i,out} = \frac{n_i v_i A_o}{4} = (TN_i)\ S \quad . \tag{2-8}$$

where n_i is the number density, v_i is molecular velocity and A_o is the area of the orifice. This equation is the rate at which molecules collide with a surface of area A_o. The surface is not present so the molecules escape from the reaction chamber into the pump region. Here they are pumped to less than 0.01 of the pressure in the reaction chamber, thus the rate of backsteaming from the pump region is less than 0.01 of the reaction rate. Typical values for the terms in Eq. (2-8) for the dehydrogenation of cyclohexane to benzene are:

$S = 10^{15}$ surface atoms, $v_i = 2840$ cm/sec the molecular velocity of benzene at 25°C, $n_i = 7\times10^{+6}$ molecules/cm^3 which corresponds to 2×10^{-10} Torr, and $A_o = 0.2$ cm^2 giving a turnover number of 10^{-5} sec^{-1}.

To form the small area orifice between the reaction chamber and the ion pump which allows the reaction rate to be determined quantitatively the gate value between the reaction chamber and the ion pump is partially closed during a reaction to reduce the pumping speed for hydrogen and hydrocarbons. An area of approximately 0.2 cm^2 is left open from the 75 cm^2 throat area. The orifice area is measured by the time response of the hydrogen pressure to a step change in input flux or orifice area. Hydrogen is used for the transient pressure measurements since it does not physisorb on the reactor walls; this eliminates any possible effects of slow reversible desorption from the walls as is found with hydrocarbons. If the assumption of low back pressure were true, the same orifice diameter would be determined by turning off the H_2 influx or by changing the orifice area. However, the ion pump on the vacuum system used in this investigation is saturated with hydrogen and the pumping speed reduced to ~12 liters/sec at 10^{-7} Torr of H_2 from a nominal 140 ℓ/s. Therefore, a step decrease in the hydrogen influx did not determine the orifice area, but a sudden decrease in orifice area from A_o to A_f which is independent of ion pump speed could be used accurately. (The two methods gave the same orifice area on another vacuum system.) A mass balance calculation on the chamber for hydrogen gives, by analogy with Eq. (2-1)

$$\left(n_{ip}\,\frac{v_H A_f}{4} + N_{H_2}\right) - \left(\frac{n_R v_H A_f}{4}\right) - (0) = \left(V_R\,\frac{dn_R}{dt}\right) \qquad (2\text{-}9)$$

I.C. $n_R = n_{R_o}$ at $t = 0$ where the input has two terms, one is flow through the variable leak value N_{H_2} and the second is backstreaming from the ion pump region of density n_{ip}; the outflow term is the same as in Eq. (28); there is no production of H_2; and the righthand term gives the rate of accumulation of H_2 in the reaction chamber. Upon integration and some manipulation, Eq. (2-9) becomes

$$A_o = \left(\frac{4V_R}{v_H}\right)\left(\frac{n_{R_f}}{n_{R_o}}\right)\frac{1}{t}\,\ln\left[\frac{n_{R_f} - n_{R_o}}{n_{R_f} - n_R(t)}\right] \qquad (2\text{-}10)$$

A typical data set for the determination of the pumping speed is shown in Table 2-5. The assumption of low pressure for hydrocarbons in the ion pump region is good. The pumping speed was measured for a light hydrocarbon, ethane, that does not adsorb on the walls appreciably by both methods. The orifice sizes obtained were the same to within 15% by either method for the two ethane and one hydrogen determinations.

2.3.5. Determination of Reaction Rates from Mass Spectra

The lowest reaction rate that can be measured is related to the lowest partial pressure that can be measured. As was seen in Table 2-4, the hydrocarbons fragment into a large number of different mass ions in the mass spectrometer, but each compound has its own characteristic pattern. For a mixture of compounds, the intensity from each compound at a particular mass peak should be additive on a mole basis. In other words, solving the system of linear equation

$$i = Hp \qquad (2\text{-}11)$$

Table 2-5. Sample data for pumping speed calculation.

T(sec)	Mass 2 Signal	$A_o=(0.333)\left(\frac{1515}{595}\right)\frac{1}{t}\ln\left(\frac{920}{1515-n_R}\right)$	Pump Speed for Benzene
0	595	0.193	
0.75	740	0.186	
		$= 1.85\ cm^2$	$1350\ \frac{cm^3}{sec}$
1.75	888	0.181	
3.75	1102	0.180	
6.76	1295		
∞	1515		

where i is the column vector of measured intensities at each mass, H is the matrix of peak intensities for each compound (the transpose of the matrix formed by Table 2-4 divided by the molecules calibration factor), and p is the row vector of partial pressures of each compound. It is not been attempted to experimentally verify this equation, but there are no known reasons why it is not true. A trivial example of the use of Eq. (2-11) is given for the separation of dehydrogenation products of cyclohexane reaction, cyclohexene and benzene. The measured intensities are for 78, 82 and 84 amu respectively, i^t = 0.0180, 0.0051 and 1.177 (data from 012875). The H matrix is

$$H = \begin{vmatrix} 1/1.4\times10^{-8} & \frac{0.0384}{6.75\times10^{-8}} & \frac{0.00224}{5.0\times10^{-8}} \\ 0 & \frac{1}{6.75\times10^{-8}} & \frac{0.00272}{5.0\times10^{-8}} \\ 0 & \left(\frac{0.0018}{6.75\times10^{-8}}\right) & \frac{1}{5.0\times10^{-8}} \end{vmatrix} \qquad (2\text{-}12)$$

Therefore, the desired vector of pressures is just H^{-1} i and gives for C_6H_6, C_6H_{10} and C_6H_{12} respectively, p_i = 2.1×10^{-10}, 1.2×10^{-10}, 5.9×10^{-8} Torr.

In a reaction where no isomerization occurs, but only dehydrogenation and hydrogenolysis occur, such as with cyclohexane or cyclohexene as the reactant, the H matrix of the expected products can be written as a semi-diagonal matrix. (The bracketed term in Eq. (2-2) is small enough to be ignored.) This allows simple back substitution to determine p_i. In the determination of all hydrogenolysis products from a reaction, back substitution is also used; this produces large cumulative errors for low molecular weight products, particularly methane, making their determination less accurate. The determining factor here, as in other

reactions, is the ability to measure mass peakheight accurately and reproducibly. When the reactant's and other product's contributions to a mass peak j are the same order of magnitude or smaller than the contribution to j from compound of interest, i, the partial pressure of i can be determined accurately. The minimum contribution from i to a peak j which can be confidentally measured varies from about 4% of the total peak height for a large peak to 20% for small peak. The major contribution to error is that the noise in the unfiltered mass spectrometer signal is proportional to the inverse square root of the flux of ions to the detector, and to the noise introduced in the sensing amplifiers. This is reduced greatly by capacitative filtering of the signal and averaging successive sweeps through the spectrum.

The pressure of compound i in the reaction chamber and, therefore, its contribution to a mass peak is inversely proportional to its pumping speed. The slower the pumping speed, the longer the residence time and the lower the reaction rate which can be measured. In the extreme, a batch reactor, an infinitely slow reaction could be measured if it proceeded for infinite time. The minimum detectable amount of a compound whose molecular weight is approximately equal to or less than the reactent molecular weight is about 1 part in 3000. At the conditions used in this study for the back-mix reactor (cyclohexane and cyclohexene reactions) of ~1 ℓ/s pumping speed and 0.8 cm^2 of catalyst, the minimum detectable dehydrogenation turnover number to benzene is approximately 1×10^{-6} sec^{-1} (an order of magnitude smaller than the actual rates), while for cracking to ethylene the minimum level is approximately 3×10^{-6} sec^{-1}. For isomerization reactions, the minimum

level is worse, $\sim 1\times10^{-4}$ sec^{-1}, because the cracking pattern of the isomers are similar and a larger increase in the pressure of i is needed for an accurate determination.

The minimum detectable amount of products for a batch reactor is again determined by the ability to measure changes in the mass spectral peak heights. Since ideally there is no pumping of products, i, a mass peak j with contributions from both i and the reactants should increase or at least decrease more slowly than mass peaks associated only with the reactants. By monitoring the peaks for several minutes, turnover numbers as low as 1×10^{-8} sec^{-1} can be determined. However, there is a great uncertainty to turnover numbers this low, which has not been evaluated, caused by pumping of the products by the walls and the mass spectrometer filament. It is possible that this effect, which may be proportional to product pressure, could cause the measured rate to be as much as an order of magnitude too low. This effect is not reduced by vapor depositing a thick layer of gold on the walls of the chamber as there are apparently enough uncoverable areas (LEED optics, mass-spectrometer head, etc) and a significant contribution from the mass spectrometer filament.

2.3.6. LEED Chamber as Low Pressure Reactor--Comparison of Modes

There are advantages and disadvantages to all the discussed methods of using a LEED chamber as a catalytic reactor. The types which will be compared are the back-mix flow reactor and the batch reactor. The reaction chamber could not be used as a plug flow reactor and it was not used as a semi-batch reactor, so these will not be discussed further.

A major advantage of the flow reactor is that the background gas impurities are lower than in the batch reactor mode. The hydrocarbon reactants and products will adsorb on the walls of the reaction chamber and displace other species, mainly CO. In the batch reactor, the impurity gas's pressure rises continuously throughout the experiment and can reach quite high levels, up to 10^{-5} Torr in a 15 min experiment. This can be kept below 10^{-7} Torr by preflushing with reactant hydrocarbon for several minutes before valving off the pump. In a flow reactor the CO is still displaced from the walls, but it is pumped rapidly with the CO pressure remaining below 2×10^{-9} Torr at all times under the flow conditions used.

Other associated problems related to wall adsorption is that the product may adsorb on the walls more strongly than the reactant and displace it from the walls. This is particularly true with an aromatic product and a parafinic reactant. The equilibrium adsorption on the walls is no doubt related to pressure, probably linearly (physical adsorption), and will increase with increasing product pressure. The reaction rate may appear up to an order of magnitude lower than it actually is. In a flow system where the steady state rate is measured, the gaseous product is in equilibrium with that adsorbed on the wall. The only effect of wall adsorption would be to increase the time required to reach steady state. This adsorption is very small, on the order of 10^{10} molecules/m^2 of surface area. At the lower pressures of reactant used in flow systems there is less background reaction and pumping by the mass spectrometer filaments. The filament removes both products and reactants from the gas phase by pyrolysis and produces

methane. With W filaments this is very large, two orders of magnitude larger than the Pt catalyzed rate of methane production, and first order in pressure in the 10^{-5} Torr range. With ThO-Ir filaments the effect is slightly less than the Pt rate under batch conditions and much less in a flow system. A source of uncertainty in the measured rate in a flow system is the ion pump. Since the pressure of the products is not zero in the pump region there is some back-streaming of molecules. Methane is always produced but in particularly large quantities with H_2 in the pumped gas. At very long times, 5 to 10 hr, of pumping cyclohexane, cyclohexene is produced. This of course is not a problem with a batch reactor. A positive displacement pump such as a turbomolecular pump or diffusion pump would eliminate this problem.

As was mentioned previously, approximately two orders of magnitude lower rate can be measured in a batch reactor than a flow reactor. The shorter residence time in the flow reactor does not allow the product to build up to a measurable level at the lower rates. The lower residence time in the flow system keeps the total conversion much lower, a few percent, instead of 50% or more in a batch reactor in 15 min. The low conversions keep secondary reactions of the products from becoming a significant portion of the total product. The flow reactor used in this investigation can measure reaction rates two order of magnitude higher than can be measured accurately in a batch reactor. With a better, faster pump much higher reaction rates could be measured at lower conversions.

The reaction rate data are easier to acquire and interpret from a flow reactor than a batch reactor. The mass spectra from the flow reactor

remain variant with time while they change in the batch reactor. The time required for a sweep of the relevant mass range 12 to 101 amu requires 2 min to complete with a reasonable time constant on the amplifier. In this time, appreciable change (up to 10%) has occurred in the total conversion in a batch reactor. For accurate analysis of partial pressure, all the relevant peaks must be interpolated to a given time and Eq. (2-11) solved at that given time for the partial pressures. With the flow system several mass spectra may be averaged to obtain the mean peak heights which are used in Eq. (2-11). The reaction rate at a given set of conditions is obtained directly from the product partial pressures in the flow reactor, but the partial pressure data must be differentiated in the batch reactor. The amount and hydrogen content of the hydrocarbon adsorbed on the surface are critical to the catalyst activity and selectivity. In the flow reactor the amount of hydrocarbon adsorbed on the surface as well as the desorption rate can readily be determined. The preflush in a batch reactor experiment saturates the catalyst surface at low temperature with hydrocarbon. When the catalyst is later heated rapidly to start the reaction, thermal decomposition products may be measured instead of a true catalytic reaction. (See Appendix A for a further discussion of this problem in connection with data of D. Hagen and G. A. Somorjai[92].)

Most of the advantages lie with a flow system for studying catalytic reactions at low pressures. The batch system can measure lower reaction rates, but the interpretation of results is more difficult. The batch reactor will prolong the life of an ion pump as an economic incentive.

2.4. Details of Experimental Procedure

The details of the experimental procedure for the two types of reactor configurations used in this investigation are given. The batch reactor system was used extensively in the studies of the n-heptane dehydrocyclization. The flow reactor (back-mixed) was used in the cyclohexane and cyclohexene dehydrogenation studies. The conditions given will be those of the standard test conditions used to compare reactivity amoungst the various catalyst surfaces.

2.4.1. The Batch Reactor

The crystal on which it is desired to run the reaction is heated to 850° to 900°C. The other crystal, which has no electrical current flowing through it, is heated by radiation only and increases in temperature to approximately 45°C under these conditions. The leak valve is then opened introducing O_2 to a background pressure of approximately 7×10^{-8} Torr with the gate valve to the pump open. This pressure is measured on an ion gauge not in the pump throat. If the surface is heavily carbon contaminated the gate valve is partially closed to increase the O_2 pressure to 1×10^{-6} Torr, otherwise it is left open. After approximately 10 min the oxygen flow is stopped and H_2 is introduced to a pressure of 1×10^{-7} Torr through a different leak valve. The crystal is cooled and the O_2 removed from the manifold. An Auger electron spectrum is taken to ascertain that all the carbon was removed from the surface and the extent of oxygen adsorption. If there is O on the surface, the crystal is heated to over 1000°C for 30 sec, another Auger spectrum is taken and the LEED pattern checked for any irregularities. This procedure cleans both sides of the crystal.

The crystal is now clean and ready for a reaction or adsorption experiment.

When the crystal has cooled to at least below 250°C, and preferably below 150°C, n-heptane is introduced. The ion gauge has been off since O_2 introduction, the n-heptane and hydrogen pressures are measured with the mass spectrometer. The manifold is flushed 3 times with the gas (vapor) being used to remove any traces of the previous gas, oxygen. The manifold is also baked after use with a hydrocarbon to hasten the hydrocarbons desorption. The n-heptane pressure does not have a fast response to changes in leak valve setting because the needle restricts the flow slightly. This causes a large amount of adsorption on the inside of the inlet tube and hence about 3 min for pressure build up to 1×10^{-7} Torr. This build-up time may be decreased but only to 1 min by removing the needle (014 gauge, approximate inside dia 2 mm). The n-heptane is allowed to flow for 2 min at this rate to replace CO on the walls of the chamber, as discussed earlier in Section 2.3.3. The gate valve is now shut and the pressures increase. The hydrogen input flux is increased and when its pressure is 5×10^{-5} Torr, the H_2 is shut off. The n-heptane flux is now increased and when its pressure is 5×10^{-6}, the leak valve is closed. The n-heptane pressure will build up to 1×10^{-5} Torr from desorption from the inlet tube. While this build up is occurring, mass spectra are taken to monitor the background reaction rates and the build up of the n-heptane. After about 5 min the mass spectra are almost invariant with increases in some peaks (mainly methane) from background reactions. At this point the crystal is heated in 10 to 30 sec to the desired reaction temperature, usually 350°C, and mass spectra are taken continuously. Two overlapping

ranges of mass spectrum are scanned; one from 12 amu to 101 amu and the other from 90 amu to 102 amu. The first allows the evaluation of all products, hydrogenolysis, isomerization and dehydrocyclization, while in the second the small toluene and dehydrogenation product peaks are amplified two orders of magnitude to allow more accurate measurement. The reaction is followed until the reference peak for the product does not increase or until 15 min have elapsed. The isomerization and dehydrocyclization reactions typically "poison" in 5 to 10 min on a platinum surface, while hydrogenolysis does not poison in 15 min.

The reactor is pumped down and the LEED pattern is examined. A picture may be taken at this point if any new diffraction features appear (besides high background). An Auger spectrum is taken to determine the amount of carbon deposited on the catalyst surface. A second batch reaction may be run to determine the amount of reversible deactivation of the catalyst. The system must be reflushed of CO, but the 3 min required to obtain a steady flux of n-heptane is sufficient. The chamber requires between 12 and 24 hr to obtain its original base pressure after the experiments.

2.4.2. The Flow Reactor

The crystal is cleaned in a manner similar to that for the batch reactor, except after the 1000°C flash the crystal is cooled to the reaction temperature, usually 150°C. The H_2 flow is adjusted to give a pump current of 200 μa, which corresponds roughly to 1×10^{-7} Torr. The gate valve is then adjusted to raise the H_2 pressure to 8×10^{-7} Torr. The hydrocarbon is introduced through the other leak valve to a pressure

of 4×10^{-8} Torr. There is again a lag time caused by adsorption of reactant on the walls; this is about equal for cyclohexene and n-heptane at 3 min, but shorter for cyclohexane at 1 min. The pressure is monitored continuously with the mass spectrometer again in two ranges, 12 to 88 and 77 to 87, for monitoring hydrogenolysis activity and a more sensitive sweep for dehydrogenation activity, respectively. Either the temperature of the catalyst is changed or the H_2 flux (pressure) is changed to determine their affect on the reaction rate. When the experiment is concluded the pumping speed of the remaining open area of the gate valve is measured. As was discussed in Section 2.3.1, the open area of the valve is decreased suddenly and the H_2 partial pressure increase is followed. The reactant flows are then turned off and the gate valve opened. An Auger spectrum may now be taken of the surface to determine the carbon coverage. The LEED patterns may be viewed intermittenly throughout the reaction period without affecting the carbon build up on the surface. It is felt that the electron beam used for the LEED experiment does not affect the patterns observed. If there is an effect, is occurs in the fraction of a second required for the electron beam to stablize when the accelerating voltage is switched on. This pattern remains constant for at least 5 min indicating the damage per electron is either very high, greater then 10,000 bonds per electron, or very low, much less than 1 bond per electron. It is thought to be the latter. Since there are about 4 eV (100 kcal/mole) required for a bond dissociation in a hydrocarbon molecule, an upper limit by energy conservation is 40 bonds per electron with an 160 eV electron beam, and more often about 10 bonds/electron at the beam

energies where the carbon structures are visible. In the LEED intensity data taken by Stair[93] for acetylene on the Pt-(111) surface, there is a 10% loss in intensity from the (1/2,1/2) beams (overlayer beams) in 3 min at 2 microamp beam current indicating a very low rate of degradation per electron, about 5×10^{-4} bonds per electron.

2.5. Background Effects on Reaction Rates

2.5.1. Blank Reactions

It is important to determine how much if any of the measured reaction is from the chamber walls. The sources of this activity might be a) mass spectrometer filament, although except for CH_4 production this is unlikely as at 1000°C it would pyrolyze the hydrocarbons; b) the stainless steel grids around the mass spectrometer filament, these are probably heated to a couple hundred degrees by electron bombardment and apparently may have catalytic activity at long times;[94] c) hydrocarbon may backsteam from the ion pump; d) the other filaments in the chamber may have activity even though they are cold, this is doubtful for the W filaments, but possible for the Ni (LEED gun) filament, or e) platinum may be evaporated from the crystal and supports onto the chamber walls. The first four would be constant from day to day, but the fifth would be a transitory effect causing irreproducability between similar runs. It appears to be a major effect if the sample was heated above 1200°C briefly or 1000°C for extended periods ($\geq$1 hr) and lasts less than 24 hr.

Several "blank" reactions were performed. There were two types made: one with the two samples in the chamber, both of which are "cold and dirty" and the second with no single crystals in the chamber but with the support wires inplace and heated to the reaction

temperatures. The first type was performed periodically throughout the investigation for a check on background rate. The second type was performed once for a check on the activity of the polycrystalline wires when clean and heated. The runs are summarized on Table 2-6. The polycrystalline wires did not make an appreciable contribution to the back ground rate. Apparently the ion pump and metal vaporized on the mass spectrometer ionizer were the major sources of background reactions.

2.5.2. Effect of Background Gases

The gases in the background which are always present may have an effect on the catalytic reaction rates measured. The background gases (those present in the chamber at its base pressure 1 to 2×10^{-9} Torr) are H_2, H_2O, CO, possibly N_2, Ar, CO_2 and slight amounts of the CH_4, C_2H_6 and C_3H_8. H_2 (75%+ of background) is used in the reaction studies and, therefore, not a problem; however, it is a problem if pure component adsorption is studied. Water does not adsorb on Pt at these pressures ($\lesssim2\times10^{-10}$ Torr).[95] N_2 and Ar are inert and CO_2 does not adsorb.[96] The light saturated hydrocarbons CH_4, C_2H_6 and C_3H_8 have very low sticking coefficients ($\lesssim10^{-3}$) and are usually produced during the reactions to much higher levels than they are present in the background ($\lesssim1\times10^{-10}$ Torr). On the other hand, CO, which is present at comparably high pressure ($\lesssim4\times10^{-10}$) and has a sticking coefficient near unity, could complete with the hydrocarbons and cover an appreciable portion of the surface during a reaction. To test if this has any influence on reaction rates a run was made in a slightly backed system. This reduced the background water peak, but had little effect on the CO pressure which was approximately 1×10^{-8} Torr. A

Table 2-6. Blank runs for dehydrogenation reactions (rates in 10^{10} molecules/sec*).

C_6H_6	$C\text{-}C_6H_{10}$	C_6H_{12}	C_3H_6	C_3H_8	C_2H_4	C_2H_6	CH_4
For 4×10^{-8} Torr CH, 8×10^{-7} Torr H_2							
0.2±0.1	0.1±1	--	3±1	2±3	0.1±1	0.5±2	10.0±4
For 4×10^{-8} Torr CH=, 8×10^{-7} Torr H_2							
3	--	0.5	3±1	1±3	3±1	1±2	2±4

*1×10^{10} molecules/sec is the rate of production of benzene from most samples.

cyclohexane run was performed with variable crystal temperature; the system throughly (CO pressure ~3×10^{-10} Torr) and the run repeated. The rate at 25°C was lowered approximately 10%, while at higher temperatures the rates were within ±5%, which is the reproducibility of the rates under "identical" conditions. The rate at 25°C has more scatter than at the higher temperatures, so even this may not be significantly lowered. The rate at 25°C should be most affected since CO adsorbs from the terraces at 150°C and step at 250°C. A large increase in the CO pressure (~50 times) is seen to have little effect on the reaction rate; this, however, does not exclude the possibility that the low pressure of CO has not already reached a saturation effect on the rate.

3. CHARACTERIZATION OF STEPPED SURFACES BY LEED

3.1. Diffraction from Perfect Surfaces

There are several features which make exact interpretation LEED patterns difficult. The strong interaction of electrons with the material causes multiple scattering and requires an exact quantum mechanical calculation including several phase shifts for complete determination of structures.[62] It is this same strong interaction which makes LEED surface sensitive so it cannot be avoided experimentally. What can be easily determined is the two dimensional periodicity of the substrate and adsorbed layers.

The total scattering amplitude from a crystal ignoring multiple scattering may be written as the fourier transform of the electron density[97]

$$A(\vec{\Delta k}) = \left\{\sum_j \left[\int C_j(\vec{\rho},\vec{\Delta k})\ e^{-i(\vec{\rho}\cdot\vec{\Delta k})}\ dV\right] \exp(-i\vec{\rho}_j\cdot\vec{\Delta k})\right\} \left\{\sum_{mnp} \exp(-i\vec{\rho}_{mnp}\cdot\vec{\Delta k})\right\} \tag{3-1}$$

where $\vec{\Delta k}$ is the electron momentum change on scattering. The effects of multiple scattering may be averaged out as shown by Lagally, et al.[98] Pendry[99] and Buchholz;[100] however, this is not of concern for this investigation since it only affects the intensity but not the positions of diffraction beams. The integral term (form factor) contains information on the electron density in the unit cell. This term is difficult to calculate for low energy electrons but contains the information on the placement of atoms with respect to each other

in different layers. The form shown is for a weakly interactive particle such as an X-ray. Since this term cannot be evaluated and again only affects intensities and not positions of beams, the term is divided into the amplitude and interference functions are calculated. The second term in the j sum is the position of the scattering centers in the basis set (the structure factor of the basis). The vectors $\vec{\rho}_j$ are the positions in real space for the j atoms in the unit cell located by $\vec{\rho}_{mnp}$. This term is easily calculated and can cause some beams to vanish (see Appendix C). From the Bragg diffraction condition, there is a diffraction maximum when $\vec{\Delta k} = \vec{G}$, a reciprocal lattice vector. The m and n summations approach infinity (the two surface directions), but since the electrons penetrate only a few layers into the bulk, the sum over ρ should be modified. It can be replaced with a damping function[100,101] or be taken only on the surface since it does effect the periodicity on the surface. The reduction of the third dimension causes diffraction beams to occur at all energies. Therefore, for the purpose of this investigation, Eq. (3-1) extremely simplified becomes

$$A(\vec{\Delta k}) = \sum_{j} \exp(-i\vec{\rho}_j \cdot \vec{\Delta k}) \sum_{m,n}^{M,N} \exp(-i\vec{\rho}_{mn} \cdot \vec{\Delta k}) \quad . \qquad (3\text{-}2)$$

When M and N, the number of unit cells in the example, are infinite, the intensity becomes a delta function in two dimensional Fourier space at the reciprocal lattice points, $\vec{G}$. Assuming one atom per unit cell and unit cell sides of $\vec{a}$ and $\vec{b}$ in real space, the interference function which is the square of the amplitude becomes, with some manipulation

$$i = AA^* = \frac{\sin^2 \frac{1}{2} M(\vec{a}\cdot\vec{\Delta k})}{\sin^2 \frac{1}{2} (\vec{a}\cdot\vec{\Delta k})} \cdot \frac{\sin^2 \frac{1}{2} N(\vec{b}\cdot\vec{\Delta k})}{\sin^2 \frac{1}{2} (\vec{b}\cdot\vec{\Delta k})} \qquad (3\text{-}3)$$

The first zeroes of Eq. (3-3) occur at $\vec{a}\cdot\vec{\Delta k} = 2\pi/M$ and $\vec{b}\cdot\vec{\Delta k} = 2\pi/N$. For M, N large, the peaks are quite narrow; but they are broad at low values of M or N ($\lesssim$50). The broadening can occur in only one direction or in both.

3.2. Diffraction from "Perfect" Stepped Surfaces

Diffraction from stepped surface models has been considered previously by others. Henzler[102] has studied cleaved Ge surfaces and found steps of monatomic height. He showed that the height of the step, in a kinematic approximation used here, is related to the intensity variation of the (0,0) beams with electron wavelength. The formula derived by considering only the top layer in an infinite array of steps is:

$$V_\infty = 150\ n^2/4d^2 \qquad (3\text{-}4)$$

where V_∞ is the energy of single maximum of the (0,0) beam, n is an integer and d is the step height. This is discussed further in Section 3.4. Equation (3-4) has been used by Lang, Joyner and Somorjai[71] on the Pt(S)-[6(111)×(100)] and Pt(S)-[9(111)×(111)] to show there is no contraction at the step edge in the z direction. Ellis and Schwoebel[103] performed a structure factor calculation to determine the position and approximate intensities of UO_2-(553) surface. Pedereau and Rhead[104] studied Cu(100) vicinal surfaces and geometrically showed what diffraction patterns would be expected. I will present a similar

argument for the hexagonal geometry of the Pt(S)-[6(111)×(100)] surface. It has been shown previously by Lang et al.[71] that this surface has monatomic height steps; this will be assumed in further discussions. Figure 3-1a shows a real space segment of this surface with equally spaced steps. The vectors $\vec{a}$, $\vec{b}$ denotes the (111) surface unit cell; $\vec{a}$, $\vec{d}$ specify the step unit cell containing two atoms at positions (0,0) and (1/2,1/2); $\vec{c}$ is the unit length vector normal to the (111) surface. In terms of the Cartesian unit vectors $(\hat{i},\hat{j},\hat{k})$ (length 2.78Å) the vectors are:

$$\vec{a} = \hat{i}$$

$$\vec{b} = \frac{1}{2}\hat{i} + \frac{\sqrt{3}}{2}\hat{j}$$

$$\vec{c} = \hat{k}$$

$$\vec{d} = +\frac{17\sqrt{3}}{3}\hat{j} + \frac{2\sqrt{2}}{\sqrt{3}}\hat{k}$$

The reciprocal space vectors for the (111) surface are given by

$$\begin{vmatrix} \vec{a}^* \\ \vec{b}^* \\ \vec{c}^* \end{vmatrix} = \begin{vmatrix} 1 & 0 & 0 \\ \frac{1}{2} & \frac{\sqrt{3}}{2} & 0 \\ 0 & 0 & 1 \end{vmatrix}^{-1t} = \begin{vmatrix} 1 & -\frac{1}{\sqrt{3}} & 0 \\ 0 & \frac{2}{\sqrt{3}} & 0 \\ 0 & 0 & 1 \end{vmatrix}$$

and shown in Fig. 3-1b the $|\vec{a}^*|$ is $\frac{2}{\sqrt{3}} \times \frac{1}{|\vec{a}|}$ because the relative volume of the unit cell is less than 1.0. The step reciprocal space vectors are given by:

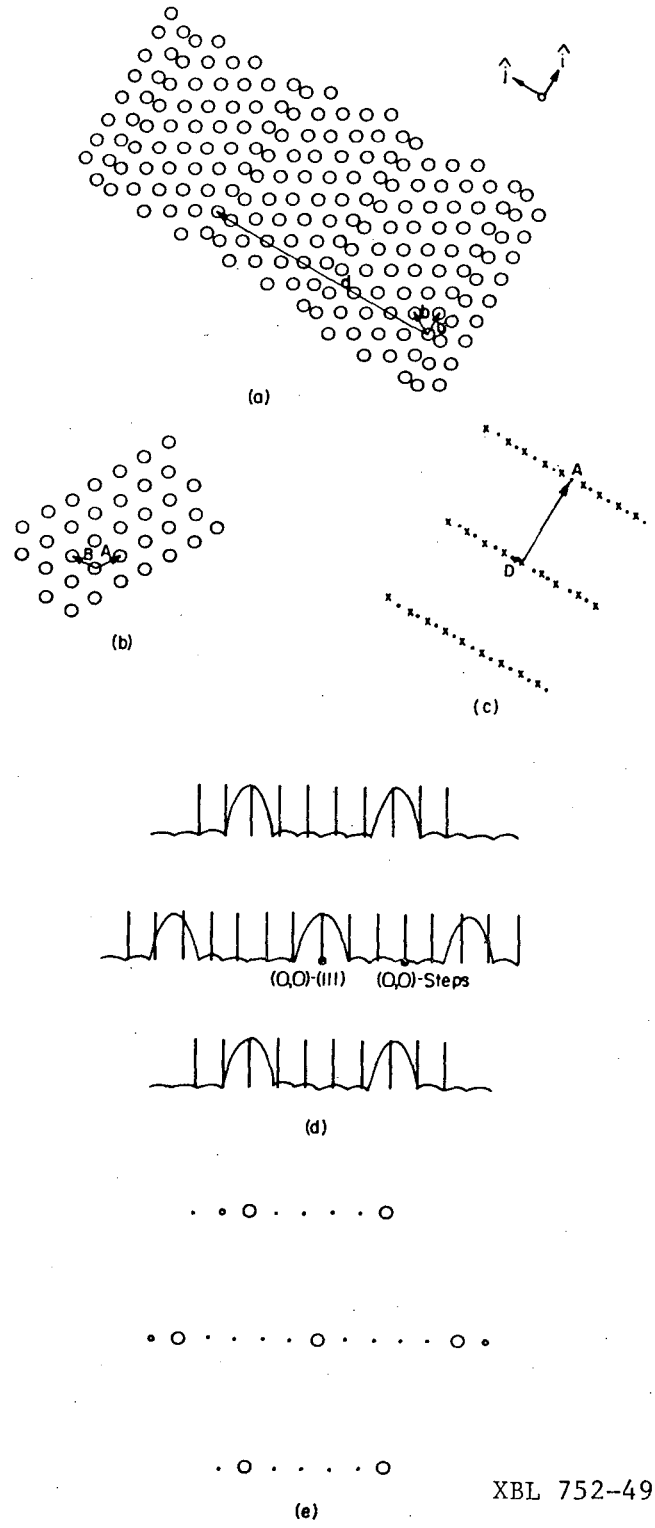

XBL 752-4956

Fig. 3-1. Diffraction from a perfect (S)-[6(111)×(100)] surface; (a) the real space schematic of the atom positions on the surface, (b) the reciprocal lattice for the (111) terrace plane, (c) the reciprocal lattice from the step plane, the beams represented by · are extincted by the structure factor, (d) interference functions from the two reciprocal space lattices, and (e) the schematic of the observable diffraction pattern with the brighter beams depicted by larger spots.

$$\begin{vmatrix} \vec{a}^* \\ \vec{d}^* \\ \vec{c}^* \end{vmatrix} = \begin{vmatrix} 1 & 0 & 0 \\ 0 & \frac{17}{\sqrt{3}} & \frac{2\sqrt{2}}{\sqrt{3}} \\ 0 & 0 & 1 \end{vmatrix}^{-1t} = \begin{vmatrix} 1 & 0 & 0 \\ 0 & \frac{\sqrt{3}}{17} & 0 \\ 0 & -\frac{2\sqrt{2}}{17} & 1 \end{vmatrix}$$

with a two atom structure factor (the ℓ or c^* term is always 0 on the surface).

$$S = 1 + \ell^{-2\pi i(1/2\ h + 1/2\ k)}$$

when h is odd S = 2 when k is odd otherwise S = 0, when h is even S = 2 when k is even otherwise S = 0. This produces the array of spots shown in Fig. 3-1c (not same scale) which are centered about the end of $\vec{c}_s^*$. With the electron beam incident normal to the (111) plane, the step pattern (0,0) beam is positioned at $\theta = 2\tan^{-1}\left(\frac{2\sqrt{2}}{17}\right)$ or for the surface shown 18.9° from the (111) specular beam. Since in each domain of (111) surface, or on each terrace, there are only six scatterers normal to the step (infinite parallel to the step), the (111) spots are broadened in the $\vec{d}^*$ direction in reciprocal space as given by Eq. (3-3). The interference function at each $\vec{\Delta k}$ from these two periodicities is multiplied together giving the diffraction pattern depicted schematically in Fig. 3-1d and seen in Fig. 3-1e. All the spots shown in Fig. 3-1e are not seen in the actual diffraction pattern, this will be discussed in Section 3-4 in detail.

Another possibility for step surfaces is that the step configuration is completely unstable and the surface facets. The stability of Pt step surfaces is discussed in Chapter 4. The surface forms two or

more distinct surface planes at an angle to each other and the macroscopic normal; each plane, of course, has a specular reflection, (0,0) beam. The determination of this angle between (0,0) beams from photographs of the displayed diffraction has been detailed by Lyon.[59] Often other diffraction beams from the facet planes are visible and aid in the identification of the planes. Generally these planes are small, the order 100Å or less across. This means there will be only a small number of scatters so the diffraction spots will be broadened. This broadening can be quantified by Eq. (3-3) if all the facet planes are the same size and the diffraction from a perfect crystal is a delta function.

The procedures described give a qualitative picture of the diffraction from the crystal surface if both the instrument and crystal are perfect. It describes features found on well annealed (i.e., highly ordered) surfaces quite well, but does not describe the streaking or non-integral step spacings found experimentally on stepped surfaces. The next two sections will discuss the possible imperfections or flaws in the instrument and crystal surfaces respectively.

3.3. Imperfections in the Instrument

3.3.1. Theoretical Imperfections

Park, Houston and Schreiner[105] have described the main inperfections found in a LEED apparatus. The effect of these flaws is to decrease the effective area over which the electrons are coherent, i.e., act as plane waves. This causes the instrument to hide a great deal of imperfection in the surface. Now this is generally good since the

surfaces used have a great deal of imperfection in the long range order. On surfaces with known lack of long range order, such as faceted step surfaces or organic molecule crystal surface, this effect needs to be characterized and removed from the diffraction pattern so the true mean domain size can be determined.

Park et al.[105] have used the term "transfer width" to describe the response of the system to each experimental flaw. If the transfer widths can be represented by a Gausian function, the width of the overall response function in reciprocal space is

$$W = \left\{ \sum_i W_i^2 \right\}^{1/2} \quad . \tag{3-5}$$

The four main effects are energy spread of the source, source extension, collector size and beam size.

3.3.1.1. Energy spread of source. The energy spread of the electron source, a 1000°C emitter, is very important at low energies. To find the uncertainty introduced to the diffraction vector, i.e., the reciprocal space lattice positions, by variation in energy, the Bragg equation for diffraction at normal incidence (Eq. (3-6)) is differentiated with respect to energy

$$\vec{\Delta k} = \frac{\sin\theta}{\lambda} = \left(\frac{E}{150}\right)^{1/2} \sin\theta \tag{3-6}$$

giving:

$$W_1 = \delta(k) = \frac{1}{2} \frac{\sin\theta}{(150E)^{1/2}} \delta E \tag{3-7}$$

The spread in energy δE can be estimated from the retarding plots by Gland[106] and is about 1 eV.

3.3.1.2. Source extension. The source of electrons is not a point source and this causes uncertainty in the direction of the incident beam. Park[107] measured this for his electron optics by a technique not useable on a Varian LEED optics. For lack of measurement, the lens aberrations are assumed to be similar. The transfer width is

$$W_2 = \left(\frac{E}{150}\right)^{1/2} \gamma \tag{3-8}$$

and their measured $\gamma = 0.012$.

3.3.1.3. Aperature width. A third source which is not applicable to the Varian display optics, but is important with a Faraday cup collector, is the aperature width of the collector. Differentiating Eq. (3-6) with respect to θ yields

$$\delta k = \left(\frac{E}{150}\right)^{1/2} \cos\theta\delta\theta \quad , \tag{3-9}$$

$$W_3 = \left(\frac{E}{150}\right)^{1/2} \cos\theta\left(\frac{d}{R}\right) \tag{3-10}$$

where d is the aperature diameter and R is the collector radius.

3.3.1.4. Beam size. The finite beam size, even if the electrons are parallel, decreases the angular resolution of the instrument. This contribution is found by multiplying Eq. (3-8) by the cosine of the diffraction angle.

$$W_4 = \left(\frac{E}{150}\right)^{1/2} \cos^2\theta\left(\frac{D}{R}\right) \tag{3-11}$$

where D is the beam diameter. (D/R) is approximately 0.015 in a Varian system.

These transfer functions are in reciprocal space, so the effective coherent area in real space is the reciprocal of W in Eq. (3-5).

$$w = \left| \sum_i W_i^2 \right|^{-1/2} \tag{3-12}$$

Two examples of the effective coherence length will be given. One is for the (10) beam of the Pt-(111) surface and the second is for a split (10) beam of the Pt(S)-[6(111)×(100)] surface at 60 eV and normal incidence to the (111) plane. The split beam is a (30) from the step unit cell. The energy spread of the source is the same for both but gives different contributions to W; for the (111) surface from Eq. (3-7)

$$W_1 = \frac{1}{2} \frac{\sin\theta}{(150E)^{1/2}} \quad \delta E = \frac{1}{2} \frac{\sin(41°)}{(150 \cdot 60)^{1/2}} \; 1 \text{ eV} = 0.0035 \text{Å}^{-1}$$

and for the split beam

$$W_1 = \frac{\sin(\theta_i) + \sin(\theta_o - \theta_i)}{n} \frac{1}{2} \frac{\delta E}{(150E)^{1/2}}$$

$$= \frac{\sin(9.6°) + \sin(31.4°)}{3} (0.00526) = 0.00064 \text{Å}$$

(The extra sine terms in the split beams are from non-normal incidence.) The uncertainty in incident beam direction is the same for both surfaces (from Eq. (3-8)) $W_2 = 0.0076 \text{Å}^{-1}$. The contribution from finite beam size given by Eq. (3-11) is for the (111) surface,

$$W_4 = \frac{\cos^2(41°)}{\lambda}\,(0.015) = 0.0054\text{Å}^{-1}$$

and for the split beam

$$W_4 = \frac{\cos\theta(\cos(\theta_o - \theta_i))}{n\lambda}\,\frac{D}{R} = 0.0020\text{Å} \quad .$$

Thus the total effective coherence width as given by Eq. (3-12) is for the (111) surface, $\omega_{111} = (0.0099)^{-1} = 101\text{Å}$, and for the split beam $\omega_{sp} = 127\text{Å}$. The major factor in both of these is W_2 which is independent of the surface since it is the same for all beams. It should be noted that W_1 and W_4, which depend on the diffraction beam, decrease greatly with the increase in unit cell size going from the (111) to the stepped surface.

3.3.2. Experimental Determination

An experimental determination of this transfer width can be made. The main assumption is that a crystal surface can be prepared which is perfect to at least the coherence length so it will appear perfect to the instrument. Equation (3-9) is inverted and the experimental variables V and Θ are inserted. The angular width is measured in the plane of the beam motion so Eq. (3-9) must be multiplied by $\cos(\Theta)$,

$$\omega = \left(\frac{150}{V}\right)^{1/2} \frac{1}{\cos^2\Theta\delta\Theta} \quad . \tag{3-13}$$

This has been measured on a well annealed, clean Pt-(111) surface which is thought to be "perfect" on large domains. The values of V, Θ and $\delta\Theta$ were 64 eV, 40° and 1.5°, which yield an effective coherence length of 95Å. This is an excellent agreement with the

calculated value. The effect of beam defocusing by the suppressor voltage is eliminated by always checking to ascertain the voltage is correct before taking a picture.

This value of $\delta\Theta$ must be deconvoluted from the diffraction spot width to determine the mean domain size from Eq. (3-3). This can readily be done if both contributions are assumed Gausian.

$$\delta\Theta_{meas} = \left\{\delta\Theta^2_{inst} + \delta\Theta^2_{pattern}\right\}^{1/2} \qquad (3\text{-}14)$$

3.4. Diffraction from Real Surfaces

There is always a statistical distribution of domains of perfect periodicity separated by some sort of imperfections. The separating imperfections may be steps on a clean metal surface or a change in the registry of an adsorbate with the substrate. The statistical distribution may be very narrow and produce a pattern in which the spots are broadened only by the instrument and the finite domain size (Eq. (3-13)). If the distribution of domain sizes is broad the spots may be broadened further than would be predicted by Eq. (3-13) for the mean domain size.

3.4.1. Order on a Surface

There are three kinds of disorder a surface may exhibit, disorder of the first kind, second kind and third kind, each affecting the diffraction from the surface in a different manner. It is easiest to see the effect of disorder with the use of the autocorrelation function or pair correlation function, $\Phi(x,y)$. $\Phi(x,y)$ is the probability of finding a pair of points separated by the real space

distance x, y. (It is the convolution square of the electron density function in Eq. (3-1)).

Disorder of the first kind is thermal disorder associated with all crystals above absolute zero and does not cause beam broadening. The long range correlation of the periodicity is preserved, and the atoms only vibrate about their lattice positions. This causes a decrease in intensity of the beam with increasing temperature but no broadening. Figure 3-2a shows this type of disorder for a line chain of atoms.

Disorder of the second kind causes diffraction beams to broaden. The correlation loses its long range periodicity and at sufficiently large distances all positions are equally probable. This would be represented by a glassy structure or an ion bombarded surface. Figure 3-2b represents this for a linear chain of atoms.

Disorder of the third kind, or registry degeneracy,[108,109] may cause some beams to broaden or split and others not to broaden. As illustrated in Fig. 3-2c, the periodicity of the substrate is maintained while the superperiod periodicity is not maintained; therefore, the beam breadth depends on the distribution of the registry degeneracies. The substrate periodicity is maintained to very long distances so, the beams associated with the substrate may be relatively unaffected.

On a real surface all three kinds of disorder are present. On Pt surfaces, disorder of the first kind is significant only above 300°C for the beam position and width investigation done here. Above 300°C,

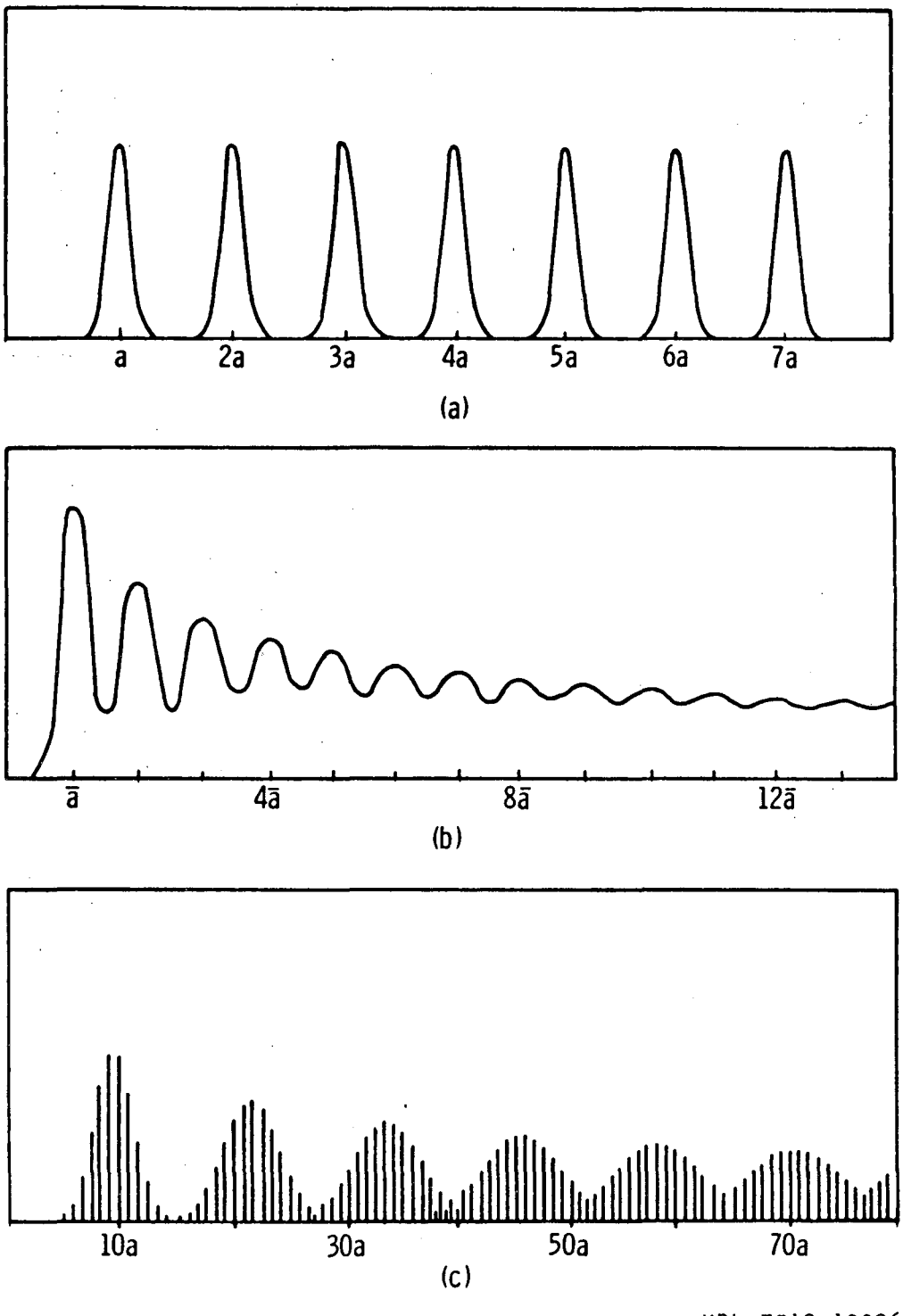

XBL 7512-10096

Fig. 3-2. Types of disorder which occur on a single crystal surface: (a) motion about the lattice position (thermal motion), (b) long range periodicity of the structure is lost (glassy structure), and (c) superperiodicity is not maintained while the periodicity of the substrate is maintained (from Houston and Park[108,109]).

the spots are difficult to see above the diffuse background. Disorder of the second kind should be insignificant at least over the effective coherence range of the electrons on annealed samples. Disorder of the third kind, however, should play a significant role in diffraction from stepped surfaces and will be discussed in the next section in greater detail.

3.4.2. Correlated Step Models

It was mentioned in the previous section that the diffraction intensity $i(\vec{k})$ is just the Fourier transform of the pair correlation function or the convolution square of Eq. (3-1). The problem becomes what is the average pair correlation function for a statistical distribution of step width and heights. The development presented here is based on that of Houston and Park.[110]

The model of the surface is shown in Fig. 3-3. It is a correlated step model in that at the end of each terrace of length Γ is a step of displacement R with both horizontal and vertical components, and the steps and terraces always alternate. The terraces are assumed to be perfectly ordered; this should be a good assumption since it demands perfection only over a few lattice spacings, (3 to 20 or 30 atoms). This model is also restricted to an ascending staircase arrangment of the terraces. Non-adjacent step boundaries are separated by the vector S.

The equation for diffraction intensity from a domain structure can be found in many books on X-ray diffraction, see Guinier, p. 52,[111] and is

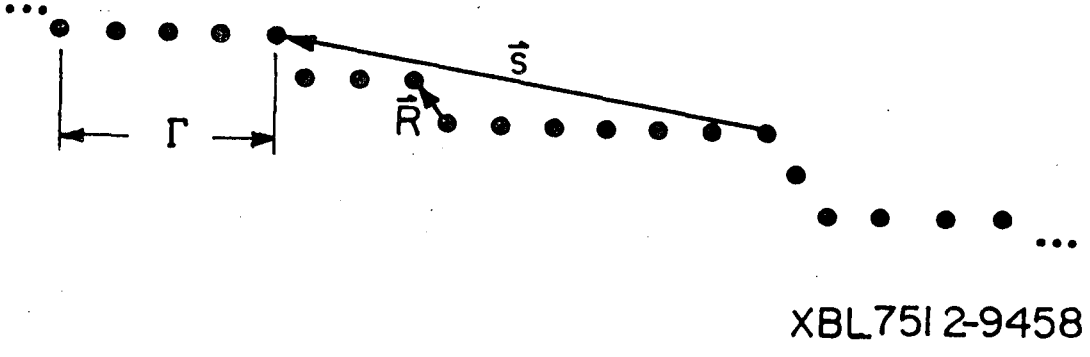

Fig. 3-3. Model of an ascending staircase correlated stepped surface, where Γ_a is the terrace width, $\vec{R}_a$ is the step displacement vector and $\vec{S}_a$ is the separation of non-adjacent step boundaries.

$$i(\vec{\Delta k}) = F\{\bar{\psi} - \bar{\phi}\} + F\{\bar{\phi}\}\ [1 + F\{\vec{p}(\vec{s})\}] \tag{3-15}$$

$\bar{\psi}$ is the weighted average of the pair correlation functions for each terrace of width Γ

$$\bar{\psi} = \int \phi_\Gamma P(\Gamma)\ d\Gamma$$

where $P(\Gamma)$ is the probability of finding a terrace of width Γ and the integral is taken over all values of Γ. $F\{\bar{\psi}\}$ is the Fourier transform of $\bar{\psi}$ and the intensity from a randomly distributed set of terraces of width $P(\Gamma)$, i.e., the intensities add incoherently. This is just the weighted average of Eq. (3-3),

$$F\{\psi\} = \sum_{\Gamma=-\infty}^{\infty} P(\Gamma)\ \frac{\sin^2 \frac{\vec{\Delta k}\cdot\vec{a}}{2}\ \Gamma}{\sin^2 \frac{\vec{\Delta k}\cdot\vec{a}}{2}} \tag{3-16}$$

$F\{\bar{\phi}\}$ is the Fourier transform of the pair correlation function of the weighted average terrace width $\bar{\Gamma}$. This form is slightly more complicated, but again just sums of Eq. (3-3) for various widths

$$F\{\bar{\phi}\} = \sum_{\Gamma=-\infty}^{\infty} \sum_{\Gamma'=-\infty}^{\infty} P(\Gamma)P(\Gamma')\ \frac{\sin^2 \Gamma \frac{\vec{\Delta k}\cdot\vec{a}}{2} + \sin^2 \Gamma' \frac{\vec{\Delta k}\cdot\vec{a}}{2} - \sin^2 (\Gamma - \Gamma')\ \frac{\vec{\Delta k}\cdot\vec{a}}{2}}{2\sin^2 \frac{\vec{\Delta k}\cdot\vec{a}}{2}} \tag{3-17}$$

$\vec{p}(s)$ is the step boundary displacement distribution function.

The first term in Eq. (3-15), $F\{\psi - \phi\}$, is a general low background which varies slowly in both $\vec{k}$ and θ, and is zero for a perfectly ordered surface. The second term in Eq. (3-15), $F\{\phi\}\ [1 + F\{p(\vec{s})\}]$ accounts for the splitting and broadening of diffraction beams. On a perfectly ordered surface, it is the mathematical description of Fig. 3-1d, a series of delta functions times the broadened beams.

3.4.3. The Step Width Distribution

Equation (3-14) is general and for any domain structure. The problem becomes to derive the Fourier transform of the distribution function $p(\vec{s})$ from a model for the probability functions $P_\Gamma(\Gamma)$ and $P_R(R)$. A reasonable guess for the terrace width distribution function $P_\Gamma(\Gamma)$ is a Gausian envelop, centered at the mean terrace width, $\bar{\Gamma}$, and of width γ, i.e.,

$$P_\Gamma(\Gamma) = \frac{1}{N} \exp\left[-\frac{\pi(x - \bar{\Gamma}a)^2}{(\gamma a)^2}\right] \delta(x - \Gamma a) \qquad (3\text{-}18a)$$

where N is the normalization factor and δ is the Dirac delta function. The step height distribution $P_R(R)$ is again a Gausian envelop centered at $\bar{R}$ and the distribution is of width r

$$P_R(R) = \frac{1}{N_R} \exp\left[-\frac{\pi(Y - \bar{R}Y_o a)^2}{(rY_o a)^2}\right] \delta(Y - RY_o) \qquad (3\text{-}18b)$$

Since for each unit R of step height, Y_o, there is a unit of step width Y_o, the step boundary distribution function is

$$P_\Gamma P_R = P(\Gamma + RX_o, RY_o) = \qquad (3\text{-}18c)$$

$$\frac{1}{N_{\Gamma R}} \exp\left[-\pi \frac{(X - (\bar{\Gamma} + \bar{R}X_o))^2}{(\gamma a)^2}\right] \exp\left[\frac{-\pi(Y - \bar{R}Y_o a)^2}{(rY_o a)^2}\right] \delta[\vec{S} - (\Gamma + RY_o, RY_o)]$$

Now, since the steps are correlated, the probability of finding the second step edge at $\vec{S}$ is the convolution of $P_\Gamma P_R$ with itself; for the n^{th} step, it is the n^{th} convolution of $P_\Gamma P_R$ with itself. Taking

the Fourier transform, the convolutions become products,[111] and the series can be written in simple form:[108,110]

$$F\{p(\vec{S})\} = \frac{F\{P_\Gamma P_R\}}{1 - F\{P_\Gamma P_R\}} \tag{3-19}$$

The Fourier transform $P_\Gamma P_R$ is

$$F\{P_\Gamma P_R\} = \sum_{R=1}^{\infty} \sum_{\Gamma=-\infty}^{\infty} \frac{1}{N_R N_\Gamma} \exp\left[-\frac{\pi(R - \bar{R})^2}{r^2}\right] \exp\left[-\frac{\pi\{\Gamma + RX_o - (\bar{R}X_o + \bar{\Gamma})\}^2}{\gamma^2}\right]$$

$$\times \cos[(\Gamma + RX_o)\ \vec{\Delta k}\cdot\vec{a} + RY_o \vec{\Delta k}\cdot\vec{b}] \tag{3-20}$$

This gives the interference function, i, by substituting Eq. (3-19) into Eq. (3-15),

$$i(\vec{k}) = F\{\psi - \phi\} + F\{\phi\}\ \frac{1}{1 - F\{P_\Gamma P_R\}} \tag{3-21}$$

Using Eq. (3-21), the result in Figs. 3-1d and e for the perfect surface are readily derived. The first term is exactly zero as seen from Eq. (3-16) and Eq. (3-17) with $P_\Gamma(\Gamma \neq 5) = 0$, $P_\Gamma(5) = 1$ and $P_R(1) = 1$. $F\{\bar{\psi}\}$ has the form of Eq. (3-3) and $[1 - F\{P_\Gamma P_R\}]^{-1}$ is an infinite series of delta functions. From Eq. (3-20), $1 - F\{P\} = 0$ when $\cos[(\Gamma + X_o)\ \vec{\Delta k}\cdot\vec{a} + Y_o\vec{\Delta k}\cdot\vec{b}] = 1$, or the argument

$$(\Gamma + X_o)\frac{a\sin\theta}{\lambda} + Y_o(1 + \cos\theta)\frac{a}{\lambda} = n \quad .$$

This is equivalent to Fig. 3-1d and gives the step height formula by Henzler,[102] Eq. (3-4), in which the step height and terrace width distributions are independent.

It is interesting that a statistically rough surface will give the exact same intensity vs voltage characteristic for the specular reflection as the perfect surface. From Eq. (3-21) the intensity will be a singularity whenever $F\{P_\Gamma P_R\} = 1.0$. In this approximation (independent distributions) Eq. (3-20) becomes

$$F\{P_\Gamma P_R\} = \sum_{R=1}^{\infty} \sum_{\Gamma=-\infty}^{\infty} \frac{1}{N} \exp\left[-\frac{\pi(R - \bar{R})^2}{R^2}\right] \exp\left[-\frac{\pi(\Gamma - \bar{\Gamma})^2}{\gamma^2}\right] \cos\left[(\Gamma + RX_o)\ \vec{\Delta k}\cdot\vec{a} + RY_o \vec{\Delta k}\cdot\vec{b}\right]$$

For the (0,0) beam at normal incidence this becomes

$$F\{P_\Gamma P_R\} = \left(\sum_{\Gamma=-\infty}^{\infty} P_\Gamma(\Gamma)\right)\left(\sum_{R=1}^{\infty} P_R(R)\ \cos(RY_o kb)\right)$$

Since P_Γ and P_R are independent the sums can be separated and $F\{P_\Gamma P_R\} = 1$ whenever $Y_o kb = 2n\pi$, the exact same condition as found for the perfect surface. This is not true in the coupled probability equation (Eq. (3-20)), but the deviations are slight. The coupling in Eq. (3-20) says a wide terrace is more likely to have a double height step than is a narrow terrace. Neglecting dynamical effects and the inner potential probably causes more error in the peak placement than the uncoupling of the probability distributions.

3.4.4. An Example

For a statistical surface the low intensity beams between the main doublets are averaged out, the doublet beam intensity is lowered, and the delta functions are broadened. An example of the calculation for a well ordered, but not perfect [6(111)×(100)] surface is now given.

The step height distribution and terrace width are shown in Fig. 3-4a. Since P_R contains some double height steps, the average terrace width has to increase to bring the overall normal back to the proper angle

$$\cot\beta = \frac{\bar{\Gamma}a + \bar{R}X_o a}{\bar{R}Y_o a} \tag{3-22}$$

where β is the angle between the terrace normal and the macroscopic normal. $\bar{R}$ the average step height, is given by

$$\begin{aligned} \bar{R} &= \int RP_R(R)\, dR = 1(0.98) + 2(0.02) = 1.02 \\ \bar{\Gamma} &= \int \Gamma P_\Gamma(\Gamma)\, d\Gamma = \sum_{-\infty}^{\infty} \Gamma P_\Gamma(\Gamma) \end{aligned} \tag{3-23}$$

therefore, using Eq. (3-22), the average terrace width, $\bar{\Gamma}$, is 5.1 This value was used in Eq. (3-18a) with a distribution width of $\sqrt{2}a$ to give the distribution of Fig. 3-4a. $F\{\bar{\psi}\}$ and $F\{\bar{\phi}\}$, the Fourier transforms of the terrace width distribution averages, are shown in Fig. 3-4b and Fig. 3-4c. It is seen that these are quite similar functions and the first term of Eq. (3-21) is a small, slowly varying function of $\vec{k}$. If the width distribution is large, the first term becomes significant and appears as streaking in the diffraction pattern. The step boundary displacement distribution function, or domain auto correlation function $p(\vec{s})$, is shown in Table 3-1. $p(\vec{s})$ is symmetric about the origin as it must be since $i(\vec{\Delta k})$ is real. Its value at the origin is 1.0, since when sitting on a step edge the probability of finding an edge there is unity. $F\{p(\vec{s})\}$ is shown in Fig. 3-4d for $a = 2.77\,\frac{\sqrt{3}}{2}$ and $\lambda = 1.583\text{Å}$ (60 eV electron energy).

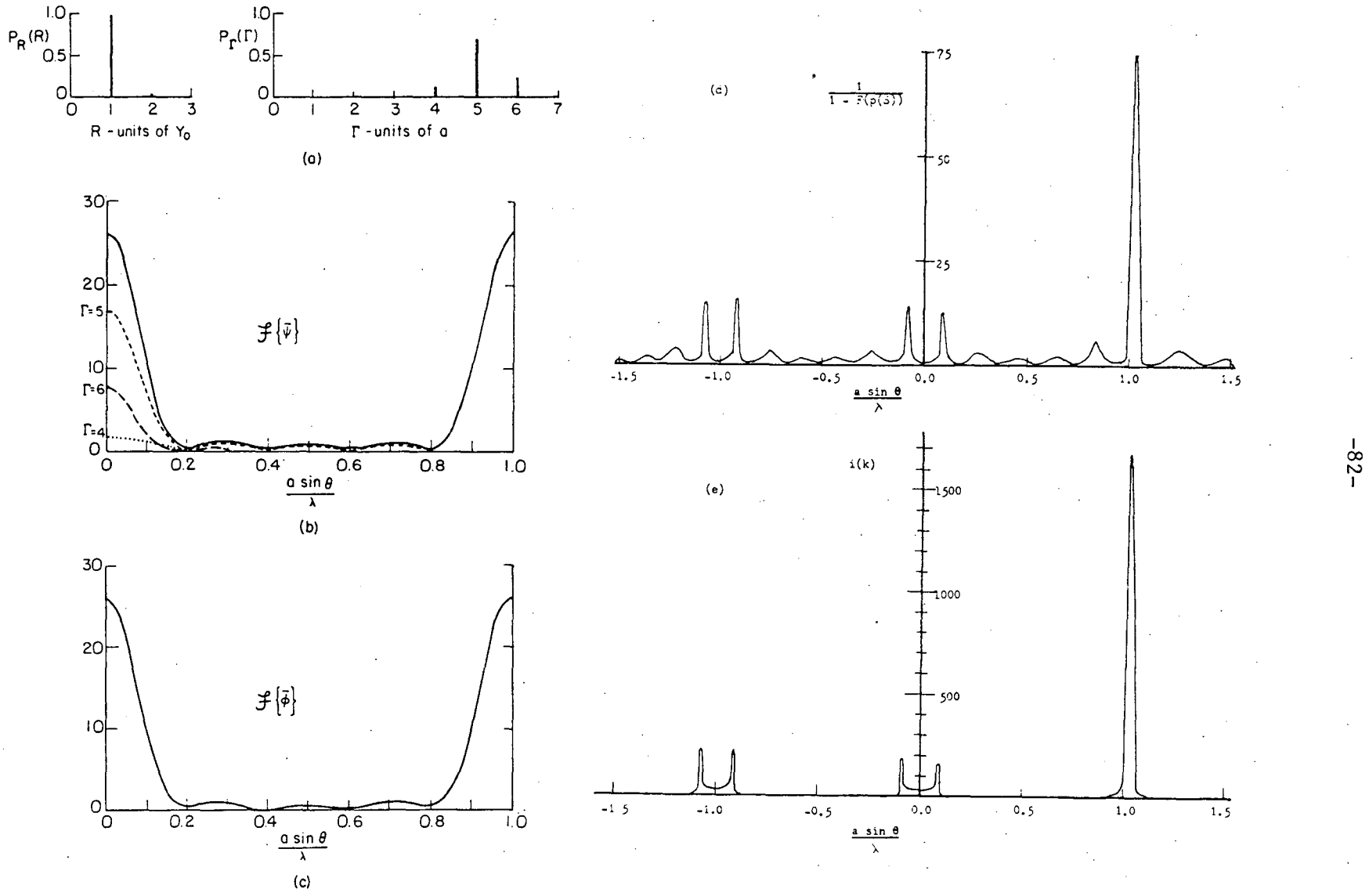

Fig. 3-4. Diffraction from an imperfect (real) surface; (a) the distribution function of step width and heights, (b) $F(\bar{\psi})$, the transform of the weighted average of the pair correlation function (c) $F\{\bar{\phi}\}$, the transform of the pair correlation function of the weighted average terrace width $\bar{\Gamma}$, (d) $[1 - F\{p(s)\}]^{-1}$, the transform of the terrace boundary distribution function, and (d) $i(\vec{\Delta k})$ the interference function at $a/\lambda = 1.52$ (60 eV electron energy for Pt(111) vicinal surfaces) and normal incidences.

XBL7512-9457

The peaks are broadened from the delta function found for a perfect surface. Finally, i(k), the interference function, is found by multiplying $F\{\bar{\phi}\}$ and $1 + F\{p(\vec{S})\}$ to give the pattern shown in Fig. 3-4e. This is only slightly broadened from that seen in Fig. 3-1e, as expected, since the distributions are narrow. When the instrument response function, W, described in Section 3-3, is convoluted into the intensity function, both patterns, from the near perfect surface in Fig. 3-4e and the perfect surface in Fig. 3-1e, appear the same.

Figure 3-5 shows the diffraction from a very broad distribution of step widths with a monatomic step height. The obvious feature of this distribution is that the terrace boundary function (Fig. 3-5c) is much lower in intensity and does not go to zero at any angle. This causes the whole diffraction pattern, represented by the interference function (Fig. 3-5d), to be of much decreased intensity. Since $F\{\bar{\psi}\}$ (Fig. 3-4b and 3-5b) is not wider with the wider distribution the pattern outside of the doublets is as sharp, but there is higher intensity between each pair of doublets.

3.4.5. Other Distributions

A large amount of disorder can be hidden by the statistical averaging of the surface. This is clearly shown by Houston and Park[108] for a simple domain structure as reporduced in Fig. 3-6. The beam broadening is not detectable until the distribution width is greater than half the mean length because of instrument response.

Using the Pt(S)-[6(111)×(100)]domensions a number of feasible surface configurations are proposed and shown in Fig. 3-7. The vicinal surfaces appeared could have a very broad distribution of terraces with

Fig. 3-5. Diffraction from an imperfect surface; (a) the distribution function of step widths and heights (all monatomic height stepps), (b) $F\{\bar{\psi}\}$, the transform of the weighted average of the pair correlation functions, (c) $[1 - F\{p(\vec{S})\}]^{-1}$, the transform of the terrace boundary distribution function and (d) $i(\vec{\Delta k})$ the interference function at $a/\lambda = 1.52$ (60 eV electron energy for Pt(111) vicinal surfaces) and normal incidence. This figure is drawn to the same scale as Fig. 3-4 to emphasize the damping effect of the broad terraces with distribution on the beam intensity.

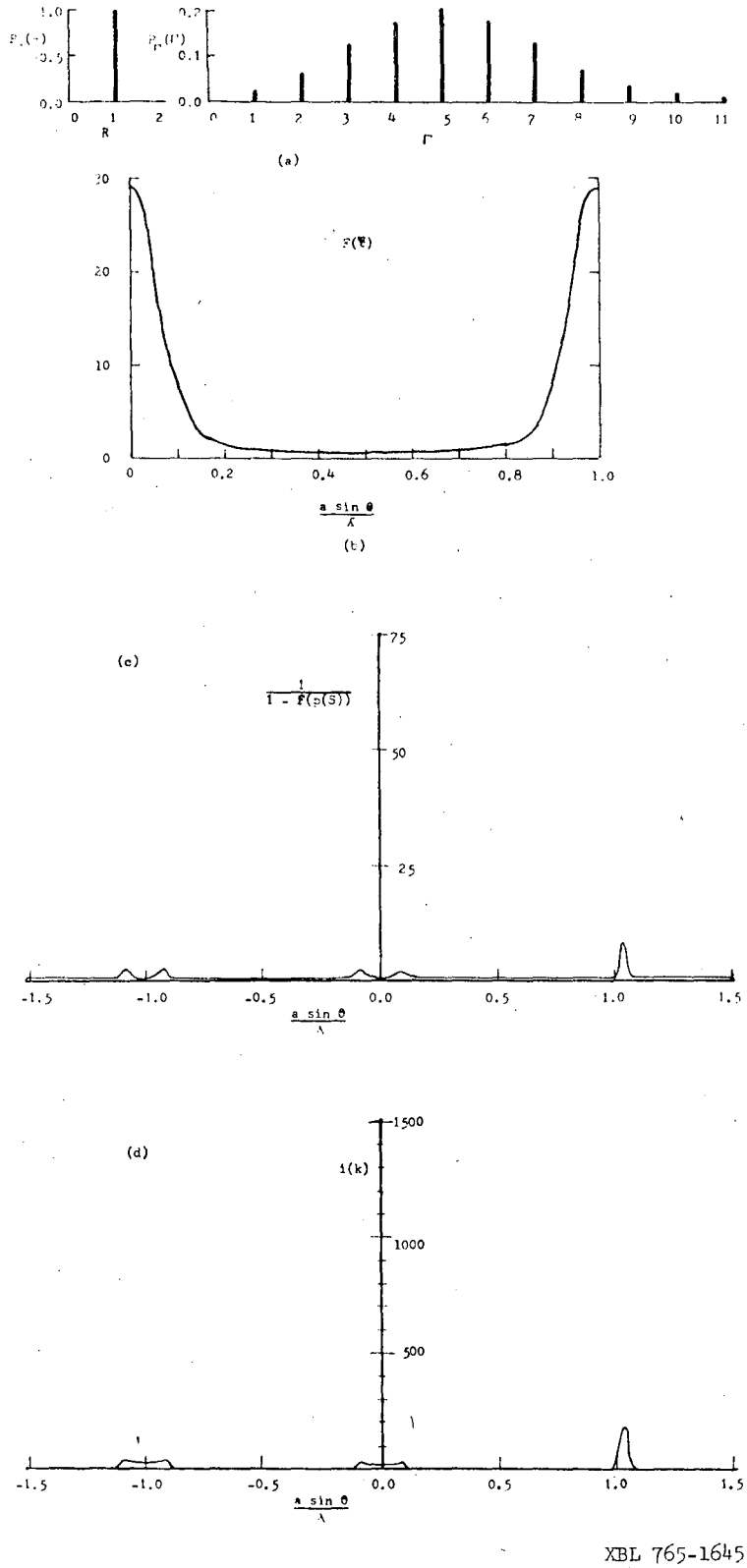

XBL 765-1645

Fig. 3-5.

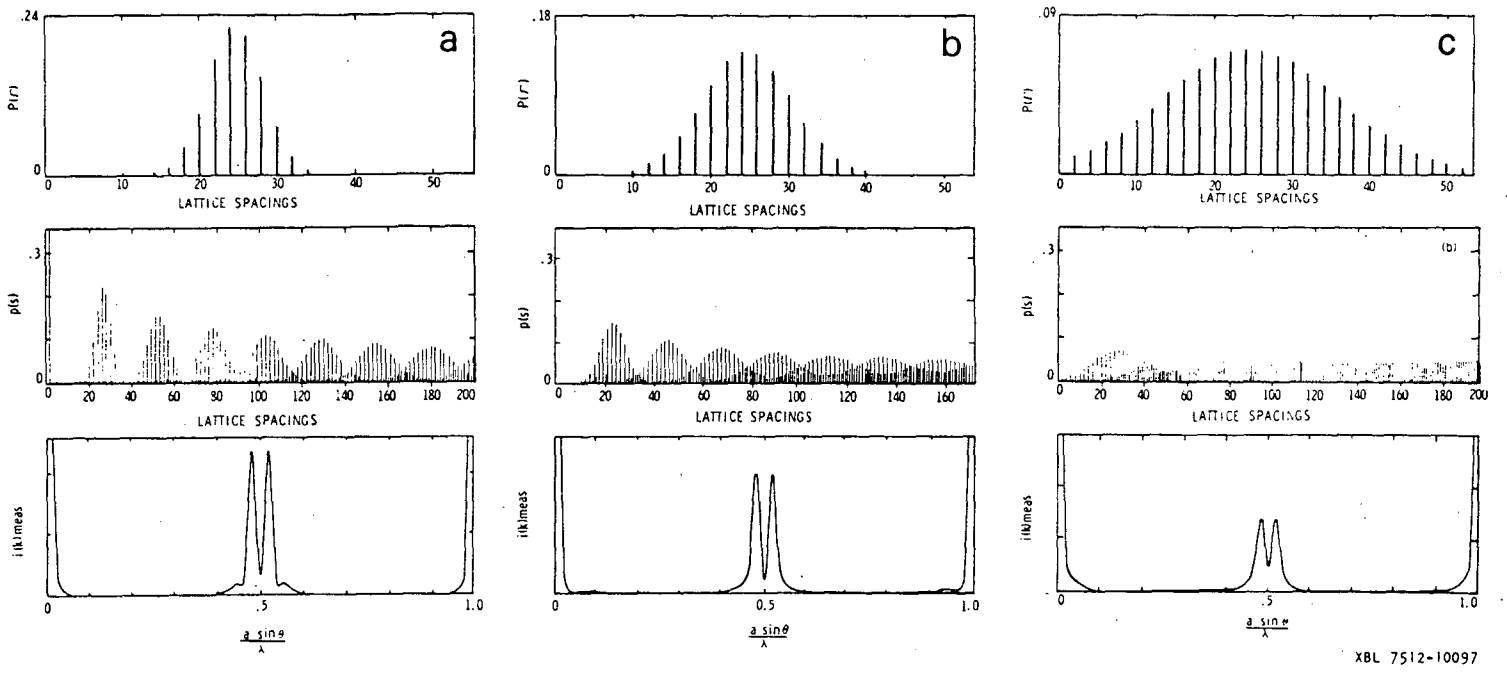

Fig. 3-6. Effect of domain width on beam broadening is not detectable until the distribution width is larger than 1/2 the mean domain width (from Houston and Park[108]).

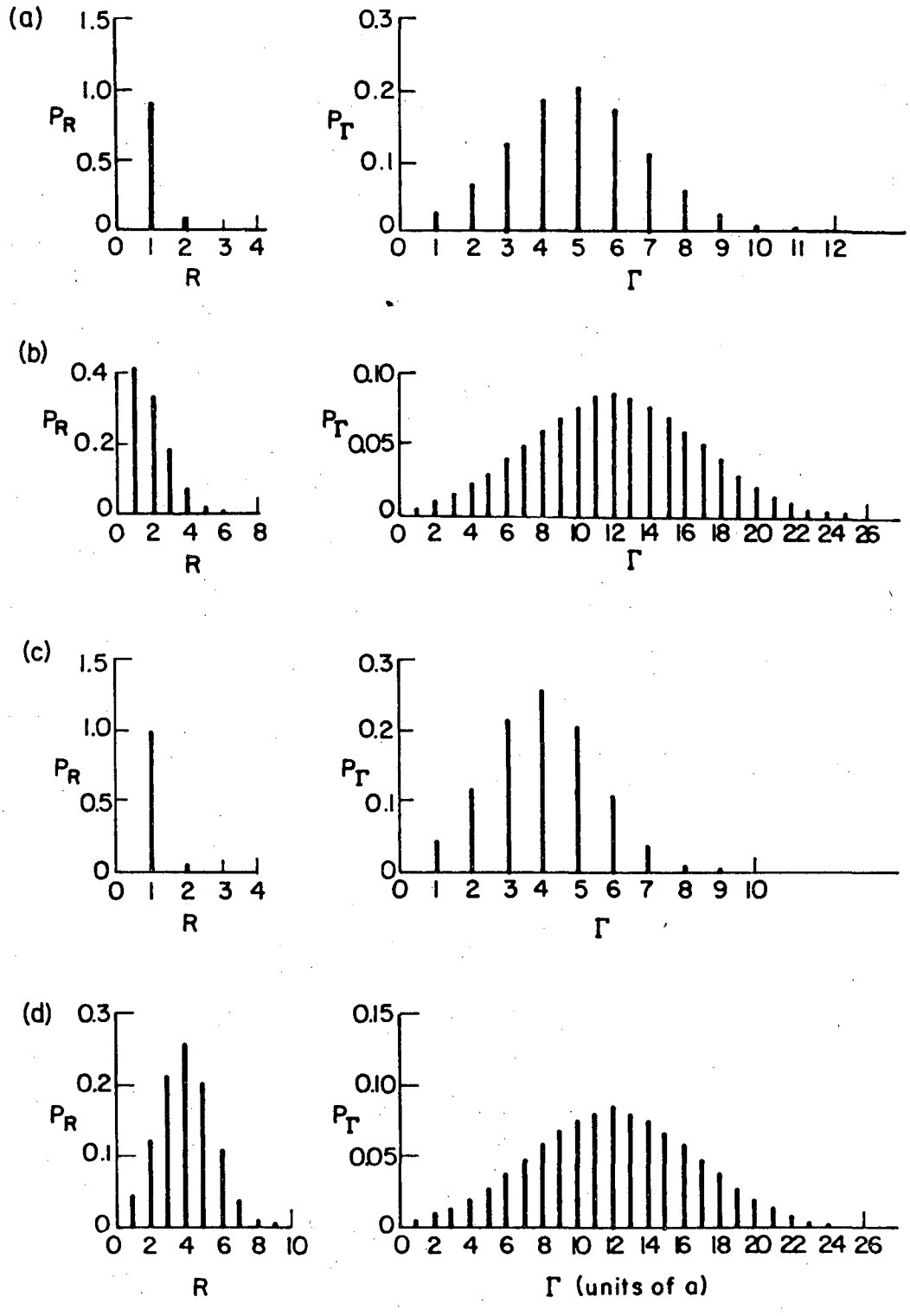

Fig. 3-7. Possible surface step configuration for a (S)-[6(111)×(100)] crystal; (a) broad terrace and singular step, (b) broad step height and terrace width, (c) unfaceted and (d) faceted surfaces with a (211) step orientation.

with a near singular step height distribution, Fig. 3-7a. For a statistically independent array the distribution width is the same order of magnitude as the mean value of the distribution.[112] In an extreme, they could have both very broad step width and height distributions, as in Fig. 3-7b. Data indicate (see Chapter 4) that this surface will facet to (111) and (211) planes instead of (111) and (100); therefore, X_o will be defined to $X_o = 2a + \frac{2}{3}a$, or in otherwords a 3(111)×(100) step. A broad distribution for this is given in Fig. 3-7c, and a possible faceted surface configuration in Fig. 3-7d. With $X_o = \frac{2}{3}a$ again, a bimodal distribution of terrace widths is needed to produce the distribution result in Fig. 3-7d. Another type of distribution which is physically conceivable would be that the terraces widths are not independent of their neighbors with. This would manifest itself in distribution similar to Fig. 3-7d with an attractive interaction or similar to Fig. 3-4a with a repulsive interaction. With carbon present on certain surfaces, areas of both 2 and 3 atom wide terraces are stablized.

3.4.6. Regularity of Actual Surfaces

Calculated interference functions, $i(\vec{\Delta k})$, could help dispell doubts that the vicinal surfaces are reasonably regularly stepped. It is felt that surfaces are regular since the split spots are sharp and the background on a clean annealed surface in the splitting direction is the same as in other portions of the pattern. The large amount of disorder in the surface causes the first term of Eq. (3-21) to become comparable to the second and streaking of the fraction pattern results. In the example in Fig. 3-4, $F\{\bar{\psi} - \bar{\phi}\}\ F\{\phi\} \approx 0.01$. Since the step width and height distributions are coupled, the split beams will broaden with a broad distribution. As apparent from Figs. 3.4c and d, a broad distribution

is necessary to produce a triplet of beams at certain energies. These triplets are generally, not seen in the experimentally observed diffraction patterns.

A few general conclusions about the platinum step surfaces can be reached from the qualitative behavior of the diffraction pattern. The width of the terrace width distribution is probably one half the mean step width or less. The step width and height distributions are independent or the surface has a near singular step height distribution. Since the step widths and heights are not necessarily independent (triplets of beams), the interaction must be repulsive on most surfaces, thereby resulting in near singular step height and narrow step width distributions (see Section 4-3). In other words, the surfaces are well behaved and stepped staircase in nature.

4. THE STABILITY AND STRUCTURE OF PLATINUM SURFACES

4.1. Introduction

The surface tension or excess surface free energy of a solid or liquid controls the shape of the samples surface. A system always tries to minimize its free energy. If it is not kinetically hindered (kinetics limit at temperatures below about 0.7 of the melting temperature in fcc metals[113,114,115]), the system will move large numbers of atoms to obtain its equilibrium configuration, whether it is monatomic height steps, multiple height steps, or large facet planes. As with any substance, and particularly solids, the system may be frozen into a state which is characteristic of equilibrium at higher temperature. This is advantageous in a LEED study, such as this investigation, where observations can be made at low temperature only.

An arbitrary crystal plane on a large sample may be stable in a monatomic height step arrangement or any facet and form a hill and valley structure depending on which configuration has the lowest free energy.[116] The criterion for stability are given in Appendix D. LEED is an ideal tool for determining faceting on surfaces since it is sensitive to small periodic structural changes, such as multiple height steps. If a surface of orientation A is unstable and facets, it can be shown that all other surfaces with orientations near A will be unstable and facet.[116] Taking this argument to its logical conclusion, it can be seen that all the orientations of surfaces between the two (or three) planes to which surface A facets will be unstable and facet to the same set of planes. Thus whole regions may be characterized with a single sample.

This chapter deals with the stability and structure of metal surfaces, in particular, Pt surfaces. Twenty-one different crystal planes of Pt have been studied, several with more than one sample, by LEED and AES. The structure and stability of these planes has been determined for the clean metal surface, and for oxygen or carbon contaminated surfaces. The results are compared with other experimental results and with theories found in the literature; possible extensions and improvements to the theories are suggested. A new structure is suggested for the reconstruction of the (001) face of Pt which came from studies of Pt (001) vicinal surfaces as well as the (001) surface.

4.2. Experimental Results

4.2.1. Samples and Nomenclature

The Pt high Miller Index surfaces which have been studied are shown in Fig. 4.1 on a stereographic projection. The stabilities of the surfaces: clean, covered with a nonolayer of graphitic carbon, and partially covered with oxygen, are tabulated in Table 4-1. The surfaces were prepared and cleaned as discussed in Chapter 2. They were clean of Ca, C and O by AES to the limit of detection, about 0.05 to 0.02 monolayers. The samples were covered with a monolayer of graphite by heating to 800°C in 1×10^{-7} Torr of hydrocarbon for a few minutes. Any hydrocarbon will work, but the experiment was usually conducted using an olefin, ethylene, or an aromatic, benzene; n-heptane was also used. The oxygen contamination was obtained by heating the samples at 850°C in 5×10^{-8} to 1×10^{-6} Torr of oxygen for 10 to 30 min.

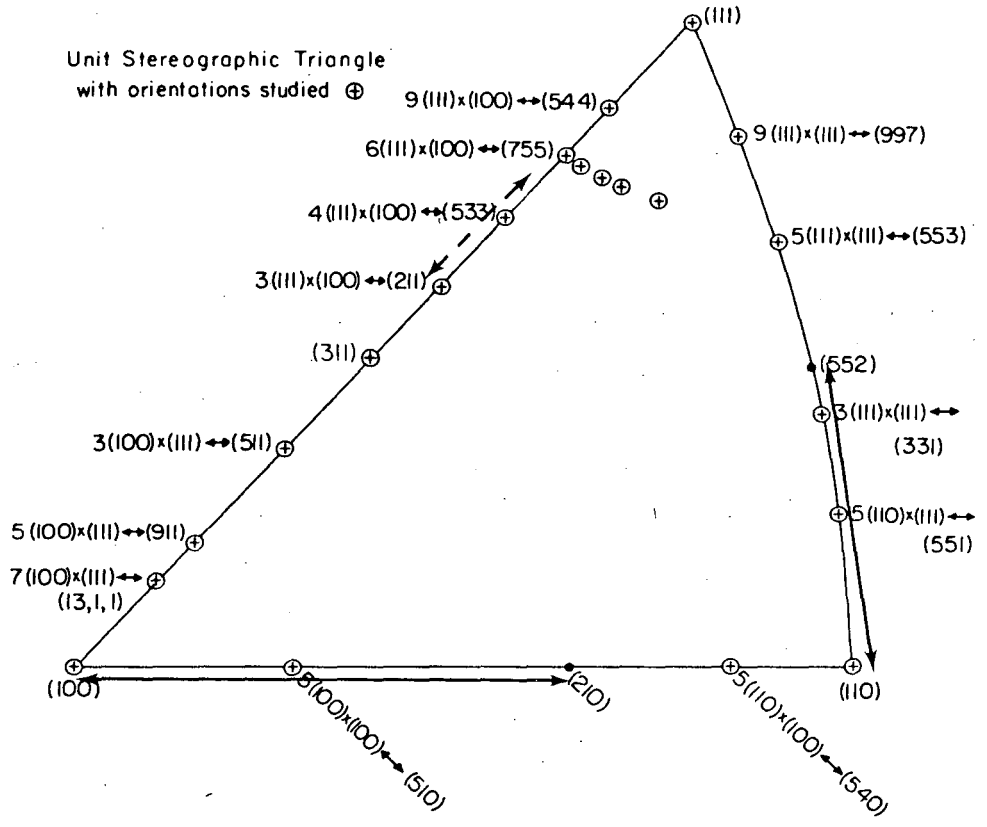

XBL 7510-7465

Fig. 4-1. Unit triangle of stereographic projection showing location and Miller Index of Pt surfaces studied.

Table 4-1. Stability of high Miller Index platinum surfaces.

Nominal Surface Structure	Miller Index	Angle from Low Index Pole (°)	Angle from Zone Line (°)	Zone Line	Clean	C-Covered (C-273 eV/Pt-240 eV Auger Peak Ratio ≈ 4)	O_2 Atmosphere (10^{-6} Torr)
(111)	$(\bar{1}11)$	0	0	[110]	Stable melt point	Stable	Stable 1500°+
Pt(S)-[25(111)×(100)]	$(\bar{12},12,13)$	2.2		[110]	Stable 1400°+	ND**	N.D.
9(111)·(100)	$(\bar{4}45)$	6.2	0	[110]	Stable 1200°+	Stable 1000°+	Streaks-step disorder
6(111)·(100)	$(\bar{3}57)$	9.6	0	[110]	Stable 1600°+	8.5(111)×(100)-C-ring + (211) 700°-	Streaks-step disorder
4(111)·(100)	$(\bar{5}35)$	14.4	0	[110]	Stable 900°C-facet (211) 900°C Stable 1000°C O_2 facet (211) 1000°C	C-ring but same facet 300°C	Facets (211) 1000°C
3(111)·(100)	$(\bar{1}12)$	19.5	0	[110]	Stable	*Stable 1000°C	Streaks
13(111)×(310)	(69,70,72)	4.2°	20 (3 atoms)	[110]	Stable 1600°+	Stable	Stable 1100+
7(111)·(210)		10.0°	33° (1 atom between kinks)	[110]	Stable 1200°+	7(111)×(210)-C-ring 900°+	" "
7(111)·(310)	$(\bar{6}79)$	10.0	20° (2 atoms)	[110]	Stable 1200°+	N.D. -C-ring 900°+	" "
7(111)·(710)	(11,12,16)	9.8	13° (3 atoms)	[110]	Stable 1200°+	0.4-0.6 layer C 8.5(111)×(?)-C-ring+(211) 700-900° Saturated (111)-C-ring+(211)+(552) 700-900°	" "
6(111)×(14,1,0)		9.6	5° (8 atoms)	[110]	Stable 1200°+	Satuated 15(111)×2(100)-C-ring+(552)-C-ring 1600°C	" "
(100)	(001)	0	0	[110] [100]	Stable-reconstructed 1600°C+	Stable-C-ring	Stable 1500+
7(100)·(111)	$(\bar{1},1,13)$	6.2	0	[110]	Stable 1100+	Facets (100)+(311)-C-ring both facets	Facets (001)+(113) all T, $\theta \geq 0.01$ monolayer
5(100)·(111)	$(\bar{1}19)$	8.9	0	[110]	Stable 1200+	Facets (100)+(311)-ordered C 700°-1900°C	" " "
9(111)·(111)	$(\bar{7}99)$	6.5	0	$[0\bar{1}1]$	Stable 1400°+	25(111) 3(111)-C 700°+	17(111)·(111)-O 700°C+
5(111)·(111)	$(\bar{3}55)$	12.3	0	$[0\bar{1}1]$	Stable 1200°+	N.D. *(111)+(110) 700°+	N.D.
6(111)·(111)	$(\bar{2}33)$	10.0	0	$[0\bar{1}1]$	Stable 1200°+	Facets-(111)+(331),(221)	N.D.
5(100)·(100)	(015)	11.3	0	[100]	(100)-(5·1)+(210)	Same as clean	Facets (100)-(5·1) and (210)
(110)	(011)	0	0	$[0\bar{1}1]$ [100]	Stable-reconstructed 1600°C	N.D.	Stable
5(110)·(100)	(045)	6.3	0	[100]	Stable 1200°C+	N.D.	N.D.
3(110)·(111)	$(\bar{1}55)$	8.0	0	$[0\bar{1}1]$	Facets (110)+(331), (221)	Same as clean	Facets (110)+(331)-(221)

*Ca Covered **No Data

The basic stereographic triangle is broken down into three regions for the discussion of the stability of the surfaces. The regions are the surfaces vicinal to each of the low Miller Index poles at the corners of the stereographic triangle, (111), (001), and (011). The structure of the monatomic height steps in each region is shown in Fig. 4-2. The geometry of the steps along each major zone line and on a representative surface with highly kinked steps is shown for each region. The different stepped surface orientations consist of the appropriate geometry step separated by terraces of the appropriate mean width to produce the proper overall orientation. For example, the Pt(S)-[6(111)×(100)] consists of (111)×(100) geometry steps (Fig. 4-2a) spaced on the average 6 atoms apart. (The distribution of step widths is discussed in Chapter 3.)

4.2.2. The (111) Vicinal Surfaces

A large number of surfaces have been studied in this region. The region includes from the [111] pole to the [122] and [112] poles on the boundary zone lines and the whole region within about 20° solid angle of the [111] pole.

4.2.2.1. Clean Surfaces. The surfaces in this region are stable in a monatomic height step configuration when clean. All the surfaces except one, Pt(S)-[4(111)×(100)], are stable at temperatures up to at least 1200°C; the few tested to 1600°C were also stable. The Pt(S)-[4(111)×(100)] surface facets reversibly near 900°C, when clean, from the monatomic height step configuration to a faceted surface with [5(111)×(100)] areas and [3(111)×(100)] areas.

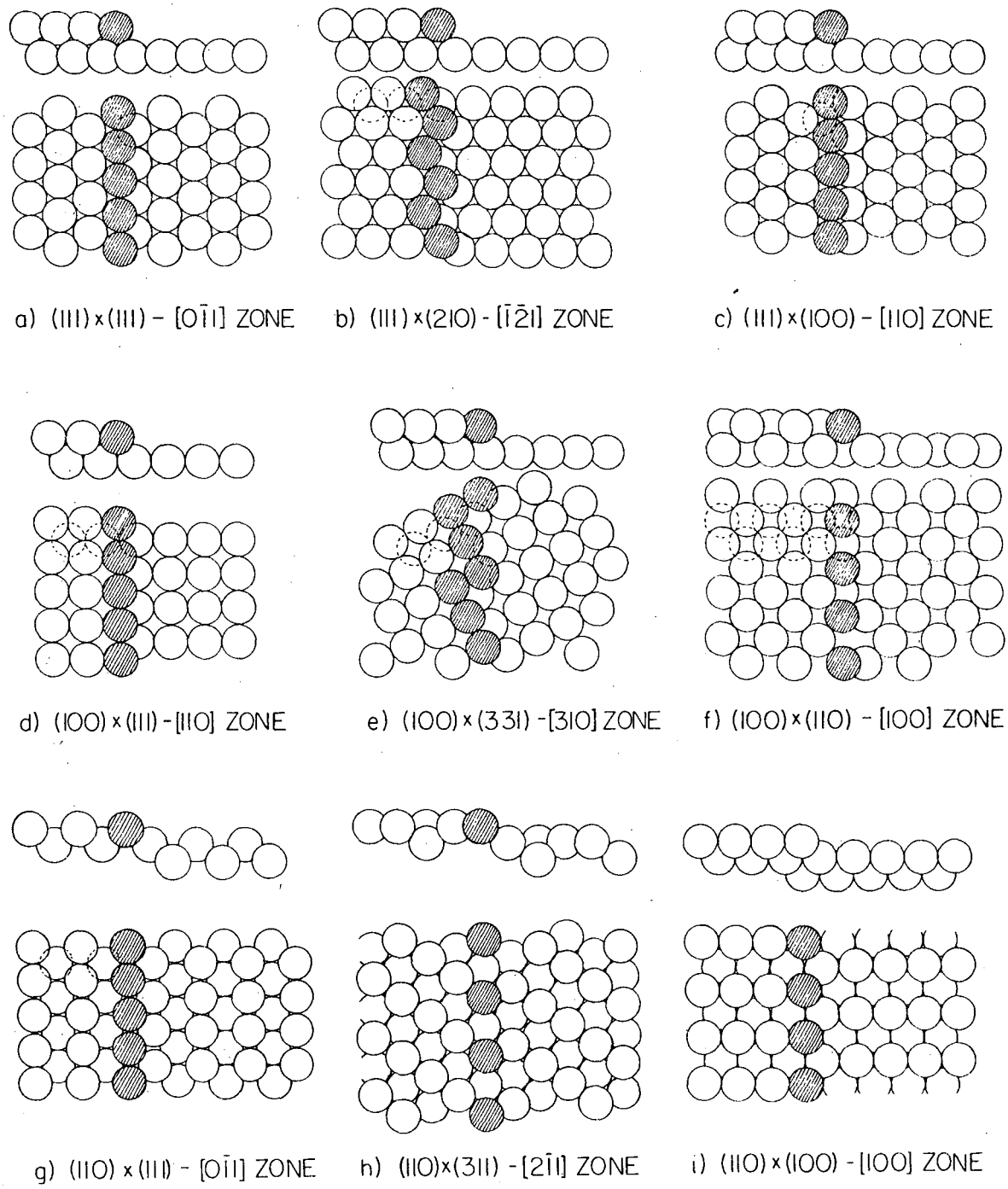

XBL 764-6734

Fig. 4-2. Schematic diagrams of the geometry associated with the steps in each region of the stereographic triangle, showing a geometry on each boundary zone line and a kinked surface in the middle of the region; (a), (b) and (c) are vicinal to the (111) plane; (d), (e) and (f) are vicinal to the (100) plane and (f), (g) and (h) are vicinal to the (110) plane. The reconstruction of the (001) and (011) vicinal surfaces is not shown.

The step width distribution on the unfaceted surface, Fig. 4-3d, is probably quite broad since all three triplet spots are quite bright. As was shown in Section 3-3, the more satelittes which are seen brightly, the broader the distribution of step widths. The width distribution may resemble that of Fig. 3-6a or possibly Fig. 3-6b. Above 900°C, the width distribution changes, with the steps apparently bunching, and may resemble Fig. 3-6d.

The full width at half maximum (FWHM) of the [3(111)×(100)] facet specular beam is ~3.6° at 60 eV. This gives approximately 25Å or ~4 [3(111)×(100)] lattice spacings. This shows that the Pt atoms have a high mobility and can obtain an equilibrium surface configuration under the conditions of our experiments. It also demonstrates that a high temperature structure can be quenched and studied by LEED at room temperature. This indicates that the step structure which is obtained by quenching rapidly from 1600°C (about 3 sec to reach 800°C below which appreciable diffusion does not occur) is the equilibrium structure at the high temperature except for some possible reordering of the steps.

The LEED patterns of several surfaces are shown in Figs. 4-3, 4-4 and 4-5. As seen all these diffraction patterns have the overall hexagonal symmetry of the (111) surface with the spot splitting inversely proportional to the step spacing (see Chapter 3) and the splitting direction normal to the step direction. The ratio of the (10)-(00) distance (close-packed distance) to the doublet splitting agrees with the nominal value to within a 1/3 of a lattice spacing, i.e., for a [6(111)×(100)] surface the ratio is 5-2/3±1/3. This agrees

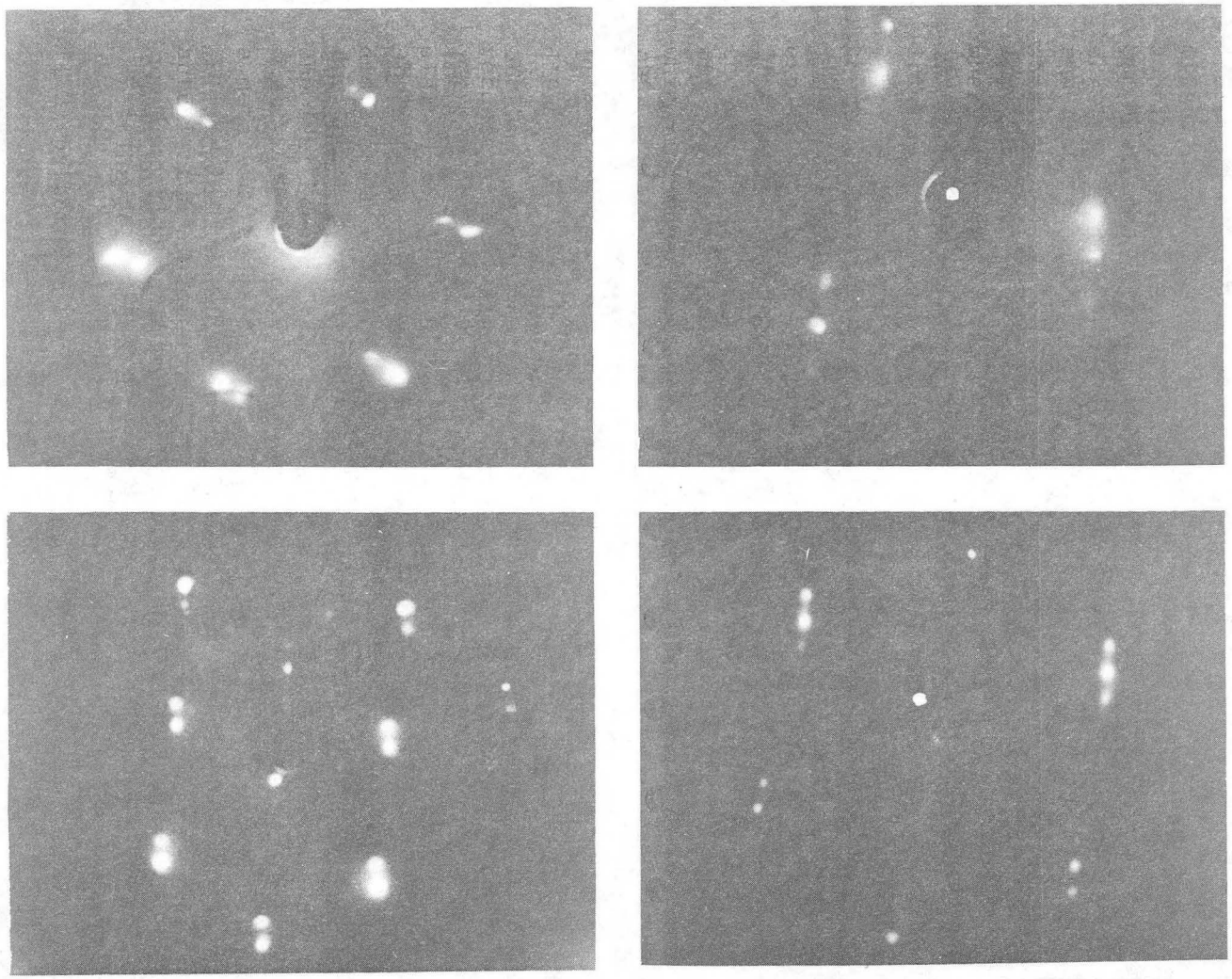

XBB 733-1571

Fig. 4-3. Photographs of the LEED patterns of the (a) Pt(S)-[6(111)×(100)], (b) Pt(S)-[7(111)×(310)], (c) Pt(S)-[9(111)×(100)] and (d) Pt(S)-[4(111)×(100)] stepped surfaces.

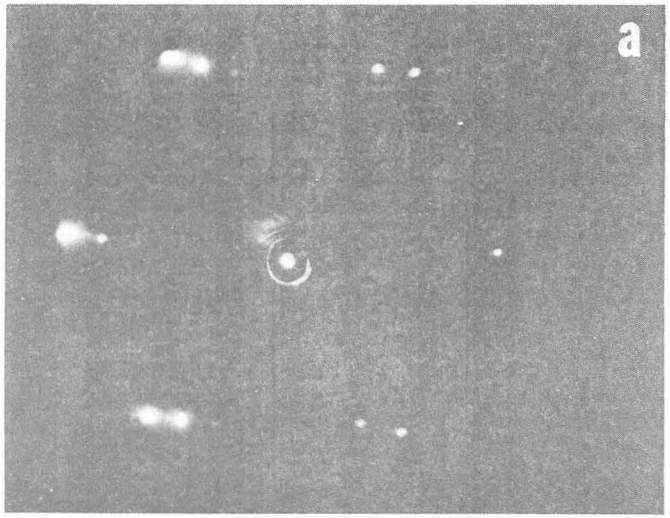

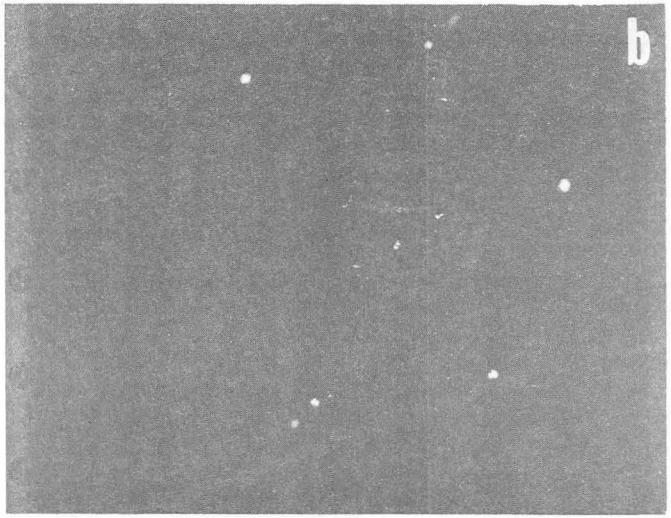

XBB 7511-8761

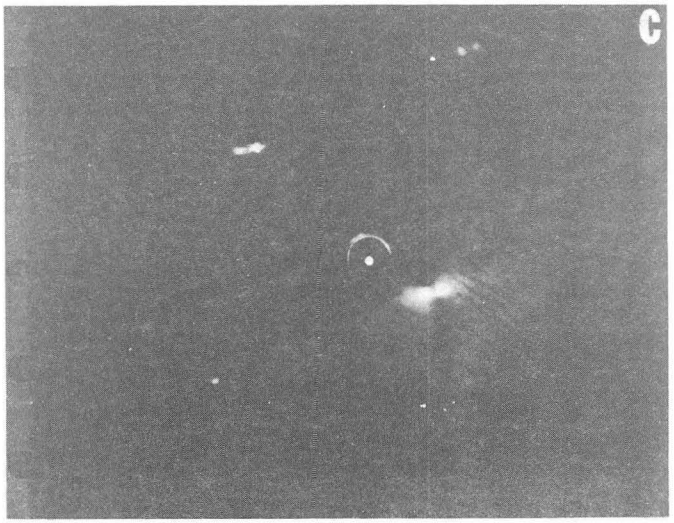

Fig. 4.4. Photographs of the LEED patterns of the (a) Pt(S)-[7(111)×(111)], (b) Pt(S)-[7(111)×(210)] and (c) Pt(S)-[13(111)×(310)] stepped surfaces.

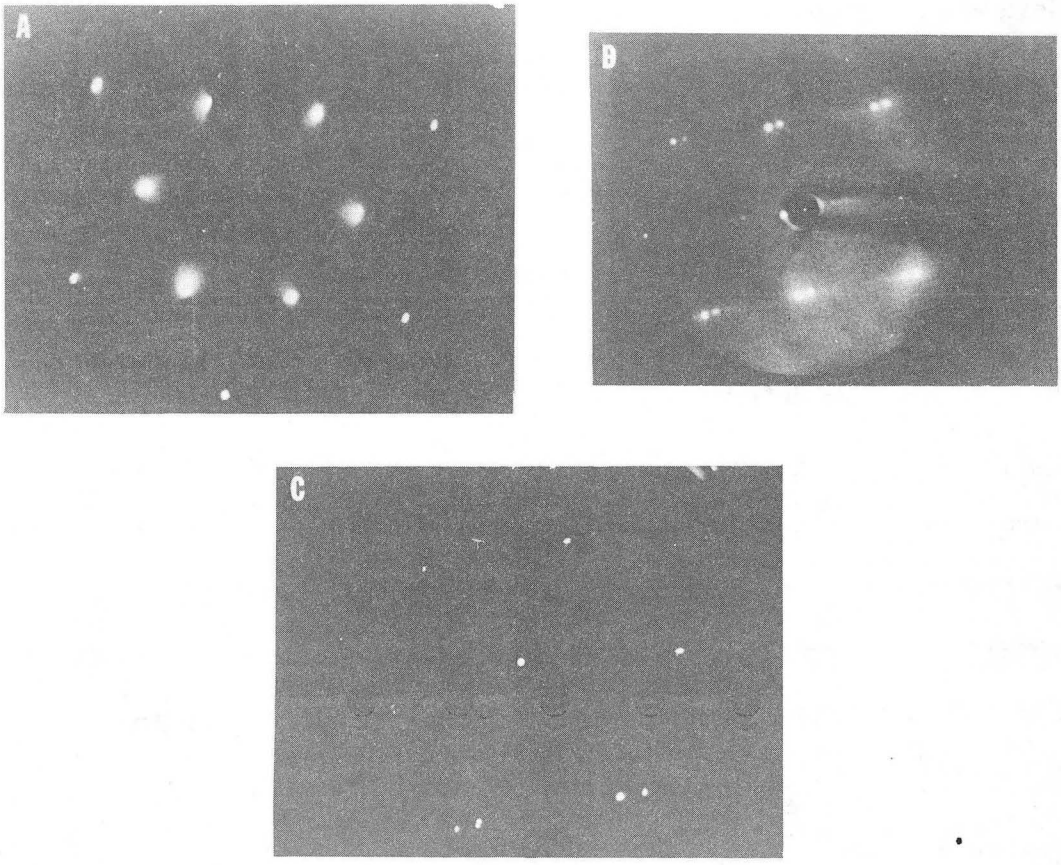

XBB 7512-9030

Fig. 4-5. Photographs of the LEED patterns of the (a) Pt-(111), (b) Pt(s)-[9(111)×(111)] and (c) Pt(s)-[6(111)×(111)] surfaces.

well with the uncertainty of cutting and polishing the crystal as described in Chapter 2. The close packed distance, (1,0)-(0,0) is determined by measuring across the flats of the hexagon perpendicular to the split direction and multiplying by $1/\sqrt{3}$. The [n(111)×(100)] and [m(111)×(111)] type surface diffraction patterns appear identical, but the splitting direction is actually along a different zone line. With a careful intensity vs voltage determination, multi-layer diffraction from the threefold symmetry of the fcc [111] allows the zone line to be determined.

4.2.2.2. Graphite Covered Surfaces. A monolayer of graphitic carbon causes interesting surface structural rearrangements in this region. On samples between the Pt(S)-[9(111)×(100)] and Pt(S)-[3(111)×(100)], graphitic carbon causes facets of [3(111)×(100)] and Pt(S)-[9(111)×(100)] to form. These are similar to the Pt(S)-[4(111)×(100)] clean surface in that it is reversible and the facets are small, again about 35Å. When the carbon is removed, either by O_2 cleaning or high temperature bulk dissolution, the monatomic height step configuration returns. Surfaces with terraces wider than 9 atoms are unaffected by the presence of graphitic carbons, at least along the [110] zone. One edge of the unit cell, $\vec{a}$, in the basal plane of graphite is 8/9 of the close packed platinum distance, 2.77Å, thus the graphitic layer apparently stabilizes the terrace width at which the Pt and graphite unit cells are in registry, i.e., Pt(S)-[9(111)×(100)].

Along the $[0\bar{1}1]$ zone, the samples also facet with graphitic carbon on their surface. The facets appear to be the (111) plane and

a combination of [3(111)×(111)] and [2(111)×(111)] planes. There is no clear facet specular reflection as along the [110] zone, but a fairly bright streak with more intensity corresponding to the [3(111)×(111)] and [2(111)×(111)] diffraction beams. The mean facet size cannot be determined. The samples along the [0$\bar{1}$1] zone have higher background and broader, less well defined beams, as compared to samples along the [110] zone, indicating that the step orientation is quite important for the nucleation and growth of stabilizing structures.

In this region between the zone lines, some samples are stable in monatomic height step while others facet to the three lower Miller Index corners, (111), [3(111)×(100)] and [2-3(111)×(111)]. The Pt(S)-[7(111)×(210)] and Pt(S)-[13(111)×(310)] are stable with a monolayer of graphitic carbon on their surfaces. The [7(111)×(710)], at 0.4 to 0.6 monolayers of carbon, facets to a [8.5(111)×(210)-C ring and a [3(111)×(100)], but when saturated, facets to the (111), [3(111)×(100)] and [2-3(111)×(111)] planes. This is very similar behavior to that found by Ellis on UO_2 kinked surfaces.[103] Upon heating and the loss of O_2, is the destabilization of steps, his surfaces faceted to the (111), (335) and (331) going through similar intermediate stages. By comparison with other studies,[117,118] it is thought, but has not been confirmed, that with multilayer graphitic carbon, even the 9(111)×(100) surfaces will be destabilized with respect to the (111) surface. However, faceting beyond the (112) and (133) surfaces is not expected to occur. The (112) and (133) surfaces are of relatively low Miller Index, and at least the (112)

surface is stable with a monolayer of graphitic carbon. The (133) has not been studied but is not stable with submonolayer coverages of Ca (surfaces along the [0$\bar{1}$1] zone facet to (111) and (011)) planes with significant coverages of Ca), therefore, it might not be stable at large multilayer carbon coverages.

4.2.2.3. Oxygen Covered Surfaces. The surfaces in this region do not facet when exposed to 1×10^{-6} Torr of O_2 at high (900°C) temperatures. However, sharp streaks form in the diffraction pattern from the surfaces on the [110] zone in 1/2 order position, as shown in Fig. 4-7 for the Pt(S)-[6(111)×(100)] and a 1/3 order positions for the Pt(S)-[3(111)×(100)] surface, Fig. 4-8. It cannot be determined if the steps are disordered, also, by the oxygen adsorption since the oxygen streak obscures the doublet diffraction beams from the step and any streaking intrinsic to the doublet. Samples on the [0$\bar{1}$1] zone form multiple height steps.[71] The Pt(S)-[9(111)×(111)] becomes Pt(S)-[17(111)×2(111)]-O when exposed to oxygen at high temperature. Kinked step samples between the major zone lines are stable with oxygen on their surface. The oxygen adsorbs randomly along the step since no extra diffraction features are observed, and the background is higher than on a clean sample.

4.2.3. The (001) Vicinal Surfaces

Several surfaces have been studied in this region. The region includes from the [001] pole to the [113] and [012] poles in the boundary zone lines and the whole region within about 25° from the [001] pole.

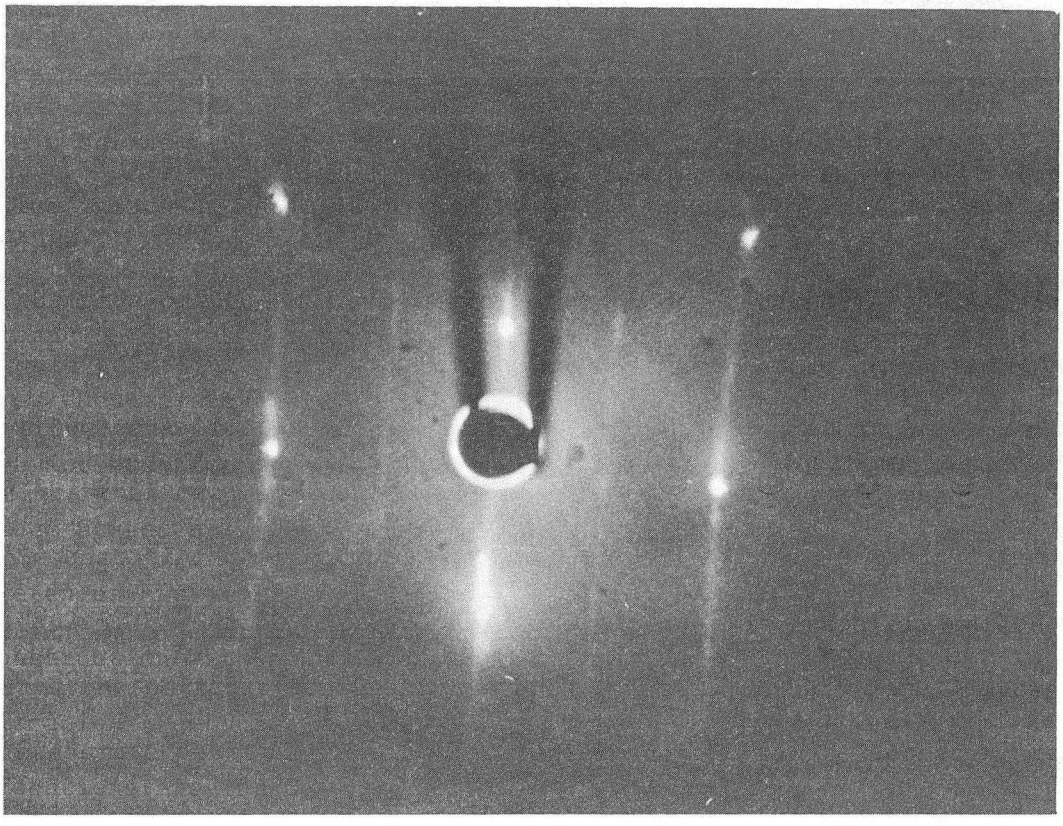

XBB 718-3671

Fig. 4-7. Photograph of the LEED pattern of the Pt(S)-[6(111)×(100)]-O showing the 1/2 order streaking which occurs with oxygen adsorption at high temperature.

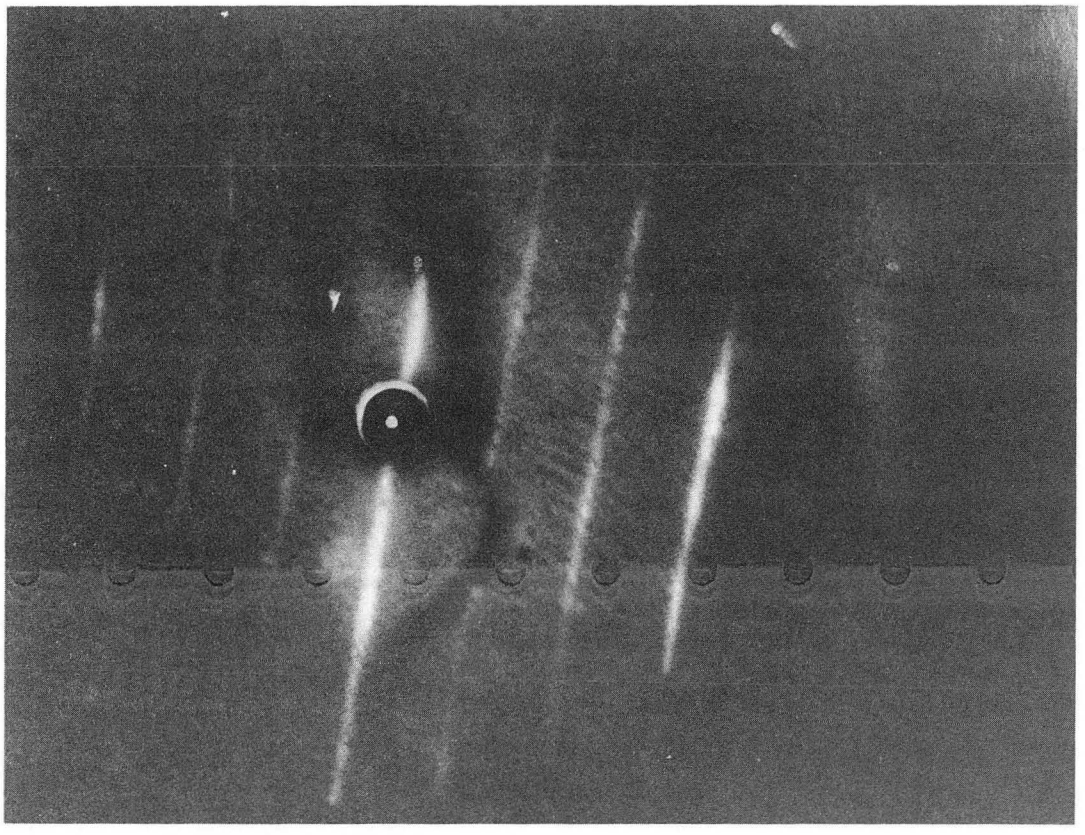

XBB 765-3883

Fig. 4-8. Photograph of the LEED pattern of the Pt(S)-[3(111)×(100)]-O showing the 1/3 order streaking which occurs with oxygen adsorption at high temperature.

4.2.3.1. Clean Surfaces. The surfaces in this region all possess a reconstructed (001) terrace as readily seen in Fig. 4-9 (see Section 4.4 for a detailed discussion of the (001) reconstruction). The samples along the [110] zone are stable in a monatomic height step configuration to above 1200°C, while along the [100] zone the samples facet to (001) and (012) planes. These facets formed upon annealing at 850°C, and were quite large compared with the facets which form in the region near the [111] pole. The angular FWHM of the facet beams is 1.5°; this gives a facet size of >22 (012) lattice spacings or >100Å.

Samples off the major zone lines were not prepared in this region. It would be of interest to determine at what angular rotation from the [110] zone line would produce stable surfaces and what amount of angular rotation away from the zone line would yield surfaces that become unstable and facet.

4.2.3.2. Carbon Covered Surfaces. A layer of graphitic carbon returns the terraces to the square bulk symmetry on both zone lines. The steps are destabilized in this region and the sample surfaces are unstable and facet to (001) and [2(100)×(111)] or [2(100)×(100)] planes, with a graphitic ring structure prominent in the diffraction pattern from all three planes. This is expected to be the equilibrium configuration in this region for carbon covered surfaces, as well as oxygen and calcium covered surfaces. The [2(100)×(111)] and [2(100)×(100)] are relatively low Miller Index planes and both are stable with a monolayer of graphite on them. Lang[118] observed similar faceting.

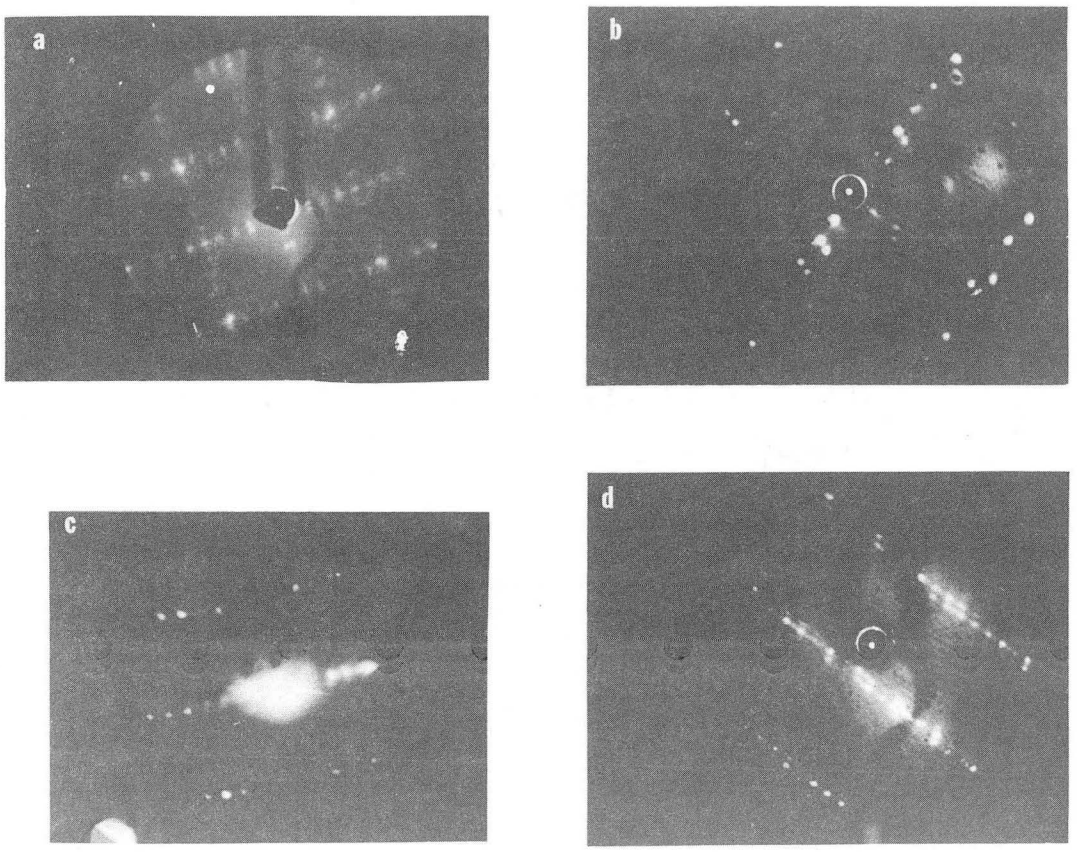

XBB 7511-9031

Fig. 4-9. Photographs of the LEED patterns of the (a) Pt(001), (b) Pt(S)-[75(100)x25(210)], (c) Pt(S)-[5(100)x(111)] and (d) Pt(S)-[7(100)x(111)] surfaces.

4.2.3.3. Oxygen Covered Surfaces. The samples along the [$\bar{1}$10] are very sensitive to oxygen. Less than 0.05 monolayer of oxygen causes the Pt(S)-[7(100)×(111)] to facet to the (001) and [2(100)×(111)] planes. When the Auger O-510 eV peak height to Pt-238 eV peak height ratio is less than 0.1, the sample still facets; noise precludes accurately determining how much less than 0.1. One monolayer of oxygen gives a peak height ratio of ~2, as was determined with 0.1 to 0.05 monolayer of Ca on a Pt surface which promotes adsorption of oxygen into the high temperature state.[115] It is expected that the oxygen stabilizes the [2(100)×(111)] stepped surface; this means that less than one O atom for every four Pt atoms along the step greatly influences the surface structures' stability. At higher coverages of oxygen a (2×1)-O pattern is present on [2(100)×(111)] facet plane, but the (001) pattern does not change. As the O coverage is lowered below ~0.2 monolayers by heat treatment the (2×1) pattern fades and is not visible at coverages less than 0.05 monolayers. This behavior indicates most of the oxygen at lower coverages of less than 0.2 monolayer is on the [2(100)×(111)] facet plane and hence its surface tension is affected more than that of the (001). The angular spread of the [2(100)×(111)] beams is the same as the instrumental broadening at all coverages of oxygen investigated. Thus a very small amount of oxygen can cause large facets to form.

The 5(100)×(100) surface on the [100] zone does not appear to exhibit this behavior in that it is faceted when apparently clean. Although this surface was studied before the extreme oxygen sensitivity was observed on surfaces on the [110] zone, the Auger

spectrum are noise free in the region between 500 and 520 eV, and the surfaces are faceted. There could be a very small amount of oxygen, $\leq$0.03 monolayer, on the surface which would be undetectable with the retarding potentical Auger spectrometer used in this investigation, as no extra precautions were taken to assure the absence of oxygen. The [(100)×(100)] step is much more open (lower coordination of atoms) than the (100)×(111) step so its stability can be rationalized.

A close packed direction of the (001) hexagonal surface reconstruction is parallel to the steps in the ([(100)×(111)]) [110] zone, but the steps on the [5(100)×(100)] surface are not in coincidence with the reconstruction overlayer; this could also promote instability on the [100] zone ([(100)×(100)] steps).

4.2.4. The (011) Vicinal Surfaces

Only two surfaces have been studied in this region, one on each zone line. The region includes from the [011] pole to the [012] pole on the [001] zone and to the [122]-[133] region on the [0$\bar{1}$1] zone and the whole region within about 17° from the [011] pole.

4.2.4.1. Clean Surfaces. The clean surfaces in this region are not stable in a monatomic height step configuration. On the [0$\bar{1}$1] zone, the sample faceted to the (011) and (122)-(133) planes, and on the [100] zone the sample had a apparent double height step and a reconstructed terrace. The (011) surface of Pt reconstructs to give a (1×2) pattern[119] which can be seen on the (011) facet in Fig. 4-10b, ([3(110)×(111)] nominal surface). The Pt(S)-[3(110)×(111)] surface's instability is not surprising with its corrugated surface structure. The ridges and valleys of the (011) surface run parallel

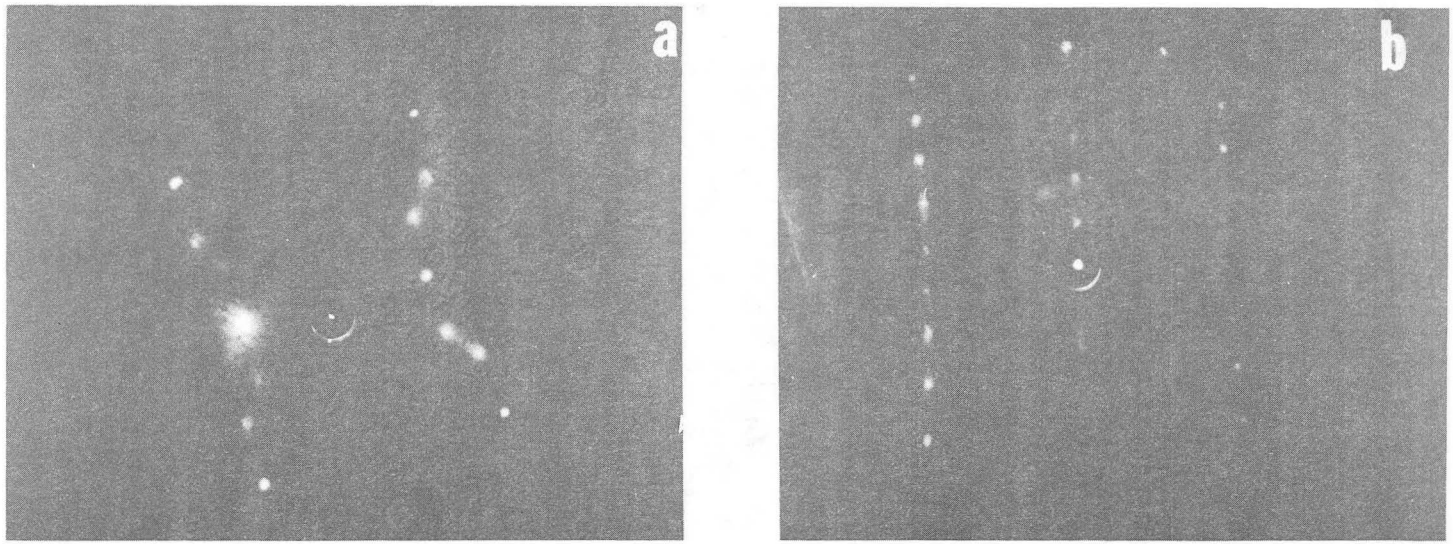

XBB 7511-8760

Fig. 4-10. Photographs of the LEED patterns of (a) Pt(S)-[5(110)×(100)], (b) Pt(S)-[3(110)×(111)]-facet and stepped surfaces.

with the steps. The (011) reconstruction is thought to be a filling of every other row to produce a double height step. These height steps might be unstable and agglomerate to form (331) planes. The facet size could not be determined because of experimental difficulties.

On the Pt(S)-[5(110)×(100)] surface, the terrace is reconstructed, but not to a (1×2), and the terrace width is doubled (see Fig. 4-10a). This is apparently the stable structure as annealled 1 hr at 850°C or 1200°C produces the same LEED pattern. Park and Houston[107] have shown using the concepts of Section 3.4 that fractional order beams, such as present here, (1×2-2/3) reconstruction, can result from mixtures of rational order structures, i.e., 1/3 of (1×2) and 2/3 of (1×3) reconstruction. These results could be affected by oxygen but the 1200°C anneal should remove any oxygen from the surface. Merrill[120] has shown that annealing an (011) surface a few minutes at 1100°C will remove oxygen from that surface, therefore 1 hr at 1200°C should remove any oxygen present on the [5(110)×(100)] surface. Intensity analysis of the "doublets" to determine the step height did not produce the proper value as it does with surfaces vicinal to [111] pole. The values obtained for the maxima are listed in Table 4-2.

4.2.4.2. The Remainder. No samples have been cut in this region which would be what is not in the (111), (011) and (001) vicinal regions. These are very rough surfaces with almost every surface atom of low coordination. They would probably be very sensitive to surface contamination possibly faceting to the (113), (012) and (122)-(133) planes instead of the low index planes. The study of these and other

Table 4-2. Doublet maximum vs voltage for the reconstructed Pt(S)-[5(110)×(100)] surface (all numbers are ±2%).

Voltage Equal Intensity (eV)	Voltage Single Maximum (eV)
10	26
50	94
140	192
265	310
380	470
572	

planes off the boundary zone lines would help to determine the behavior and stability of the stepped surfaces of Pt.

4.3. Discussion of Step Stability

4.3.1. Comparisons with other Measurements

4.3.1.1. γ-Plot Determination for Pt-Clean Surface. It is interesting to compare the results for the stability of Pt surfaces presented in Section 4.2 with other similar determinations found in the literature. Mclean and Mykura[121] reported the rotational angle averaged value of the surface free energy for solid angles out from the three low index poles. They used the twin boundary groove technique to measure the surface tension (this method is discussed in Appendix D). The results have been replotted in a form amenable to the Herring analysis[116] of stability and are shown in Fig. 4-11. Their "clean" surfaces are probably highly contaminated since with no pretreatment they were annealed several days at elevated temperature in 10^{-5} Torr vacuum. The carbon and other possible impurities in bulk material would segregate to the surface at least in the lower portion (900-1100°C) of their temperature range (900-1500°C). They also annealed a sample in air at 1100°C which would remove all the carbon from the bulk and surface, but would leave some oxygen as well as Ca on the surface. As seen in Fig. 4-12, annealing at 1100°C in air or in vacuo makes a large difference in the stability of the Pt surface.

M and M found their "clean" surfaces to be generally stable in the monatomic height step configuration. At 1300°C, surfaces near the (001) faceted and at 1500°C surfaces, near the (111) faceted. At 900°C, the temperature where the LEED data is most reliable, a number of

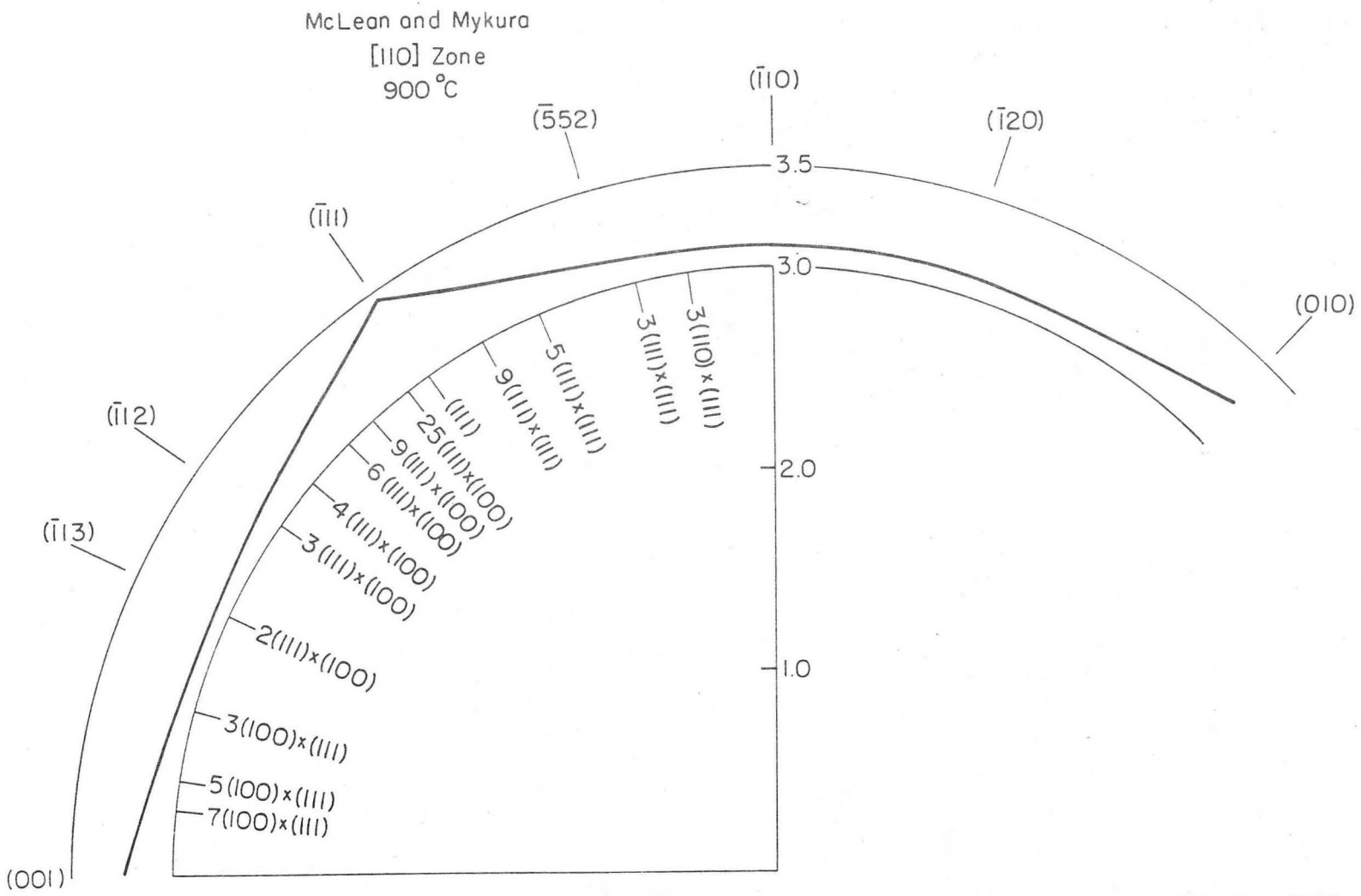

XBL 753-5922

Fig. 4-11. Polar plot of $1/\gamma$ for Pt from McLean and Mykura.[121] Regions of stability are determined by Herring analysis[116,229] at 900°C for "clean" surface. All regions are stable in monatomic height steps, but vicinal to the {100} and {111} planes all step configurations are stable.

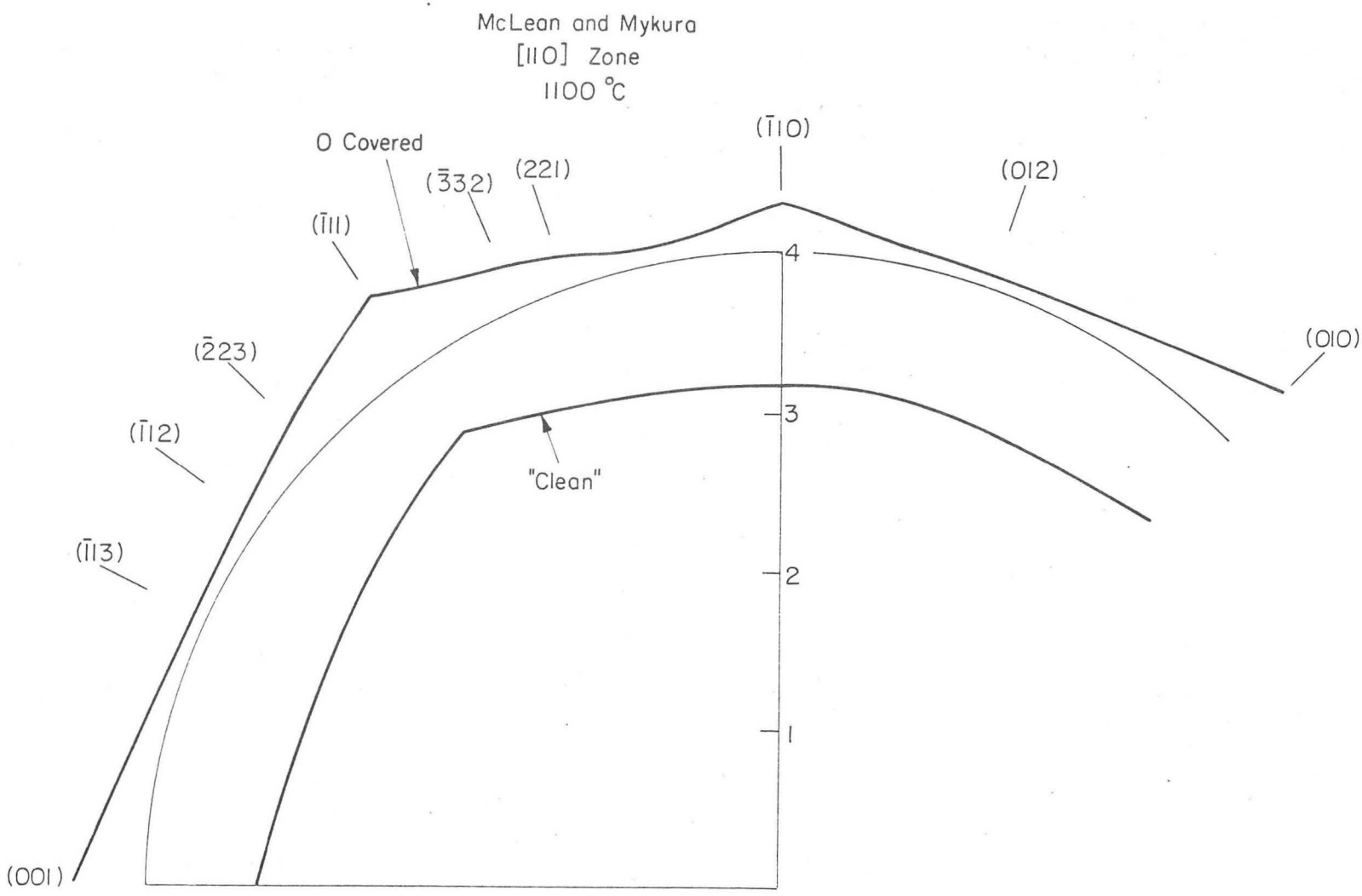

XBL 763-6614

Fig. 4-12. Polar plot of $1/\gamma$ for Pt annealed in air at 1100°C from McLean and Mykura.[121] Faceting was observed near all three low index poles and analysis indicates that the {111} and {110} vicinal planes facet. Near the {100}, all step configuration are equally stable but the surfaces facet in O_2 and are stable clean.

planes were found unstable. Since LEED patterns cannot be seen at high temperatures (above about 700°C), the surface might relax during the cooling period and return to a more ordered lower temperature structure. This can be significant above about 800°C where diffusion is fast enough for measurable relaxation to occur in a few seconds. Burton, et al.[122] have observed a similar relaxation phenomena with alloy surface composition. They found significant changes in the surface composition with rapid quenching from above 700°C to room temperature. This would involve moving atoms only one or two lattice spacing which would not cause significant structural changes.

Quenching the Pt crystals from 900°C, does not allow sufficient time to move the large number of Pt atoms associated with facet formation. The instability along the [100] zone and on part of the $[0\bar{1}1]$ zone by LEED are not observed by the twin boundary method. On the [100] zone near the (001) pole there is marginal stability measured by the groove method, but no anisotropy was found near the (011) pole. This lack of anisotropy cannot be rationalized in light of the instability by LEED on Pt and definite cusping on other metals. Vicinal to the [111] pole, the $1/\gamma$ plot from the groove data is a straight line; this indicates that any and all possible surface structures would be stable.[116] The LEED intensities need to be examined carefully in light of Section 3.4 to be sure the steps are monatomic height and not a broad distribution.

On the [110] zone there is a reversible faceting at 900°C in the region between the (112) and the (335) by LEED, that is not seen by the twin boundary method. This is significant in that the curvature

of the γ-plot must change sign twice between low index poles rather than just once as along the [0$\bar{1}$1] zone. The standard step-ledge-kink theories[123,124] do not predict that a region away from the low index poles will be unstable when there are stable regions on both sides closer to low index poles. If the (112) plane has the extra stability to be considered a low index plane (i.e., there is a cusp in γ-plot at (112)), then the theories can be satisfied.

An interesting observation made by M and M on the "clean" surface is that the slope of the γ v: T plot changes; the farther a surface is from a low index pole the lower the temperature of break. They[121] interpret this as a surface melting of the particular crystal face.[125] This disordering particularily on the (001) vicinal surface was not observed by LEED, but the surface could have recrystallized during the quench. The crystal would emit too much light above 1000°K to use a LEED post-acceleration display system, but a Faraday cup detector would allow discrimination of diffraction beams from the background and a possible determination of a surface phase transition. Another possible interpretation is the dissolution of surface segragated impurities such as C or Ca, both of which have endothermic heats of solution. Different surface-bulk equilibrium for different crystal planes has been noted for C and S on Ni[126,127] and could account for the differences in temperature where the change in slope occurs.

4.3.1.2. γ-Plot-Oxygen Covered Surface. The air-annealed surfaces were unstable and faceted in the work of M and M.[121] The planes in each of the three regions discussed in Section 4.2 faceted to the corner surfaces of that region; the fourth region (the left

over portion) was stable and did not facet. These results are generally similar to the LEED results for the oxygen covered surfaces. The (001) vicinal surfaces faceted to (001) and (113) or (012) with very little oxygen on the surface by both LEED and the groove method. The relative rate of change of the surface free energy with and without oxygen allows the determination of the relative oxygen adsorption density.[128] The oxygen density is higher on (001) than on its vicinal surfaces by the twin boundary method; however, LEED results say the (001) remains relatively oxygen free and the (113) facet has a (1×2)-O pattern at higher coverages. This is probably an anomally of the interpretation of the groove method.

The (011) vicinal surfaces studied are unstable by the groove method and marginally stable by LEED. On the [110] zone faceting occurred to (122) and (011) by both methods. While on the [100] zone multiple height steps are detected by LEED, instead of the faceting to the (012) and (011). Possibly the oxygen average of the surface is greater in the grooving experiment resulting in greater stabilization of the (011) plane; a strong adsorption of oxygen was noted on the (011).

The (111) vicinal surfaces were found to facet to (111) and an indeterminate plane about 12° from the [111] pole by the groove method. This is contradictory to the LEED results where the vicinal surfaces are all stable when annealed in oxygen. These surfaces did facet when a greater than one monolayer coverage of CaO was present (see Section 2.3 for discussion of Ca on Pt) indicating the possibility of contamination on N and M samples. Oxygen adsorption on (111) vicinal surfaces

causes a one dimensional streaking in the diffraction pattern at the 1/2 order positions on the [110] zone and double height steps on the $[0\bar{1}1]$ zone,[71] neither of which would appear as faceting. This discrepancy may again be explained by a different oxygen coverage as well as contamination.

The data of McLean and Mykura[121] are nearly straight lines on a $1/\gamma$-plot vicinal to the (001) and (111) surfaces, so a slight stabilization by impurity adsorption could lower the step energy in these cusps and cause faceting. If all the binding energy of adsorbed O_2 (97 kcal/mole)[129] at 1/100 monolayer total coverage were used to stabilize the steps on a 7(100)×(111) crystal surface, the surface energy would be lowered 70 erg/cm^2 ($\gamma_{100} \sim 2800$ erg/cm^2). With total anisotropy of about 7% this is a sizable amount and could cause the faceting.

4.3.1.3. Other Measurements on Pt. Lang[118] used LEED to determine the stability and structure of four carbon covered single crystal surfaces, the Pt-(111), Pt-(001), Pt(S)-[6(111)×(111)] and Pt(S)-[5(100)×(111)]. His observations on the stability of surfaces are in general agreement with the results presented in this thesis. The (111) surface was stable with a large amount of carbon on it. The exact coverage of C on their surfaces was not determined from the lack of an Auger spectrometer; however, it is at least as large, if not larger, that the level in this study. The (111) vicinal surface was found to facet to the [2(111)×(100)], [3(111)×(100)], [3(111)×(111)] and (111) surfaces at high C coverages. The intermediate facet structure discussed in Section 4.2 (faceting to [3(111)×(100)] and

and [9(111)×(100)]) was not distinctly observed by Lang,[118] but at his lower C coverages streaking was observed in the proper locations. Thus he did not obtain as much order at the low C coverages and the distinct pattern was not observed. Lang observed the (001) surface to facet at high C coverages to the [2(100)×(111)] and [3(100)×(111)], but not uniformly across the single crystal. This faceting was not observed in this work or that of Morgan and Somorjai,[96] and since it was not uniform across the surface of Lang, may be caused by contamination or improper surface preparation (maybe a bent crystal). The (001) vicinal surface faceted to the [2(100)×(111)] as in this study, but Lang detected facets off the zone line which were not observed in this study on the [7(100)×(111)] surface. The comparison of this work and the work of Lang demonstrate the sensitivity of the surface to the exact conditions of the experiment, surface contamination and the carbon coverage of the surface.

Blakely and Mykura[114] measured the surface self-diffusion and surface energy of Pt foils by annealing of scratches. They obtained a value of the mean surface diffusion coefficient of $\bar{D}_s = 4\times10^{-3}$ cm^2sec^{-1} $\exp(-26{,}400/kT)$. This gives $D_s = 5\times10^{-8}$ cm/sec at 900°C which is sufficient to form a facet of the size measured by LEED in about 100 sec, therefore, this again says that the LEED experiment measured equilibrium properties of the surface. They found a six to eight-fold variation in the surface diffusivity at a given temperature with variation of crystallographic orientation. The fastest diffusion was along low index terraces, particularly (111); the slowest was perpendicular to steps and particularly near (001). Ayrault and Ehrlich[130] using a

field ion microscope with a Rh tip, UHV conditions, and much lower temperatures (50 to 200°K) found a similar effect of crystallographic orientation on the diffusion coefficient. Blakely and Mykura[114] found "clean" (001) vicinal surfaces facet at 1300°C as did McLean and Mykura,[121] however after >150 hr annealing the (001), facets of Blakely and Mykura disappeared. This is indicative of inpurities from the bulk diffusing to the surface and slowly being depleted. A small oxygen leak, which is possible in the 10^{-5} Torr vacuum conditions used, could remove C and Ca slowly under the experimental conditions (see Chapter 2). This casts further doubt on McLean and Mykura's surface melting interpretation.

Melmed[115] measured the surface diffusion activation energy on Pt field-electron emission tip. An activation energy of 29 kcal/mole was measured, which agrees quite well with those of Blakely and Mykura.[114] The region around the (001) pole was quite sensitive to C contamination in the temperature range 1200-1600°C, as it was with Blakely and Mykura[114] and apparantly McLean and Mykura.[121]

4.3.1.4. Other Metals. A comparison of the stability of Pt surfaces by LEED can also be made with other metals which might be expected to behave similarly, group VIII and IA metals. The anisotropy of the surface energy of Au has been measured by Winterbottom and Gjostein[131] by the twin boundary groove method. All surfaces were found stable at 1030°C. An interesting flattening of the curvature of the γ plot was found on the [110] zone near the (111) pole. The region corresponds very closely to the region on Pt surfaces where carbon causes an instability. There are many impurities in the bulk

Au samples which segragate to the surface and could cause instabilities.[95] As with grove data on Pt,[121] there are no instabilities at the (011) or (001) poles, as evidenced by LEED and considered reasonable since the (011) and (001) surfaces reconstruct to lower their surface free energy on both metals.

On Ir, the other metal whose (001) and (011) surfaces reconstruct, twin boundary groove measurements have not been made. Measurements have been made with field ion microscope tips on the relative energy of the lower index faces.[132] The anisotropy is very similar to that found on Pt and Au by the groove method. What is interesting, is that during the zero field annealing process the (012), (113), (112) and (133) type surfaces reached their equilibrium very rapidly compared with the low index planes, (111), (001) and (011). This has implications for the self-diffusion of atoms and the equilibrium structure, as discussed in Section 4.3.2.

Low Energy Electron Diffraction results have shown Cu surfaces to be stable on the [100] zone[104] in regions where Pt is not stable. A kinked step Ni surface vicinal to the (001) pole off the [100] zone is stable;[126] it is not known if the equivalent Pt surface is stable. These metals might be expected to be stable vicinal to the (001) whereas Pt is not since neither 3d metal reconstructs its (001) plane to lower the free energy. This extra lowering may make clean Pt facet where Ni and Cu are stable. Mykura[133] found that Ni faceted by the groove method, but his samples were highly contaminated. McLean[134] found that all Cu surfaces are stable and that cusps in the γ-plot might occur at [3(111)×(100)] and [4(111)×(111)] planes similar to what LEED data indicate for Pt.

4.3.1.5. Synopsis. Low Energy Electron Diffraction is a much more sensitive tool for the detection of faceting on clean crystal surfaces than are the twin boundary or grain boundary groove techniques. They have the advantage of being able to determine a relative surface tension for each orientation measured and in this way construct a γ-plot. The groove techniques are not highly accurate and are subject to surface comtamination as the samples must be annealed for days instead of the few minutes required by LEED at similar temperatures. An intriguing experiment would be to grow a large spherical single crystal so the stability of all orientations could be studied at once. A Cu or Al spherical crystal would be easy to produce in a graphite mold; most other metals could be produced with a spark cutter lathe. The deviations from spherical with annealing would give information on diffusional rate anisotropy with orientation, but probably not equilibrium configurations since the diameter would be large enough (greater than 40 mm) to preclude sufficient mass transport in a reasonable time to approach equilibrium.

These LEED results on Pt agree generally with the experimental results found in the literature. The LEED results are summarized in Table 4-3 and in Fig. 4-13. Since these samples are known to be clean by AES, the discrepancies can be attributed to contamination on the samples used in other investigations. The oxidized surfaces may have higher coverages than could be obtained in the UHV apparatus used in this investigation. The agreement is good near the (111) and (001) poles, but not near the (011). In the region near the (011), only two samples have been studied; thus indicating a need for further experimental work.

Table 4-3. Summary of the stability of stepped platinum surfaces at conditions of experiments (see text).

Clean	Carbon Covered	Oxygen Covered
Stable in Monatomic Height Step Configuration		
25(111)×(100)	25(111)×(100)	13(111)×(310)
9(111)×(100)	9(111)×(100)	7(111)×(210)
6(111)×(100)	13(111)×(310)	7(111)×(310)
3(111)×(100)	7(111)×(210)	7(111)×(610)
2(111)×(100)		2(111)×(100)
9(111)×(111)		4(111)×(111)
6(111)×(111)		3(111)×(111)
5(111)×(111)		2(111)×(111)
13(111)×(310)		
7(111)×(210)		
7(111)×(310)		
7(111)×(610)		
6(111)×(14,1,0)		
7(100)×(111)		
5(100)×(111)		
2(111)×(111)		
Stable in Multiple Height Steps		
5(110)×(100)	5(110)×(100)	5(110)×(100)
	9(111)×(111)	9(111)×(111)
	6(111)×(14,1,0)	9(111)×(100)
	7(111)×(310)	6(111)×(100)
		4(111)×(100)
		3(111)×(100)
Stable in Hill and Valley Structure		
5(100)×(100)	6(111)×(100)	7(100)×(111)
3(110)×(111)	4(111)×(100)	5(100)×(111)
	7(111)×(610)	5(100)×(100)
	7(100)×(111)	3(110)×(111)
	5(100)×(111)	
	6(111)×(111)	
	5(100)×(100)	
	3(110)×(111)	

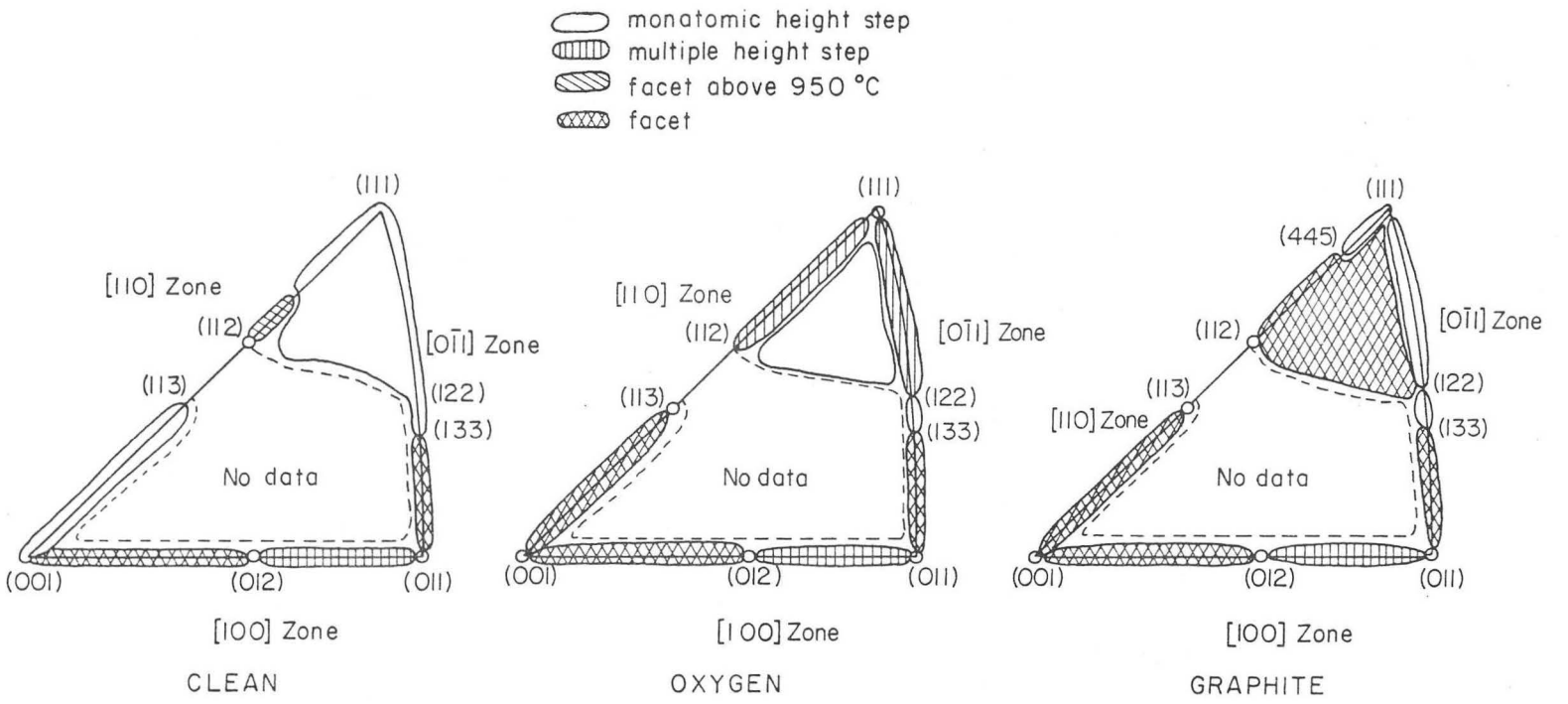

XBL 763-6633

Fig. 4-13. Stereographic projection unit triangles indicating regions of stability in monatomic height steps, regions where reversible faceting occurs, regions where multiple height steps are stable, and regions where steps are unstable and a hill and valley structure forms for (a) the clean Pt surfaces (b) Pt surfaces heated in an oxygen ambient, and (c) Pt surfaces covered with a monolayer of graphitic carbon.

4.3.2. Discussion of Stability-Comparison with Theories

4.3.2.1. Equilibrium Theories. The stability of a surface is determined by the free energy; if it can be lowered in another configuration the surface will move toward that configuration at a rate governed by the kinetics. As was shown previously, it is thought that our measurements are of equilibrium properties of the surface, and it will be demonstrated in the next section that they are not kinetic controlled "psuedo" equilibrium configurations which can be generated at high evaporation or condensation rates. The excess surfaces free energy of a subject is given by Eq. (4-1)

$$G^S = \int \gamma(n)\, dA \quad . \tag{4-1}$$

If the surface tension, γ, or surface energy and entropy, can be calculated for all possible configurations, the free energy of the stable statistical average surface of orientation, $\vec{n}$, could be determined.

There are several theories which try to predict the surface energy and entropy of a solid.[116,125,135-139,124,140] Pairwise additive potentials have been used for a number of years[135,136] in the calculation of surface energy anisotropy of metals. Herring[116] has shown that this assumption produces a special case of the γ-plot where the steps are non-interactive. The $1/\gamma$-plot consists of planes (the γ-plot consists of spheres through the origin), which makes it degenerate with respect to faceting to any pair of orientations. In this case the surface configuration would be kinetically controlled, and if the same pairwise potential is used for the determination of activation energies, the surface would not smooth or roughen with annealing

(this will be discussed further in the next section). This is of course not what is experimentally observed and casts doubt on the use of pairwise-additive potentials.

Gruber and Mullins[123] have proposed a much less restrictive model of a surface containing terraces, ledges, and kinks. Their model is restricted to either repulsive or no interactions between neighboring steps, i.e., faceting is not permitted. A stepped surface has an excess energy over a flat surface as in the pair-wise models, but random thermally generated kinks are allowed in the steps which give rise to a configurational entropy term and, therefore, a temperature dependence of the surface tension. Since the step edges wander considerably, two adjacent edges could become quite close together and with an attractive interaction cause a doubling of the step height. This would cause a breakdown of the model and is, therefore, not allowed. This model qualitatively fits data for surface tension anisotropy on several surfaces of several metals with two adjustable parameters on each surface. The fit is good from the low index pole out to about 10° on almost all the surfaces to which it has been applied. For terraces narrower than this, about a five or six atom wide terrace, the model breaks down, probably from the neglect of interactions between steps. The sizeable difference in the entropy is predicted for (001) vicinal surfaces on the [100] zone and [110] zone (experimentally one facets and the other is stable on Pt). (111) vicinal surfaces on both zones and in between have essentially the same entropy, with the kinked surface being slightly higher, and experimentally all these surfaces are stable. The predicted temperature at which surface

melting would occur on Pt using the data of McLean and Mykura[121] with the Gruber-Mullins theory[123] is approximately 3500°K near the (111) and 2500°K near the (001), both well above the actual melting temperature of Pt. There are clearly deficiencies in this model also although it is a marked improvement over the previous theories. The exclusion of an interaction between steps is probably the major fault of this model.

As was shown experimentally, there are attractive interactions between steps which cause agglomeration and faceting. This faceting terminates on surfaces which are often "two" atoms wide terraces, (211), (210), and (331), and in one case one atom wide, (311). This implies that up to 4th nearest neighbor interactions may be important. (The 4th nearest neighbor in an fcc crystal is at a distance two atomic diameters, i.e., diagonally across a face of the cubic unit cell.) Inelastic neutron scattering measurements of phonon dispersion curves[114] indicate strong interactions to 4th nearest neighbors on Pt and most other fcc metals (about 10% of nearest neighbor force constant) with possible weak interactions at longer distances. The interactions beyond 4th nearest neighbor are questionable since the data reduction model does not include phonon-electron interaction.[141,142] Field ion microscope data of Erlich and Tsong[143] indicate atoms diffuse as pairs, but not touching pairs, which again says that up to 4th nearest neighbor interactions may be important. Calculations of interactions of adsorbates by Schreiffer,[144] indicate interactions occur through the metal atoms. A calculation by Kesmodel and Falicov[145] of the effect of a step on the S electron density has much shorter range effect, essentially dying out over one

lattice spacing. Effects of d electrons and any rehybridization were not included, which might extend the range of the interaction. Recent data on Cu by a boundary groove technique[134] indicate that a shallow cusp in the γ-plot might occur at (211), (311), and/or (552) ((221)-(331) region) which was unresolvable at the temperatures necessary for the groove formation. Thus interactions in fcc metals appear to occur to at least 4^{th} nearest neighbor and possibly further.

A model which might be useful treats step boundaries as adsorbed molecules on a lattice with near neighbor interactions. The simplest form of this is a linear lattice, i.e., the steps are straight but the whole step moves forward or backwards simultaneously. This problem has been solved with a nearest-neighbor interaction[112] (or 2^{nd} nearest neighbor with no near neighbor attraction). From this the fraction of ledges with multiple height steps is readily calculated. With a repulsive step interaction, the higher the temperature the more grouping of ledges into multiple height steps (the repulsion is weaker). There is no sharp transition temperature as was found on the Pt(S)-[4(111)×(100)], just a gradual bunching of the steps. From Chapter 3, this gradual change would only produce gradual changes in the diffraction pattern. It also does not explain the stability of the Pt(S)-[7(100)×(111)] surface to annealing 48 hr at 800°C. Therefore, a repulsive interaction between steps is probably not thermodynamically justifiable. An attractive interaction would cause bunching, but again only gradual changes with temperature.

As the temperature increases, the distribution becomes random, i.e., Gáusian; this distribution would still give sharp diffraction beams as seen in Fig. 3-4. It explains the low temperature anneal stability of several surfaces and the entropy is the right order of magnitude. A more realistic model would be a two dimensional model where a kink interaction is allowed also. This is similar to Gruber and Mullins model[123] although less restrictive. This model could be solved by a matrix formalism.[146] By analogy with a two dimensional lattice gas, it could have a phase transition, i.e., a temperature at which ledges condense to multiple height steps.

As seen there are no equilibrium theories yet put forth which can adequately describe the structure of a metal surface even in the ideal case where all surfaces are stable and do not facet. Realistic interaction potentials have not been used so the predicted surface structures are not realistic. Most of the models predict straight lines in the $1/\gamma$ plot which is not observed experimentally. The dynamic theory presented in the next section may be easier to handle with realistic potentials.

4.3.2.2. Kinetic Theories of Surface Roughening. Schwoebel,[147,148] has proposed a model for step motion (and surface stability) which depends on the probability of a step capturing a diffusing atom. It is essentially a one dimensional lattice with higher potential barriers in place of steps. The key feature is that the probabilities for capture and/or detachment of an atom are not necessarily equal and depend on the direction of approach to the step, as shown in Fig. 4-14a.

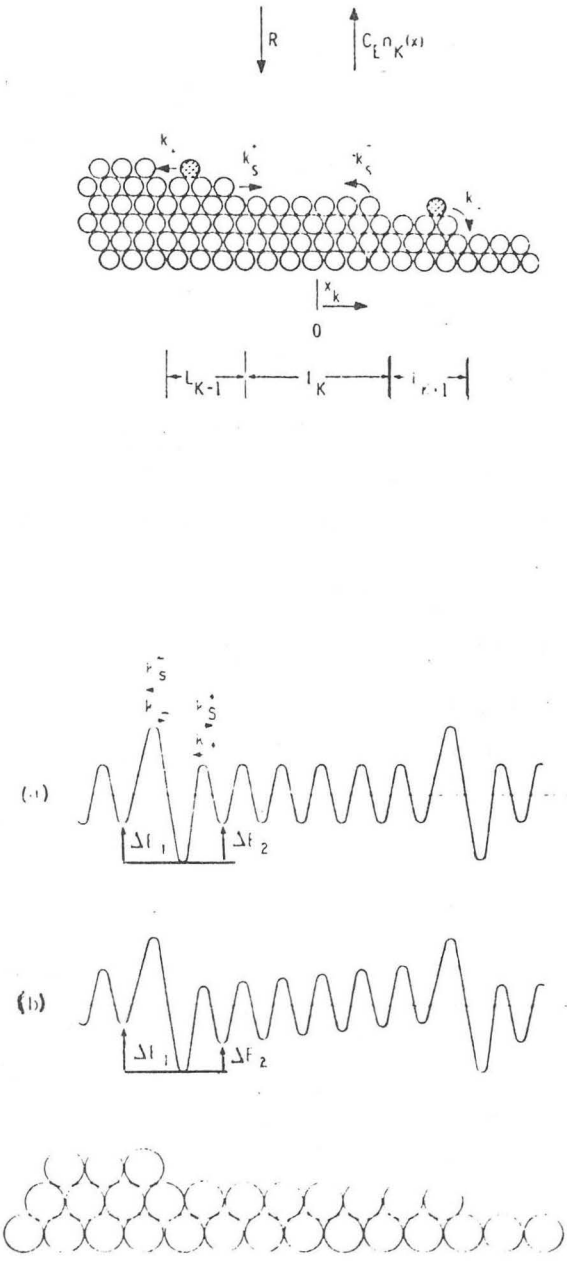

XBL 764-1602

Fig. 4-14. (a) An idealized crystal surface model for characterizing step motion. Surface diffusing atoms are captured with probability k_- and k_+ from above and below the step respectively, and adatoms are created on the terrace above or below the step with the probability k_s^- and k_s^+, respectively. (b) Hypothetical form of potential energy for a diffusing adatom in the absence of long-range interactions. A possible form of the potential when long-range interactions occur (from Schwoebel, Ref. 148).

The probability for capture of a diffusing atom from the terrace above (-) and below (+) the step is denoted by k_- and k_+, respectively, while the probability for creation of an adatom from a step is given by k_s^- and k_s^+ for the adatom being on the terrace above and below the step, respectively. On the samples used in this investigation, R, the flux to the surface is always zero, the rate of evaporation is negligible at 800°C (vapor pressure 10^{-13} Torr[149] or $\sim 10^{-7}$ monolayers evaporate/sec) but significant at 1500°C (vp $\approx 10^{-6}$ Torr). The vapor pressure of PtO_2 is approximately 10^{-3} Torr at 900°C,[150] so vapor transport effects (PtO_2 also decomposes readily on hot Pt metal) as well as surface diffusion and evaporation should be considered in O_2 atmospheres. This extra effect could cause some of the descrepancies in the O_2 data of M and M[121] and the LEED results. For a freely evaporating crystal, if $k_+ > k_-$ individual steps may coalesce into multiple height steps, while if $k_- > k_+$ the step spacing will become more even.

This becomes obvious in an extreme case where $k_+ \Rightarrow 1.0$ and $k_- \Rightarrow 0$. Given two adjoining steps, one wide and one narrow, diffusing atoms are produced at each step at equal rates. The atoms diffuse across the terrace, are reflected by the top of the next step and diffuse back. Now while an atom is on the terrace it can evaporate. On the wide terraces the number which return to the step is much smaller than on a narrow terrace, therefore, the wide terrace will become wider at the expense of narrow terraces above it, even though both ledge positions are moving as the crystal evaporates. By a similar argument it can be shown that the terraces even out if $k_- \Rightarrow 1$, $k_+ \Rightarrow 0$. For the annealing case where both evaporation and condensation are small,

step motion is controlled by detachment of atoms from the step. If $k_s^+/k_+ > k_s^-/k_-$, the surface is stable and a uniform distribution of step results, while if $k_s^-/k_- > k_s^+/k^+$ the steps may coalesce into multiple height steps. This again becomes obvious in an extreme case where $k_s^+/k_+ \to \infty$ and $k_s^-/k_- \to 0$. Diffusing atoms are created in equilibrium amounts on the + side of the step and diffuse across the terrace to the sink at the top - side of the next step. The wider terraces have smaller gradients and, therefore, smaller fluxes. Thus the narrow terraces widen faster than the wide terraces and the surface becomes uniform. A similar argument shows that in the other extreme, $k_s^+/k_+ \to 0$ and $k_s^-/k^- \to \infty$, the steps will coalesce, i.e., the wide terraces become widened at the expense of the narrow terraces.

To qualitatively explain the differences in the probabilities Schwoebel[148] proposed the hypothetical potential shown in Fig. 4-14b and c. If $\Delta E_1 = \Delta E_2$ and the curvature of the potential wells are equal (Fig. 4-14b), then $k_s^+/k^+ = k_s^-/k^-$ and, therefore, no step motion occur on annealing. This is obviously not the case and, therefore, $\Delta E_1 \neq \Delta E_2$ and the potential in Fig. 4-14c is more realistic. However, as pointed out previously, strong interactions exist to about two diameters, at least on fcc metals, and probably not over the long range shown.

What are felt to be more realistic potentials for various Pt stepped surfaces are shown in Fig. 4-15. The potential is essentially the same for all orientations when the step is wider than four or five atoms and a hypothetical example is shown in Fig. 4-15a which includes interactions to two diameters. The magnitude of ΔE_{dif} is about 25 kcal/mole[114] and includes both the activation energy of detachment

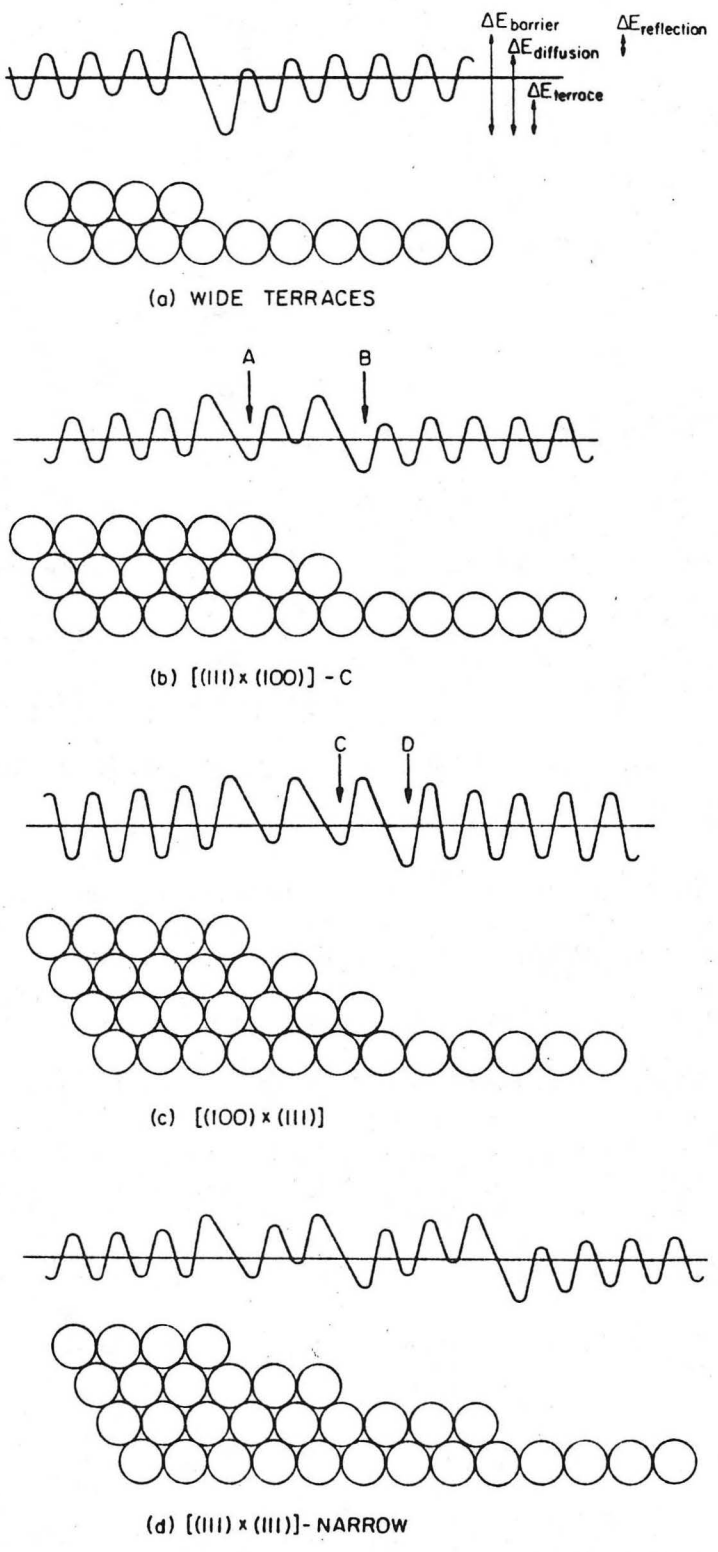

XBL 763-6635

Fig. 4-15. Hypothetical diffusion potentials for Pt surfaces; (a) for any surface with wide terraces, (b) for the [(111)×(100)] with carbon produced facet, (c) for the [(100)×(111)] with oxygen produced facet and (d) for the [(111)×(111)] with carbon produced facet (interlayer position are drawn for ease of interpretation. For actual placement of atoms see Fig. 4-2).

and diffusion.[129] The approximately 8 kcal/mole difference found in the heat of diffusion[114] with crystallographic orientation probably has contributions both from ΔE_{terr}, the excess energy to hop away from a step, and the different terrace orientations. The height of $\Delta E_{reflection}$, the barrier for adatoms escape from a terrace to the next lower terrace is very small on Rh[130] and may also be small on Pt. Significant differences between the various combinations of step and terrace orientations appear when the terraces narrow or impurities adsorb at the steps. The postulated potentials are shown in Fig. 4-15b,c,d along with a schematic of the step under discussion. On a clean (Pt(S)-[4(111)×(100)]) or carbon covered [n(111)×(100)] or [n(100)×(100)] type step, a facet of two atom wider terraces (112) or (012) respectively is stabilized over the uniform distribution. The agglomerated step potential might be as in Fig. 4-15b. An atom in the A position is slightly metastable with respect to diffusing on the terrace, so the two atom wide step would not be narrowed. An atom at the B position could easily be detached, or with B filled, site A becomes favorable for capture of a atom and the two atom wide terrace is maintained. Figure 4-15c shows the postulated potential for a [n(100)×(111)] type step with a 1/100 monolayer or less of O where a one atom wide terrace is stabilized, (113). An atom at position C is highly unstable with respect to both D and a terrace site. Without the oxygen the well at C is probably below the $\Delta E_{terrace}$ line. The [n(111)×(111)] does not have a distinct facet, but facets to both 2 (331) and 3 (221) atom wide terraces with about half of each width well interspersed (a (552) specular LEED beam is also often present). A speculative

shape for the potential is shown in Fig. 4-15d. It is essentially similar to the potential in Fig. 4-15b except the 3 atom wide step well is shallower. For the same terrace width, the distance between like step boundaries is closer on the [n(111)×(111)] type of step than a [n(111)×(100)] by a 1/3 diameter which might explain some interaction to 3 atom wide terraces.

With no mass transfer from the surface, the equilibrium configuration determined by these potentials, Fig. 4-15, should be related to the thermodynamically most stable configuration. The change in the potential for diffusion when step spacing becomes small are the interaction potentials which would be used in the type of statistical analysis of the surface free energy discussed in the previous section. It would be interesting to reformulate Schwoebel's model to include variable k's and compare this with the statistically derived equilibrium result using the same potentials.

The dynamic theory of surface stability[148] presented in this section does not describe the surface accurately in its present form. It is more flexible than the equilibrium theories and could be readily reformulated to include more realistic experimentally observed interaction potentials. It can be simply related to equilibrium theories. The appropriate diffusion data from stepped surfaces could be obtained by radioactive isotope tracer techniques similar to that of Rhead and Oudar for S diffusion on metals.[151] Perhaps then the necessary information to truly describe the diffusion on and the stability of metal surfaces would be available.

4.3.3. Effect of Surface Structure Stability on Catalysis

The size of metal catalyst particle effects the rate of many catalytic reactions (see Chapter 6 and Ref. 22); presumably this occurs from a change in the surface structure of the particles with size. Changing support material (for example, alumina to silica or graphite) while keeping the particle size constant also can cause the specific reaction rates of catalytic reactions to vary,[55] again presumably by a change in the stable surface structure. These conclusions are drawn from initial rate data; on many industrial catalysts as the rate decreases over long periods of time, the selectivity to the desired products also changes[152] indicating a restructuring or selective carbon deposition possibly with concomitant metal destabilization and rearrangement. Oxygen adsorbed on a surface can effect the rates of reaction by two possible means, a simple site blockage by adsorption at steps as observed with cyclohexane (discussed in Chapter 6) or through a restructuring of the particle shape as discussed in this chapter. Pareja, Amariglio and Amariglio[43] found ethylene hydrogenation was promoted on Ni catalysts by traces of O_2. This could produce a small surface coverage of oxygen and cause rearrangement to surface orientations which enhance hydrogenation. Somorjai[45] suggested that S poisoning of a catalyst results from the restructuring of the particle surface. It has been suggested[3,4] the main effect of alloying metals in the catalytic reaction rate is through a geometrical effect. Selectivity might be increased by site blockage as suggest for Pt-Au and Ir-Au alloys by Hagen and Somorjai,[92] or the second component may cause the stabilization of certain planes

similar to O_2, which are more selective and/or active.

High temperature oxidation-reduction cycles can disperse large metal particles ($\geq$100A) into small particles ($\lesssim$20A).[153] The addition of small amounts of HCl or Cl_2 (~1%) to the gas speed the dispersion. The effects of Cl were not studied on single crystals, but are probably equivalent to O effects, only greater because of Cl's higher electronegativity. The oxidation at around 500°C causes the adsorption of O and the destabilization of most planes (Section 4.2). It is well known that metals have much higher surface tensions than their oxides;[129] thus a larger semi-spherical particle of metal would be transformed to a flat platlet structure with only the stabilized low Miller Index planes exposed. The subsequent reduction cycle return the metal to semi-spherical particles, but smaller. This is demonstrated schematically in Fig. 4-16.

The nature of the oxide support and the activity of the oxygen should have an effect on the orientation of the metal particles surface, at least the orientation of the plane in contact with support. Only the few oxygen stable planes would be in equilibrium with the support. The effect this has on the planes in contact with the gas phase would become less the larger the metal particle; (111) planes would dominate on large particles (lowest free energy), while some other orientation planes might be stabilized on small particles. The non-reducibility of Re to metal at low (<1%) Re loadings on alumina indicates a strong interaction with the alumina which could effect another metals surface orientation and stability. This might be the reason for the Rheniforming catalysts[152] increased stability.

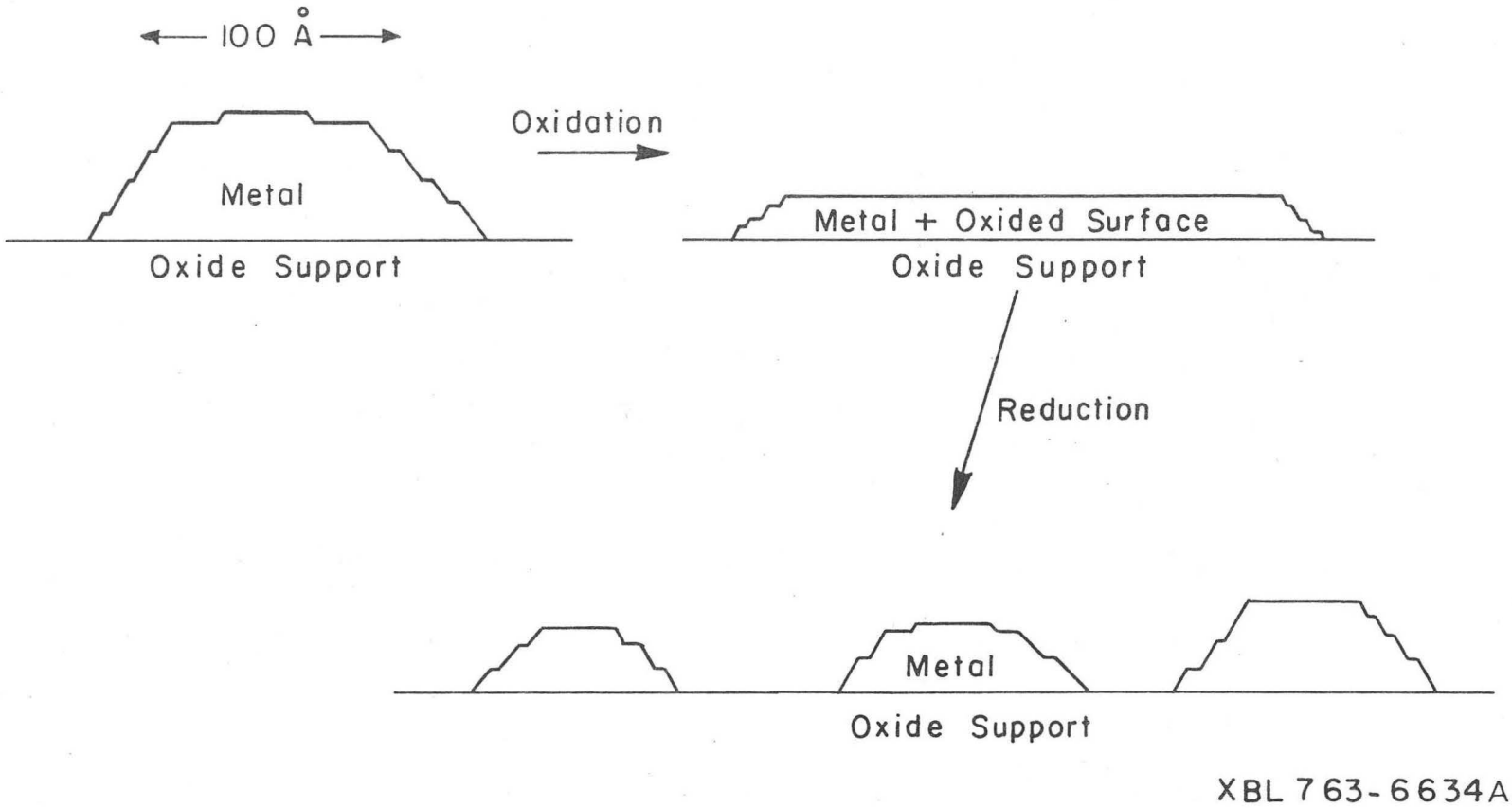

Fig. 4-16. Schematic diagram of possible mechanism for dispersion of metal by oxidation-reduction cycles.

The knowledge of the stability and structure of the Pt metal surface has lead to increased insight into the nature of the supported metal particle.

4.4. The Pt-(001) Reconstruction

4.4.1. Introduction

The surfaces of many materials are not stable in the bulk configuration: semiconductors such as Si and Ge contract into a strained configuration to reduce the free surface valency;[154] some oxide surfaces are stable in a reduced state;[155] the only metals where a surface instability is definitely found are the 5d metals iridium, platinum and gold. It has been known for 10 years that their (001) surface is unstable[156] but a completely satisfactory explanation has not been put forth because the effects of strain in the surface layers have been ignored until now. A model is proposed which includes for the first time (or any surface) the effect of surface stresses on the geometry of the surface. It explains the differences and similarities between the Ir, Pt and Au (001) surface reconstruction with a hexagonal overlayer which is strained, but dislocation free on Ir, however, on the Pt and Au surfaces misfit dislocations are introduced. Chemical forces, the strong directional chemical bonds of the d electrons, are thought to control whether a metal surface reconstructs; but once it has strain will control the actual atom placements in the reconstructed layer.

The (011) surface of Ir, Pt and Au also reconstruct to form a (1×2) pattern.[158,181] This has been interpreted as a filling of every other valley with a row of metal atom to produce a two atom

high ridge and valley network or as an attraction between two neighboring rows of atoms and a compression. In the first case, there is no strain and all three metals would behave similarily, and in the second case the displacements would differ, but qualitatively the LEED patterns would be identical. Therefore, the reconstruction on the (011) surface cannot reinforce or detract from the proposal put forth.

The reconstruction of the (001) surfaces of the 5d metals Ir, Pt and Au is an established fact. It was first observed on Pt-(100) by Hagstrom, Lyon and Somorjai[156] in 1965. It was then observed on Au(100) by Mattera, Goodman and Somorjai,[160] and by Fedak and Gjostein[161] and on Ir(100) by Grant.[162] Rhodin and co-workers showed that the Au reconstruction was one or two layers thick by evaporating Au onto an MgO substrate[163] and demonstrated that the reconstructed layer on Ir has hexagonal symmetry.[164] The structure proposed by Somorjai, et al. to explain the reconstruction was two domains rotated 90° of a 4% contracted hexagonal layer of atoms atop the square bulk unit cell. This hexagonal layer on the surface would lower the number of broken directional bonds associated with the 5d electrons from four for the square symmetry surface to three for the hexagonal symmetry surface thus lowering the surface free energy.

There are extra features observable in the Au(001) and Pt(001) diffraction patterns which are not observed from Ir(001) and are unexplained by the model first proposed. These differences are shown in Fig. 4-16. In Fig. 4-16a Ir is seen to have single beams directly in the ten directions and a $\begin{vmatrix} 5 & 0 \\ 0 & 1 \end{vmatrix}$ diffraction pattern (see Ref. 129, for example, for explanation of matrix notation), while Pt and Au, in

XBB 759-6734

Fig. 4-16. Photographs of the diffraction patterns from the clean (001) surfaces of (a) Ir (from Grant, Ref. 162), (b) Pt and (c) Au (from Fedak and Gjostein, Ref. 165).

Figs. 4-16b and c, respectively, have diffraction spots slightly off the [10] directions and a more complicated diffraction pattern. Fedak and Gjostein[165] proposed a contraction of each hexagonal domain in both the [10] and [01] directions to produce a $\begin{vmatrix} 5 & 0 \\ 0 & 20 \end{vmatrix}$ diffraction pattern and account for the extra diffraction spots.

4.4.2. Experimental Characterization of (001) Surfaces

We have observed the diffraction from a single domain of the reconstructed Pt-(001) surface. A Pt-($\bar{1}$,1,13) [Pt(S)-[7(100)×(111)] crystal was prepared vicinal to the (001) surface along the [110] zone 6.2° from (001) pole toward the ($\bar{1}$11). With a small amount ($\lesssim$0.02 monolayer) of oxygen, this surface was unstable and faceted to the (001) and ($\bar{1}$13) surfaces (see Section 4.2 and Ref.166) from stabilization of the ($\bar{1}$13) surface by the oxygen. The diffraction spots from the ($\bar{1}$13) are quite sharp indicating a 50 to 100Å step height and correspondingly 150 to 300Å terrace width of (001) surface. The diffraction pattern of the slightly contaminated surface is shown in Fig. 4-17a, there is only one domain of a $\begin{vmatrix} 5 & -3 \\ 1 & 12 \end{vmatrix}$ diffraction pattern. The real space lattice is shown in Fig. 4-17c. Four domains of this pattern would reproduce the observed diffraction patterns from the Pt(001) surfaces and probably the Au(001). On the clean Pt-($\bar{1}$,1,13) sample, the (001) terraces are still reconstructed as seen in Fig. 4-18a. The steps are generally stable in the monatomic height configuration giving a Pt(S)-[7(100)×(111)]. Since the terraces are six (001) unit cells wide (the seventh is the step itself) as shown in Fig. 4-18c and the normal reconstruction is five (001) unit cells wide, the steps modify the reconstruction to be the six (001) unit cells wide. This can be seen by comparing

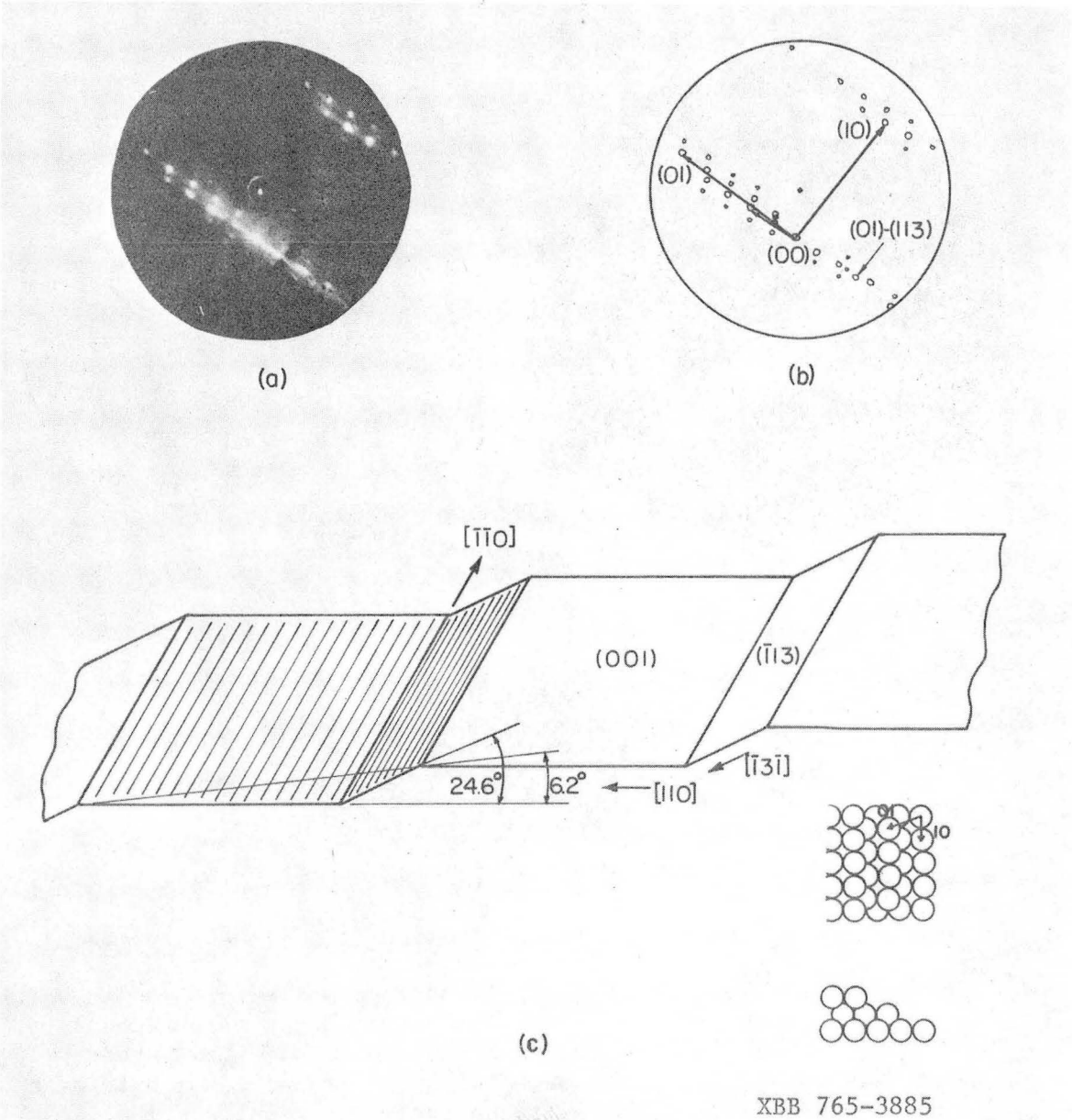

Fig. 4-17. The faceted Pt-(1,1,13) surface with 0.02 monolayer O contamination. (a) The LEED pattern of the surface at 38 eV, (b) a schematic drawing of the LEED pattern with the substrate beams and (113) facet beams labeled, and (c) a schematic drawing of the mean surface configuration with the orientation of reconstruction shown.

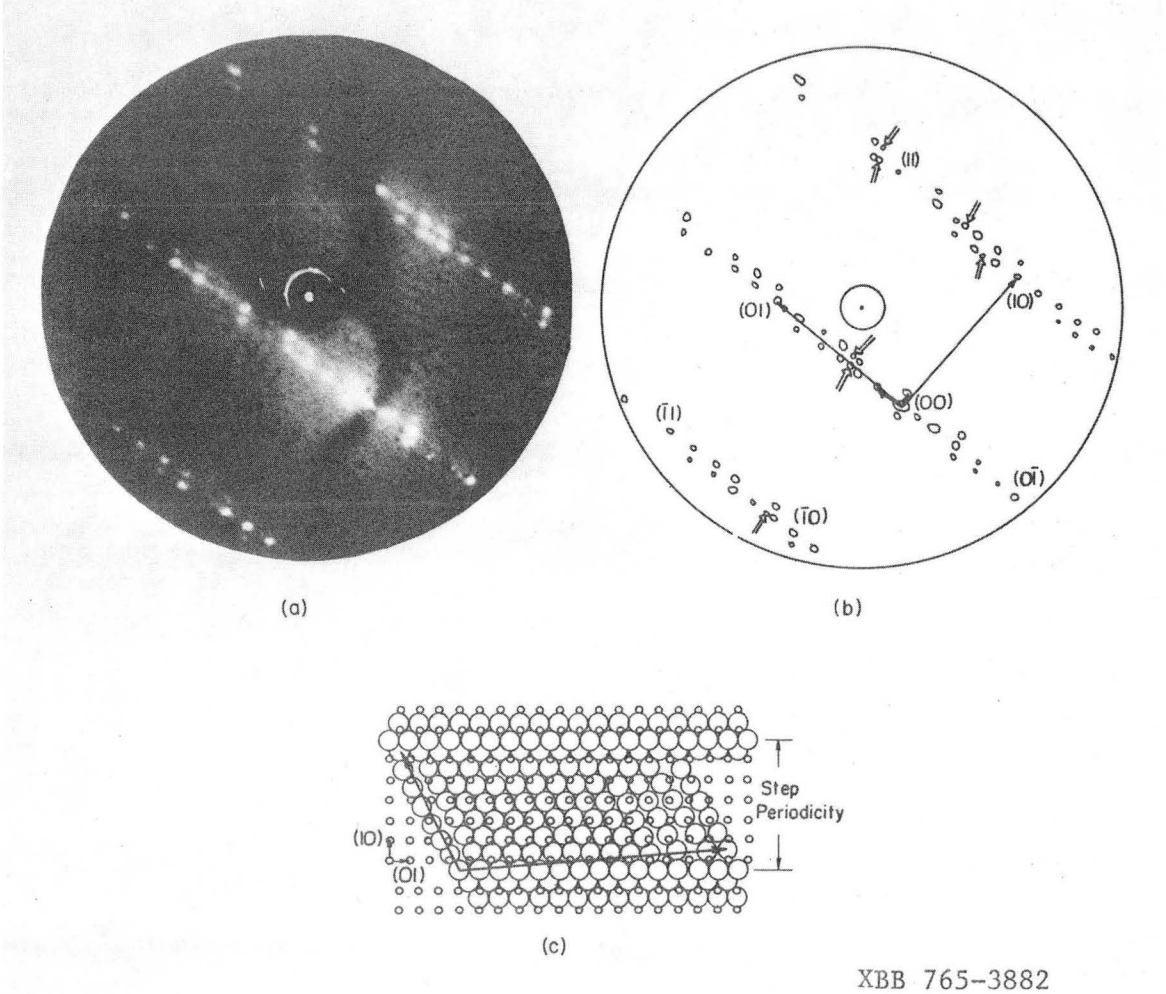

XBB 765-3882

Fig. 4-18. The stepped Pt-(1,1,13) surface which is free of contamination. (a) LEED pattern of the surface at 60 eV, (b) a schematic drawing of the LEED pattern with substrate beams labeled, arrowed beams originate from wide steps with undistorted reconstruction, and (c) a schematic drawing of the average configuration of the monatomic height stepped portion of the surface.

Figs. 4-17c and 4-18c. The reconstruction unit cell on the 6 atom wide steps is $\begin{vmatrix} 6 & -3 \\ 1 & 13\text{-}1/2 \end{vmatrix}$ and is shown in Fig. 4-18c. The fractional order beam can be readily explained by the development in Section 3.4. There is a distribution of distances between the dislocations, with the average distance being about 13-1/2 unit cells. The width of the distribution is probably narrow; wider the strain would be to great and narrower the energy cost of the dislocation would not be repaid in decreased strain. The arrowed spots in the schematic, Fig. 4-18b, of the LEED pattern, Fig. 4-18a, are from wider terraces where the steps are too far apart to modify the reconstruction, and are from the normal $\begin{vmatrix} 5 & -3 \\ 1 & 12 \end{vmatrix}$ reconstruction unit cell. It would be interesting to determine the width at which steps will no longer modify the reconstruction; this would help determine the long range faces and the ability of a monolayer to support shear. A second crystal, Pt-($\bar{1}$19), cut 9.0° from the (001) toward the ($\bar{1}$11) produced a similar diffraction pattern displaying only one domain of reconstruction the steps are 5 atoms apart on this surface, so the distortion if present is not readily visible. A vicinal surface on the [100] zone, Pt-(015) faceted to (001) and (012) surfaces but produced two of the four domains of reconstruction as shown in Fig. 4-19. An (001) surface produced the four domain pattern until it was thermally stressed, i.e., heated above 1100°C. It then displayed only one domain of reconstruction in the strained areas. This has previously been observed by Palmberg.[167] The Pt-($\bar{1}$,1,13), (119) and (015) crystals were "thick" crystals approximately 0.7 to 0.8 mm thick and did not deform or bend when heated. However, the Pt-(001) crystal was thinner, approximately 0.30 mm thick, and deformed with

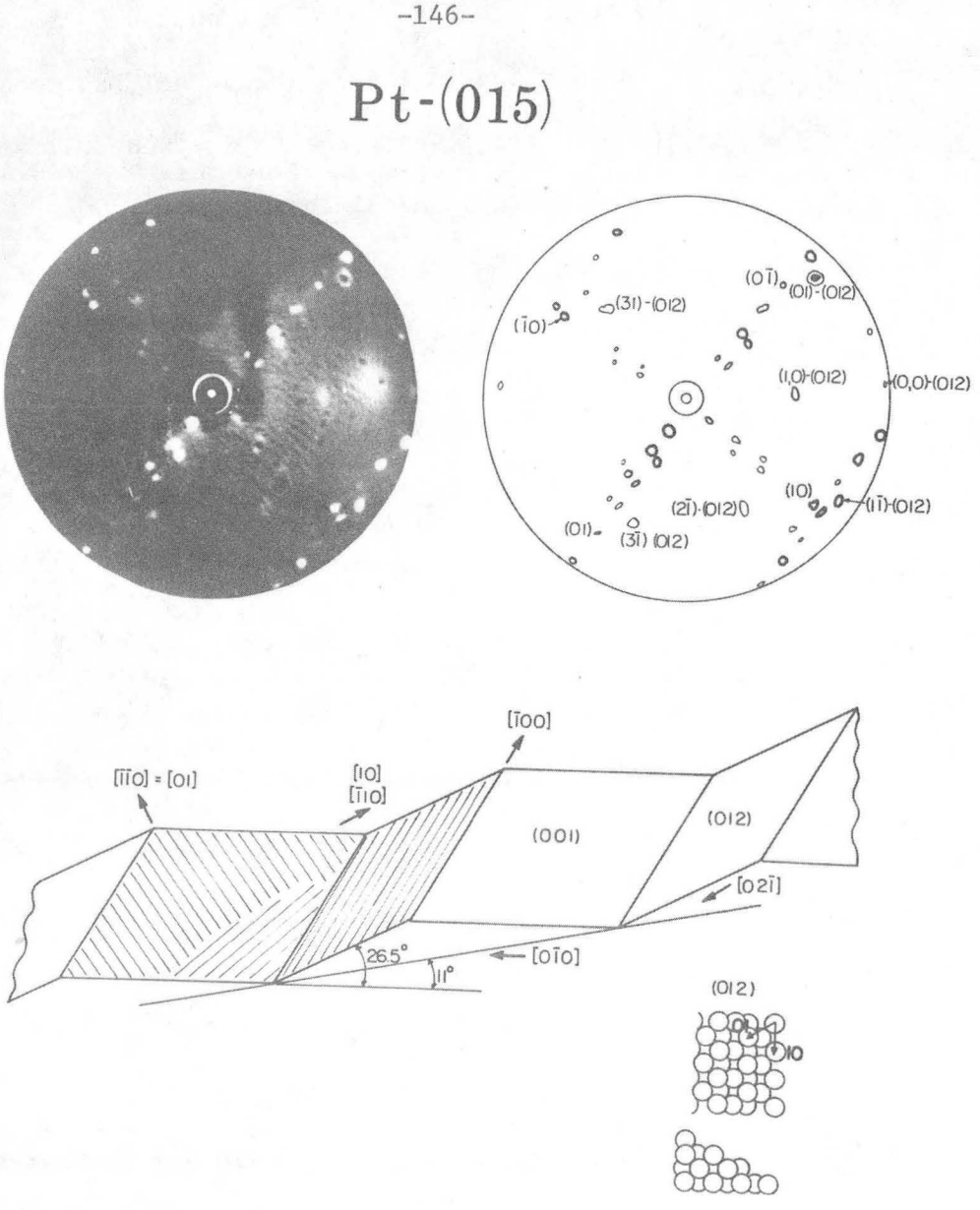

Fig. 4-19. The faceted Pt-(015) surface which is thought to be free of contamination. (a) LEED pattern of the surface at 45 eV, (b) a schematic drawing of the LEED pattern with substrate beams and (012) facet beams labeled, and (c) a schematic drawing of the mean surface configuration with the orientation of the reconstruction shown.

heating thereby introducing a series of line dislocation from which one domain could nucleate and grow. The intensity of the four domains of reconstruction varied over the face of the crystal from equal intensity in unstressed areas to only one domain where the crystal was deformed.

These surfaces are considered to be clean and free of Ca. They were cleaned by Ar ion bombardment and O_2 heat treatment to below the Auger electron spectroscopic and chemical limits of detectability of Ca. With Ca present on the surface, oxygen adsorbed readily at high temperatures. When the Ca was removed to below the limit of detectability by Auger spectroscopy through ion bombardment, oxygen still adsorbed readily. With further ion bombardment the sticking coefficient of oxygen at high temperature dropped drastically indicating that the surface was clean to a chemical probe as well as by Auger electron spectroscopy. The surface shown in Figs. 4-17, 4-18 and 4-19 behave similarly to the Pt-(001) reconstructed surface. The extra diffraction features disappear with exposure to CO or hydrocarbons, but remain with exposure to O_2 or H_2.

4.4.3. Discussion of Surface Structure

A very interesting question to consider now is the difference between Ir, Pt and Au reconstruction. It is well known that Pt and Au are very malleable and elastic with Poisson's Ratio, ν, of 0.39 and 0.42, respectively.[168] Poisson's Ratio is the inverse of the linear extensional strain divided by the concomitant contractual strain, being 0.5 for a perfect elastomer and 0.30 to 0.35 for various steels. Iridium, on the other hand, should have a lower value of Poisson's Ratio

of 0.25 to 0.30.[169] This means that Ir can support more strain before misfit dislocations appear. A simple model calculation of the strain, ε^*, which minimizes the sum of the elastic strain energy and the energy required to form a line dislocation (see, for example, Ref. 170) is

$$\varepsilon^* = \frac{b}{8\pi h(1 + \nu)} \ln \frac{h}{b} + 1$$

where h is the thickness of the overlayer, in this case 1 monolayer, and b is the strength of the Burgers vector. The elastic strain in this model an Ir layer can take is 0.031 and Pt and Au about 0.026 before misfit dislocations are introduced. At values of strain greater than ε^* the lower energy configuration contains misfit dislocations to relieve the strain or with less strain than ε^*, the lattice supports the strain. The atomic radius of the atoms in the surface layer is expected to change, and might decrease if the rehybridization were accomplished with a partial electron transfer similar to that proposed in alloys by Brewer.[171] The 3% compressional strain (or the reduced lattice size) of the overlayer in the [10] direction which matches the hexagonal overlayer and square substrate lattices should be accompanied by an expansion of overlayer lattice in the [01] direction. There is also a 1° torsional strain in the hexagonal overlayer associated with the compression. Iridium with its ability to support more elastic strain will maintain the hexagonal overlayer with a 3% [10] contraction and the bulk lattice spacing in the [01]. This will produce the $\begin{vmatrix} 5 & 0 \\ 0 & 1 \end{vmatrix}$ diffraction pattern seen in Fig. 4-16a and the lattice shown in Fig. 4-20a. Platinum which cannot support as much strain apparently has misfit dislocations in the [01] direction as well as the obvious

Fig. 4-20. Possible real space configuration of the hexagonal overlayer on a (001) terrace. (a) The configuration of a perfect $\begin{vmatrix} 5 & 0 \\ 0 & 1 \end{vmatrix}$ surface structure as found on Ir-(001), (b) a possible $\begin{vmatrix} 5 & -3 \\ 1 & 12 \end{vmatrix}$ structure with a large region on complete misfit, and (c) another possible $\begin{vmatrix} 5 & -3 \\ 1 & 12 \end{vmatrix}$ structure with a smaller region of complete misfit. The large circles are in the hexagonal overlayer and the small circles represent the substrate atoms.

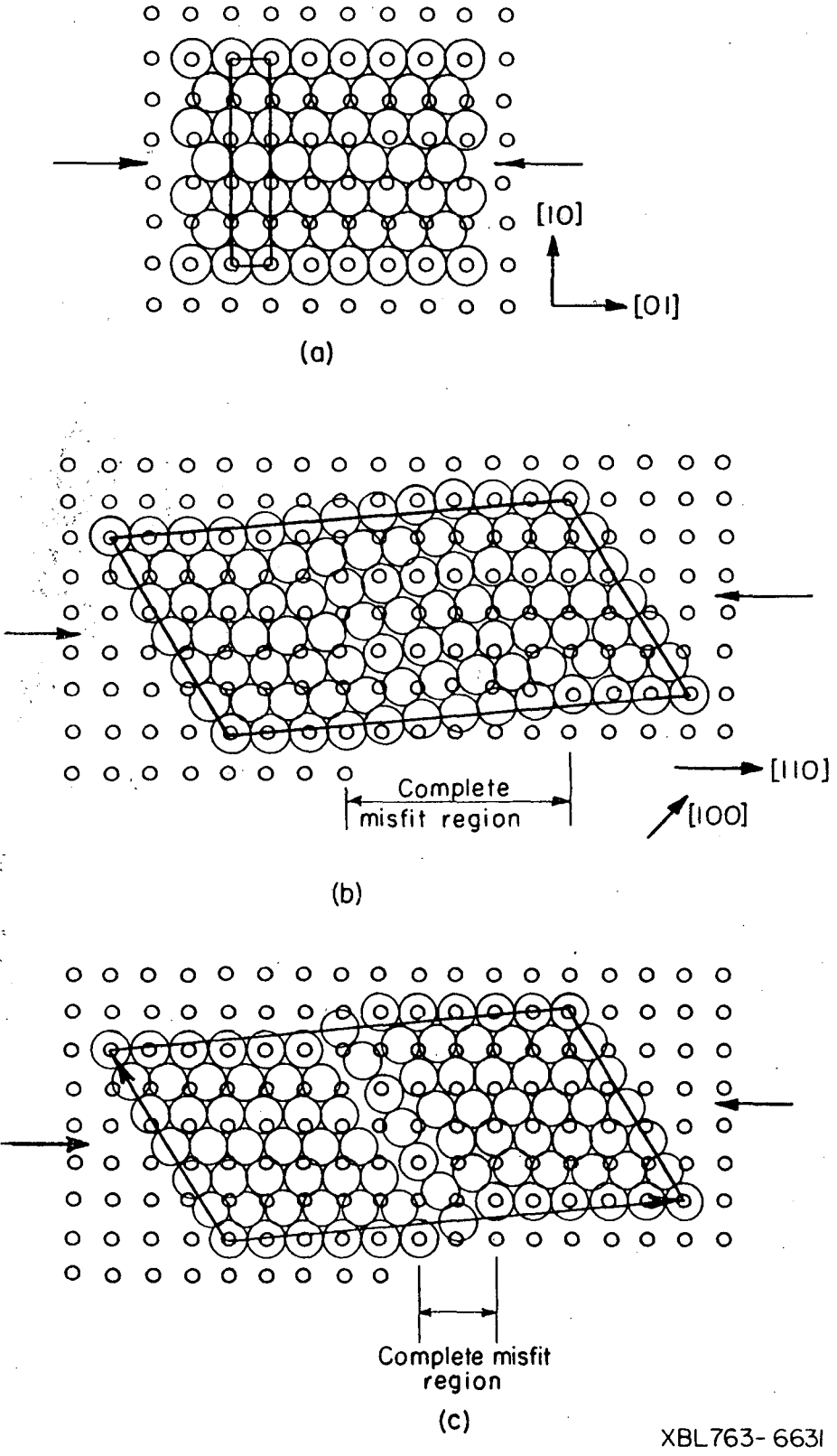
[10]
[01]
(a)
Complete
misfit region
[110]
[100]
(b)
Complete misfit
region
(c)
XBL763-6631

Fig. 4-20.

large hexagonal to square misfit in the [10]. The length of the misfit region as shown in Figs. 4-20b and 4-20c depends on the energy of the interaction with the substrate, the energy required to create a dislocation, and the supportable strain. The interaction with the substrate in platinum is probably not decreased much over the normal interaction between (001) planes as the hexagonal layer forms on top of a square substrate with a resulting large misfit region in the [01] as in Fig. 4-20b. This is discussed in Frank and van der Merwe[172] in a classic article. They also calculate that a larger amount of strain can be supported than was calculated by the simple model but the conclusion of Ir supporting more strain than Pt or Au remains valid.

Details of the Au diffraction patterns are difficult to see since the low Debye temperature causes a large amount of diffuse scattering. It can be seen, however, that the fractional order spots are split, but whether the pattern is two domains of $\begin{vmatrix} 5 & 0 \\ 0 & 20 \end{vmatrix}$ as proposed by Fedak and Gjostein[165] or four domains of $\begin{vmatrix} 5 & -3 \\ 1 & 12 \end{vmatrix}$ as on Pt cannot be readily determined. Since the mechanical properties of Au are similar to Pt, it is felt the same type of reconstruction occurs. The pattern is probably a $\begin{vmatrix} 5 & -3 \\ 1 & N \end{vmatrix}$ where N would be between 10 and 15. If N is less than 10, the angle would become prominently noticeable; above 15 the splitting of the diffraction spots from the [01] mirror would be too small to provide the 1/20 split of Fedak and Gjostein.[165]

The appearance of only one domain of reconstruction on the $(\bar{1},1,13)$ and $(\bar{1}19)$ crystal surfaces (see Figs. 4-17 through (4-19)) and domains on the (015) crystal surface is readily explained. Two domains of reconstruction would be expected on perfect $(\bar{1},1,13)$ surface since the

of HCP $(10\bar{1}1)$ unit cells back to back with a vacant row between each pair of strips in the [01] direction. The vacant row would increase the surface valency greatly to at least what it would be for the termination of a square lattice. This, coupled with the unsymmetric and unequivalent positions of most atoms, would probably result in an increase instead of a decrease of the surface energy. In their Fourier transform method of intensity analysis they ignored the splitting and probably have significant truncation errors.[100,101]

The chemical arguments put fourth previously to rationalize the reconstruction and summarized by Clarke[176] are not affected by the present interpretation of the diffraction pattern. The number of broken bonds is decreased by a rehybridization of the surface layer to form the close packed layer of the hcp structure. The favorability of this configuration can be shown by using the Engel-Brewer correlation[171] or with more regorous quantum mechanical arguments.

For the first time a satisfactory explanation of the reconstruction of the (001) surface of Ir, Pt and Au has been put forth. It incorporates the important considerations of the mechanical properties of a solid as well as the chemical (bonding) properties. The hexagonal overlayer on Ir is strained into a perfect $\begin{vmatrix} 5 & 0 \\ 0 & 1 \end{vmatrix}$ surface structure while on Pt and Au the hexagonal surface layer introduces misfit dislocations instead of straining to produce a $\begin{vmatrix} 5 & -3 \\ 1 & 12 \end{vmatrix}$ structure.

[110], a close packed direction, is ±4.8° from the [1,12] and [1,$\bar{1}\bar{2}$]. However, the crystals may not be better than 1/3° of solid angle from the specified pole, which corresponds to approximately 7° of rotation. Therefore, one domain only was nucleated at widely spaced kinks in the step. Since both the ($\bar{1}$,1,13), ($\bar{1}$,1,9) and thermal stressed (001) give the orientation of 4.8°, it is unlikely the rotation is controlled by the kink spacing. The modification of the reconstruction on the Pt(S)-[7(100)×(111)] surface is reasonable given the ability of the Pt surface layer to shear to lower its total energy. Changing the rotation and size of the reconstruction unit cell allow it to mesh in an apparent lower energy position at the step. The steps of the (015) crystal surface are parallel to the [100] which would not preferentially nucleate one domain of reconstruction, but could nucleate one of each pair of mirror image domains as seen in Fig. 4-19.

The Burgers vector of the [01] direction misfit dislocation is a $\underline{d}$[10] or 1/2 $\underline{a}$ ⟨110⟩. Dislocations generally glide on the most densely packed planes the {111} in the FCC crystal system. The ⟨110⟩ are in the {111} planes.

The recent finding by Bonzel, et al.[173] that the Pt-(001) surface is stable at low temperature ($\lesssim$150°C) and the difficulty of initially forming the reconstruction on Ir[162,157] (heat treatment to 170°C+) can be explained with this model. Frank and van der Mewre[172] calculated that there is an activation energy barrier extending to approximately twice the critical strain, ε^*, which prevents the overlayer from dislocating to relieve the strain. They estimated the height to be the order of the heat of vaporization near ε^* decreasing to zero at

$\sim 2\ \varepsilon^*$. Apparently at 150°C for Pt and 1700°C for Ir the first dislocations are nucleated and then there is a spontaneous conversion to the reconstruction in the neighborhood of the dislocation.

The hexagonal overlayer must be buckled out of the plane of the surface to lie atop the square substrate. Figure 4-21 shows the vertical displacement of the arrowed row of atoms in Fig. 4-20 for several x-y placements of the overlayer. The row of atoms is in the normal four-fold site (as used in Fig. 4-20) in Fig. 4-21a; several atoms of the unit cell are reaised approximately 0.8Å. Displacing the overlayer atoms 1/2 $\underline{d}$ ⟨10⟩ to a two-fold site for the arrowed row, Fig. 4-21b, will not narrow the maximum displacement for Pt and Au but fewer atoms will be at the extremes. For Ir the maximum displacement is narrowed to ~0.6Å. Placing all the atoms in an unsymmetric binding site, Fig. 4-21c, will lower the out of plane displacements greatly. It has been suggested by Cabrera [174] following Herring[175] that this could decrease the energy of the surface layer by relieving some of the stress. This might occur in Ir but probably does not in Pt and Au since the surface introduces defects to relieve the surface stress. Moving the hexagonal layer to an unsymmetric site might increase the interaction between the triangular and square bonding symmetries of the two interfaces. The position at (1/4,1/4) in the substrate unit cell minimizes the vertical strain in the hexagonal layer (maximum vertical difference of 0.25A) and appears to put the overlayer atoms in nearly equivalent positions.

The arrangement of surface atoms proposed by Clarke, et al.[176] can be ruled out. They suggest a structure which resembles two strips

Fig. 4-21. Hexagonal overlayer-substrate positions demonstrating vertical strain introduced into overlayer from Ir, (a) one row (arrowed) of atoms in four-fold sites (1/2,1/2), (b) rows in two-fold sites (1/2,0) and (c) all rows in one-fold site (1/4,1/4), position of minimum vertical strain. For Pt and Au overlayers there is larger vertical strain in areas of two dimensional misfit shown in Figs. 4-20b and c.

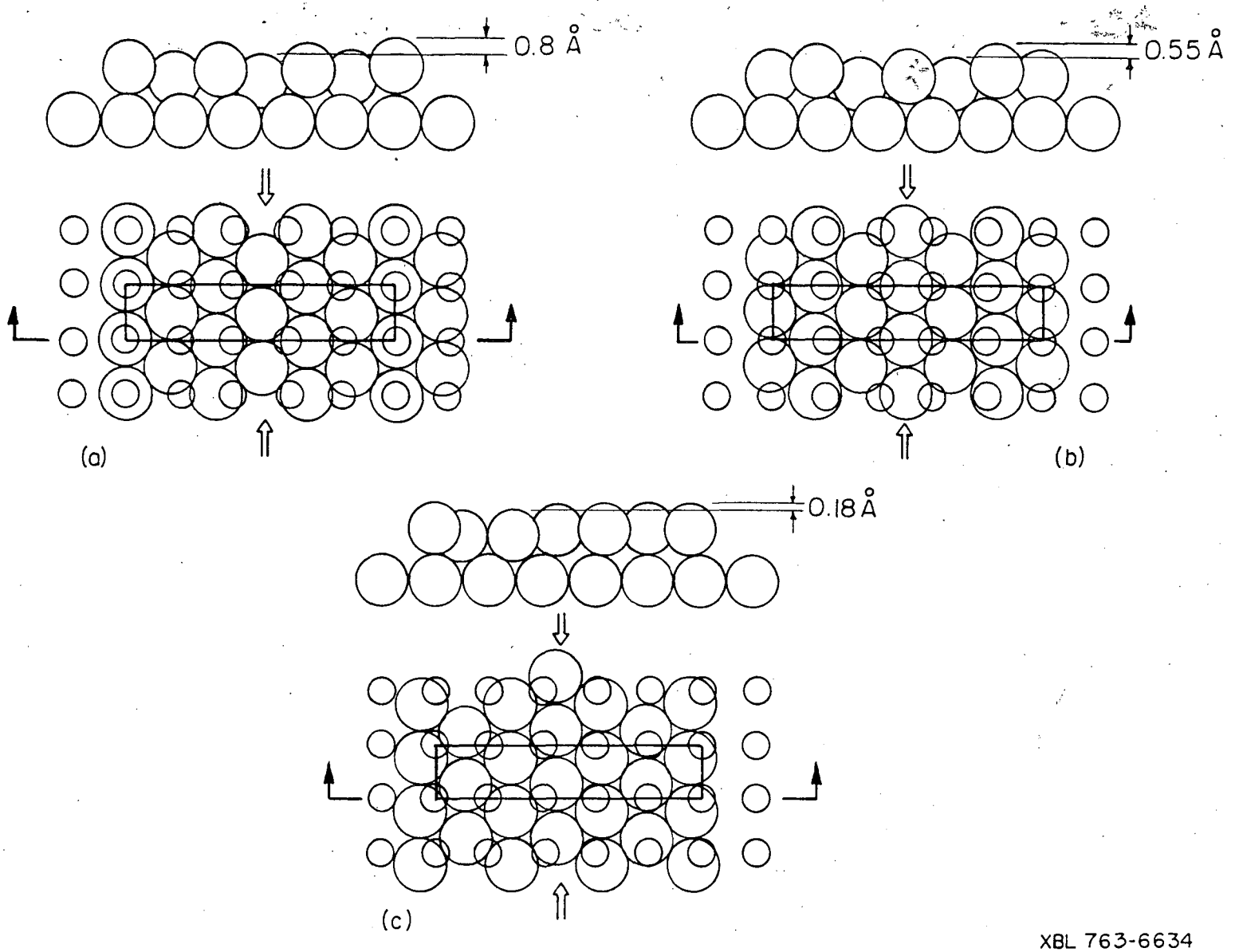

XBL 763-6634

Fig. 21.

4.5. Summary of Findings on Stability of Surfaces

The stability of Pt surfaces has been investigated by LEED and AES. The surfaces have been studied atomically clean, graphite covered and in an oxygen ambient. This is probably the first investigation of surface structure stability where the cleanliness of the surface is known and can be monitored and small amounts of known impurities have been added. On clean Pt surface, monatomic height steps are stable in ⟨110⟩ type zones except near a [110] pole. On the ⟨100⟩ zones of Pt, the surface is not stable in monatomic height steps, but facets near the [001] poles and has double height steps near the [110] poles. A reversible instability is found near the (335) surface: above 900°C, the surface facets and below 850°C, it is stable as monatomic height steps. These results are generally consistent with those found in the literature. The largest disagreement is found near the [011] pole. The discrepancies are probably contamination related.

None of the proposed theories which predict surface stability can describe the experimental results satisfactorily. Equilibrium theories of the surface are satisfactory at wide step spacings where interactions between steps are not important. At narrower step spacings they become progressively worse, caused at least in part by their failure to consider interactions between steps. It is felt interactions are important to at least two atomic diameters and possibly further.

Finally, it was shown that the surface stress tensor can be important in describing the structure of a surface on a large atomically flat crystalline sample. The difference in the reconstruction of Ir, Pt and Au (001) surface, can be rationalized by considering surface strain.

Iridium will support the strain of a hexagonal layer on top of a square bulk and has a $\begin{vmatrix} 5 & 0 \\ 0 & 1 \end{vmatrix}$ reconstruction structure, while Pt and Au will not support the strain. Dislocations are introduced and the resulting reconstruction structure on Pt is a $\begin{vmatrix} 5 & -3 \\ 1 & 12 \end{vmatrix}$.

5. ADSORPTION OF CO ON PT STEPPED SURFACES

5.1. Introduction

The adsorption of CO on low index Pt surfaces has been studied extensively.[96,177-183,119] The most commonly used techniques are flash desorption mass spectroscopy (FDMS) and LEED. Since adsorbed CO is sensitive to electron impact,[177] AES has not been used to monitor surface coverage. On the Pt-(111) surface, there is generally found one flash desorption peak and, therefore, one adsorption state. The FDMS are described by first order kinetics, i.e., CO is molecularly adsorbed, with a heat adsorption of 27 kcal/mole. The LEED pattern is a very diffuse C(4×2). The Pt-(001) displays a more complex behavior.[178] The LEED pattern is again a C(4×2), but there are three peaks in the flash desorption spectra. The temperature maxima are at 130°C, 180°C and 450°C or 650°C.[96,178] The lower two peaks are overlapping and the splitting is probably caused by adsorbate-adsorbate interactions similar to those described by Adams.[184] The heats of adsorption without considering interactions would be 25 and 27 kcal/mole. The upper state which comprises about 5% of the surface coverage may be a different binding state. The kinetics of this state have not been characterized; however, if first order desorption is assumed, the heat of adsorption is 40 to 53 kcal/mole. The (011) surface of Pt has two flash desorption peaks. Their heats of adsorptions are 25 and 31 kcal/mole.[181,182] felt that the two peaks are again caused by adsorbate-adsorbate interactions, as on the (001) surface. The LEED pattern of CO on the Pt-(011) is a (2×1) with certain spots missing from increased symmetry, as discussed in Appendix C. At high coverages the CO molecules have

a zig-zag pattern down the valleys of the ridge and valley structure of the (011) surface. The 6 kcal/mole decrease in binding energy of the lower temperature state could be from repulsive interactions forcing the molecules out of the bottom of the valley. Polycrystalline samples have been studied by FDMS [185] and ultraviolet photoelectron spectroscopy (UPS). [183] Four flash desorption peaks were found for CO adsorption on a filament, with two main peaks at 25 and 31 kcal/mole. These are identical energies to those found on (111) and (011) surfaces of Pt. Evidence for only one adsorption state was found by UPS on a Pt foil. The energy differences in the binding to various planes may be small enough that it does not shift the position of the electron orbitals by a detectable amount.

The coadsorption of CO and H_2 on Pt has been studied deliberately by some[71,179] and probably unitentionally by others. On the (111) surface, the main features of both the pure CO and pure H_2 FDMS remain after coadsorption; however, the peaks are broadened. CO coadsorption spectra have a second peak with desorption energy of about 28 kcal/mole, but in the H_2 coadsorption FDMS, the upper peak is washed out. No new peaks appeared on the (111) surface, at higher binding energies which would indicate dissociation of the CO or association of H and CO on the surface.

This investigation uses FDMS and LEED to characterize the adsorption of CO on high Miller Index surfaces of Pt. The introduction of steps to the surface provides a higher binding energy site for the adsorption of CO. The phenomenon that steps are higher binding energy sites has been observed for other high bond strength diatomic molecules.[71] These

higher binding energy sites provide a suitable site for the associated of CO and H, the onset of the Fisher-Tropsch reaction.

5.2. Experimental

5.2.1. Flash Desorption Mass Spectra Analysis

The FDMS can be described by two equations.[186,187] A mass balance on the desorbing species yields Eq. (5-1) (neglecting readsorption), and the rate of desorption of the species, f_d, is assumed to be given by Eq. (5-2),

$$V \frac{dN}{dt} = r_d A - SN \tag{5-1}$$

$$r_d = \frac{dn}{dt} = n^m \nu^{(m)} \exp(-E_d/kT_S) \tag{5-2}$$

where V is the volume on the vacuum system, N is the change in density in the gas phase, A is the area of the sample, S is the pumping speed, n is the species concentration on the surface, m is the order of the desorption reaction, $\nu^{(m)}$ is the pre-exponential factor, and E_d is the heat of desorption. Since N is proportional to the change in the gas phase pressure on the desorbing species, Eq. (5-1) may be re-written to give

$$\frac{dn}{dt} = \frac{V}{AkT_g} \left[(P - P_o)\left(\frac{S}{V}\right) + \frac{dP}{dt} \right] \tag{5-3}$$

where P_o is the partial pressure of the species at the beginning of the experiment. The pumping speed of the vacuum chamber is much higher than the rate of desorption of molecules from the surface, $dP/dt << (P - P_o)\, S/V$, in this investigation. This will be shown to be valid for this investigation in Section 5.2.2. The total coverage

of the surface can be found by integrating Eq. (5-3)

$$n_s = \frac{S}{AkT_g} \int (P - P_o)\, dt \quad . \tag{5-4}$$

Once the coverage of the surface is known, the sticking coefficient, σ, may be found. The sticking coefficient is defined as the rate of change of surface coverage with time divided by the incident flux of molecules, as given by Eq. (5-5),

$$\sigma \equiv \frac{\frac{dn_s}{dt}}{\left(\frac{p}{kT}\right)\left(\frac{\bar{v}_m}{4}\right)} \tag{5-5}$$

where p is the gas pressure and $\bar{v}_m$ is the mean molecular velocity.

The sample is assumed to be heated linearly from the temperature of adsorption, T_o,

$$T_s = T_o + \beta t \tag{5-6}$$

until all the adsorbed gases have desorbed. The heating rate, β, is generally in the range of 1 to 1000°/sec. As the sample is heated the pressure in the chamber goes through a maximum, and T_M the surface temperature of this maximum can be related to E_d, β and $\nu^{(m)}$. For a first order desorption process, Eqs. (5-2), (5-3) and (5-6) may be solved to give

$$\frac{E_d}{kT_m^2} = \frac{\nu^{(1)}}{\beta} \exp(-E_d/RT_m)$$

Redhead[187] has shown Eq. (5-7) may be written with less than 2% error as

$$\frac{E_d}{RT_m} = \ln\left(\frac{\nu^{(1)} T_m}{\beta}\right) - 3.64 \qquad (5\text{-}8)$$

Eq. (5-8) can easily be solved for the heat of desorption, E_d.

5.2.2. Experimental Procedures

The single crystal samples when mounted as shown in Fig. 2-8 can be heated resistively. The support wires heat at a rate of several thousand degrees per second to about 700°C, and then slower to about 1000°C. The crystal is heated by conduction from the wires, and the heating rate of the sample is almost linear to about 600°C. Figure 5-1 shows a typical temperature vs time plot for heating a crystal; the non-linearity present does not significantly affect the results. The temperature was measured with a Pt--Pt-10% Rh thermocouple spot welded to the top of the samples. During the rapid initial heating period, the adsorbed gases on the heating wires are removed almost instantaneously. The rate at which these gases are pumped out of the chamber allows the pumping speed to be determined. As readily seen from Figs. 5-2c or d, the time constant for the exponential decay of this initial burst of gas is about 0.1 sec. This gives a 150 liter/sec pumping speed for CO.

The sample under experiment is turned away from the gas inlet needle. Thus the gas pressure measured by the mass spectrometer or ionization gauge is equal to the pressure at the crystal. The second sample blocks direct exposure of the sample from the needle. The flux distribution from the needle is peaked,[188] so even the side of the

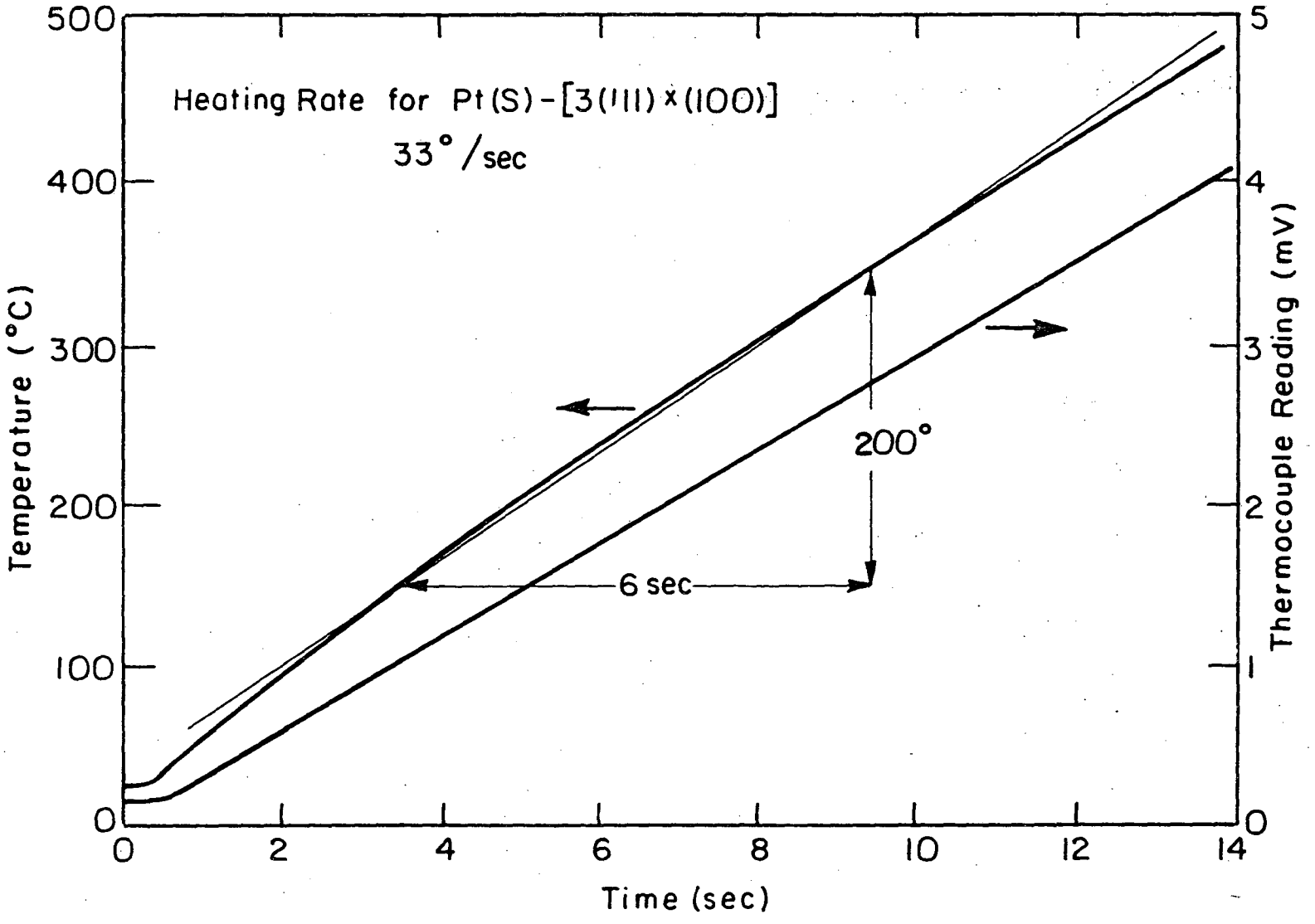

Fig. 5-1. Typical temperature vs time plot for determination of the heating rate, β, and linearity of the heating rate.

XBL 7510-7542

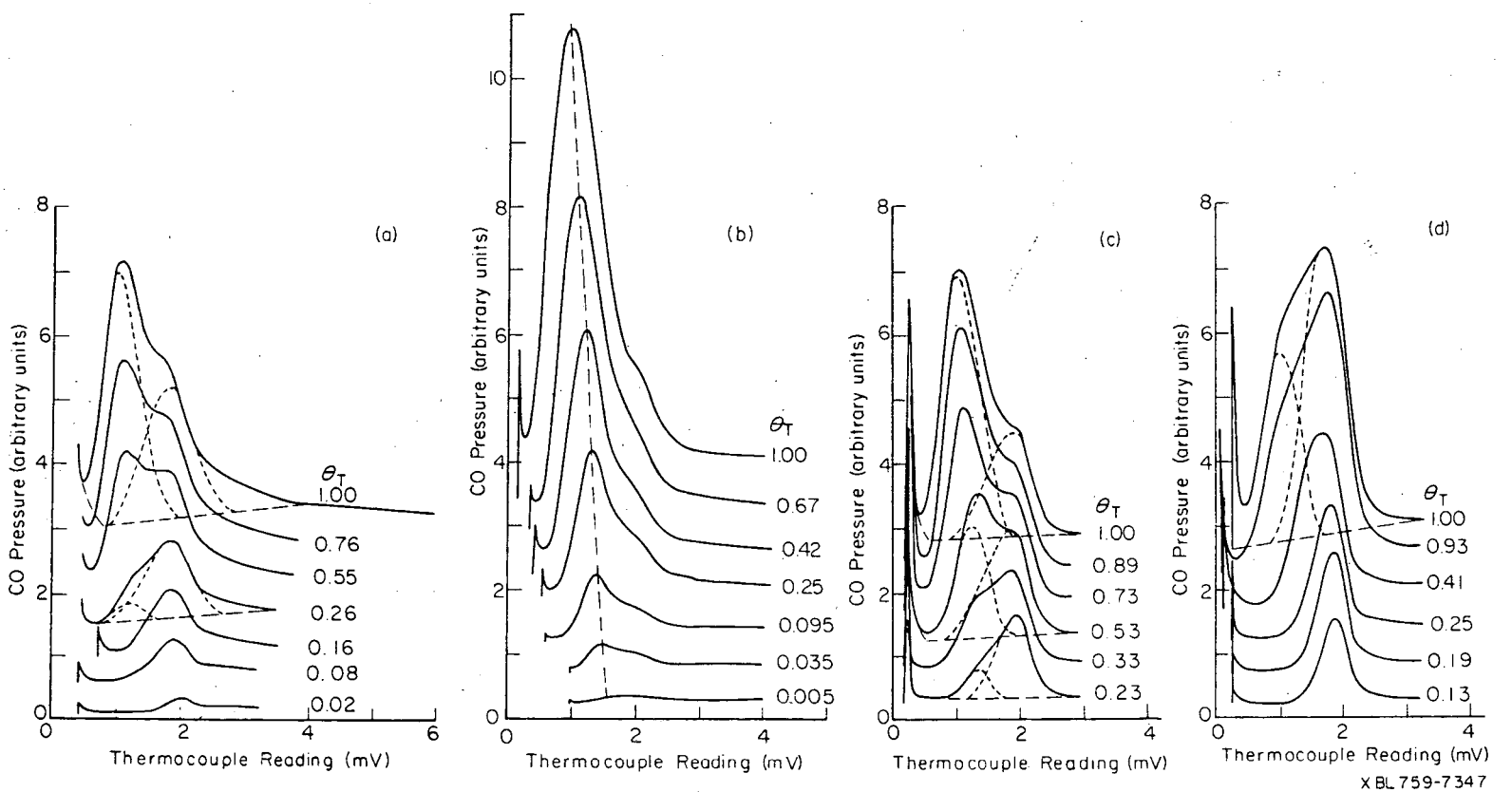

Fig. 5-2. Flash desorption mass spectra for CO desorbing from the (a) Pt(S)-[7(111)×(310)], (b) Pt-(111), (c) Pt(S)-[6(111)×(100)] and (d) Pt(S)-[3(111)×(100) surfaces. The origin for curves corresponding to higher coverages are displaced arbitrarily upwards.

crystal which faces the needle would not be exposed evenly. With an even pressure of gas the relative sticking coefficients can be measured more confidently.

5.3. Results and Discussion

5.3.1. CO Adsorption on Pt-(111) Vicinal Surfaces

The Pt-(111) vicinal surfaces are all characterized by two flash desorption peaks for CO. The desorption spectra are shown in Fig. 5-2 for the Pt(S)-[7(111)×(310)], Pt-(111), Pt(S)-[6(111)×(100)], and Pt(S)-[2(111)×(100)] surfaces, and Fig. 5-3 for the Pt(S)-[6(111)×(111)] surfaces. The shoulder on the high temperature side of the 1 mV peak from the Pt-(111) surface (Fig. 5-2b) is an edge effect from the relatively thick, 0.4 mm, sample. The edge is approximately 10% of the total area. The absolute peak areas cannot be compared on Fig. 5-2 since the heating rates, β, are slightly different (57, 50, 62 and 59°K/sec respectively) and the gain of the electron multiplier in the mass spectrometer is not constant. The zero of the ordinate in Fig. 5-2 and Fig. 5-3 is shifted to higher values for spectra of higher initial coverage. The lower temperature peak corresponds to a heat of desorption of 23.5 ± 0.5 kcal/mole and the upper peak corresponds to a heat of desorption of 29.6 ± 0.3 kcal/mole. These values are an average over all the surfaces calculated from Eq. (5-8) assuming that $\nu^{(1)}$ is 10^{13}.

The two peaks in the FDMS can be discussed as either adsorbate-adsorbate interactions, similar to the low index surfaces, or as two binding sites, one on the terrace and one at the step. The second choice is taken because, as shown in Fig. 5-4, the ratio of number of molecules

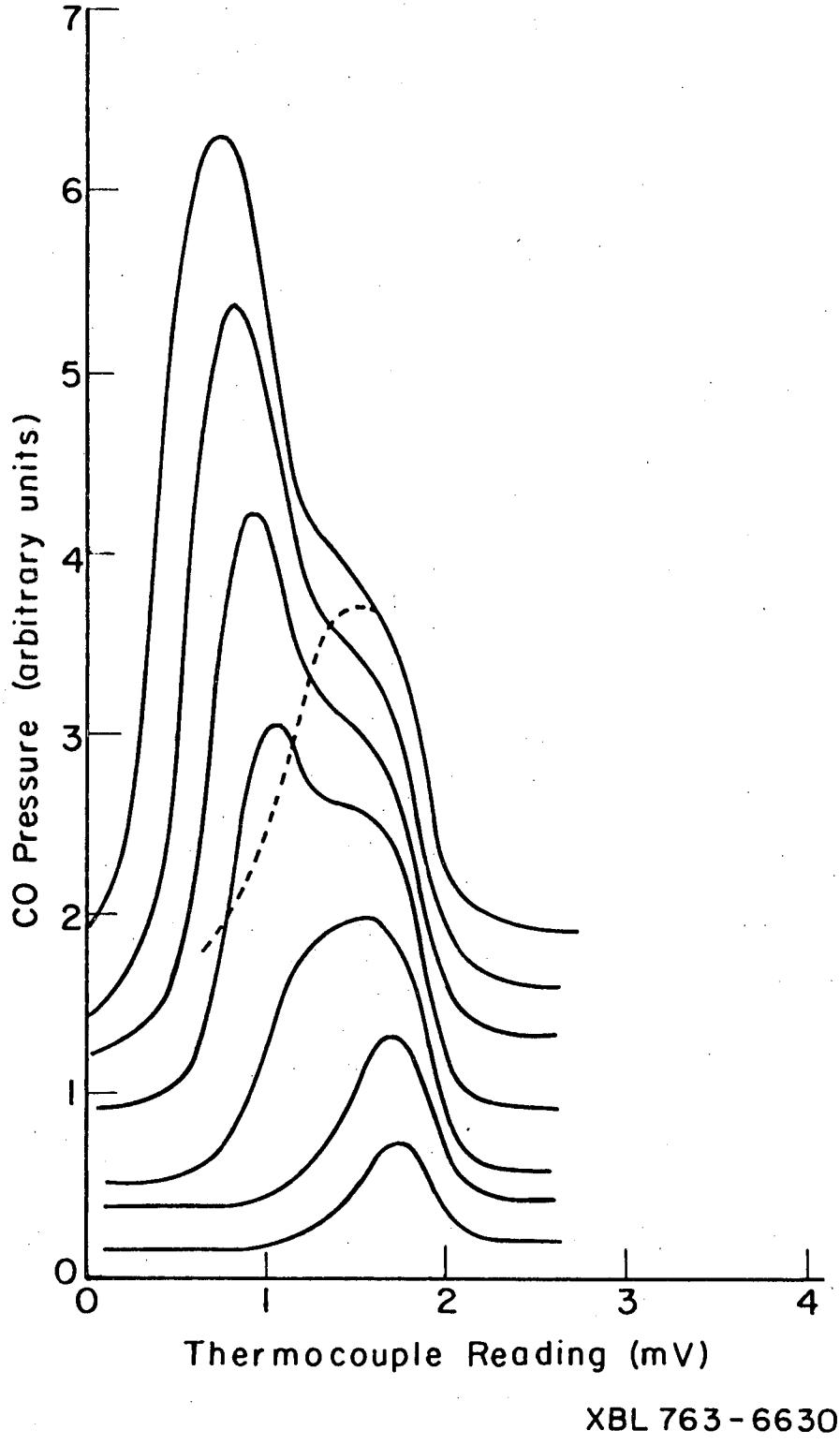

Fig. 5-3. Flash desorption mass spectra for CO desorbing from the Pt(S)-[6(111)×(111)] surface. The origin for curves corresponding to higher coverages are displaced arbitrarily upwards.

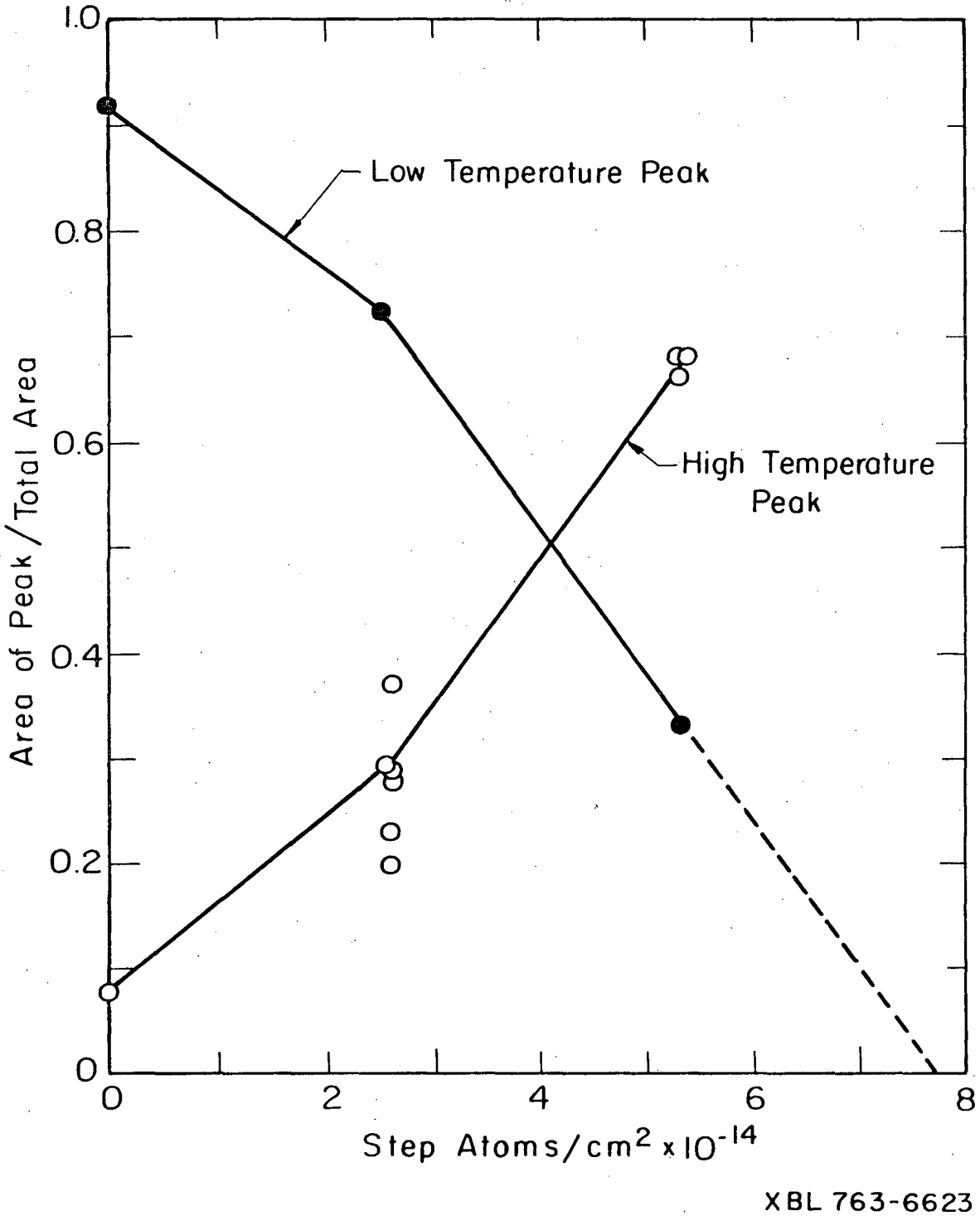

Fig. 5-4. The ratio of high temperature peak area to the total peak area increase with step density, indicating the high temperature peak is associated with the steps.

in the higher temperature peak to the total number of molecules on the surface, as determined by Eq. (5-4), increases with increasing step density. The saturation coverage FDMS from the Pt(111), Pt(S)-[6(111)×(100)], Pt(S)-[7(111)×(310)] and Pt(S)-[3(111)×(100)] and Pt(S)-[6(111)×(100)] and Pt(S)-[6(111)×(111)] are shown in Figs. 5-5 and 5-6, respectively, for ease of comparison. Since the areas of the two peaks are separated manually, there is a large scatter in the relative areas of the two peaks. If the per cent terrace from the relative areas is extrapolated to zero in Fig. 5-4, the line crosses the absisca at about 8×10^{14} step atoms/cm^2. This is very close to the value for the Pt(S)-[2(111)×(100)] surface, and is not surprising since the diameter of CO, approximately 3.6A, is a reasonable match for the width between steps of the Pt(S)-[2(111)×(100)], 4.45A.

It is interesting to note that there is little difference in the FDMS spectra from the Pt(S)-[6(111)×(100)] and the Pt(S)-[7(111)×(310)], as seen from Figs. 5-2a and c or 5-4b and c, respectively. It is expected that the kink would be an even stronger site for adsorption than at a step. In the spectra from the Pt(S)-[7(111)×(310)], there is a high temperature tail not seen on the Pt(S)-[6(111)×(100)]. This could easily be an experimental artifact, since its size varies directly with the high temperature peak size; its size does not increase first as a stronger binding site would. The average value of the relative area of the high temperature peak is higher on the kinked surface, 0.29 to 0.25 but may not be significantly higher considering deconvolution errors. Consequently, the adsorption of CO on Pt surfaces is not affected by kinks in the step.

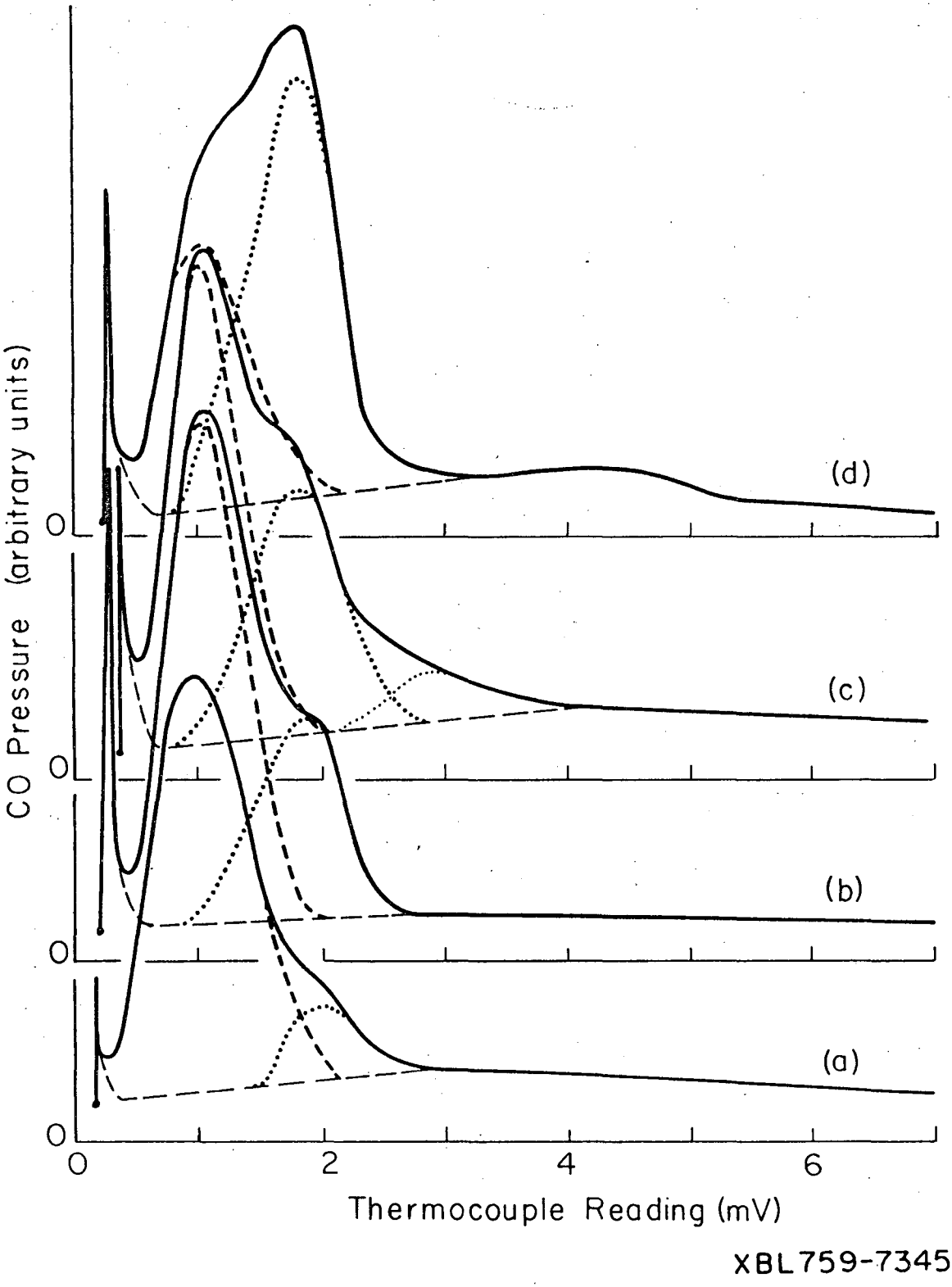

Fig. 5-5. Saturation coverage FDMS from the (a) Pt-(111), (b) Pt(S)-[6(111)×(100)], (c) Pt(S)-[7(111)×(310)], and (d) Pt(S)-[3(111)×(100)] surfaces.

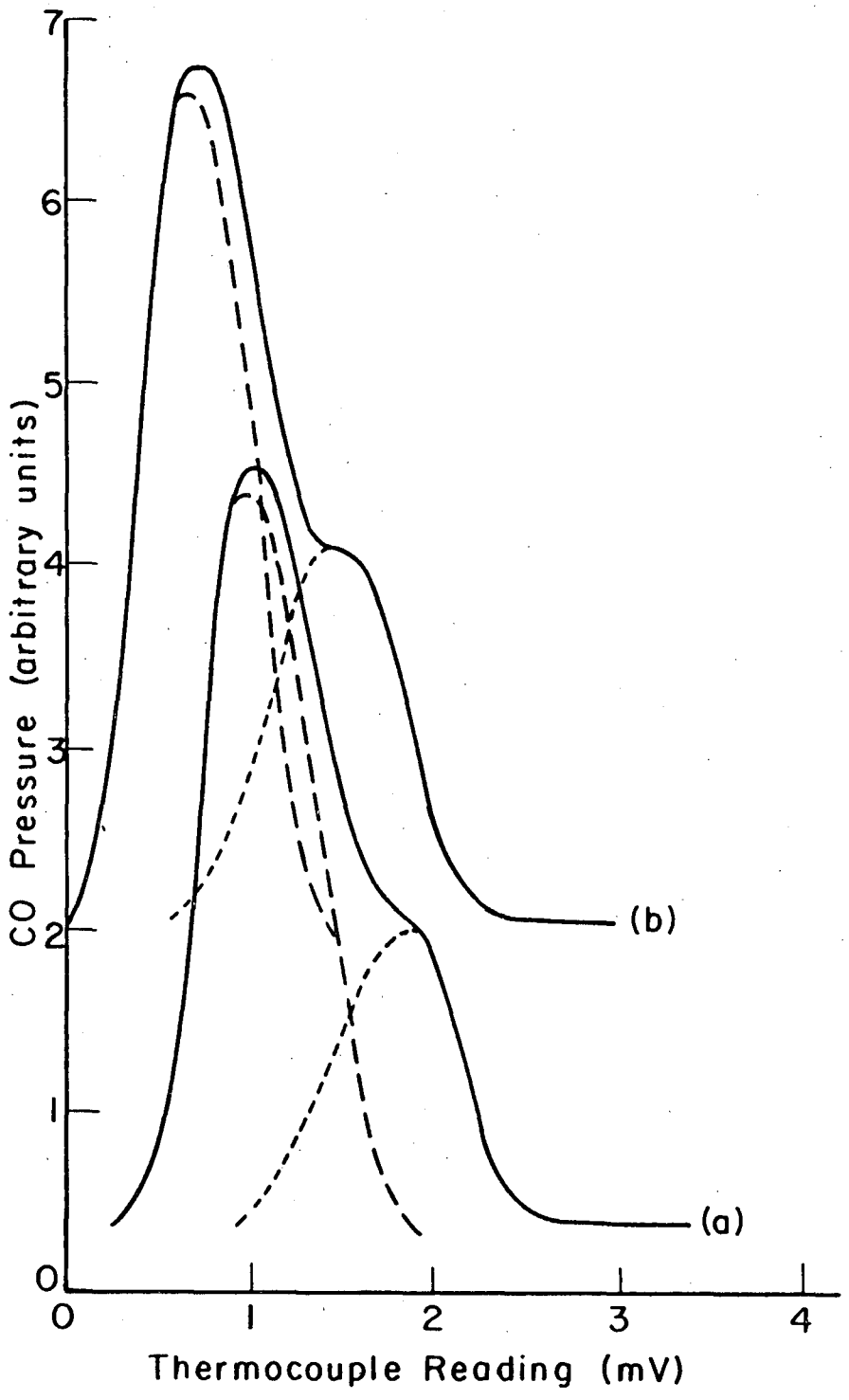

XBL 763-6629

Fig. 5-6. Saturation coverage FDMS from the (a) Pt(S)-[6(111)×(100)] and (b) Pt(S)-[6(111)×(111)] surfaces.

There is little effect of step orientation on the FDMS peak positions or amplitudes. Figure 5-6 shows the FDMS from the CO saturated Pt(S)-[6(111)×(100)] and Pt(S)-[6(111)×(111)]. The relative areas under the upper FDMS peaks are almost identical, the Pt(S)-[6(111)×(111)] has 4% more area but this is again probably not larger than the error in the deconvolution of the peaks. Both peak positions are about 0.35 to 0.40 mV lower on the Pt(S)-[6(111)×(111)]. The cause of this lowering in temperature is not known, but it is undoubtedly an experimental artifact since the peak associated with the (111) terrace, which is very consistent on all the other (111) vicinal surfaces, is lowered. When the temperature of the (111) terrace peaks maxima is made to correspond with that of the other (111) vicinal surface, the FDMS from the Pt(S)-[6(111)×(100)] and Pt(S)-[6(111)×(111)] are identical, as is the FDMS from the Pt(S)-[7(111)×(310)]. Consequently, we can conclude that there is no effect of step orientation on CO adsorption on (111) vicinal surfaces.

There is a very diffuse c(4×2) LEED pattern from the Pt-(111) surface when CO covered, which is the same as that observed by Morgan and Somorjai.[189] However, other than an increased background intensity no new features were observed in the LEED patterns from the vicinal surfaces, which is indicative of a highly random or highly mobile species. Absorbate LEED patterns on stepped surfaces are generally more diffuse than from low index surfaces.

The sticking coefficient for CO on Pt-(111) vicinal surfaces appears to be close to unity. Plots of total relative coverage and the coverage in each binding state vs exposure are shown in Fig. 5-7a-e for the Pt-(111), Pt(S)-[6(111)×(100)], Pt(s)-[7(111)×(310)],

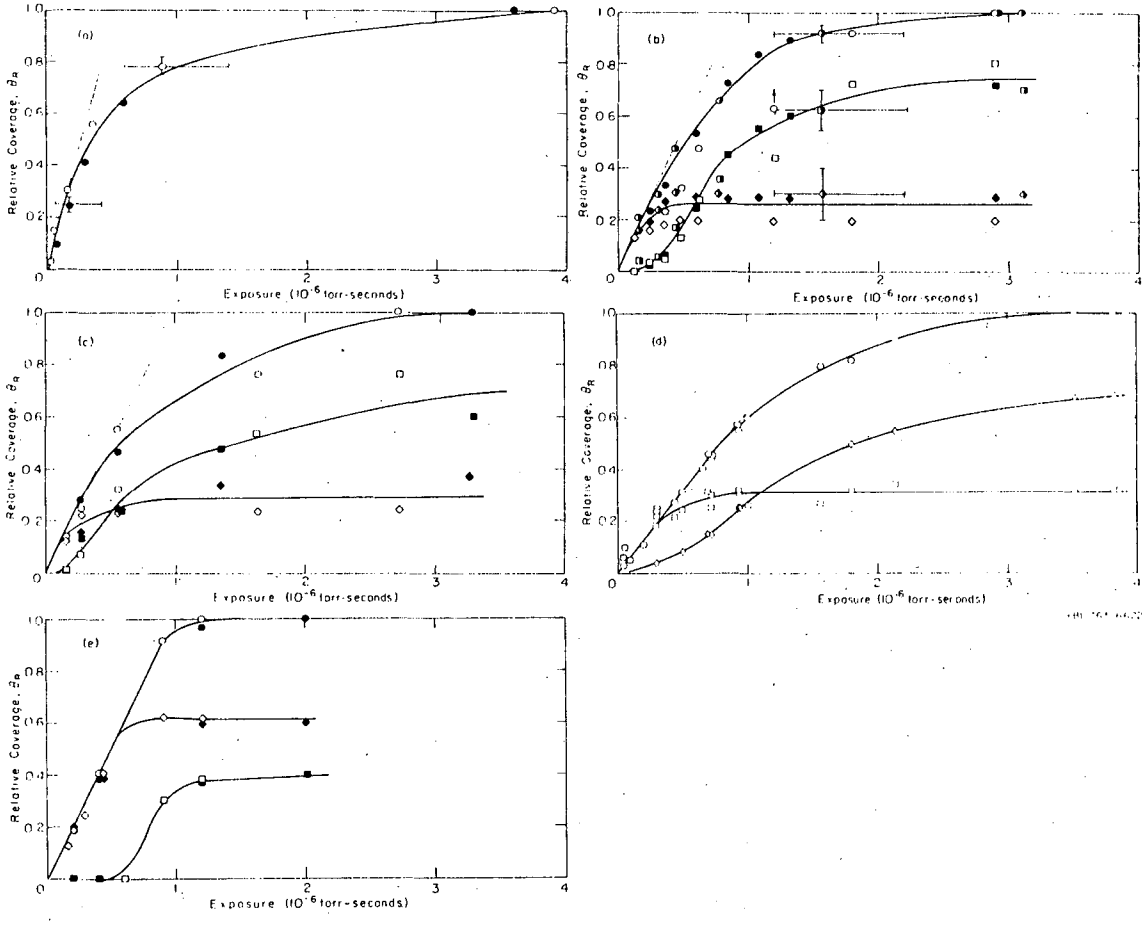

Fig. 5-7. Exposure dependence of the relative total coverage (-○-), coverage in the high temperature binding state (-◇-), and coverage in the low temperature binding state (-□-) for the (a) Pt-(111), (b) Pt(S)-[6(111)×(100)], (c) Pt(S)-[7(111)×(310)], (d) Pt(S)-[6(111)×(111)] and (e) Pt(S)-[3(111)×(100)].

Pt(s)-[6(111)×(111)] and the Pt(S)-[3(111)×(100)], respectively. In Fig. 5-7a, the sticking coefficient for CO on the Pt-(111) surface is high, between 0.5 and 1.0, at low coverages up to about 60% of saturation and decreases slowly to zero after 8×10^{-6} Torr-sec. The total coverage sticking coefficient for the vicinal surfaces Figs. 5-7b-e is also close to one at low coverage and decreases to zero after about 8×10^{-6} Torr-sec. However, on these surfaces, the high temperature flash desorption peak reaches about 70% of its saturation value before the low temperature peak appears. The high temperature peak coverage quickly saturates, and the low temperature peak fills with near unity sticking coefficient until about 70% total coverage is reached similar to the (111) surface and then σ falls off to zero. The adsorbed CO must be highly mobile, since, on an area basis, the "sticking coefficient" at the step on the Pt(S)-[6(111)×(100)] surface is about 4.5 molecules per incident molecule. Whether the CO molecules diffuse to the step at the temperature of adsorption or during the heating cannot be determined. The uniformly high background intensity of the LEED patterns indicates that there is probably high mobility at low temperature, 25°C. The (100) orientation step may be able to trap diffusing CO molecules more efficiently than the (310) or (111) orientation step. The relative coverage curves for the (100) orientation step (Fig. 5-7b and c) have a more abrupt leveling off than the other orientations (Fig. 5-7c and d). Two binding states have been found for CO on (111) stepped Pt surfaces. Both states are probably molecularly adsorbed with a 6 kcal/mole difference in the heats of desorption. This stronger binding at the step could be from

increased overlap between the Pt d-orbitals and the CO $2\pi^*$ orbitals. Doyen and Ertl[193] have calculated the interaction energy of CO with Pd and Ni by a self-consistent Hartree-Fock method, and found very little effect of the steps in the Pt(s)-[2(111)×(100)] surface on the adsorption energy over the (111) surface. The expected result on Pt would be similar, so their model might not correctly account for the geometry of the step. They allowed the metal atom to rehybridize to maximize the overlap between the CO and metal orbitals. Perhaps, with the narrow terraces of the [2(111)×(001)] surface, the step atoms hybridized differently than they would on a wider step, thus not giving a high enough heat of adsorption.

An even more surprising difference, is that the isosteric heat of adsorption[190] of CO on the Pd(S)-[9(111)×(111)] was found to be identical with that on the Pd-(111) surface at all coverages.[191] This is in marked contrast with Pt where there is a second binding state associated with the steps. However, this discrepancy may be caused by the experimental method (change in work function) employed to measure the isosteric heat of adsorption. On a Pt foil near (111) orientation, Spicer, et al.[192] have measured the work function change from CO adsorption and compared this with subsequent FDMS. They found the work function saturated before the surface saturated with CO and that there was not a linear correlation between work function change and coverage. If the same or similar non-uniformities occur on Pd, the lack of an increased binding energy on the Pd stepped surface may be only an effect of the experimental technique. It would be of interest to determine by a second technique, such as FDMS, if Pd does behave

differently for the adsorption of CO. Perhaps if the difference is real, the greater binding energy at a Pt step may be a reason for Pt's unique catalytic properties.

The calculation of Doyen and Ertl[193] predicts a small difference in the energy of adsorption of CO on Pd-(111) for any position relative to the Pd atoms. This difference, the effective diffusional activation energy is expected to be even lower on Pt than the 2.5 kcal/mole predicted for Pd (Ni is larger than Pd). This small activation energy for diffusion could readily explain the apparent high mobility of CO on the Pt-(111) terraces.

5.3.2. CO Adsorption of the Pt-(001) Vicinal Surfaces

The Pt-(001) vicinal surfaces are characterized by three flash desorption peaks for CO. The desorption spectra are shown in Fig. 5-8 for the Pt-(001) and the Pt(S)-[7(100)×(111)] surfaces. On the low index face, the main peak maxima appear at 150° and 240°C and the small high temperature peak is at 540°C. There is rather poor agreement on peak positions between the two previous studies[96,194] and with this study. There are, however, three peaks reported in all three studies. The peak maxima in this study give by Eq. (5-8), desorption activation energies of 24.1±0.3 kcal and 28.8±0.6 kcal for the low temperature peaks and 46.0±0.1 for the high temperature peak, if they are first order desorption processes with $\nu^{(1)} = 10^{13}$. Doyen and Ertl[193] in their calculations found that the (100) surface of both Ni and Pd had a higher heat of adsorption of CO than did the Pt(S)-[2(111)×(100)] stepped surface. The increase in the heat of adsorption from the Pt-(111) to the (001) upper state agrees with their calculation, about

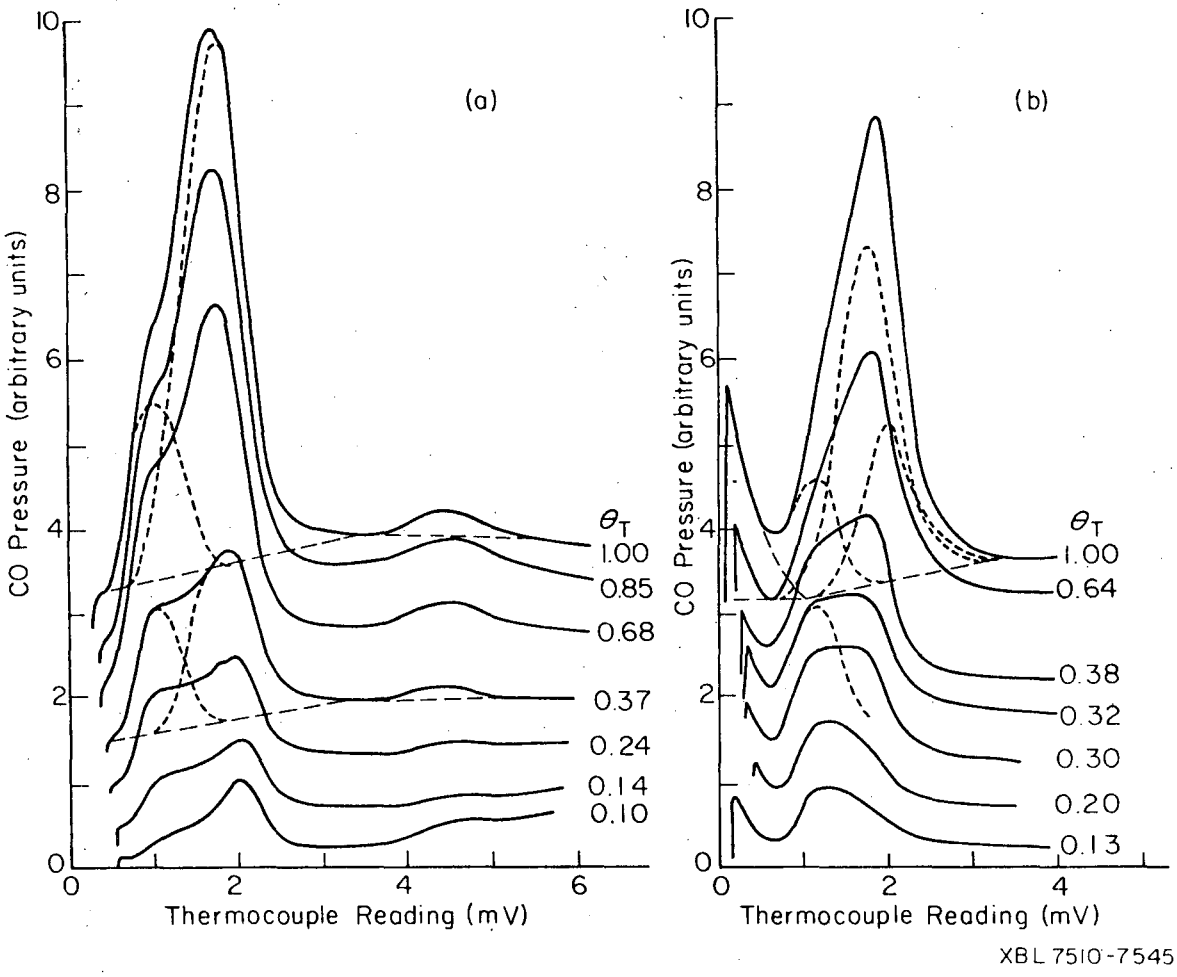

Fig. 5-8. Same as Fig. 5-2 except (a) Pt-(001) and (b) Pt(S)-[7(100)×(111)].

4 kcal/mole increase. The heat of adsorption calculated for the stepped surface of Pd is ~3 kcal/mole less than for the (001) surface instead of the ~1 kcal/mole higher bound on Pt.

The previous investigations[96,194] found two low temperature peaks to be about the same size; however, in this investigation, the 240°C peak is twice as large as the 150°C peak. When the FDMS spectra were taken, the LEED pattern from the clean Pt-(001) surface was not the symmetric $\begin{vmatrix} 5 & -3 \\ 1 & 12 \end{vmatrix}$ four domain pattern shown in Fig. 4-6a, but a one domain pattern similar to those seen on stepped surfaces (the crystal had been thermally stressed, see Section 4-4). The literature FDMS spectra were taken on surfaces displaying symmetric LEED patterns. The H_2 background may also have been higher in this investigation.

The Pt(S)-[7(100)×(111)], which has only one domain of reconstruction of its surface, has an analogous FDMS spectra. The small peak at 540°C is not present, but the two main peaks are observed. Figure 5-9 shows the saturation coverage desorption spectra of both the low index and stepped surface for comparison. As shown, when T_m and the full width at half maximum from the low index surface are used to separate the peaks on the stepped surface, a third peak must be included in the description to shift the overall maximum to a higher temperature. The maximum temperature of the third peak is at 270°C which corresponds to a heat of desorption of 30.0±0.4 kcal. This is very nearly the same desorption energy as found at a step site on the (111) vicinal surfaces, 29.6±0.3 kcal/mole, and it, therefore, most likely associated with the steps.

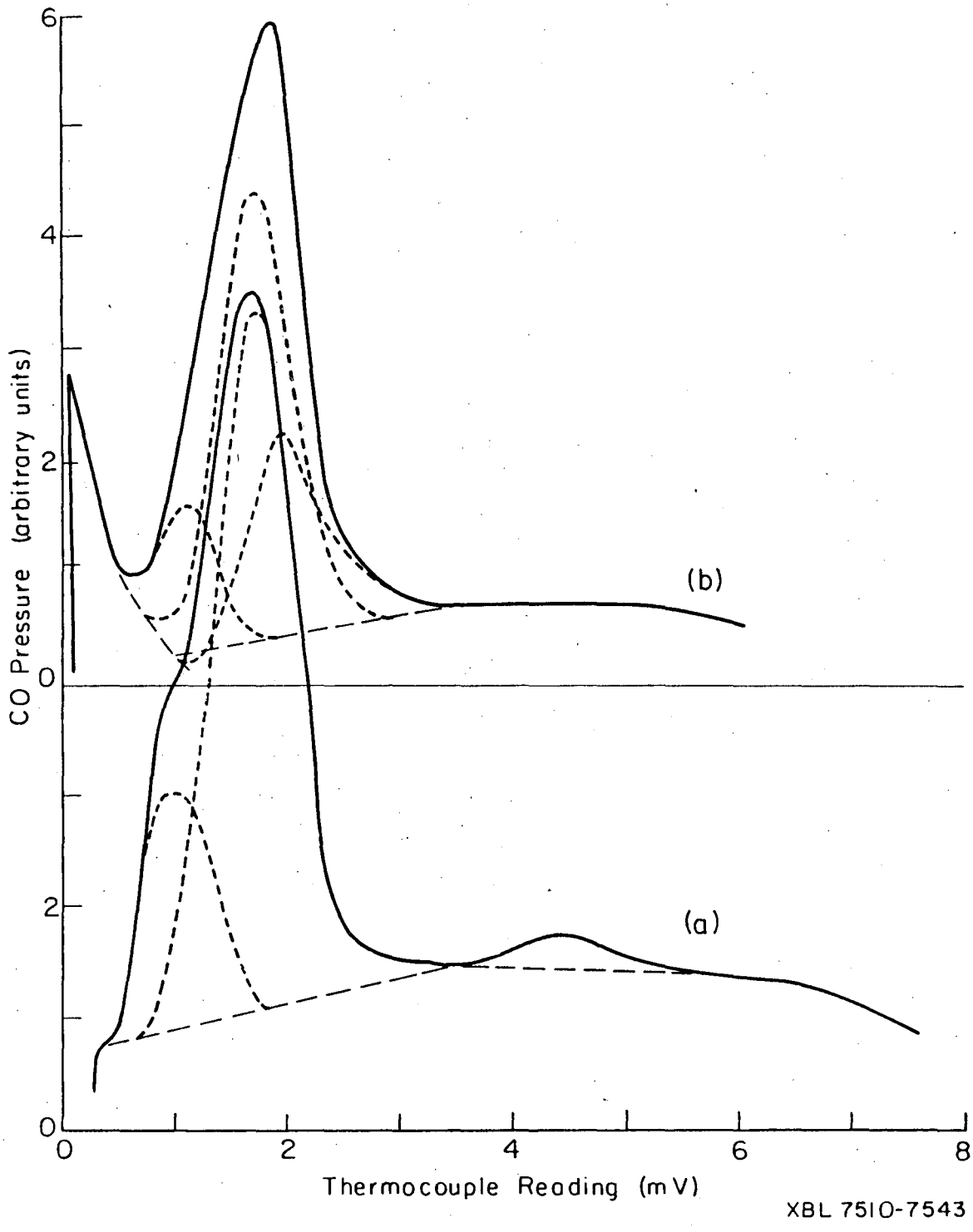

Fig. 5-9. Saturation coverage FDMS from the (a) Pt-(001) and (b) Pt(S)-[7(100)×(111)] surfaces.

The sticking coefficient for CO on the Pt-(001) vicinal surfaces is very high. If the saturation coverage is 0.75 monolayers as suggested by Morgan and Somorjai,[96] the initial sticking coefficient is 1.0 on both surfaces. The sticking coefficient falls off at higher coverages, above 0.2, with saturation reached at approximately 20×10^{-6} Torr-sec. Plots of total relative coverage and the coverage in each peak vs exposure are shown in Fig. 5-10a and b for the Pt-(001) and Pt(S)-[7(100)×(111)], respectively. The two low temperature peaks associated with the (001) plane behave similarly on both surfaces, the 150°C peak saturating at low exposure ($2\text{-}4\times10^{-6}$ Torr-sec) and the 240°C peak slowly filling in about 20×10^{-6} Torr-sec exposure. It is interesting that on the Pt(S)-[7(100)×(111)] surface the peak associated with the steps does not fill first as was found on the (111) vicinal surfaces. The lack of molecules in this state until about 2×10^{-6} Torr-sec may not be real and may be caused only by the method of separating the desorption peaks. The step site coverage is probably linearly proportional to the exposure up to its saturation value. However, the terrace sites are appreciably filled before the step sites are filled, indicating a much slower diffusion of CO on the (001) terraces of Pt than on the (111) terraces. This difference in diffusivities could be responsible for the more diffuse CO LEED patterns observed from the (111) surface.

No new features were observed in the LEED pattern from the (001) vicinal surface. A c(4×2)-CO pattern was observed from the (001) surface at saturation coverage;[96,194] this discrepancy may again be caused by the differing domain structure on the vicinal surface used

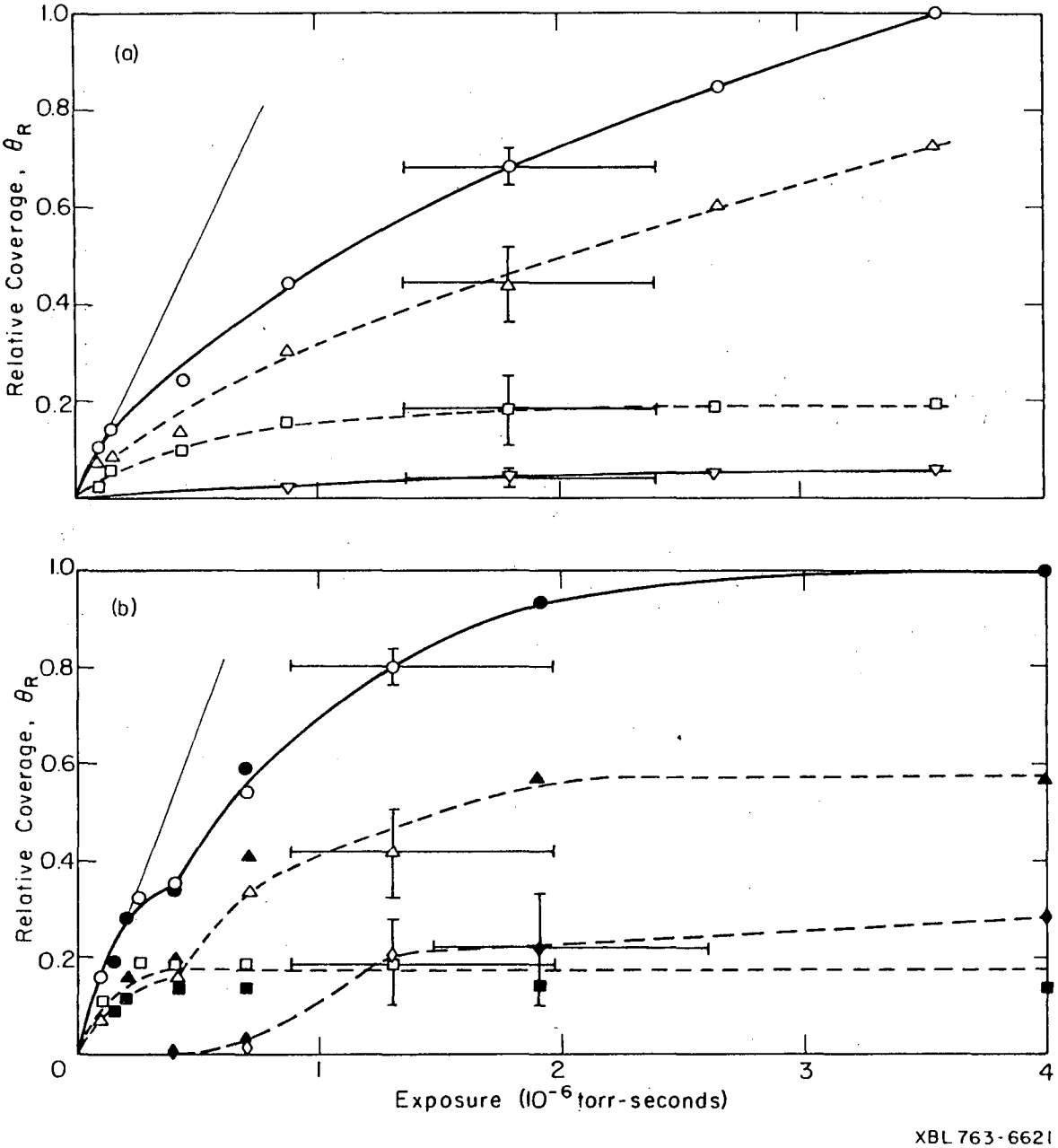

XBL 763-6621

Fig. 5-10. Exposure dependence of the relative total coverage (-○-), coverage in the low temperature terrace peak (□), coverage in the high temperature terrace peak (-△-), coverage in the step associated peak (-◇-) and coverage in the reconstruction associated peak (520°C) (-▽-) for (a) the Pt-(001) and (b) Pt(S)-[7(100)×(111)] surfaces.

in this investigation form those on the (001) surface. The reconstruction LEED pattern disappeared after ~3×10^{-6} Torr-sec exposure on both surfaces (coverage of 0.3 monolayers). The reconstruction did not reappear until the temperature was raised above 550°C and the CO in the high temperature peak was removed. Morgan and Somorjai[96] also observed that the high temperature CO peak controlled the reconstruction. Since the removal of the CO in the high temperature state is related to the formation of the reconstruction, the preexponential factor and consequently the heat of desorption of this state may be modified.

It has been postulated that the reconstructed surface of Pt-(001) is deficient in electrons, and that the adsorption of an electron donor would cause the reversion to the unreconstructed surface.[96] This has been verified experimentally in that adsorption of O_2 and other electron acceptors does not cause the reconstruction to disappear and may in fact stabilize the reconstruction.[195] The adsorption of an electron donor, such as most hydrocarbons, causes the reconstruction to disappear. CO, which is thought to adsorb as a slight electron acceptor (0.1 electron),[195] must donate 5σ electrons to the proper orbitals of the metal to destablize the reconstruction.

On the Pt-(001) surface, there are three FDMS spectra peaks. The larger two peaks, which are lower in energy, are associated with the normal adsorption sites of the low index planes. The upper peak, which comprises less than 5% of the total CO desorbed, is associated with the formation of the reconstruction. Frank and van der Merwe[172] have calculated the energenics of misfit dislocation; they find that near a critical value of lattice misfit there is an activation energy for the formation of the dislocations (as opposed to a strained

absorbate lattice). This activation energy varies for a van der Waals solid from about 2/3 of the heat of vaporization at the critical value to zero at about twice the critical value of lattice misfit. Helms and Bonzel[173] found for a clean Pt-(001) surface that the unreconstructed surface was stable below 150°C; above this temperature it spontaneously reconstructed. They prepared this surface, Pt-(001)-(1×1), by adsorbing CO to remove the reconstruction, and then O_2 ion bombarded the surface at room temperature to remove the CO, as determined by AES. The overlayer will start to dislocate at an edge of a domain, which is probably at a step or impurity atom, and proceed from there across the domain's region.[172] If the edge atoms of the domain are stabilized such as through the adsorption of CO, then the dislocations cannot form at the domain edge and propagate. Consequently, a higher temperature is expected for the formation of the reconstruction. A 5% coverage of CO at the domain edges yields an approximate domain size of 140Å or 50 Pt atoms across. This is large enough to produce the sharp LEED features seen in the patterns from the (001) surface (see Section 3-2 for details of this statement). The 450°C to 650°C FDMS peak maximum temperature at which this CO state desorbs yields a 41 to 53 kcal/mole binding energy, if the preexponential is 10^{13}. It is doubtful if the CO binding energy is more than about 30 kcal/mole, even at a step, so the preexponential factor might be lowered. Considering the large number of Pt surface atoms which may now be included in the transition complex, it should not be regarded as a first order desorption and a 10^4 lower pre-exponential factor is feasible. A UPS experiment might determine if the CO in this state is bound different (dissociated) or similar to

to the lower temperature states of CO. This could refute or confirm the above conjecture of a lowered pre-exponential factor. If the activation energies of the two processes, CO desorption and reconstruction formation, add, then a 47 kcal/mole activation energy (28 + 2/3 × 28 kcal/mole) is reasonable for either a first or second order desorption process.

On the Pt(S)-[7(100)×(111)] surface, the reconstruction is more highly strained as discussed in Section 4-4, and the activation energy for the formation of dislocations is expected to be less. The FDMS peak which is associated with the steps, the domain boundaries on the stepped surface, is at the same energy as the peak from the steps on the (111) vicinal surfaces. Thus it appears that the activation energy for reconstruction formation has been lowered to zero (less than 0.5 kcal/mole).

On the Ir-(001) surface, Rhodin, et al.[157] have found a similar behavior. They adsorbed CO to remove the reconstruction of the surface, and then carefully heated the surface to desorb the CO. This produced an Ir-(001)-(1×1) LEED pattern from the surface and no CO left on the surface as determined by AES. The temperature required to form the reconstruction on the Ir surface is approximately 1700 K[162] which is well above the temperature at which the CO desorbed. Consequently the surface temperature is not high enough to overcome the activation barrier for the formation of the reconstruction and the (1×1) remains. While on Pt the CO does not completely desorb until 500°C, well above the 150°C temperature of the spontaneous formation of the reconstruction, thus the (1×1) disappears. This is an interesting

confirmation on three surfaces of two different metal of the Frank and van der Merwe theory of dislocation formation, where a surface layer will spontaneously form dislocations if the strain is high enough, and has an activation energy at lower values of strain.[172]

5.3.3. Coadsorption of CO and H_2

When CO and H_2 are coadsorbed and immediately flashed off (within 10 min), there is no change in the CO desorption spectra from the Pt(111) vicinal surfaces. On the (001) vicinal surface, the 240°C peak fills preferentially over the 150°C peak in the presence of H_2, but does not obtain a larger total value than then CO is adsorbed alone. The amount of H_2 in the background gases in this investigation may have caused the increase in the relative size of the 240°C peak over the 150°C peak from previously reported results, and further increases in H_2 pressure over the background might not change this ratio.

The FDMS spectra of H_2 from the Pt(S)-[6(111)×(100)] and the Pt(S)-[7(100)×(111)] surfaces are shown in Fig. 5-11a and b, respectively. The desorption spectra from the (111) vicinal surfaces are very similar to those reported by Baldwin and Hudson[177] for the (111) surface. The highest temperature state at 3.9 mV (468°C) is not visible in their data on the (111) surface and may be associated with the steps. Conrad, Ertl and Latta[190] found H_2 adsorption on Pd was effected by steps. The FDMS spectra in Fig. 5-11b from the Pt(S)-[7(100)×(111)] surface have only one broad desorption peak whose maximum temperature increases from 240°C to 265°C with coverage. This increase in peak temperature is not characteristic of a second order flash desorption kinetics where the peak maximum decreases with increasing coverage.

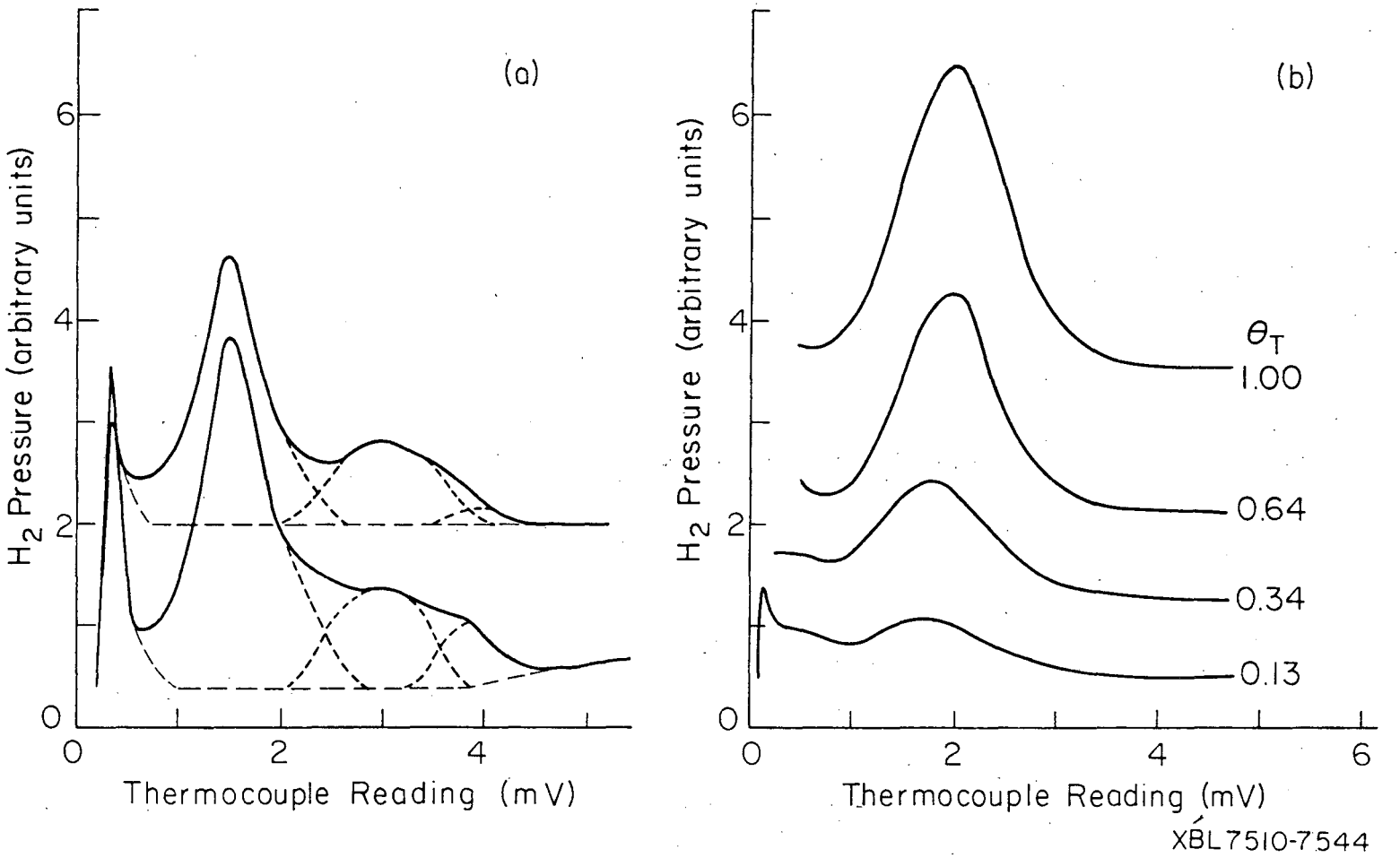

Fig. 5-11. Flash desorption mass spectra for H_2 from the (a) Pt(S)-[6(111)×(100)] and (b) Pt(S)-[7(100)×(111)] surfaces.

Thus indicating an attractive interaction of the surface and the presence of two unresolved FDMS peaks. Tracy[197] has observed both attractive and repulsive interaction of CO on the (001) surfaces of Pd, Ni and Cu, therefore, it is not surprising that H_2 and CO interact on the surface and cause shifts in the peak positions. The shape and maximum temperature of the peaks are not effected by the amount of coadsorption of CO. The sticking coefficient for H_2 on the Pt(S)-[7(100)×(111)] surface is between 0.1 and 0.01 with CO coadsorption. This is lower than the σ reported by Netzer and Kneringer[194] for pure H_2 adsorption of the Pt-(001) surface, and their FDMS peak temperature maximum was considerably lower at equivalent heating rates.

If CO is adsorbed on the Pt surfaces and then allowed to set at least 6 hr in vacuo at 25°C, a new peak appears in the CO FDMS. The major portion of the background gas is H_2 (approximately 1×10^{-9} Torr), so this state may involve the association of CO with H_2. Figure 5-12 shows the FDMS spectra of CO from the Pt(S)-[6(111)×(100)], Pt(S)-[7(111)×(310)], Pt(S)-[3(111)×(100)], Pt-(001) and Pt(S)-[7(100)×(111)]. The new peak in the spectra appears between 625°C and 825°C. The heating rate in this region is not accurately known and is non-linear; therefore, heats of desorption cannot be determined, but they are high in the range of 50 to 65 kcal/mole. H_2 also appears in the FDMS of pure CO adsorption when the sample has set in vacuo for several hours. An accurate spectrum has not been recorded, but it appears to be similar to the CO + H_2 coadsorption spectra. The large variation in the peak temperature from surface to

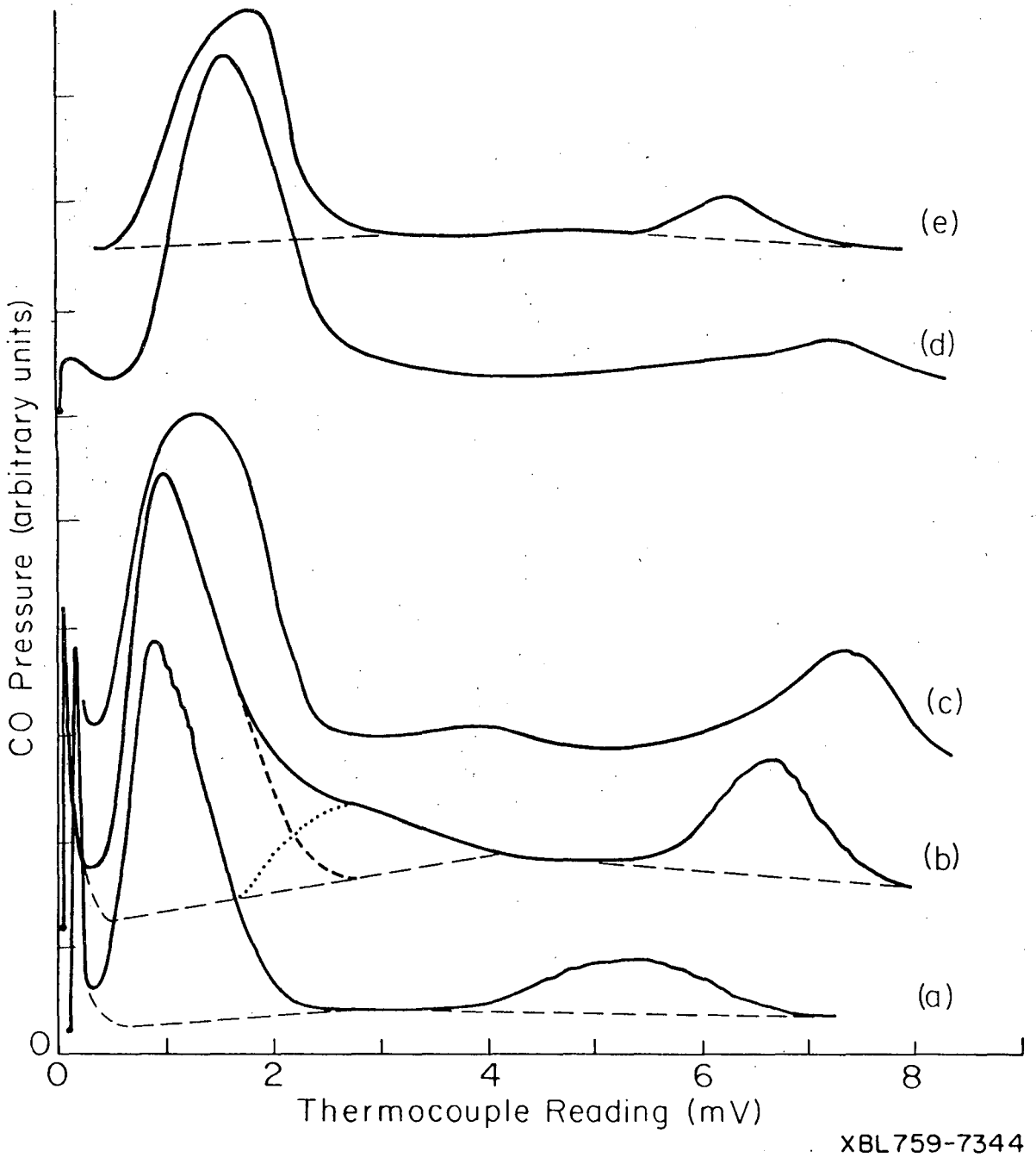

Fig. 5-12. FDMS showing the disappearance of the 270°C peak associated with the steps and its reappearance at above 600°C. (a) Pt(S)-[6(111)×(100)], (b) Pt(S)-[7(111)×(310)], (c) Pt(S)-[3(111)×(100)], (d) Pt-(001) and (e) Pt(S)-[7(100)×(111)].

surface may be from the variation in the H_2 background pressure over the period of 1-1/2 yrs, or more likely from the large non-linearities in heating rate in this temperature region. These vary greatly from sample to sample because of sample thickness and non-uniformity of spotwelds.

The (111) vicinal surfaces all have a common trait, whether they were taken with high or low H_2 background, the 250°C peak has disappeared from the spectra and reappeared at a higher (650°C +) temperature. The 150°C peak which was associated with the (111) terrace does not change in area to within the experimental error. The peak at 650°C + is slightly smaller than the corresponding peak at 250°C and a small carbon peak appears in the AES spectra of the surface after the flash. The carbon peak corresponds to about 5% of a monolayer of carbon, which is close (within experimental error) to the decrease in the flash desorption peak area. The spectrum from the Pt(S)-[3(111)×(100)] surface (curve C, Fig. 5-10) does not exactly follow this description, although it was only allowed to set 1/2 to 1 hr before the FDMS spectrum was taken. The correct trend is observed, the 250°C peak is greatly lowered and the 150°C peak is unaffected. Again the relative heights of spectra from the various surfaces cannot be compared (differences in heating rates and spectrometer gain).

The FDMS spectra from the Pt-(001) and Pt(S)-[7(100)×(111)] surfaces also display a high temperature peak when allowed to sit over night in vacuo and at room temperature. The peak at high temperature from the (001) is quite small, approximately 3% of the

total, but it is about 13% from the stepped surface. The third peak on the stepped surface which was associated with the steps is removed by setting over night, and the two peaks associated with the terrace become approximately equal in area. As on the (111) vicinal surfaces, a small amount of carbon is left on the surface after the flash desorption spectra is taken.

When the stepped surfaces covered with adsorbed CO are allowed to sit in vacuo at 25°C, a very strong interaction occurs between the H_2 which adsorbs from the background gas and the pre-adsorbed CO. Only the molecules which appear in the desorption peak associated with the step are affected, so the interaction involves both the step and the H_2. Weinberg and Merrill[198] calculated that the activation energy for CO dissociation on Pt-(111) was at least 58 kcal/mole, above the molecular adsorbed state, consistant with the experimental result that CO does not dissociate on Pt(111). The activation energy of dissociation at a step would have to be about 23 to 24 kcal/mole for the dissociation to occur in 6 hr. If the activation energy was 24 kcal/mole at a step, there would be appreciable dissociation during a flash desorption done immediately after the adsorption. Most of the H_2 desorbs from the surface around 200°C while the CO associated with the steps does not desorb until about 270°C; this leaves little H_2 on the surface to interact with the CO at a temperature where the rate would be fast during the flash desorption. Consequently, there is no detectable dissociation when coadsorbed H_2 and CO are flashed off immediately.

The possible roll of the H_2 is now considered. The H_2 may have an indirect affect on the CO through the rehybridization of the Pt orbitals at the step. The hybridization may change at a step because of the change in symmetry of the crystal field around the Pt atoms at the step.[199] The combined effects of binding with CO and H could further modify the Pt orbitals making CO dissociation an energetically more favorable process. This is not thought to be a large effect in the system and it is doubtful if this could cause the 25 kcal/mole reduction in activation energy. A direct effect of the H atoms on the CO molecules could be through the formation of a chemical bond with the CO. By a simple bond energy-bond order calculation[196,200,201] it can be shown that an alcoholate intermediate species will lower the activation energy for dissociation of the CO.

The proposal of an alcoholate intermediate species is reasonable, for the Fischer-Tropsch (F-T) synthesis reactions are thought to proceed through an alcoholate intermediate species on transition metal catalysts.[202] Pt is a poor F-T reaction catalyst[203] and produces few long chain products. It is interesting to note that Sexton[204] observed a very high temperature flash desorption peak from CO adsorbed on a Ni-(011) surface after the sample set a few hours in vacuo and Joyner[205] observed CO dissociation on Fe foils in less than 1/2 hr. In these three examples, Pt, Ni and Fe, the ability of the metal to perform F-T reactions[203] is inversely proportional to the amount of time required to dissociate the adsorbed CO. There should be a marked particle size effect for the F-T reaction on Pt and any other metal requiring a similar initiation step. The Pt(111)

surface will dissociate CO extremely slowly, if at all; the (001) may dissociate CO very slowly, and steps on the surface should perform practically all the reaction. Thus with changes in particle size, the step density would vary and also the reaction rate.

Vannice [55] has found a marked particle size effect on the ability of Pt catalyze the production of methane from CO and H_2. The rate decreased over two orders of magnitude in going from a 12Å diameter particle to a Pt black with 4000Å diameter particles. He attributes this change in reaction rate to a change in the adsorption energy of the CO. From infrared adsorption work[206] and kinetic studies[203] he concluded that a more weakly bonded CO species is necessary for the high reaction rate, and that this species predominates on very small particles of Pt. The increased rate on small particles is predicted from the flash desorption results, but from a more strongly bound species. This discrepancy is not readily explained.

5.4. Summary

Carbon monoxide has been found to adsorb more strongly at a step than on either the (111) or the (001) terrace of a Pt surface. The binding energy is about 5 kcal/mole higher at a monatomic height step than on the terrace of (111) vicinal surfaces and about 1 kcal/mole higher at a monatomic height step than on the terrace of the (001) vicinal surfaces of Pt. No effect has been found of the step orientation on the heat of desorption of CO; the (001), (111) and (013) step orientations all have the same increase in binding energy over the (111) terraces.

Four flash desorption mass spectra peaks have been found on the Pt-(001) vicinal surfaces. The lower two peaks are associated with the terraces and may be a result of CO-CO interactions on the surface and occur at 24 and 28 kcal/mole. The third peak, which is found on stepped surfaces only, has a binding energy of 29 kcal/mole, the same as produced by the same step geometry on the (111) vicinal surfaces. The high temperature state on the Pt-(001) surface is associated with the reformation of the reconstruction of the (001) face of Pt. This is not present on the stepped surface because of the higher strain associated with the reconstruction on the step terraces.

The interaction of CO adsorbed at a step with the ambient H_2 causes the dissociation of the CO molecule through the formation of an alcoholate intermediate. This species may be important in the Fischer-Tropsch synthesis reactions.

6. CATALYTIC REACTIONS OF HYDROCARBONS ON Pt STEPPED SINGLE CRYSTAL SURFACES

6.1. Introduction

One of the important aims of studies of hydrocarbon catalysis is to uncover the sites where C-H, C-C and H-H bonds are broken followed by suitable rearrangements of the hydrocarbon fragments. Identification of these active centers might permit the architecture of catalyst surfaces with optimum concentrations of surface sites with a variety of bond breaking activities.

The dehydrogenation and hydrogenolysis of cyclohexane (CH) and cyclohexene (CH=) were studied on platinum single crystal surfaces at low pressures (about 10^{-6} Torr (1 Torr = 133.3 N/m^2)) to find the correlation between the reactivity and the atomic surface structure. Two such surface sites have been discovered and identified on platinum crystal surfaces that differ in the number of nearest neighbor platinum atoms surrounding them. H-H and C-H bond breaking processes predominate at one of the sites while C-C bond breaking occurs in addition to breaking H-H and C-H bonds at the other. During the catalytic reactions the platinum surface is partially or completely covered with a layer of carbonaceous deposit, ordered to disordered, whose properties play a significant role in determining both the resistance to poisoning and product distribution during the catalytic reactions.

The reactions of cyclohexane and cyclohexene are well suited for identifying active surface sites with various bond breaking activities for several reasons. The dehydrogenation occurs rapidly at relatively

low temperatures and at low partial pressures of hydrogen, since it is thermodynamically favored at these conditions. Since dehydrogenation requires only C-H bond breaking activity, the effectiveness of the platinum crystal surfaces to breaking C-H bonds could be investigated in a systematic manner. The appearance of hydrogenolysis products such as n-hexane would signal the presence of sites with C-C bond breaking activity. Since the mass spectra of benzene and n-hexane are readily distinguishable from cyclohexane both the dehydrogenation and hydrogenolysis activity of a given crystal face were readily monitored using a quadrupole mass spectrometer.

The dehydrocyclization of n-heptane (Hp) to toluene (T) has been studied at 1×10^{-4} Torr total pressure to find a correlation between the reaction rate and the surface structure and composition of the catalyst. It has been found that for this complicated structural rearrangement of the organic molecule to occur, an ordered carbonaceous overlayer is required on the catalyst. On Pt metal structures which promote the formation of this ordered residue, a significant amount of T is produced, while on surfaces where the residue is disordered, a much smaller amount of toluene forms.

The isomerization of n-butane (B) to isobutane (iB) has been studied only slightly. This reaction gives information of the bond shifting ability of various surface structures, which is not as readily available from the two previous reactions. However, to obtain accurate data a much higher reaction rate is required than in the other reaction systems (see Section 2.3.5). Thus, little information was acquired on this important class of reactions. This study has

concentrated on the dehydrogenation reaction since it is agreed that the metal exclusively performs the dehydrogenation in an industrial catalyst.[207,1] Almost all the combinations of low index planes of Pt have been studied to determine their catalytic activity. The structure and stability of these surfaces is known and has been characterized (see Chapter 4). All of the surface configurations studied may not be present on the actual metal particle in a supported catalyst, but if the activity of all types of configurations is characterized the most probable surface structure of the small metal particles may be hypothesized.

6.2. Equilibrium of Hydrocarbons at Low Pressure

The equilibrium ratio of hydrocarbon partial pressures can be drastically different at the low pressures ($<10^{-6}$ Torr) of this investigation than at atmospheric pressure, if there is addition or subtraction of hydrogen during the reaction. The equilibrium constants are of course the same, but, the partial pressure of H_2 is also in the pressure term. The pressure of H_2 may be raised to as high as the fourth power ($Hp \rightarrow T + 4H_2$) and is a very small number, approximately 10^{-9} atm, in these studies.

6.2.1. Cyclohexane Reaction System

The equilibrium constants as a function of temperature[208] for the six membered ring dehydrogenation system are shown in Fig. 6.1. The standard conditions used in this investigation are 4×10^{-8} Torr of the reactant and 8×10^{-7} Torr of H_2. For CH as the reactant, the equilibrium pressure of the various products at 150°C is 1×10^{-13} Torr of Hx, 1×10^{-5} Torr of CH=, and 8×10^{13} Torr of Bz. Obviously, if kinetically allowed, the CH would convert entirely to benzene at this

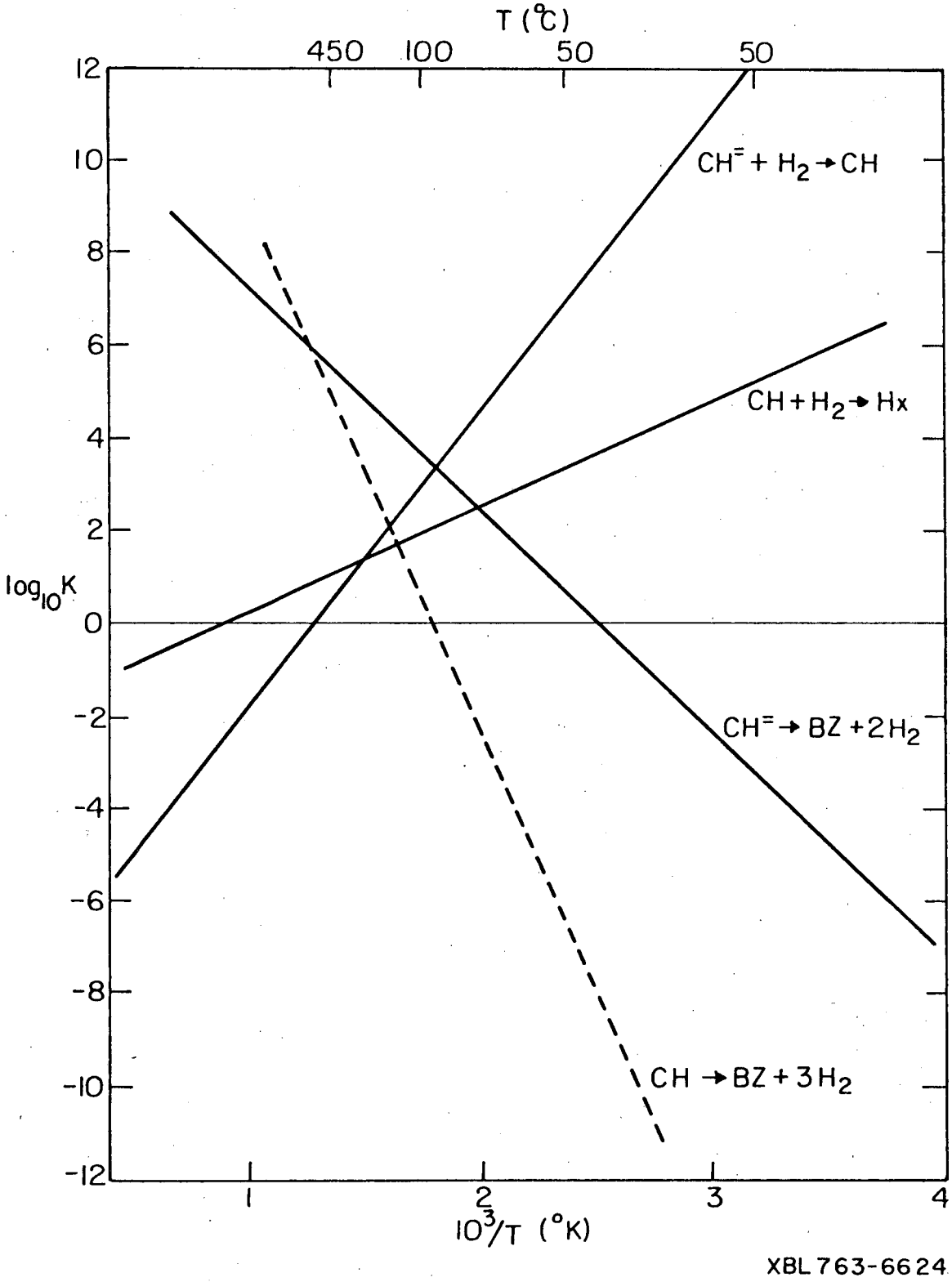

Fig. 6-1. Equilibrium constant variation with temperature for cyclohexane-cyclohexene-benzene-hydrogen system (from Ref. 208).

low pressure of H_2. At one atmosphere of H_2 and 150°C, the equilibrium conversion of Bz is nill ($Bz/CH \approx 5\times10^{-7}$). Table 6-1 shows what hydrogenolysis products are thermodynamically possible from CH in the temperature range of these experiments and a 20:1 hydrogen to hydrocarbon ratio. The hydrogenolysis equilibrium of the cycloparaffin to all paraffinic products is decreased at low total pressure (P_T^{-1}), and the equilibrium to all olefinic products is increased at low pressure (P_T^1). If the product was produced at a rate of 10^{-5} mol/sec/surface atom, its partial pressure in the reaction chamber, at the average pumping speed for most runs, would be 1.5×10^{-10} Torr. Benzene is produced at a rate of 10^{-5}/sec on most surfaces. Thus, it can be seen that the olefinic as well as paraffinic products would be produced in large quantity over the whole range of temperature studied. Table 6-2 shows the effect of temperature on the cyclohexene product distribution. Table 6-3 shows the effect of H_2 pressure on the equilibrium pressures of the various products from a cyclohexane pressure of 4×10^{-8} Torr and a 150°C temperature. Ethylene (E=) and propylene (P=) are equally favorable with ethane (E) and propane (P), respectively, at a 20:1 hydrogen to hydrocarbon ratio, but the paraffins become favorable at the higher pressures of H_2.

6.2.2. Isomerization Equilibria

The isomerization equilibrium is independent of pressure since the number of products and reactant moles are the same. Figure 6-2 shows the equilibrium constant for the isomerization of isobutane to butane and isopentane to n-pentane.[208] Starting with either the pariffin or the branched molecules there should be substantial

Table 6-1. Equilibrium pressure of products from cyclohexane (4×10^{-8} Torr) and hydrogen (8×10^{-7} Torr).

T	CH_4	C_2H_2	C_2H_4	C_2H_6	C_3H_6	C_3H_8	C_6H_6	C_6H_{10}	C_6H_{12}	C_6H_{14}
	M	Ac	E=	E	P=	P	Bz	CH=	CH	Hx
300°K	3×10^{2}	10^{-24}	8×10^{-11}	4×10^{-2}	6×10^{-11}	5×10^{-5}	4×10^{2}		4×10^{-8}	
500°K	3×10^{-2}	10^{-5}	10^{-5}	8×10^{-6}	10^{-5}	5×10^{-7}	10^{17}		4×10^{-8}	
700°K	2×10^{-4}	10^{3}	10^{-2}	3×10^{-7}	10^{-3}	10^{-9}	10^{24}		4×10^{-8}	

Table 6-2. Equilibrium pressure of products from cyclohexene (4×10^{-8} Torr) and hydrogen (8×10^{-7} Torr).

T	CH_4	C_2H_2	C_2H_4	C_2H_6	C_3H_8	C_6H_8	C_6H_6	C_6H_{10}	C_6H_{12}	C_6H_{14}
	M	Ac	E=	E	P=	P	Bz	CH=	CH	Hx
300°K	10^{3}	10^{-31}	10^{-8}		10^{-8}	10^{5}		4×10^{-8}		
500°K	7×10^{-3}	10^{-15}	10^{-4}		10^{-6}	10^{-2}		4×10^{-8}		
700°K	3×10^{-5}	10^{-8}	10^{-3}		10^{-5}	10^{-12}		4×10^{-8}		

Table 6-3. Equilibrium pressure of products from CH (4 10^{-8} Torr) and 150°C.

H_2/HC	CH_4 M	C_2H_2 Ac	C_2H_4 E=	C_2H_6 E	C_3H_6 P=	C_3H_8 P	C_6H_6 Bz	C_6H_{10} CH=	C_6H_{12} CH	C_6H_{14} Hx
20:1			12×10^{-6}	9×10^{-5}	6×10^{-7}	3×10^{-7}				
100:1			12×10^{-6}	5×10^{-4}	6×10^{-7}	1×10^{-6}				
300:1			12×10^{-6}	1×10^{-3}	6×10^{-7}	4×10^{-6}				

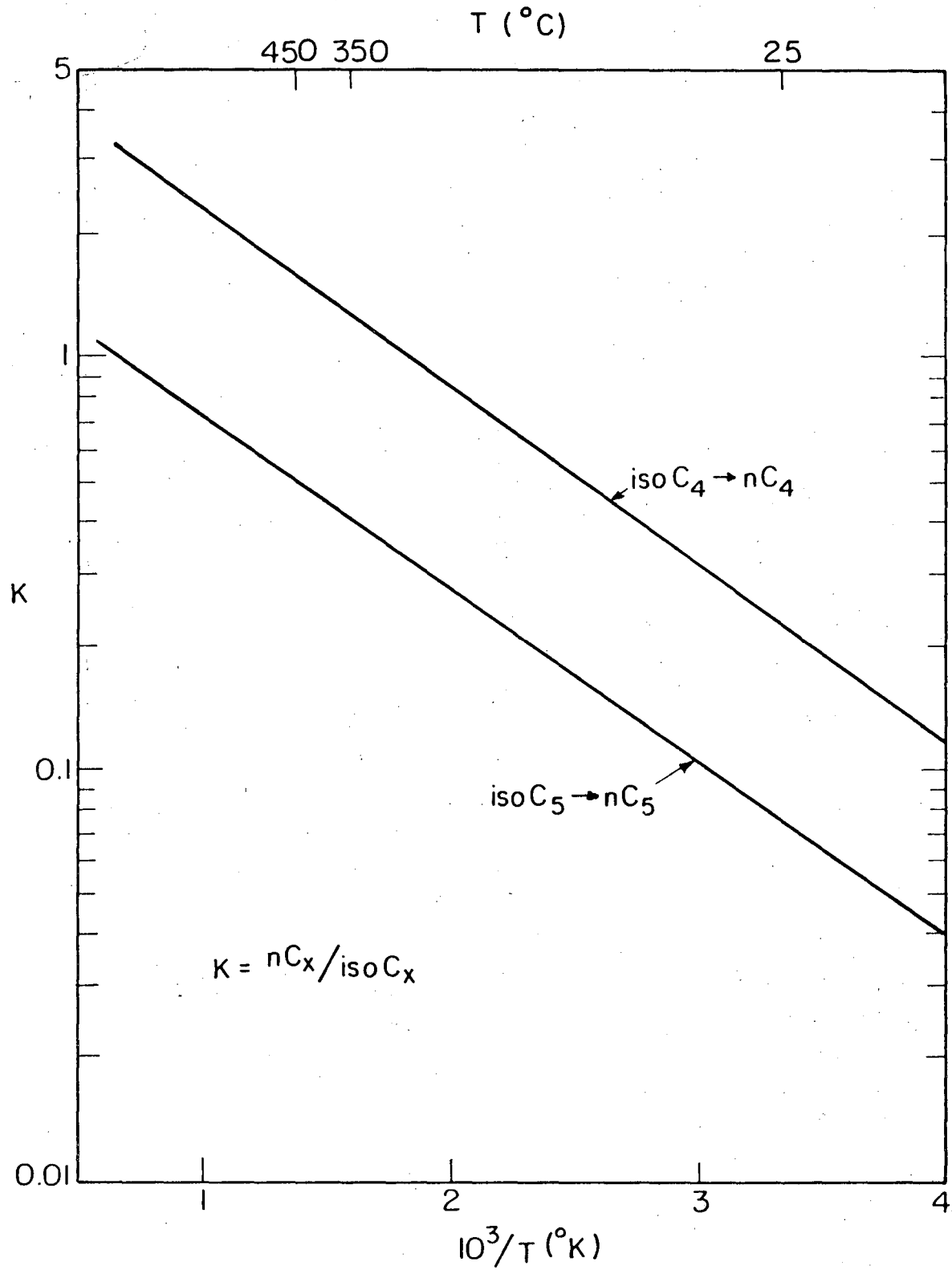

XBL 763-6628

Fig. 6-2. Equilibrium constant variation with temperature for isobutane-n-butane system (from Ref. 208).

conversion allowed by thermodynamics over the temperature range of this study.

6.2.3. Dehydrocyclization Equilibria

The aromatic product, toluene, is highly favored thermodynamically over n-heptane reactant at the H_2 pressures in this investigation, similar to Bz over CH. The hydrogenolysis products are, as in the CH system, producible in large quantities under the experimental conditions. In this case, the hydrogenolysis equilibrium to all paraffins is independent of the total pressure. The ultimate equilibrium of these systems is not known, but probably consists of mainly the aromatic and some ethylene and methane.

6.3. Experimental

The details of the experimental method of obtaining the rates of reactions are given in Chapter 2. Both the flow and batch reactor configurations described in Chapter 2 have been used, but predominantly the flow system. The batch reactor is more sensitive (can detect lower reaction rates), but is much less versatile. To ascertain if a true catalytic process is occurring (see Appendix A), the use of a flow reactor with its more readily determined surface coverage, composition and structure is desirable. The flow type reactor configuration has been used for all the CH dehydrogenation experiments and all the butane isomerization experiments, and for a few of the n-heptane dehydrocyclization experiments.

6.4. Results

The experimental results for each type of hydrocarbon reaction, dehydrogenation, dehydrocyclization, and isomerization, will be discussed separately. The results for hydrogenolysis of each type of hydrocarbon will be included in the section on primary reaction of that molecule.

6.4.1. Dehydrogenation Reactions

6.4.1.1. Introduction. The dehydrogenation of cyclohexane, cyclohexene, and cyclohexadiene on the Pt(111) crystal face has recently been studied by Gland, Baron, and Somorjai.[209] The (111) crystal face of platinum is catalytically quite inactive; it apparently lacks the active sites that must be present in large enough concentration for efficient dehydrogenation and hydrogenolysis. Both cyclohexane and cyclohexene were maintained on the surface without much dehydrogenation at 300°K and their ordered surface structures were identified. Cyclohexadiene, however, instantaneously dehydrogenated to benzene even on this inactive platinum surface. The rate-limiting steps in dehydrogenating cyclohexane to benzene was the dehydrogenation of the cyclohexene intermediate. The Pt(111) crystal face will not dehydrogenate cyclohexane beyond cyclohexene even at higher temperatures (>425°K).

In this section it is shown that the reactivity of cyclohexane and cyclohexene is entirely different on platinum surfaces with a high concentration of atomic steps than it is on the (111) crystal face; in this case these molecules dehydrogenate readily. Atomic steps, which were found responsible for breaking H-H bonds in studies of hydrogen-deuterium exchange,[36] were also effective in breaking the

C-H bonds. It appears that atomic steps are the active sites on platinum surfaces for performing these important bond scissions. The atomic surface structures where C-C bond scissions occur efficiently, in addition to C-H and H-H bond scissions, have been identified as kinks in steps. The quantitative reaction rates (as turnover numbers) for dehydrogenation and hydrogenolysis were determined and correlated with the various atomic surface structures. Thus, the structure insensitivity of the cyclohexane to cyclohexene dehydrogenation reaction, and the structure-sensitivity of the dehydrogenation of cyclohexene and hydrogenolysis of cyclohexane have been established.

6.4.1.2. Catalyst Samples Studied. The orientation of the samples used in the CH system investigation are shown in Fig. 6-3 on a stereographic projection unit triangle. The surfaces are listed in Table 6-4. The first seven samples differ only in the step density and the number of kinks in the steps; all catalysts have (111) orientation terraces and monatomic height steps. The first three samples are cut on the [110] zone and have (001) orientation steps. The fourth, fifth and sixth samples were obtained by cutting the crystal rod off the [110] zone toward the $[0\bar{1}1]$ zone. The seventh sample was cut on the [011] zone and had steps of (111) orientation. The eighth and ninth samples were cut to expose the (001) orientation terraces. The (001) orientation surface of platinum reconstructs to form a buckled hexagonal layer of Pt atoms atop of the square bulk lattice characterized by a $\begin{vmatrix} 5 & -3 \\ 1 & 13 \end{vmatrix}$ low-energy electron diffraction pattern (see Section 4.4). These samples are stable in the monatomic height step configuration, but facet readily in the presence of

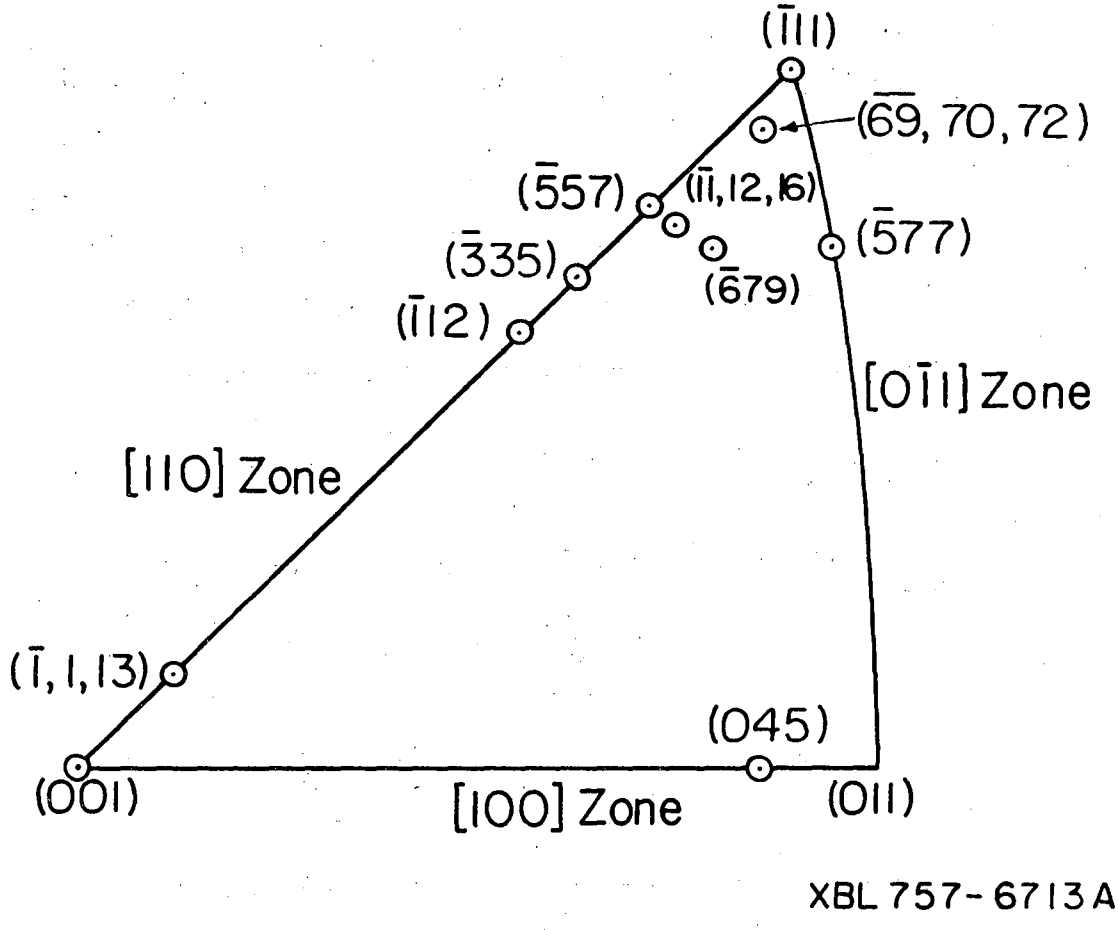

Fig. 6-3. Crystallographic orientation and Miller Index of the pltainum single crystal catalyst surfaces studied.

Table 6-4. Angle of cut, Miller indices and designation of stepped platinum surfaces.

Angle of Cut	Miller Index	Designation
0° from $(\bar{1}11)$	$(\bar{1}11)$	Pt-(111)
9.5° from $(\bar{1}11)$	$(\bar{5}57)$	Pt(S)-[6(111)×(100)]
19.5° from (111)	$(\bar{1}12)$	Pt(S)-[3(111)×(100)]
9.5° from $(\bar{1}11)$ rotated 7°	$(\bar{1}\bar{1},12,16)$	Pt(S)-[6(111)×(710)]
9.5° from $(\bar{1}11)$ rotated 20°	$(\bar{6}79)$	Pt(S)-[7(111)×(310)]
4.2° from $(\bar{1}11)$ rotated 20°	$(\bar{6}\bar{9},70,72)$	Pt(S)-[13(111)×(310)]
9.5° from $(\bar{1}11)$ rotated 30°	$(\bar{5}77)$	Pt(S)-[6(111)×(111)]
6.2° from (001)	$(\bar{1},1,13)$	Pt(S)-[7(100)×(111)]
0° from (001)	(001)	Pt-(001)
6.3° from (011)	(045)	Pt(S)-[8(110)×2(100)]

oxygen to (001) and ($\bar{1}$13) orientation terraces (see Section 4.2). The tenth sample was cut along the [100] zone and was stable in a double height step configuration (see Section 4.2). The diffraction patterns from these various surfaces can be seen in Fig. 4-2 through Fig. 4-7.

6.4.1.3. The Dehydrogenation and Hydrogenolysis of Cyclohexane. Effect of Hydrogen Pressure. In a series of studies, we have determined the variation of the turnover number, the number of product molecules per platinum surface atoms second, with the hydrogen to hydrocarbon ratio at a constant hydrocarbon pressure of 4×10^{-8} Torr. The results are shown in Fig. 6-4 for the several stepped surfaces studied. The variation is very similar for all catalyst surfaces. The reaction rates increase with increasing hydrogen to hydrocarbon ratio. If no hydrogen is introduced into the reaction chamber the catalyst behaves very differently. No benzene is produced and cyclohexene production is reduced greatly. There is approximately one monolayer of carbonaceous residue on the surface, which is greater than normal. Pretreating the catalyst in hydrogen and then removing it prior to hydrocarbon introduction does not increase the activity for dehydrogenation or hydrogenolysis.

The turnover number for various hydrogenolysis products is shown in Table 6-5 at constant hydrocarbon pressure of 4×10^{-8} Torr and a 150°C catalyst temperature for a few of the samples studied. The ($\bar{1}$11) surface and the Pt(S)-[8(110)×2(100)] are seen to be quite inactive for hydrogenolysis as compared to the other surfaces. It must be remembered that the rates reported are calculated using ionization gauge pressures, so the absolute rates to various hydrocarbon species

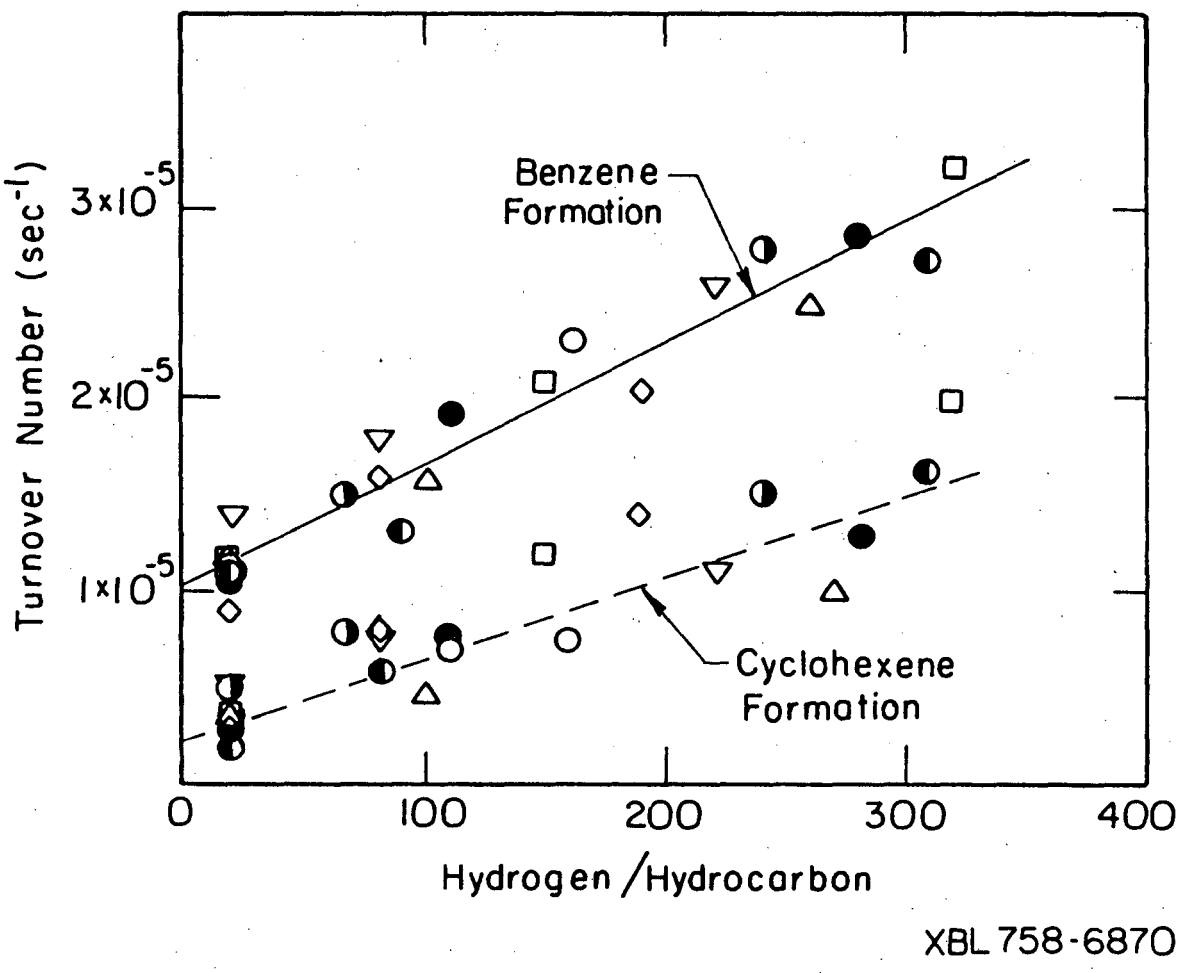

Fig. 6-4. Initial steady state rate of Bz (———) and $CH^{=}$ (---) from CH. The reaction conditions are 4×10^{-8} Torr of CH and 423°K catalyst temperature (Δ-Pt(S)-[7(100)×(111)]; □-Pt(S)-[3(111)×(100)]; ○-Pt(S)-[6(111)×(100)]; ◐-Pt(S)-[6(111)×(710)]; ●-Pt(S)-[7(111)×(310)]; ◑-Pt(S)-[13(111)×(310)]; ▽-Pt-(001); ◇-Pt(S)-[8(110)×2(100)]).

Table 6-5. Rate of hydrogenolysis product formation from 4×10^{-8} Torr of CH and 150°C surface temperature (all rates are turnover numbers in units of 10^{-5} sec^{-1}).

	M	E=	E	P=	P	H_2/He
Pt-(111)	10	0.5	1	1.5	0	20
	100	10	2	2	2	90
	200	5	50	15	25	260
Pt(S)-[7(111)×(310)]	20	ND	9	10	30	20
	560	ND	60	20	35	110
	1200	ND	130	40	85	280
Pt(S)-[8(111)×2(100)]	1.0	1.5	1	0	0	20
	60	3	30	1	2	80
	150	10	45	6	20	190
Pt-(001)	10	2	1	18	65	20
	200	200	35	20	75	80
	450	450	85	30	95	220
Pt(S)-[7(100)×(111)]	10	ND	2	5	5	20
	150	ND	20	11	40	100
	650	ND	95	20	90	270
	(±40)	(±10)	(±15)	(±10)	(±30)	Relative Error

cannot be compared accurately. The rates between catalyst samples of the same product may be compared using the relative error figures at the bottom of Table 6-5 as a guide. The kinked step surface, Pt(S)-[7(111)×(310)], appears to the most active hydrogenolysis catalyst, at least for the production of alkanes. The (001) surface has a very high rate of production of E=, however, without further supporting data, the validity of this very high rate on (001) surfaces cannot be confirmed. For the rest of the reaction products, the (001) and the Pt(S)-(7(100)×(111)] surfaces have an intermediate hydrogenolysis ability, greater than the ($\bar{1}$11) and less than the Pt(S)-[7(111)×(310)].

Effect of catalyst surface structure. Results of the reaction rate studies for dehydrogenation and hydrogenolysis obtained on stepped platinum surfaces are presented first. Then the same rate data obtained for stepped surfaces which have a large concentration of kinks in the step is proffered. In Fig. 6-5a the turnover numbers for dehydrogenation to benzene and 20 to 1 hydrogen to hydrocarbon ratio and hydrogenolysis to n-hexane at 300 to 1 hydrogen to hydrocarbon ratio are shown as a function of step density at 423°K. The dehydrogenation rate is independent of step density, while the hydrogenolysis rate increases with increased step density. The hydrogenolysis rate that was measured via the rate of formation of n-hexane, one of the hydrogenolysis products, was lower than the rate of dehydrogenation to benzene.

The peak used to determine the amount of Hx produced is a very small peak in the spectrum, mass 84, and is subject to measurement error. It is, however, very convenient for the determination of the amount of Hx in that there is only one other overlapping cracking pattern,

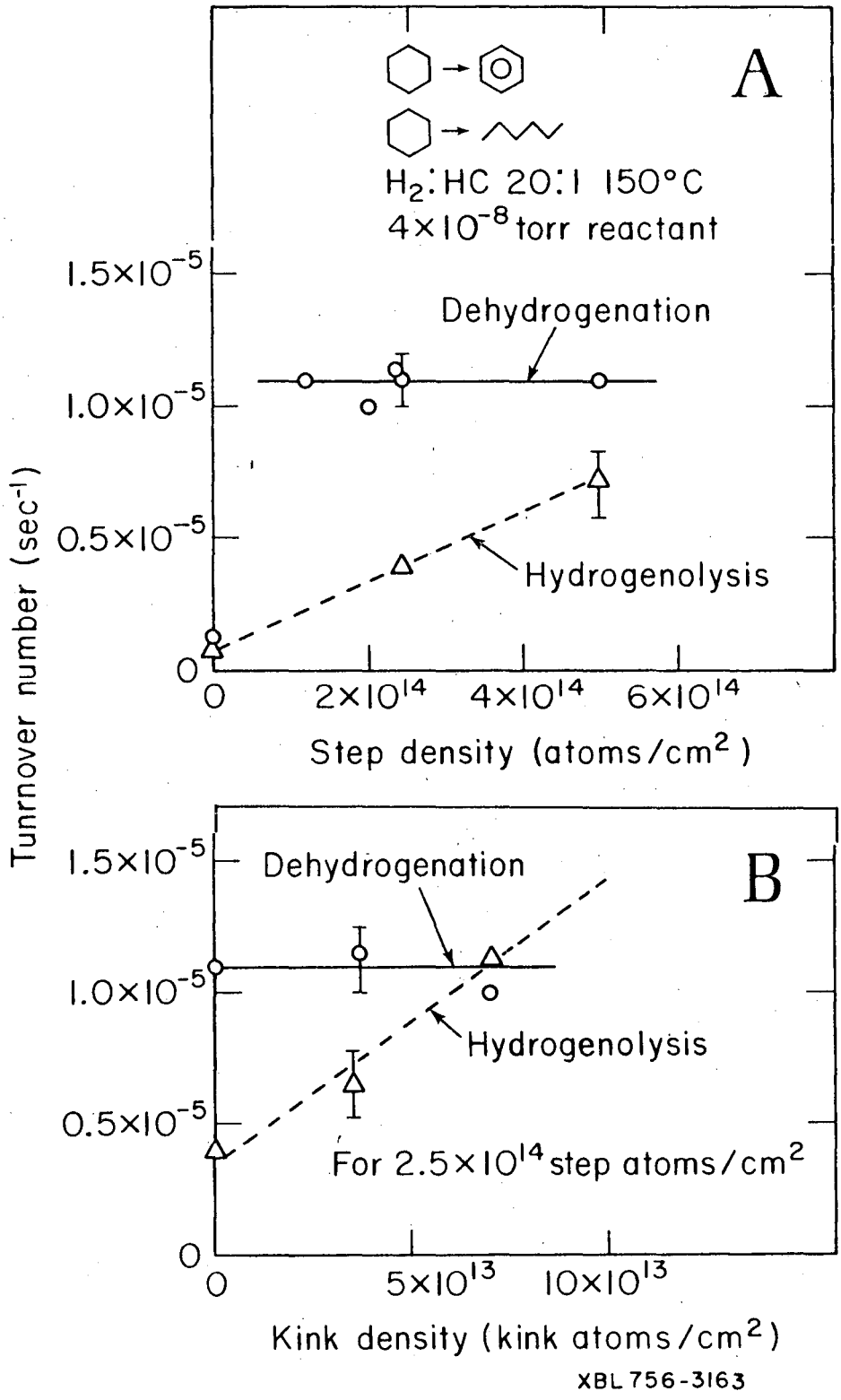

Fig. 6-5. CH dehydrogenation to Bz (-O-) and hydrogenolysis to Hx(-Δ-) as a function of (a) step density and (b) kink density.

that of CH. From a large number of measurements (~200) on many different runs (~25), the standard deviation for the measured rate of hydrogenolysis to Hx is $\pm 0.65\times10^{-6}$/sec. Using this value as the true standard deviation and measuring the rate as a function of H_2 pressure to obtain values for the rate which are much larger than the error limit, allows confident values of the rate to be reported at constant H_2 pressure.[210] Values obtained in this manner are used in Fig. 6-5 for the Hx rates of reaction. The details of this calculation are given in Appendix E.

The turnover numbers for dehydrogenation and hydrogenolysis on kinked surfaces are shown in Fig. 6-5b. The kink density is defined as the number of kink sites per square centimeter (the total number of atoms on the surface is approximately $1.5\times10^{15}/cm^2$). For example, on the Pt(S)-[7(111)×(310)] surface, every third atom along the step should, on the average, be in a kink position. Therefore, for this surface the step density is $2.0\times10^{14}/cm^2$ and the kink density is approximately $7\times10^{13}/cm^2$. By comparing the turnover numbers with those obtained from stepped surfaces that were shown in Fig. 6-5a, it appears that the rate of hydrogenolysis is markedly higher in the presence of kinks. An obvious way to make this comparison is through the slope of the curves for the hydrogenolysis rate in Fig. 6-5a and Fig. 6-5b. The slopes give 2.5×10^{-4} molecules/kink atom/sec and 2×10^{-5} molecules/step atom/sec. Thus a kink atom is about an order of magnitude more effective in breaking C-C bonds than is a step atom. The dehydrogenation rate is approximately constant and remains unaffected by variation of kink density while the hydrogenolysis rate

increases by an order of magnitude from a surface free of steps, Pt(111). The kinks in the stepped surface appear to be very effective in breaking C-C bonds leading to much enhanced hydrogenolysis rates.

The molar hydrogenolysis product distribution of smaller saturated aliphatic hydrocarbons, appears to be Hx:P:E:M = 1:6±3:1±1:10±10. Even through n-hexane is a minority hydrogenolysis product, it is a reliable measure of the degree of hydrogenolysis because of its ease of mass spectrometric detection and because it is not formed in a background reaction with the walls of the reaction chamber. The product distribution of saturated hydrocarbons does not seem to vary with surface structure to within experimental error on the samples studied. Much less data is available on these hydrogenolysis products than with Hx so the error in the reported rates is much larger.

Besides the saturated hydrogenolysis products and benzene, we find the olefinic products, cyclohexene, ethylene, and propylene. Cyclohexene is an intermediate in the dehydrogenation to benzene and its various reactions will be discussed separately in the next section. The olefinic product distribution varies with the surface structure. From the limited data, the ratio on $(\bar{1}11)$ vicinal surfaces of Bz:CH=:P=:E= is 2:1:3:4 and on the (001) surface the ratio is 2:1:3:8. A larger production of ethylene on the (001) is also observed at low H_2 pressure as well as at higher H_2 pressures. The various rates are shown in Table 6-6.

The rate of benzene and cyclohexene production on the (001) and (011) vicinal surfaces is the same as on the (111) vicinal surfaces shown in Fig. 6-5. Preliminary data[211] on the Pt(S)-[6(111)×(111)]

Table 6-6. Hydrogenolysis products from CH 4×10^{-8} CH, 8×10^{-7} H_2 (all rates are turnover number in units of 10^{-5}/sec).

Sample	CH_4	C_2H_4	C_2H_6	C_3H_6	C_3H_8	T(°C)
(111)	0	4	0	0	6.	25
	6	3	1	0	7	150
	4	7	2	0	4	300
	6	2	1	0.5	3.5	450
7(111)×(310)	0	4.5	1	3	6.	25
	6.5	4	1	1.5	0	150
	8.	1.5	1.5	1	6.	300
	9.	2.	2	2.5	3.	450
8(110)×2(100)	0	4	2	5	6	25
	1	3	3	3	5.5	150
	1	1±2	2.5	3	5	300
	4.5	4	4	3	8.5	450
(001)	1	9	0.5	2	2	25
	7	7.5	1	1.5	2	150
	6	4	1	1	4	300
	6	1.5	1.2	0	4	450
7(100)×(111)	1	3	4.5	3.5	10	25
	3	2	3.5	1.5	11	150
	2	3	0	2	14	300
	4	0	5	0	13	450
Error	±4	±1	±1.5	±1	±3	

surface indicate that it behaves very similarily to the ($\bar{1}11$) surface, in that it is catalytically inactive. The hexagonal close-packed ($\bar{1}11$) surface apparently cannot break the C-H bond efficiently. The hydrogenolysis rate increases with kink density just as with increasing step density, thus, hydrogenolysis appears to be structure-sensitive.

There was always an induction period of 10 to 20 min before the benzene product reached its steady state rate of production as detected by the mass spectrometer after the introduction of cyclohexane onto the crystal surface. This is shown in Fig. 6-6 for several catalyst temperatures on the Pt(S)-[6(111)×(100)]. The catalyst was initially at 300°K. When steady state reaction rates were obtained, the catalyst temperature was rapidly increased (in approximately 30 sec) to 423°K and the reaction rate monitored. This was repeated with heating to 573°K and 723°K. The benzene desorbed during rapid heating of the catalyst surface is approximately 1×10^{13} molecules or less and represents only a small fraction of the carbon on the surface. The steady state reaction rates at a given temperature are the same whether the catalyst was initially at that temperature or another. This induction period coincides with a higher than steady state uptake of cyclohexane as seen in Fig. 6-6. A mass balance calculation on carbon, utilizing the known adsorption and desorption rates of reactants and products during the induction period indicated carbon was deposited on the surface. The amount calculated agreed reasonably well with that determined by the Auger electron spectra taken after the reaction mixture was pumped from the chamber, since the electron beam may induce polymerization of hydrocarbons and further carbon deposition.

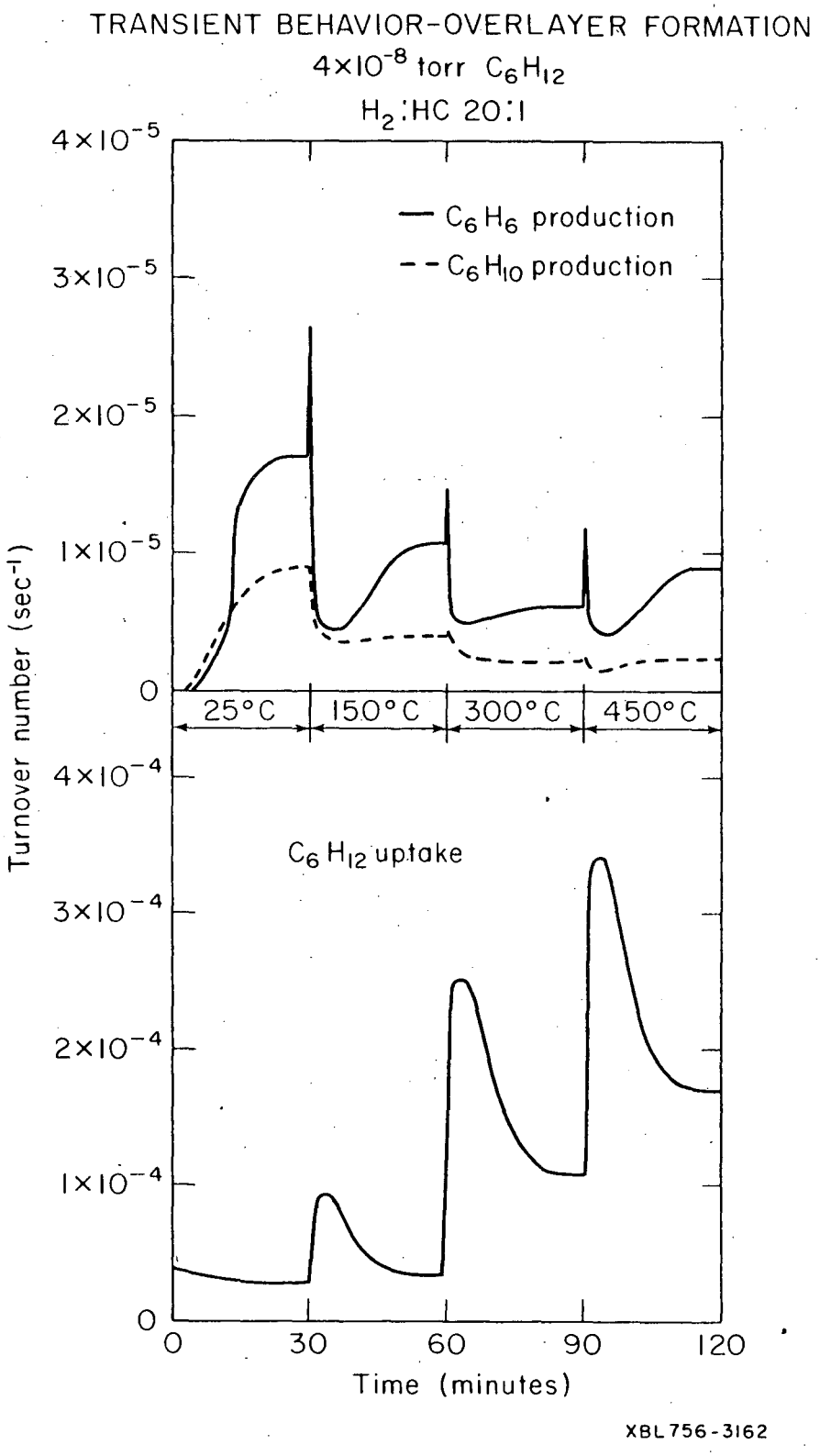

Fig. 6-6. Induction period for production of Bz (——) and CH (---) from CH. H_2:CH ratio 20:1; CH pressure 4×10^{-8} Torr; Pt(S)-[6(111)×(100)].

The formation of the adsorbed carbon layer always precedes the desorption of benzene and olefinic products. However, the amount of adsorbate changes as a function of temperature. This is shown in Fig. 6-7 for the Pt(S)-[6(111)×(100)] surface. A 4:1 ratio of the carbon 274 eV Auger peak to the platinum 238 eV Auger peak corresponds to a complete monolayer of carbon by calibration with acetylene. The carbon coverage ranges from 0.1 monolayer at 300°K to almost 1.0 monolayer at 723°K. The line has a slope of 2±0.2 kcal/mole. During and after reaction this carbon deposit was always present on the surface not only at low pressure reaction conditions, but also after reactions that were carried out in another apparatus at higher pressures[34] (approximately 200 Torr total pressure).

The rate of production of benzene, CH= and rate of uptake of CH is similar on all the surfaces studied to that shown in Fig. 6-6 for the Pt(S)-[6(111)×(100)]. The (111) vicinal surfaces, the first five surfaces listed in Table 6-4, all show identical trends. The steady state hydrogenolysis rate to saturated products, as shown in Fig. 6-8 for the Pt(S)-[6(111)×(100)] surface, increases with temperature with the same slope of 3±0.3 kcal/mole. The absolute value of the rate at a given temperature varies with the step and kink density on the surface in the manner already discussed for Hx production. The cyclohexane uptake and consequently the amount of carbon on the catalyst surface increase with temperature with a 2 kcal/mole slope as is shown in Fig. 6-7 for the Pt(S)-[6(111)×(100)]. A few hundredths of a monolayer of benzene is flashed off the surface upon heating, with the largest desorption occurring with heating from

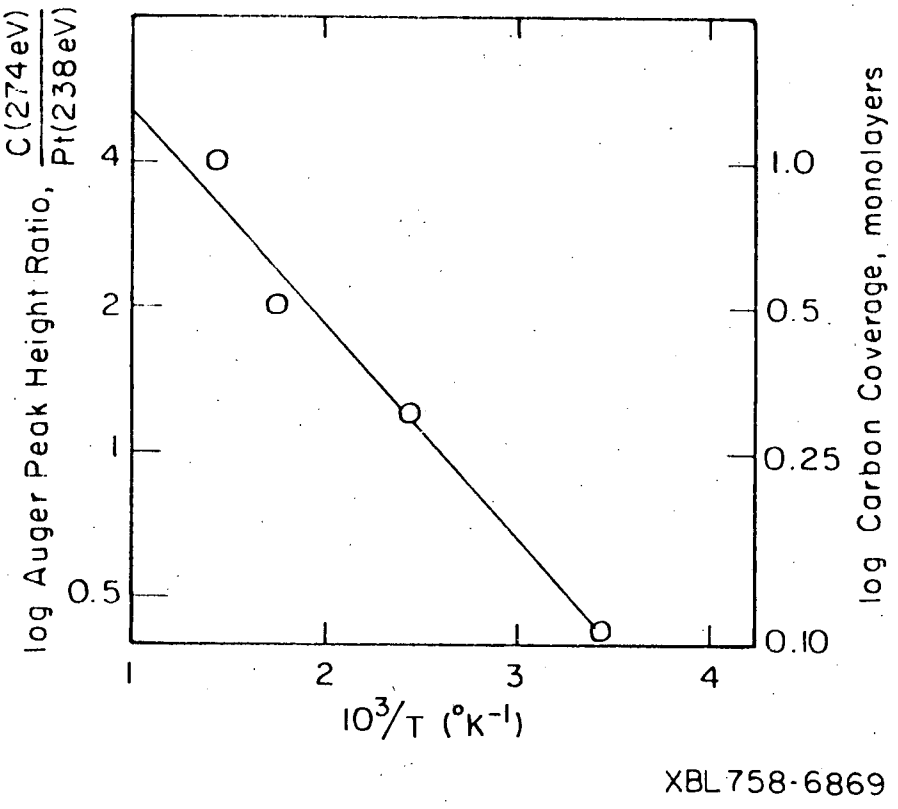

Fig. 6-7. The amount of carbon on the catalyst surface at steady state reaction under standard conditions. An Auger peak height ratio of 4.0 corresponds to ~1.0 monolayers of carbon. Line through points has a 2 kcal/mole slope.

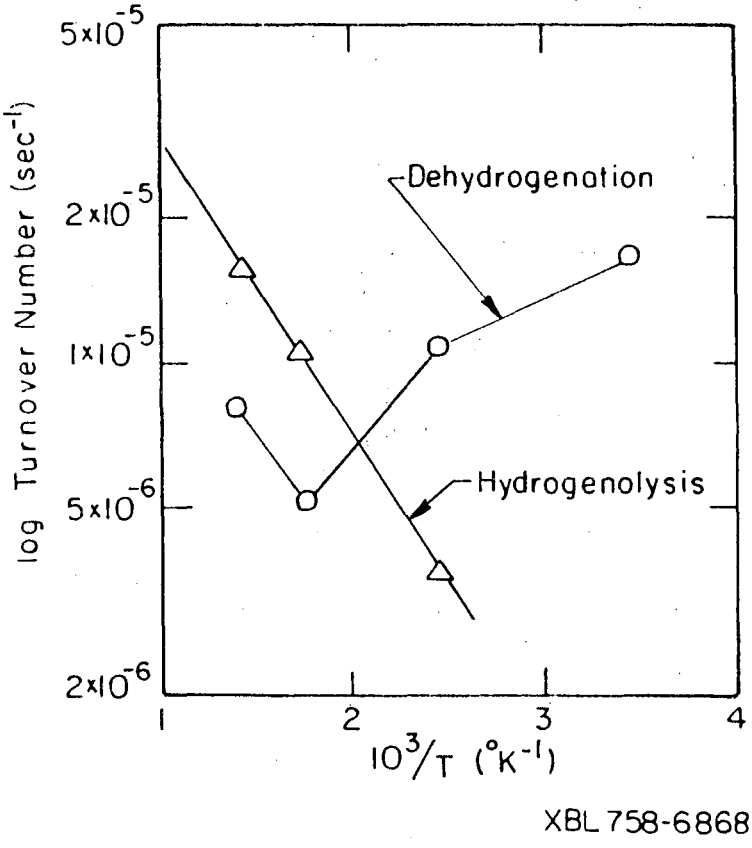

Fig. 6-8. Temperature dependence of dehydrogenation of CH to Bz (-O-) and hydrogenolysis (-Δ-). The overall activation energy for hydrogenolysis is 3±0.5 kcal/mole. Reaction conditions: 4×10^{-8} Torr of CH and H_2:CH ratio 20:1, data for Pt(S)-[6(111)×(100)].

25°C to 150°C. On the Pt(S)-[6(111)×(100)] surface, when either Bz, CH=, or CH is adsorbed at room temperature in the absence of H_2, only Bz appears in the mass spectrum upon heating. The temperature at maximum desorption rate is 100°C for all three initially adsorbed species. The pumping speed is not known that sufficient accuracy to determine the amount of benzene desorbed; it is, however, considerably less than a monolayer. After the removal of the reversibly adsorbed Bz by heating, the surface is almost completely covered with a carbonaceous overlayer. The LEED patterns of adsorbed Bz on the (111) vicinal surfaces also indicate both a reversibly and irreversibly adsorbed species on the surface. The pattern which first forms is shown in Fig. 6-9 and consists of an approximately 1/3 order, diffuse hexagon. This resembles in position the intense inner row of diffraction beams observed from Bz adsorption on the $(\bar{1}11)$ surface[212] and probably represents the close-peaking of the molecules. With further exposure at 1×10^{-7} Torr, the background intensity in the diffraction pattern increases and the hexagon remains. When the Bz flux is removed, the background intensity decreases in about 5 min to a low level. The 1/3 order hexagon remains and is stable overnight in vacuo. Thus there are two quite different types of carbonaceous species on the Pt surface from six-membered ring adsorption: one which is reversibly held with a heat of adsorption of about 21 kcal/mole and which desorbs as the product Bz, and the second is very tightly held, probably dissociatively, and desorbs only as small fragments such as ethylene or methane with heating to very high temperature (~700°C) or with H_2 treatment.

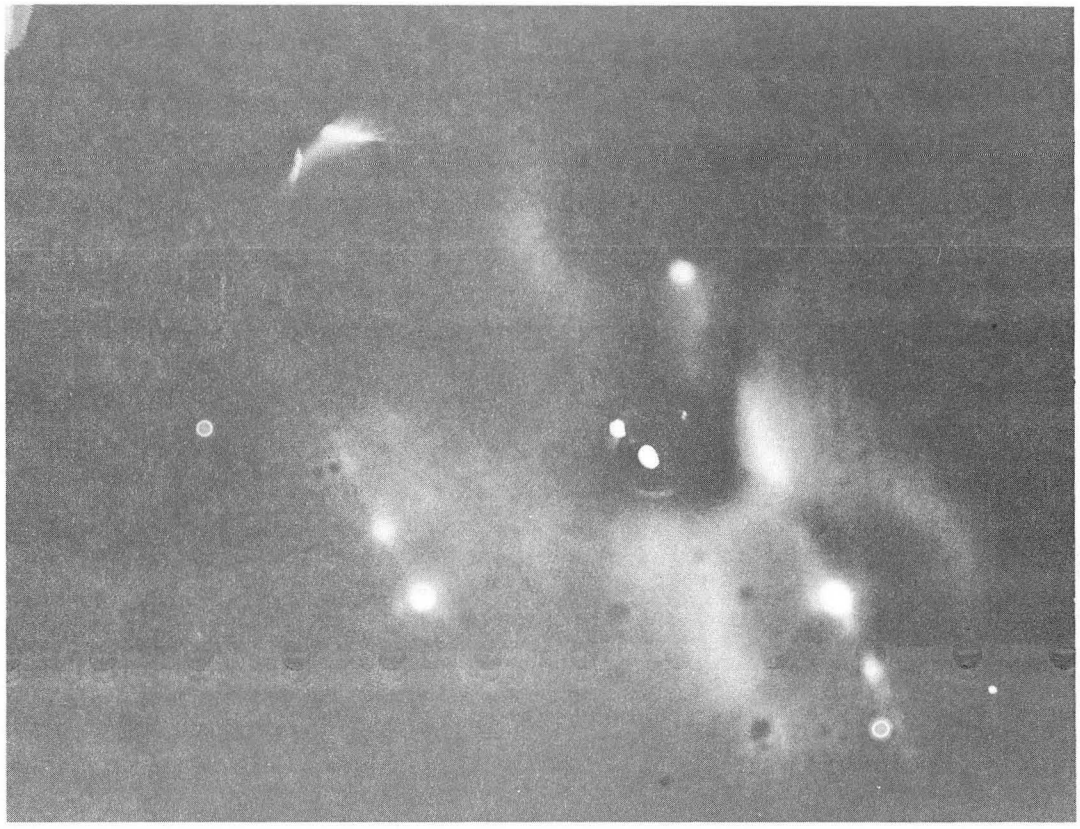

XBB 761-567

Fig. 6-9. Photograph of LEED pattern from Bz irreversibly adsorbed on the Pt(S)-[6(111)×(100)] surface.

The ($\bar{1}11$) surface itself behaves differently than the stepped surfaces. Little hydrogenolysis occurs and the uptake of CH upon heating is small. The amount of Bz which flashed off the ($\bar{1}11$) surface when it was heated from 25°C to 150°C is the same as from the P(S)-[6(111)×(100)]; however, upon heating to higher temperatures, no benzene desorbed from the surface. The amount of carbon on the ($\bar{1}11$) surface at 150°C was approximately 0.8 monolayer, which is much higher than on the stepped surfaces. Apparently, on the ($\bar{1}11$) surface, a large amount of adsorption occurs at low temperature (25°C). Some of these adsorbed molecules are dehydrogenated to Bz; the remaining become the beginnings of the carbonaceous residue.[213] The same adsorption would occur on the stepped surfaces, but H_2 would also be dissociatively adsorbed by the steps[36] and keep the steady state (equilibrium ?) amount of carbonaceous residue low on these surfaces. Some preliminary data on the Pt(S)-[6(111)×(111)] surface[211] are parallel to the ($\bar{1}11$) surface, and indicate that the (111)×(111) type step may not dissociate H_2 as readily at low temperatures as the (111)×(100) type step.

The Pt-(011) and Pt(S)-[7(100)×(111)] surfaces exhibit analogous trends. The rates of Bz, and CH= production and CH uptake are shown in Fig. 6-10 for the Pt-(001) surface. The rate of hydrogenolysis to saturated products increases with temperature with a slope of 1.4 kcal/mole as seen in Fig. 6-11. The rate on the stepped surface is somewhat higher than on the (001) surface. The CH uptake is much lower at 150°C than on the (111) vicinal surfaces, but at 450°C, the rate on both the (001) vicinal surfaces is higher. Again a few hyndredths of a monolayer of benzene flashed off the surface when the

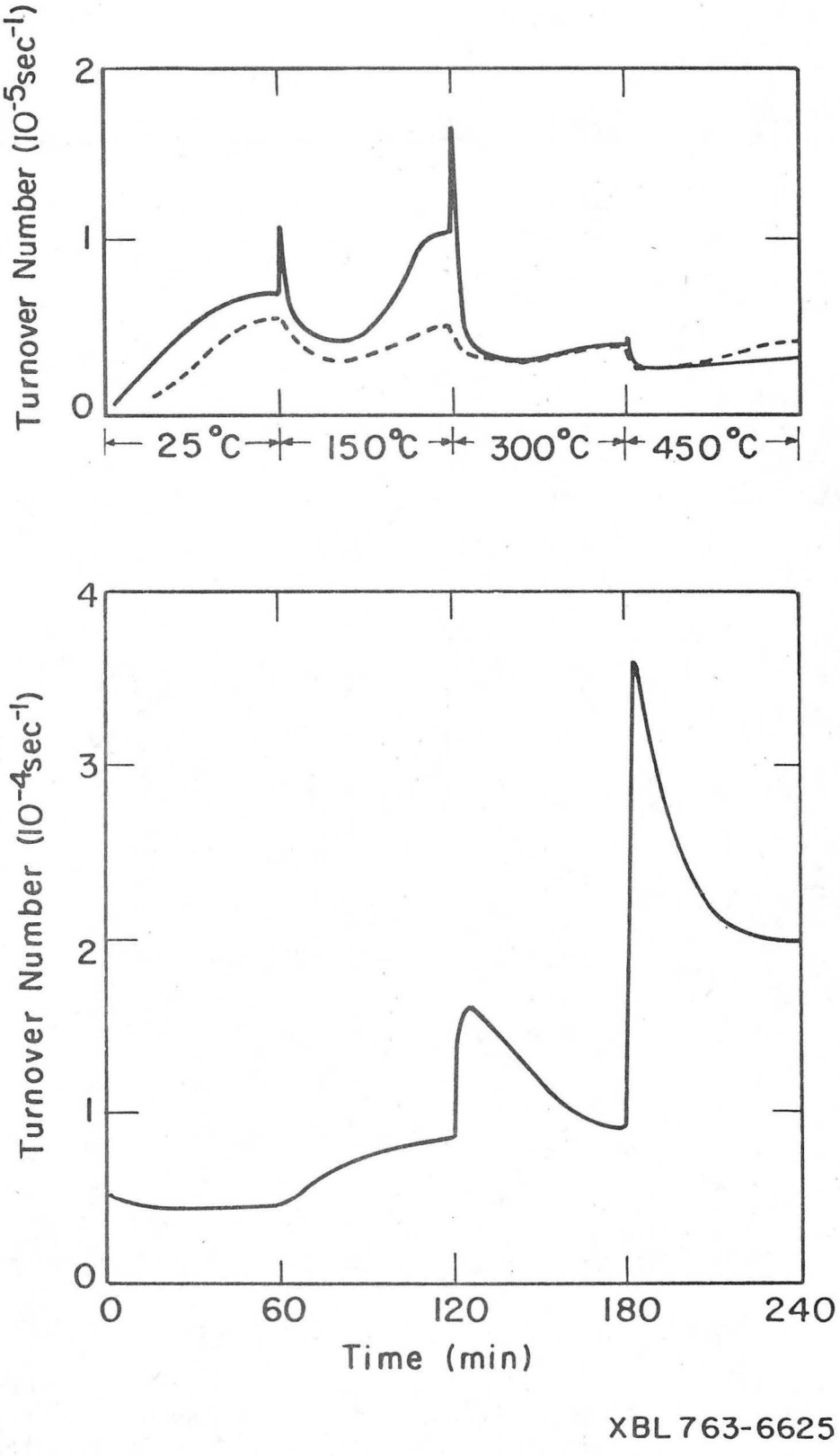

XBL 763-6625

Fig. 6-10. Induction period for production of (——) and $CH^{=}$ (---) from CH. H_2:CH ratio 20:1, CH pressure 4×10^{-8} Torr, Pt-(001).

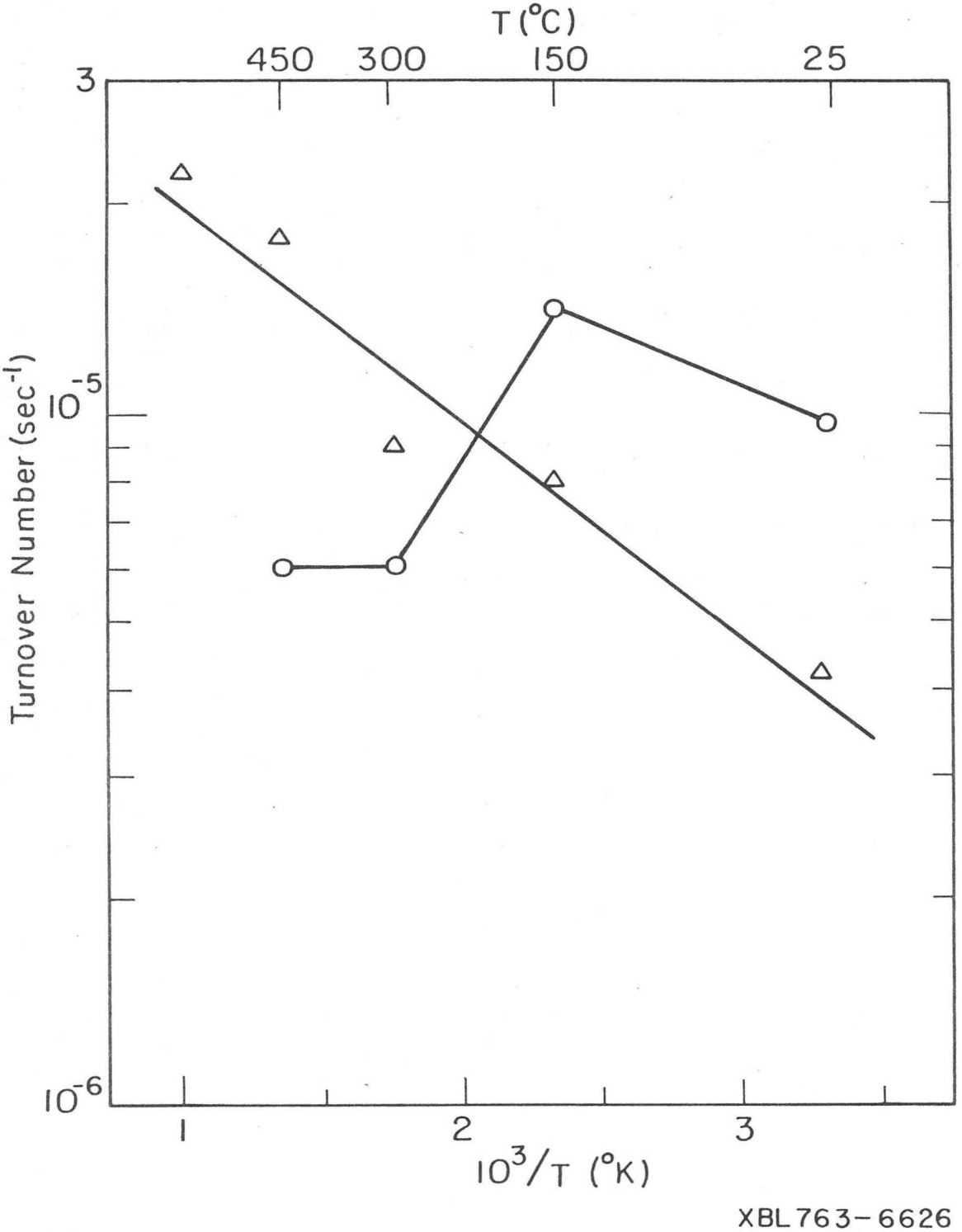

Fig. 6-11. Temperature dependence of dehydrogenation of CH to Bz (-O-) and hydrogenolysis (-Δ-). The overall activation energy for hydrogenolysis is 1.4 kcal/mole. Reaction conditions: 4×10^{-8} Torr CH and H_2:CH ratio 20:1, Pt-(001).

catalyst was heated. The largest amount of Bz, however, desorbed from the surfaces when the samples were heated from 150°C to 300°C, indicating a slightly higher heat of adsorption of Bz on the (001) surfaces than on the (111) vicinal surfaces. The Bz molecule is much larger than the Pt adsorption sites at the steps (Bz's van der Waal's radius is 7.36Å) and the terrace adsorption sites would be expected to control the associative adsorption energy, where as the step could control the dissociative adsorption.

The only (011) vicinal surface studied, the Pt(S)-[8(110)×2(100)], exhibited slightly different behavior. The hydrogenolysis rate is very low, about the size of the experimental error. The CH uptake is largest at 300°C and almost as large at 450°C. The only heating at which Bz desorbed for the surface was from 25°C to 150°C, indicating a more weakly held reversible species than on either the (111) or (001) vicinal surfaces.

The sticking coefficient, σ, for cyclohexane on the various surfaces can be estimated from the data presented in Figs. 6-6 and 6-10. The sticking coefficient at zero coverage is defined in Eq. (5-5) and repeated here,

$$R_{ads} = \sigma_o(1 - \theta) \frac{\bar{v}}{4} n \qquad (6\text{-}1)$$

where R_{ads} is the rate of adsorption, $(1 - \theta)$ is the amount of bare surface and $n\bar{v}/4$ is the incident flux to the surface. As can be seen in Fig. 6-6, σ_o is temperature dependent. The sticking coefficient determined from Eq. (6-1) the maximum rate of CH adsorption, immediately after the temperature jump, is shown in Fig. 6-12 for the

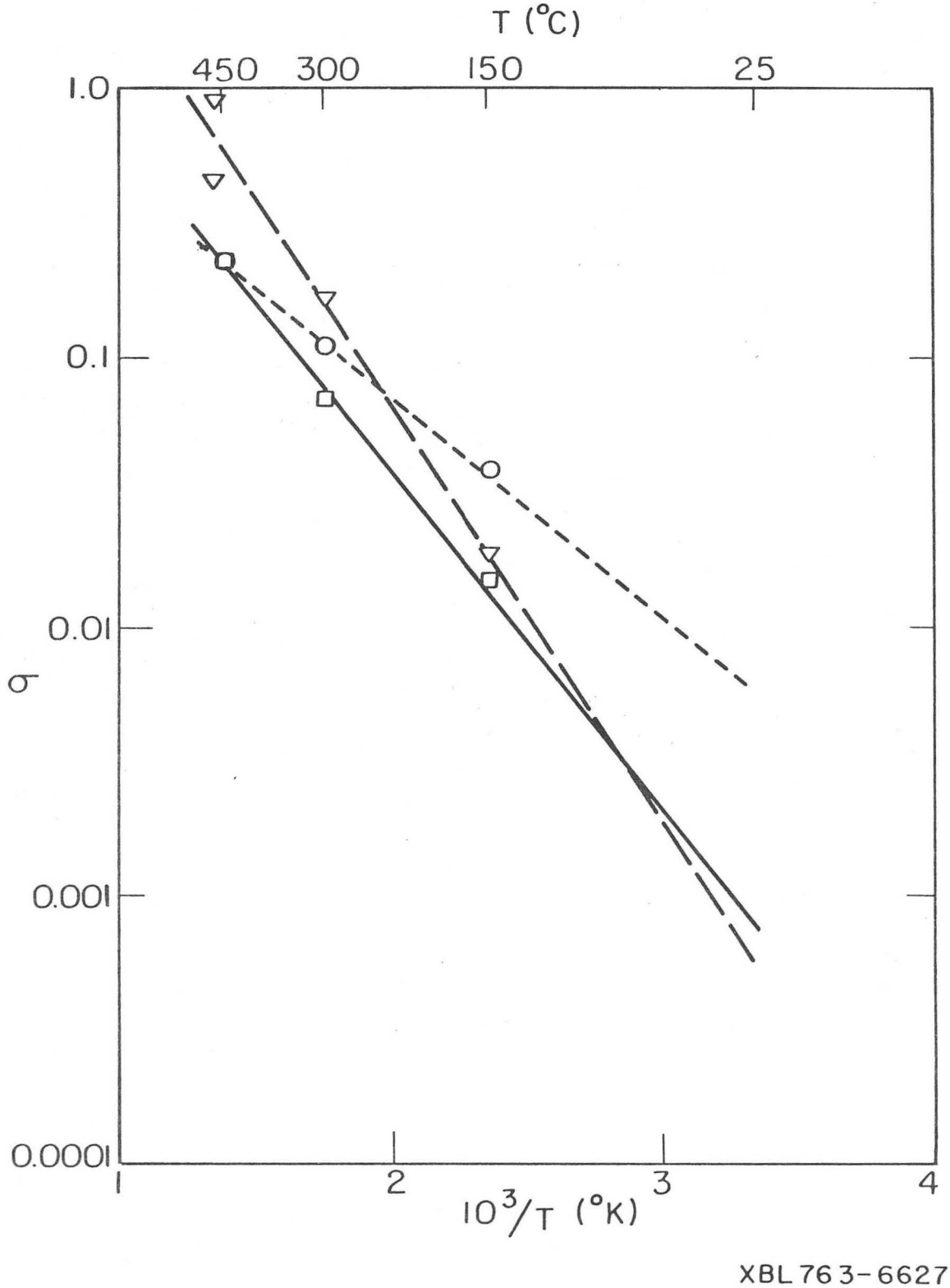

XBL 763-6627

Fig. 6-12. Sticking coefficient at zero coverage for CH on the Pt(S)-[8(110)×2(100)] surface. Temperature dependence gives a 7 kcal/mole activation energy. ▽-[8(110)×2(100)], □-(001), and ▽-[6(111)×(100)].

Pt(s)-[8(110)×2(001)]. If σ_o is written as a rate constant

$$\sigma_o = A\exp(-E_a/RT)$$

then A and E_a for the three surfaces are given in Table 6-7. The activation energy is very high on the Pt(S)-[8(110)×(100)], 7 kcal/mole and lower on the other two surfaces. There is a compensation effect in that the pre-exponential becomes larger simultaneously with E_a.

The temperature dependence of the dehydrogenation and total hydrogenolysis rates for the various (111) vicinal crystal faces at a fixed hydrogen to hydrocarbon ratio of 20:1 is shown in Fig. 6-8. The dehydrogenation rate to benzene decreases with increasing temperature, reaches a minimum of 573°K, then increases slightly at 723°K. The rate of formation of E= products has a similar temperature dependence as that of the rate of formation of benzene as seen in Table 6-6. The hydrogenolysis rate to saturated products increases with increasing temperature and an Arrhenius plot gives an activation energy of 3±0.3 kcal/mole which is the same for all of the crystal faces within our experimental accuracy.

The temperature dependence on the dehydrogenation and total hydrogenolysis rates for the (001) surface is seen in Fig. 6-10. The dehydrogenation rate to Bz is a maximum at 150°C. The rate of formation of E= is similar to Bz, high at both 25°C and 150°C and falls off at higher temperatures. The hydrogenolysis rate to saturated products increases with temperature at a slope of 1.4 kcal/mole.

Table 6-7. Parameters for sticking coefficient of CH on Pt surfaces, 4×10^{-8} Torr CH and 20:1 H_2:CH $\sigma = A\exp(-E_a/kT)$.

	A	E_a(cal/mole)
6(111)×(100)	3	3700
(001)	12	5700
8(110)×2(100)	80	7000

Effect of carbonaceous overlayer on reaction rate. The dehydrogenation reaction of cyclohexane to form benzene was sensitive to the ordering of the carbonaceous overlayer as shown in Fig. 6-13. Initially, the overlayer was ordered on all of the stepped surfaces that were studied and dehydrogenation yielded more benzene than cyclohexene. The LEED pattern from the carbon deposit formed on stepped surfaces in 20:1 hydrogen to hydrocarbon reaction mixture at 423°K and above has a hexagonal unit cell approximately 5.1Å on a side. The diffraction pattern from this ordered residue on the Pt(S)-[6(111)×(100)] and Pt(S)-[13(111)×(310)] surfaces is shown in Fig. 6-14. From these photographs this pattern could be a $\begin{vmatrix} 1 & 1 \\ 2 & -1 \end{vmatrix}$ ($\sqrt{3}\times\sqrt{3}$ R30°); however, in other photographs the second order diffraction beams from the overlayer can be seen and are definitely inside the Pt substrate beams. The 5.1Å unit cell size is about 5% larger than the next nearest neighbor distance of Pt in the {111} plane and considerably smaller than the Van der Waal's radius of either benzene (7.3Å) or cyclohexane (7.6Å)[106] indicating that the adsorbed layer is at least partially dehydrogenated and the diffraction pattern is certainly not due to the intact reactant or product molecules. Complete dehydrogenation that occurs on heating the adsorbed layer to above 1000°K yields graphitic deposits characterized by ring-like diffraction features of 2.46Å unit cell size.[214] The platinum diffraction features after a reaction are readily visible and identical to those from the clean surface (except Pt(S)-[7(100)×(111)] and Pt-(001) where some of the surface reconstruction disappears).[96] The diffuseness of the extra diffraction features correlates with the terrace width, sharper spots on wider

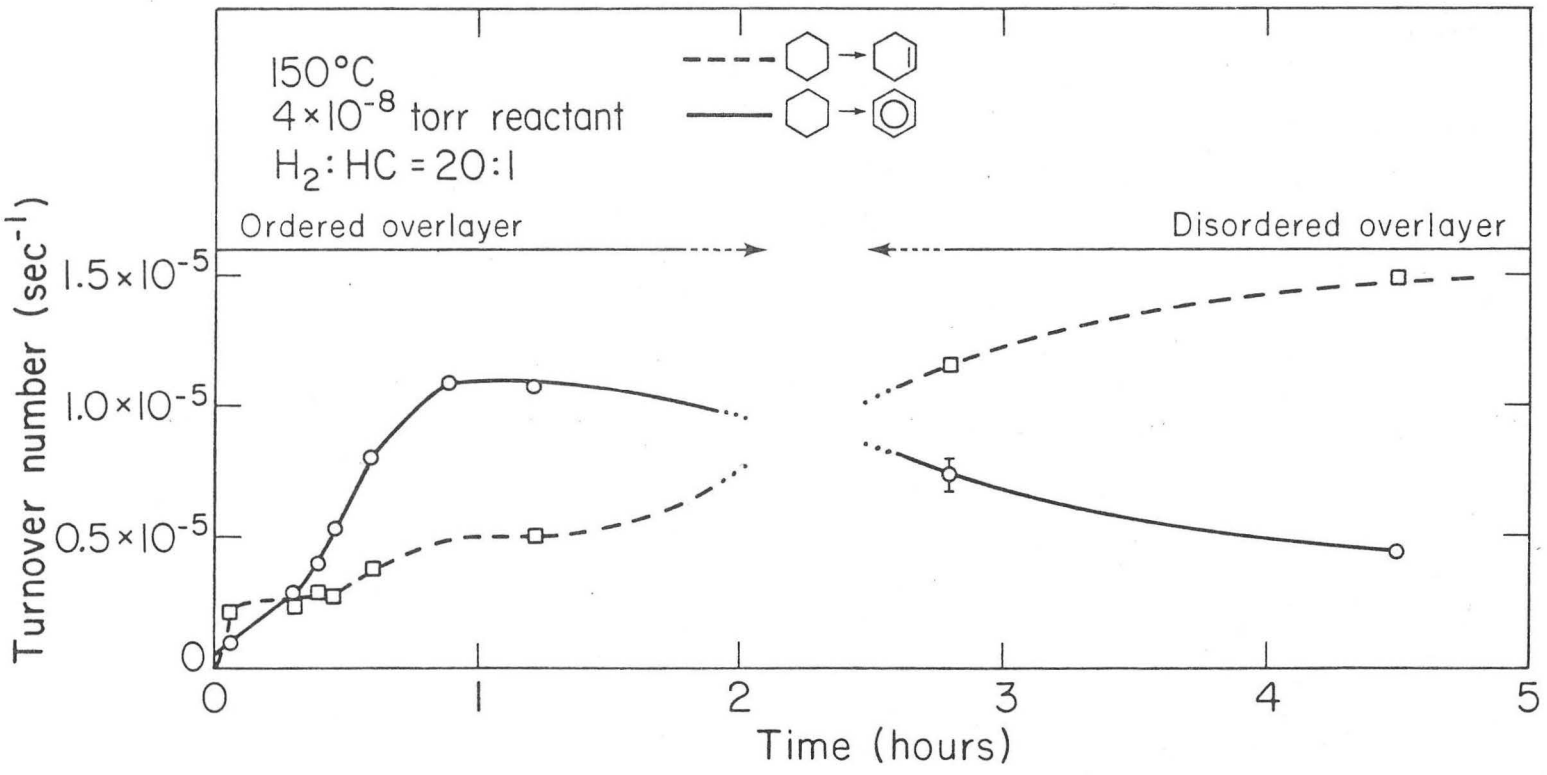

XBL 756-3166

Fig. 6-13. Inhibition of Bz (-⬡-) with time on Pt(S)-[6(111)×(100)] surface. All catalysts with (111) orientation terraces behave similarly.

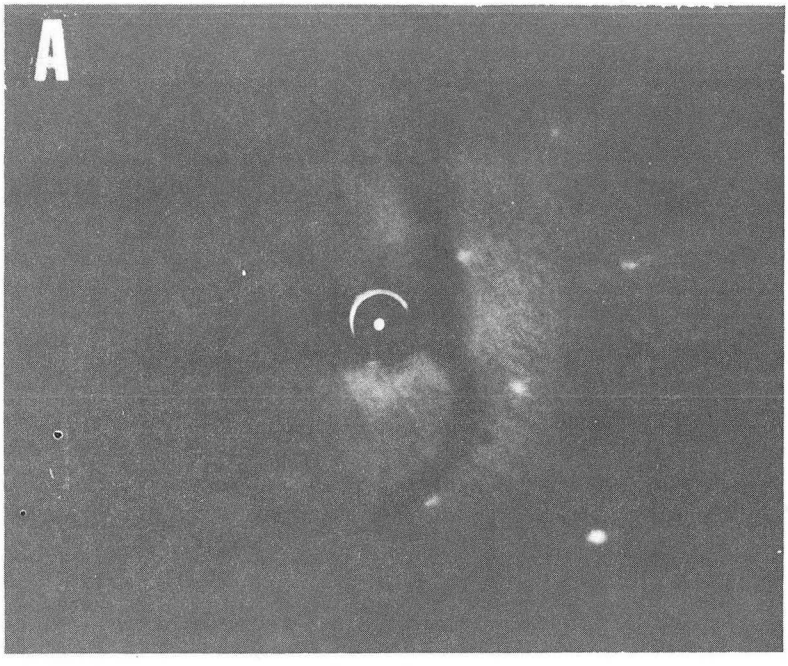

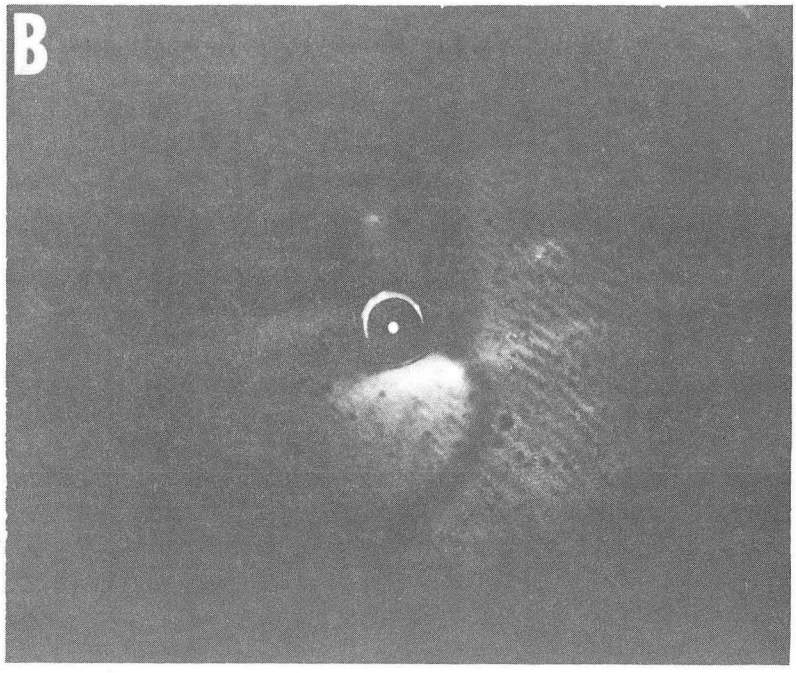

XBB 761-566

Fig. 6-14. Photographs of the LEED pattern of an ordered carbonaceous residue formed from CH at 150°C and H_2:CH ratio of 20:1 on (a) Pt(S)-[6(111)×(100)] and (b) Pt(S)-[13(111)×(310)] surface (see text for discussion of extra beams).

terraces.[105,109] This and the different diffraction pattern on the Pt-($\bar{1}$11) surface indicate that the formation of the carbon overlayer is intimately associated with the steps. After several hours of reaction time, the carbonaceous overlayer slowly disorders. Simultaneously, the rate of production of cyclohexene increases while the rate of benzene formation decreases until the product becomes predominantly cyclohexene. As shown in Fig. 6-13 for the Pt(S)-[6(111)×(100)] surface at 423°K, the initial 2:1 benzene to cyclohexene product ratio typical for dehydrogenation on ordered carbonaceous overlayers becomes 1:3 on a disordered overlayer. Thus, for all practical purposes, the dehydrogenation on disordered overlayers produces cyclohexene as further dehydrogenation to benzene is poisoned.

A similar behavior for the rates of formation of Bz and CH= has been observed on the Pt-(100) and the Pt(S)-[8(110)×2(100)] surfaces. On the Pt-(001) surface the decrease in the rate of formation of Bz occurred more slowly, the crossover point being reached in about 8 hr instead of 2-1/2 hr on the Pt(S)-[6(111)×(100)] shown in Fig. 6-13. The deactivation on the Pt(S)-[8(110)×2(100)] occurred on the same time scale as on the (111) vicinal surface.

The Effect of oxygen on reaction rate. A small amount of oxygen on a stepped surface is an effective poison for dehydrogenation. If the catalyst sample was not vacuum reduced at 1375°K after oxygen cleaning, approximately 0.1 of a monolayer of oxygen (by AES) would be left on the catalyst. This was enough to completely stop the production of benzene and decrease the cyclohexene production by 50% at 423°K on the Pt(S)-[6(111)×(100)]. The LEED features were the

smae as seen in Fig. 4-4b, but the background intensity was higher. The 0.1 monolayer coverage would be less than one oxygen atom per step atom if all the oxygen was adsorbed at the steps. (However, since the cyclohexene production, as well as the benzene production is increased, there may be some oxygen on the terraces as well as at the steps.) The oxygen was still present on the surface after 1 hr of reaction at 423°K and standard pressure conditions of 4×10^{-8} Torr of CH and 8×10^{-7} Torr of H_2.

6.4.1.4. The Dehydrogenation and Hydrogenolysis of Cyclohexene. Effect of surface structure on reaction rate. The turnover number for the dehydrogenation of cyclohexene to benzene is about two orders of magnitude greater than for the dehydrogenation of cyclohexane. In Fig. 6-15a, we plot the dehydrogenation rate as a function of step density. The turnover number increases rapidly with step density indicating that unlike the slower dehydrogenation reaction of cyclohexane, this reaction is structure-sensitive. In Fig. 6-15b, the turnover number is plotted as a function of kink density. Although there is a small increase in the dehydrogenation rate, it may be considered insignificant compared to the marked change of rate with step density and within experimental error could be constant.

The rates of CH= dehydrogenation on the (001) vicinal surfaces are about the same as on the Pt(s)-[6(111)×(100)]. Steps on the surface do not seem to affect the rate of reaction. Since the (001) terrace is active this will be more difficult to determine experimentally; two points are not sufficient. The Pt(S)-[8(110)×(100)] is more active than the (001) vicinal surfaces. A higher activity might be expected

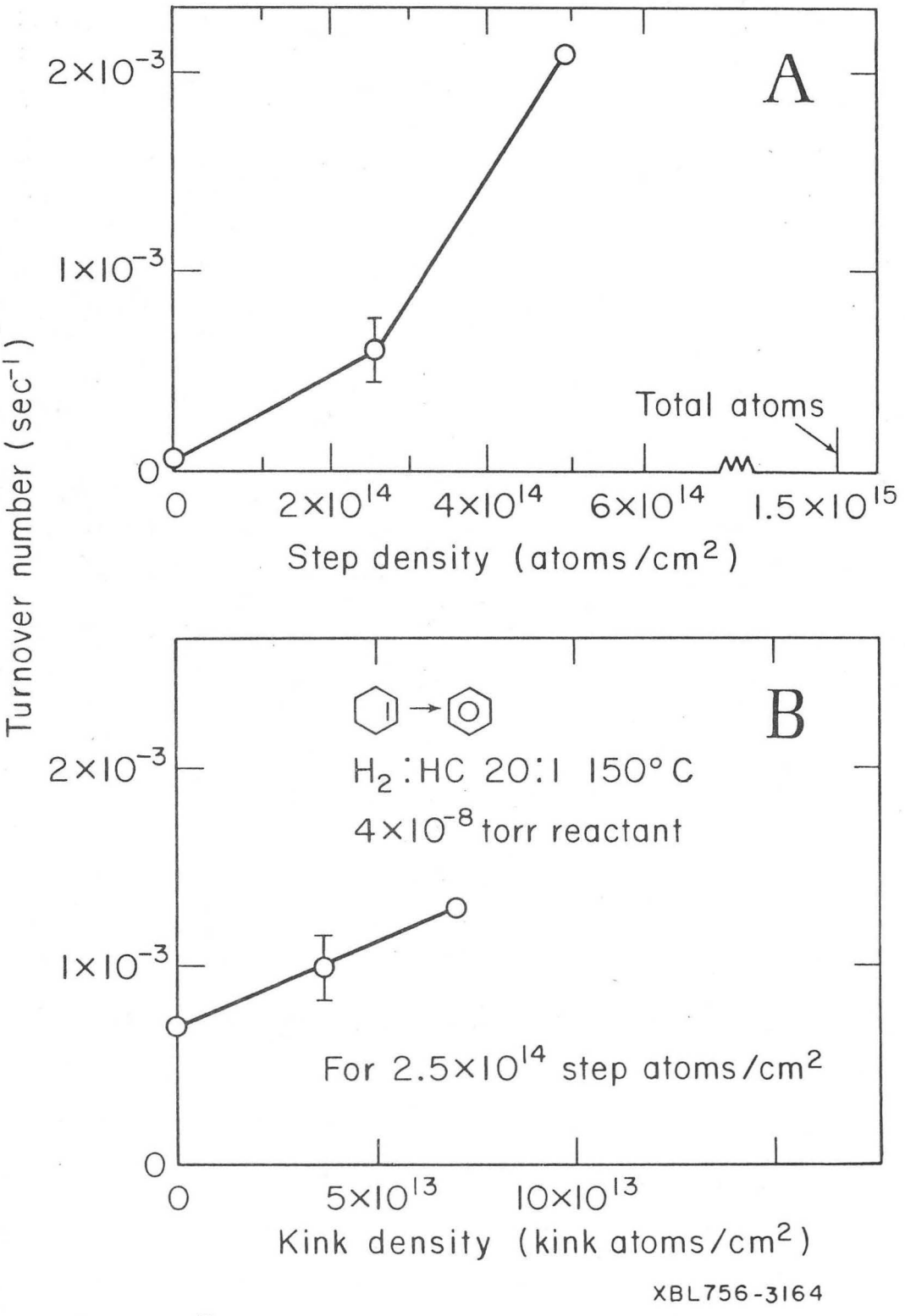

Fig. 6-15. CH^{-} dehydrogenation to Bz as a function of: (a) step density and (b) kink density. Reaction conditions 4×10^{-8} Torr of $CH^{=}$, H_2:$CH^{=}$ ratio 20:1 and 150°C surface temperature.

since the (011) terrace may resemble a stepped surface of narrow terraces.

The hydrogenolysis of CH= is small compared to the amount of Bz which is produced. The only products which are produced in a measurable quantity are E= and P=. From the (001) surface, the mole ratio of Bz:P=:E= is 15:1:1, and is typical of the ratio from most surfaces. The dehydrogenation of CH= is much "cleaner" than the dehydrogenation of CH. The hydrogenolysis products are made at approximately the same rate from both reactants; the primary product is produced much faster from CH= so the selectivity is higher.

The initial rate of CH= dehydrogenation to Bz has close to a first order pressure dependence on the Pt(S)-[6(111)×(100)]. This is in contrast to approximately 2/3 order pressure dependence of the CH dehydrogenation to Bz. This combined with the high probability of reaction of CH= suggests that the dehydrogenation of CH= is rate limited by the flux to the surface, while the cyclohexane dehydrogenation is limited by a surface process.

Effect of carbonaceous overlayers on the reaction rate. Unlike the dehydrogenation of cyclohexane, the cyclohexene dehydrogenation reaction poisons rapidly on many catalyst surfaces. Using a hydrogen to cyclohexene mixture of 20:1, the rate of dehydrogenation reaches a maximum, then it decreases rapidly as poisoning occurs; the catalysts lose approximately 1/2 of their activity in 10-12 min. Figure 6-16 shows a representative plot of the turnover number as a function of time. On many catalyst surfaces, particularly on those with (111) orientation terraces, a disordered carbonaceous overlayer forms which

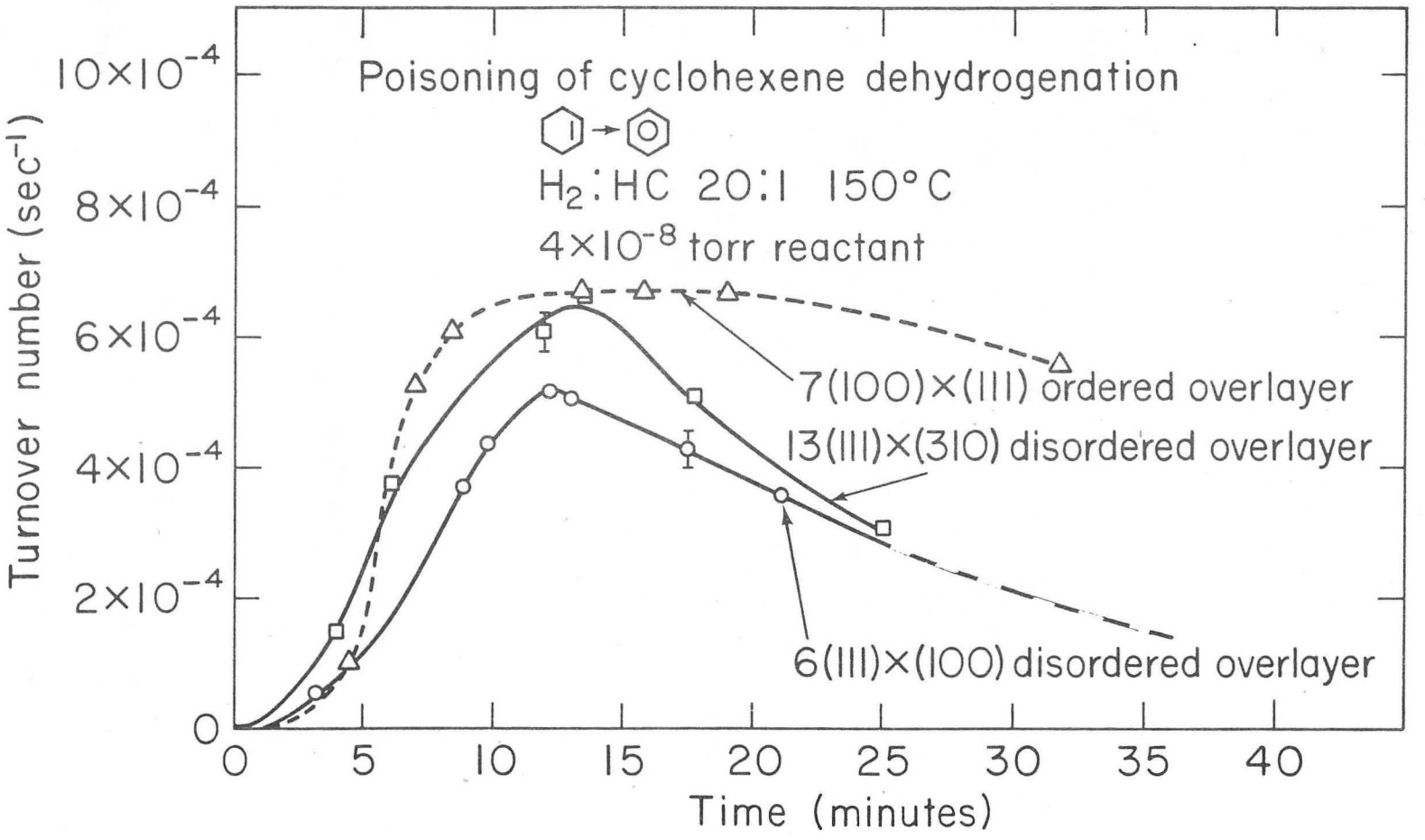

XBL 756-3165

Fig. 6-16. Inhibition of Bz formation from $CH^{=}$ on disordered carbonaceous overlayers (——), Pt(S)-[6(111)×(100)] and Pt(S)-[13(111)×(310)] and lack of inhibition on ordered carbonaceous overlayer (---), Pt(S)-[7(100)×(111)].

poisons further dehydrogenation of cyclohexene. The poisoning is greatly decreased, however, if the carbonaceous overlayer is ordered.

The overlayer is disordered on (111) orientation terraced stepped surfaces while the overlayer orders on surfaces with (100) orientation terraces upon cyclohexene-hydrogen adsorption at 423°K. With an ordered overlayer, the rate of dehydrogenation remains high and there is slower deactivation of these catalysts. On both types of catalyst surfaces the coverage is approximately 1.0 monolayer of carbon after the induction period. The LEED pattern from the ordered CH= overlayer formed at 4×10^{-8} Torr of CH= and 8×10^{-7} Torr of H_2 and a 150°C surface temperature on the Pt(S)-[7(100)×(111)] is shown in Fig. 6-17. The pattern consists of an approximate 1/2 order square, which gives a lattice size of 5.6Å. This is again too small a unit cell for the CH= or, more likely, aromatic adsorbed species to be undissociated molecules. The adsorption of Bz and CH= on the Pt-(001)[106] indicate that at 150°C there is dissociation whereas at 25°C there may not be dissociation.

If the pressure of the CH= reactant is reduced to 4×10^{-9} Torr and the H_2 pressure is kept at 8×10^{-7} Torr, the reaction behaves more like the cyclohexane dehydrogenation on (111) vicinal surfaces. Less than a complete monolayer of carbonaceous residue forms at 150°C, and the reaction does not deactivate completely. Since the residue formed is still disordered, deactivation occurs at the same rate; there is just a partial reduction in rate.

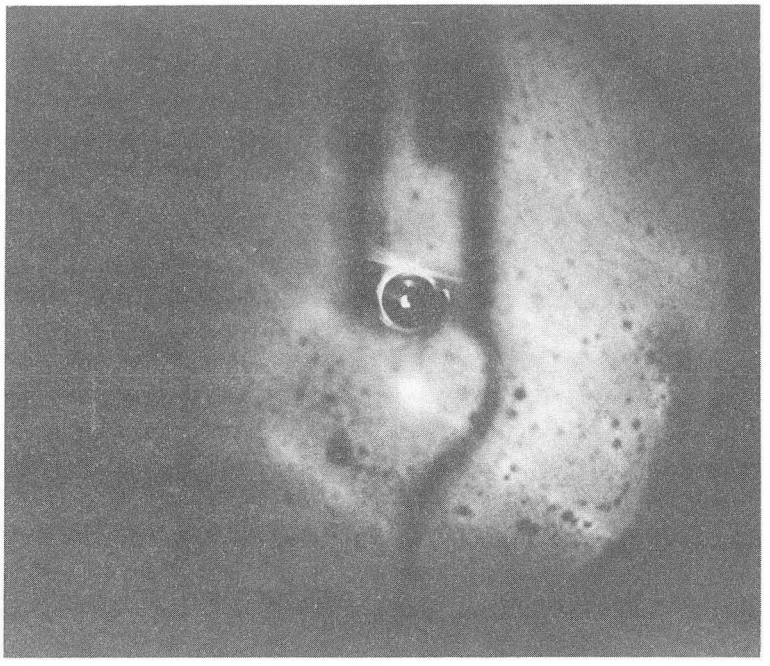

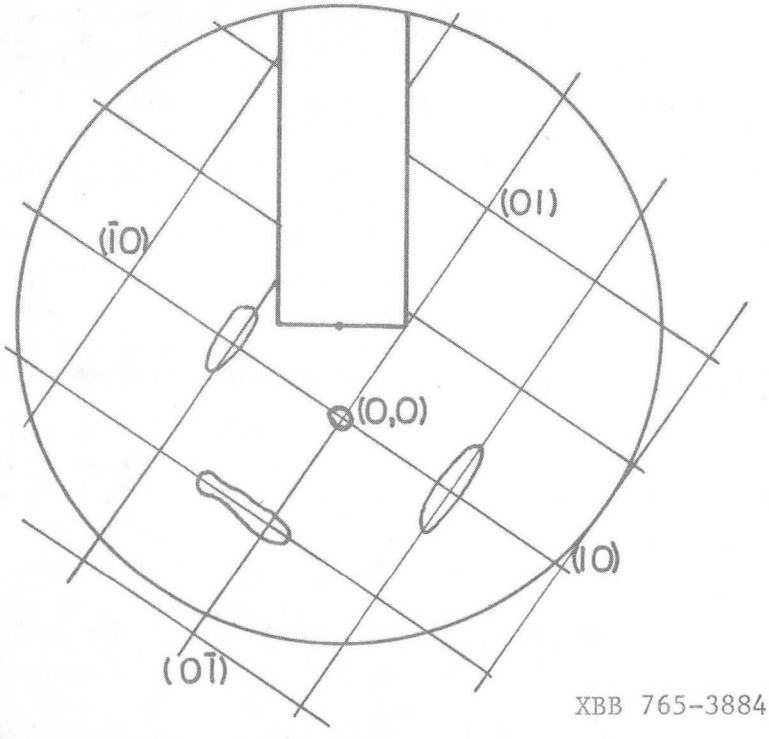

XBB 765-3884

Fig. 6-17. Photograph of the LEED pattern of an ordered carbonaceous residue formed from $CH^{=}$ at 150°C and H_2:$CH^{=}$ ratio of 20:1 on the Pt(S)-[7(100)×(111)].

6.4.2. Dehydrocyclization Reactions

6.4.2.1. Introduction. The dehydrocyclization of n-heptane (Hp) to toluene (T) has been studied on stepped Pt surfaces by Lang, Joyner, and Somorjai[48] and Baron, Blakely and Somorjai.[49] By studying a series of (111)×(100) stepped surfaces at low pressure, it was found that the rate of T production when through a maximum at a six atom wide terrace, Pt(s)-[6(111)×(100)].[49] These results are shown in Fig. 6-18. The intriguing part of these investigations is that the rate of T formation was high on surfaces which formed ordered carbonaceous deposits. The LEED pattern from these deposits was similar to those shown in Fig. 6-14 for CH dehydrogenation. On a slightly wider terrace, Pt(S)-[9(111)×(100)], the rate of toluene formation could be increased by raising the H_2 pressure and simultaneously forming an ordered carbonaceous overlayer like on the Pt(S)-(0$\bar{1}\bar{1}$) the adsorption and bonding character of these surfaces have been discussed by Baron, Blakely and Somorjai.[213] Whether the increased T production is the cause or the effect of the ordering in the overlayer is not known, but whenever T is produced there is also an ordered overlayer present. These results have not been substantiated, but the deactivation of the dehydrogenation reaction indicates a similar behavior for the ordering of the carbonaceous overlayer in that system.

6.4.2.2. Further Results. Some attempts have been made to determine the distribution of products produced by the single crystal catalysts simultaneously with the dehydrocyclization. This is much more difficult than the determination of toluene because of the overlapping peaks in the mass spectral cracking patterns, as discussed in

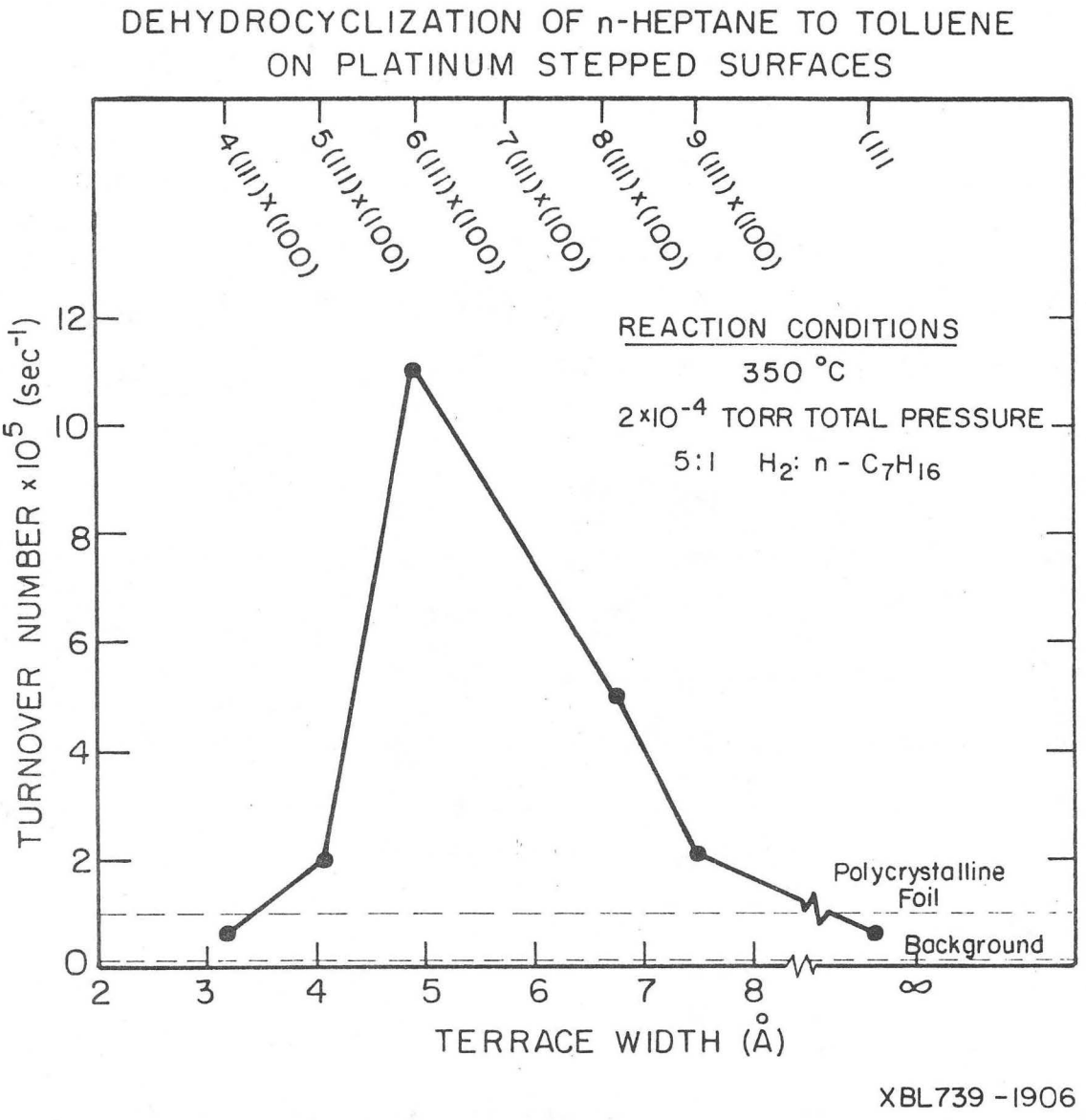

Fig. 6-18. Rate of production of toluene from n-heptane on Pt stepped surface at 5×10^{-5} Torr of n-heptane in a batch reactor.

Section 2.3.5. In several batch reactor runs with a Pt(S)-[6(111)×(100)] catalyst surface, the hydrogenolysis products are dominated by methane. There was succeedingly less of each higher alkane, with no pentane or hexane being detectable. The ratio of initial rates of the total hydrogenolysis to aromatization is about 20:1 with methane being almost half of the hydrogenolysis. The dehydrocyclization products dimethly-cyclopentane (DMCP) and methlycyclohexane (MCH) were also detected. The ratio of the initial rate of T:DMCP:MCH was 10:5:<1. This very small quantity of MCH could be an intermediate to the production of toluene, but considering rate of dehydrogenation of cyclohexane to benzene the partial pressure of MCH would have to be 10^3 higher to be the sole source of the toluene. Paal and Tetenyi[215] have proposed that the intermediate species in the dehydrocyclization reaction to form toluene at low H_2 pressures are the -ene, -diene and -triene of the starting n-alkane molecule, with the thermal cyclization of the -triene to the armoatic. These unsaturated species could not be detected with the mass spectrometer in the gas phase, but may very well be surface intermediates. The DMCP is an intermediate in the formation of iso-alkanes isomerization products. Methyl-hexanes could be detected with great uncertainty and in very small amounts.

The initial rate of toluene formation was 8×10^{-5}/sec, but the reaction poisoned very quickly, dropping to zero after 2 to 3 min. This is similar behavior to that found by Hagen and Somorjai[92] on polycrystalline foils. Lang, Joyner and Somorjai[48] found the pressure of toluene went through a maximum after 7 to 10 min of reaction on surfaces which formed ordered carbonaceous overlayers. From the

analysis of the data in Appendix A, it can be seen that for a true catalytic reaction to take place (with the regeneration and reuse of the active site), the ordered carbon layer is somehow important.

In a flow reactor, the n-heptane reaction was run on the (001) catalyst surface with 1×10^{-7} Torr of Hp and 10^{-6} Torr of H_2. The reaction behavior parallel the cyclohexane dehydrogenation, with an induction period upon heating where the uptake of n-heptane is high, followed by a period of steady-state reaction. The (001) surface again produced substantial quantities of ethlyene; propane and isomerization products were also produced. The rate of toluene formation at 350°C was $1\pm0.5\times10^{-7}$/sec and $2\pm0.5\times10^{-7}$ at 500°C. The ratio of E= to T formation at 350°C is 400:1 and about 180:1 at 500°C. The E= desorption to the gas phase decreases to almost zero during the induction as did the toluene desorption. On the Pt(S)-[8(110)×2(100)] surface, the n-heptane reaction produced ethylene, propylene, methane, ethane, and butane as well as toluene. No isomerization was detectable, and no toluene was formed at 350°C, while at 500°C the rate of production was $2.5\pm0.5\times10^{-7}$/sec. Both E= and P= production were substantial on this surface, but were desorbed at about 1/2 the rate on the (001) surface under identical conditions.

6.4.3. Isomerization Reactions

The reactions of n-butane, methylpropane, and n-pentane have been studied in both the batch and flow configuration reactors on several different orientation surfaces in an attempt to determine the isomerization rate. There is substantial hydrogenolysis of the reactant; when the contribution of the hydrogenolysis products are

removed from the mass spectra, there is not a consistent amount of isomerization shown between the various mass peaks. The expected rates of isomerization correspond to small changes in the mass peak heights, only slightly larger than the measurement errors. Thus large variations are expected in the data, and much more data is required to obtain statistically confident rates.

These are an important class of reactions which are thought to be structure insensitive, as is dehydrogenation. It, therefore, would be of interest to determine if there is any structure sensitivity on single crystals. The results of Hagen and Somorjai[92] suggest that no structure dependence will be found.

It might prove easier to measure the rate of isomerization of the olefins, isobutene or isopentene. At sufficiently high H_2 pressure, the catalyst would not deactivate rapidly (as with cyclohexene) and the reaction could proceed at a much higher rate from the ease of adsorption of the alkene compared to the alkane. Carter, Cusumano, and Sinfelt[40] showed that, at high pressure, the rate of skelatal isomerization is the same for both the alkene and the alkane. The conversion should be kept low so 1- to 2- isomerization of the butene product would not be appreciable.

6.5. Discussion

6.5.1. Active Sites for C-H, H-H, and C-C Bond Breaking

Dehydrogenation of cyclohexane and cyclohexene to benzene occurs readily at low pressures (less than 10^{-6} Torr) on stepped platinum catalyst surfaces. This is in contrast with the very slow or negligible dehydrogenation rate of these molecules on the Pt(111)

catalyst surface.[209] Thus, C-H bond breaking takes place at atomic steps, the same steps that are effective in breaking H-H bonds as revealed in studies by Bernasek and Somorjai[36] of the hydrogen-deuterium exchange reaction at low pressures, using molecular beam scattering techniques. Atomic steps on platinum surfaces appear to be the active sites for C-H and H-H bond scissions.

Another active site has been identified by studying the ratio of the dehydrogenation rate to hydrogenolysis rate of cyclohexane to benzene and n-hexane, respectively. While the benzene:n-hexane ratio is 3:1 on a stepped surface (with roughly 17% of the surface atoms in step positions), the ratio decreases rapidly with increasing kink density (Fig. 6-5b). Using a set of catalyst surfaces that were cut to maintain the same terrace width (step density equal to $2.5\times10^{14}/cm^2$), but with variable kink density in the steps, it was found that the hydrogenolysis rate increases linearly with kink density while the dehydrogenation rate remains unaffected. On a Pt(S)-[7(111)×(310)] catalyst surface, approximately 30% of the atoms in the step are in kink positions (in addition to the thermally generated kinks). For this surface the benzene to n-hexane ratio has reached unity. Thus, the microstructure of kinks in the steps is effected in breaking C-C bonds in addition to C-H and H-H bonds. The selectivity of these bond breaking processes at different atomic surface sites on platinum is certainly significant in that the atomic surface structure of platinum may be properly tailored to provide selectivity in chemical reactions where C-H and C-C bond breaking processes are to be separated.

6.5.2. The Carbonaceous Overlayer

During dehydrogenation of cyclohexane and cyclohexene, the platinum crystal surfaces are always covered with a carbonaceous deposit of 0.1-1.0 monolayer judged by the carbon to platinum Auger peak intensity ratio. The coverage appears to increase with increasing reaction temperature, but is rather independent of pressure as indicated by recent high pressure studies on the Pt(S)-[6(111)×(100)] catalyst surfaces by Herz and Kahn.[34] The overlayer coverage also depends on the particular surface reaction: higher molecular weight reactants and products (cyclohexene, benzene, n-heptane, toluene) yield greater coverage than low molecular weight reactants and products (cyclopropane, propane, etc). Low molecular weight hydrocarbons (cyclopropane, ethane) which do not form carbonaceous overlayers do not readily react on platinum surfaces at low pressures. The build-up of adsorbates during the induction period for cyclohexane and cyclohexene dehydrogenation to benzene indicates the need for the formation of a carbonaceous overlayer to obtain the products. This is not a build-up of the product benzene since it will desorb at a two orders of magnitude higher rate as evidenced by the rate of cyclohexene dehydrogenation and the LEED pattern which is entirely different than those observed from benzene.

During the dehydrogenation of cyclohexane, the carbonaceous overlayer is ordered initially. After a few hours of reaction at 423°K, the overlayer becomes successively more disordered as judged by its LEED pattern. The amount of carbon in the overlayer, however, remains constant at approximately 0.3 monolayers as determined by AES.

Simultaneously, the product distribution in the dehydrogenation reaction changes. While benzene is the dominant product in the presence of the ordered overlayer, cyclohexene becomes the major product of the dehydrogenation reaction in the presence of the disordered overlayer. This is shown in Fig. 6-13. Thus, the disordering of the carbonaceous overlayer poisons the formation of benzene, i.e., the dehydrogenation of cyclohexene, and under the reaction conditions the cyclohexene intermediate becomes the final product. It should be noted that the turnover number for the cyclohexene-benzene reaction is two orders of magnitude higher (approximately 10^{-3}/sec) than for the cyclohexane-benzene reaction (approximately 10^{-5}/sec). Thus, the presence of the disordered overlayers poisons the fast second step, but not the first slow step in the dehydrogenation of cyclohexane to benzene.

The marked effect of the ordering characteristics of the carbonaceous deposit on the reaction rate is also clearly displayed by the dehydrogenation of cyclohexene. As shown in Fig. 6-16, there is rapid poisoning of the dehydrogenation rate within minutes as the disordered carbonaceous overlayer forms. However, when the overlayer is ordered (on (100) orientation terraced surfaces), the catalytic activity decreases much more slowly. Again, the poisoning of benzene production is prevented by the formation of an ordered overlayer. Since the platinum catalyst surface is covered with a carbonaceous layer at low, as well as at high pressures, we must consider this layer an important part of the surface reaction.

Carbonaceous overlayers can have an important effect in both the catalytic activity and selectivity of a metal surface. Weinberg,

Deans, and Merril[216] postulated that the carbonaceous overlayer is the catalytic site for the hydrogenation of ethylene on the Pt(111) surface and similarly, by Gardner and Hansen[217] for tungsten stepped surfaces. Yasumori et al.,[47] found preadsorbing acetylene prevents poisoning or restores the activity of a palladium film for the hydrogenation of ethylene. In all three cases, the structure of the carbonaceous overlayer has a marked effect on the catalytic activity in a manner which is not simple site blockage poisoning. Holbrook and Wise[218] found a specific pretreatment of their Pd catalyst which involved oxygen activation and hydrocarbon preadsorption could markedly affect the selectivity of an isomerization reaction. The rate of dehydrocyclization of n-heptane, as well as the selectivity to isomerization and hydrogenolysis, was observed[48,49] to be dependent on the ordering of the carbonaceous overlayer. These observations, in addition to the data presented in this thesis indicate that the formation of the carbonaceous overlayer on the catalyst surface can affect the selectivity as well as the activity of a catalytic reaction. The presence of these effects at both atmospheric and low pressures and on a variety of metals indicates the importance of the carbonaceous overlayers and the need for their further characterization. This leads to the conclusion that not all carbon on a catalyst surface is deleterious and only amorphous forms cause site blockage poisoning.

6.5.3. The Mechanism of the Dehydrogenation of Cyclohexane and Cyclohexene

In dispersed metal catalysts, the metal is dispersed into small particles, the order of 5-500Å in diameter, which are generally located in the micropores (20-1000Å) of a high surface area support. This

provides a large metal surface area per gram for high, easily measurable reaction rates, but hides much of the structural surface chemistry of the catalytic reaction. The surface structure of the small particles is unknown; only their mean diameter can be measured and the pore structure could hide reactive intermediates from characterization. Some of the same difficulties also hold for thin films. However, the surface structure of single crystal catalysts can be accurately characterized and easily varied and reactive intermediates can be readily measured in a low pressure reactor; both are prerequisites for the mechanistic study of the catalysis on the atomic scale.

Two types of structural features of platinum surfaces have been identified which influence the catalytic surface reactions: (a) atomic steps and kinks, i.e., sites of low metal coordination number and (b) carbonaceous overlayers, ordered or disordered. The surface reaction may be sensitive to one or both of these structural features or it may be totally insensitive to the surface structure. The dehydrogenation of cyclohexane to cyclohexene appears to be a structure-insensitive reaction. It takes place on the Pt(111) crystal face that has a very low density of steps and proceeds even in the presence of a disordered overlayer. The dehydrogenation of cyclohexene to benzene is very structure-sensitive. It requires the presence of atomic steps (does not occur on the Pt(111) crystal face) and the presence of an ordered overlayer (it is poisoned by disorder). Others have found the dehydrogenation of cyclohexane to benzene to be a structure-insensitive [27-31] on dispersed metal catalysts. On the single crystal catalyst surfaces which contain steps, this is

also true, but on the Pt(111) catalyst surface, benzene formation is much slower. Dispersed particles of any size will always contain many step-like atoms of low coordination; therefore, the reaction will display structure-insensitivity.

A complete mechanistic study has not been performed, but based on these findings, a mechanism may be written for these reactions by identifying the sequence of reaction steps:

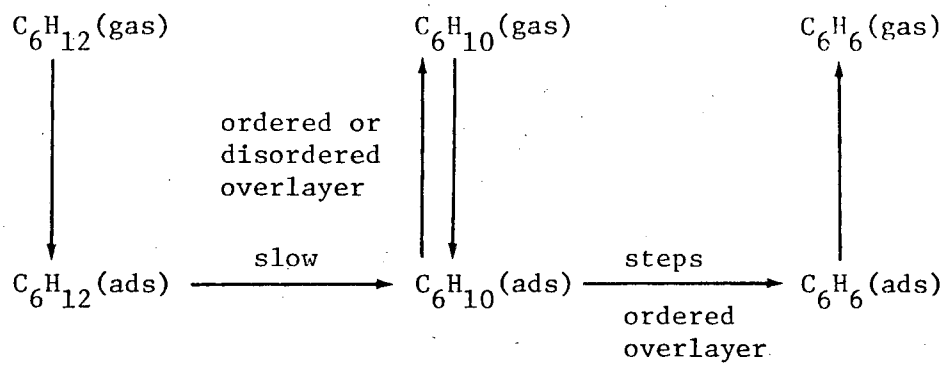

The slow step in the dehydrogenation of cyclohexane to benzene is the production of the cyclohexene intermediate at these low pressures on stepped surfaces. Cyclohexene dehydrogenates very rapidly at a step to form benzene; approximately 1 in every 3 collisions of a cyclohexene molecule with an unpoisoned step results in the formation of a benzene molecule. However, on the Pt($\bar{1}$11) surface, which is practically free of steps, the rate of dehydrogenation of cyclohexene had become slow enough to be rate-limiting.[209] Sinfelt, Hurwitz and Shulman[219] concluded the dehydrogenation of methylcyclohexane to toluene, a reaction parallel to cyclohexane dehydrogenation to benzene, was rate limited by the desorption of toluene. Their arguments are equally valid if the slow tep was the desorption of methycyclohexene, followed

followed by its very rapid dehydrogenation to toluene which would be hidden by the pore structure. This might also be limited by a different step under their high pressure conditions. It is felt that Be desorption is not the slow step in the dehydrogenation sequence at low pressure because it will desorb at a rate two orders of magnitude higher in the CH= dehydrogenation experiments from a surface which is almost entirely covered with a carbonaceous deposit. After the induction period, the surface has a dynamic equilibrium carbon coverage and any benzene formed at this point would be expected to desorb with the same elementary step rate constant as when produced from CH=, i.e., fast compared to its rate of production from CH. Only a fraction of the carbon on the surface is in the form of benzene molecules as estimated from the 1/100th of a monolayer or less of benzene which desorbs upon heating the crystal. The LEED pattern of the carbonaceous overlayer is not characteristic of Bz as discussed earlier. If the desorption of Bz was rate limiting, the temperature dependence of the reaction should be characteristic of a much higher activation energy. A Langmuir isotherm with a 22 kcal/mole heat of desorption predicts 0.9 coverage of Bz at 150°C, much higher than the observed total coverage of 0.3 monolayers. From the low activation energy of the hydrogenolysis reactions, Figs. 6-8 and 6-11, these reactions may be limited by diffusion to a step which is also the probable limiting step in the dehydrogenation. Maatman, et al.[31], postulated the slow step, in agreement with these results, as the formation of an intermediate species. Haensel, et al.,[220] have observed the intermediate cyclohexene species at very high (approximately 30,000 LHSV) space velocities. This indicates the

intermediate is also found at atmospheric pressure reaction conditions and is very reactive at the step and edge atoms which must exist on the dispersed metal particles.

Between 25°C and 300°C the carbon coverage increases (Fig. 6-7) and the rate of Bz production decreases (Fig. 6-8), thus the carbonaceous overlayer may not be as active for dehydrogenation as the metal. However, the carbonaceous overlayer always forms under the conditions of the low pressure experiment; therefore, it must be considered a part of the catalytic process. Even though the carbon coverage increases to almost a complete monolayer at 450°C, the rate of benzene production increases over that found at 300°C. Consequently, even an almost completely carbon covered surface can still produce benzene at an appreciable rate if the temperature is high enough.

In addition to dehydrogenation reactions, hydrogenolysis is also taking place on the platinum surfaces. By monitoring the benzene to n-hexane ratio on the various catalysts as a function of surface structure, steps are identified as primarily responsible for C-H and H-H bond breaking and kinks break C-C bonds in addition to C-H and H-H bonds. Thus, hydrogenolysis is initiated at kinks in the atomic steps. Since specific surface sites are needed for hydrogenolysis to occur, this is also a structure-sensitive reaction. However, hydrogenolysis is insensitive to the state of ordering of the carbonaceous overlayer; it proceeds whether the carbonaceous overlayer is ordered or disordered.

6.5.4. Expanded Classification of Reactions According to their Structure Sensitivity

It appears that the classification of structure-sensitive reactions[23] should be expanded to separate those reactions that exhibit step (or kink) sensitivity into one group and those that are also sensitive to the structure of the overlayer into another group. These expanded classification is shown in Table 6-8. In addition to the dehydrogenation and hydrogenolysis reactions described in this thesis one other reaction that was studied recently is included.[212,221] It would be of great value to include in this classification several other hydrocarbon reactions (isomerization, hydrogenation, exchange). More reactions are presently being studied by others to expand these results on well characterized surfaces. Monogue and Katzer[25] have proposed a subdivision of structure-sensitive (demanding) reactions along very similar lines. "Primary structure-sensitivity" is the effect of changing particle size or step and kink density. Their "secondary structure-sensitivity" includes effects of self-poisoning and oxygen impurity on reaction rate. The self-poisoning phenomena is, for hydrocarbon reactions on platinum, at least at low pressure, the sensitivity of a reaction of the order in the carbonaceous overlayer. However, caution must be exercised in studies of structure-sensitivity as the reaction mechanism or the surface structure may change markedly with pressure, temperature, and reactant ratio. Most of the surface structure-sensitivity of various catalytic reactions was derived from the particle size dependence of the reaction rate on dispersed metal catalyst systems. Although there is excellent agreement between the classifications of the various

Table 6-8. Classification of reactions by step density and carbonaceous overlayer dependence.

Surface Structure-Sensitive		Surface Structure-Insensitive	
Overlayer Structure Sensitive	Overlayer Structure Insensitive	Overlayer Structure Sensitive	Overlayer Structure Insensitive
Cyclohexene → Benzene	Cyclohexane → n-hexane		Cyclohexane → Cyclohexene
n-heptane → Toluene	Cyclohexane → Ethylene		Cyclopropane → Propane

reactions based on studies using supported metal catalysts with variable particle size and these studies using various single crystal surfaces, this may not be the case for all reactions. Perhaps the step density or the kink density is proportional to particle size while the ordering characteristics of the carbonaceous overlayer may or may not be affected by changes of particle size. In addition, studies similar to those reported on platinum must be carried out using crystal surfaces of other transition metals to ascertain that these artuments are more broadly applicable to describe the catalytic chemistry of transition elements. There is evidence that the heat of adsorption of hydrogen on palladium crystal surfaces varies markedly with step density[190] while gold crystal surfaces exhibit chemisorption behavior that is independent of step density.[95]

The discovery that kink sites in steps are effective in breaking C-C bonds in addition to C-H and H-H bonds, thereby initiating hydrogenolysis reactions, may also explain the effect of trace impurities or second component metals that introduce selectivity. Since these kink sites have fewer nearest neighbors than step or terrace sites, they are likely to bind impurities or other metal atoms with stronger chemical bonds. Thus, these sites are readily blocked by impurities. As a result, selective "poisoning" of hydrogenolysis may be obtained by minute concentrations of well-chosen impurities or another metal component.

6.5.5. A Descriptive Model of Hydrocarbon Catalysis on Platinum Surfaces

Studies to correlate the reactivity and the surface structure and composition of platinum surfaces indicate that the active platinum crystal surface must be heterogeneous. The heterogeneity involves the presence of various atomic sites that are distinguishable by their number of nearest neighbors (atoms in terraces, in steps and in kinks), and also variation in surface chemical composition. The variation in surface chemical composition may be as important as, if not more important than, the variation in geometric structure for the ability to perform a chemical reaction selectively.

The same catalytic reactions when performed in a high pressure of H_2 are much "cleaner" in that far fewer hydrogenolysis products are formed. This is not a thermodynamic equilibrium effect since hydrogenolysis of an alkane has no total pressure dependence. Therefore, the H_2 must be performing the same function at high pressure as the carbonaceous overlayer is performing at the low pressures of the experiments described in this thesis. This function is to saturate the excess bonding power of the surface. At low pressure there is not enough H_2 on the surface to reduce the bonding power of the surface to the point where it leaves the reactant molecules whole and a carbonaceous overlayer forms from the decomposed hydrocarbons. The carbonaceous overlayer coverage stops increasing when the excess valency is tied up. The two species of Bz that were found on the single crystal catalysts illustrates this point; the first benzene which adsorbs is very strongly bound. The aromaticity in the ring

may be lost increasing the bond strength to the metal surface, while the reversibly held Bz may adsorb atop the other benzene (fragments), or to the metal with the weaker bonds which are left. In either case, the weakly held Bz can diffuse on the surface to a site favorable to hydrogenation, exchange, etc. This may demonstrate the effect of ordering of the carbonaceous overlayer on the reaction rate; a disordered surface does not allow the diffusion of the reactant or product to or away from the actual site of the reaction. At high H_2 pressure, the equivalent can take place, only the strong surface bonds are saturated with H instead of C bonds. Using the results of Bernasek[36] for the residence time (10^{-2} sec) and sticking coefficient at low coverage (10^{-2}), a flux of 10^{22} molecules of $H_2/sec/cm^2$ is necessary to maintain an 0.97 surface coverage at elevated temperature, which corresponds to about 10 Torr pressure. At these conditions, the selectivity for hydrogenolysis is reduced to a level equivalent to high pressure (20 atm) industrial reaction conditions. The carbonaceous overlayer which is formed at low pressures is hydrogenated off as low molecular weight products, such as methane and ethylene. The rate of turnover of the carbon in the carbonaceous overlayer could easily be measured with either ^{13}C mass spectrometrically or with ^{14}C radioactively. With high H_2 pressure, there is very little carbon on the surface in a decomposed state (i.e., strongly bound), so little carbon is available for hydrogenation to low molecular weight species. Since larger metal particles (>100Å), exhibit higher hydrogenolysis rates and faster deactivation,[27] they must contain areas of lower H_2 concentration which permit carbon deposition and subsequent hydrogenation

to hydrogenolysis products. A possible explanation could be the dominance of the {111} planes on large crystallites (thermodynamically most stable plane). Bernasek[36] has demonstrated that the (111) surface is much less active for H_2-D_2 exchange and there probably is a lower concentration of H atoms on a terrace than at a step, even if the H atoms diffuse from the steps onto the plane. On small metal particles, either the steps are closer together or the predominant surface plane is different, hence there is a higher H atom concentration on all surfaces of the crystallite. The lower rate of hydrogenolysis and the slower poisoning on the (001) surfaces at low pressure, may be indicative of a change in the predominant plane on the small metal particles. This could be easily justified by changes in the surface stress as the particle becomes small (see Eq. (D-3)).

Using this model, some otherwise tenuously explained observations may be readily interpreted. The large difference in the rates of hydrogenolysis observed with the same reactions and the same catalysis at low (1×10^{-4} Torr) and high[212] (>10 Torr) pressures have already been explained. The strong poisoning effect of olefins[222] is caused by their ability to adsorb more strongly than an associated alkane; therefore, they can break into the H saturation and become strongly adsorbed dissociatively and inhibit the reaction. This has been confirmed at low pressures with the CH= dehydrogenation reaction. With 1×10^{-6} Torr of H_2 and 1×10^{-8} Torr of CH=, the reaction poisons rapidly on the (111) vicinal surfaces. However, if the CH= pressure is lowered to 4×10^{-9}, the surface does not saturate with a carbonaceous overlayer and complete deactivation does not occur. Benke[223] has found

that there is a residual activity after the cyclopropane hydrogenolysis reaction has "poisoned". This poisoning is the formation of the carbonaceous overlayer which apparently stops at 0.9 coverage (residual activity of 10% on small particles and 5% on large particles) under the high pressure conditions of his experiment. The partial coverage corresponds to the partial coverages of the surfaces in this study of the CH reaction. Cyclopropane is almost an olefin, so equilibrium coverages might be expected to be higher than with an alkane. It has been found that Ir is a better dehydrocyclization catalyst at low pressure than is Pt;[92,224] this is surprising since Ir does not form toluene at high pressures.[8] At low pressures Ir-(111) planes have a partial, well ordered carbonaceous overlayer[224] which allows the n-heptane to remain whole and form toluene. On an Ir(S)-[6(111)×(100)] surface, there is little order in the carbonaceous overlayer and the decomposition of the reactant occurs with little T formation.[224] At high pressures, the H_2 may "saturate" the surface, but it does not prevent rapid single hydrogenolysis of the reactant.[8] While on Pt at low pressure, the entire surface becomes covered with carbonaceous residues and at high pressure, the H_2 protects the reactant molecules from hydrogenolysis because of different intrinsic bonding ability.

Consequently, the effects of the carbonaceous overlayer at low pressure and of excess hydrogen at high pressures are seen to be one and the same. They saturate the excess surface valency of the metal. With the strong bonding ability saturated, the hydrocarbon molecule to metal surface bonds of the reactant are of the proper strength

to dehydrogenate, exchange, isomerize or dehydrocyclize the reactant without a large amount of hydrogenolysis. These are the exact conditions necessary for a selective efficient catalyst.

ACKNOWLEDGEMENTS

I would like to acknowledge Professor Gabor Somorjai, my benevolent, protective advisor, for his encouragement and faith and for his glowing examples of what the persuit of truth could being forth. I would like to thank Eugene Peterson for being the Devil's advocate and not believing anything I told him and Bob Madix for introducing me to the world of surface science. I would like to thank Jules Rabo for a stimulating discussion of how this work relates to the real world of industrial catalysis. I am grateful to Micheal Boudart for not taking me as a student.

I am indebted to my peers here at Berkeley and in Palo Alto for enjoying a few beers and discussing science with me, particularly the Thursday night seminar group: Jeff Buchholz, Larry Firment, Pete Stair, Rich Herz, Steve Overbury, Dave Kastner, Jim Klickner and Peter Hollings. I an deeply indebted to Tom Taylor for leading me through the Valley of the Bears and Bees, and to Steve Brumbach and Tom Kaminska for being friends. I would like to thank my friends and colleagues here starting with Bernard Lang, Lenny Szalkowski, Steve Bernasek and Sandy, Wigbert Siekhaus, John Gland and Wanda, Ken Baron, Dave Hagen, Mike Chesters, Christoph Steinbruchel, Becky Johnson, Sylvia Ceyer, Carol Smith, Miguel Salmeron, Brett Sexton, Larry Kesmodel, Cliff Megerle, Steve Berglund, John Wasilczek, Rober Baetzold, Dan Kahn, Edwardo Wolf, Edwardo Saucedo, Larry Jossings and lastly Alan Benke. In Palo Alto I was indebted to Alan Ullman for exposing me to science and my friends Frank Williams, Jon McCarty, John Falconer, Al Susu, Tom MacDonald, and Frank Hansen.

I am grateful to Emery Kozak for the help in maintaining my apparatus, to Jim Severns for electronics maintainence and to "Pat" Patenaude for guidance in the shop. I am indebted to Jean Wolslegel for typing my thesis and Gloria Pelatowski for the drafting work.

And finally I am appreciative of my wife, Judy, for putting up with me working evenings and weekends, and for going to grad school herself to keep quiet and not bother me.

This work was done under the auspices of the U. S. Energy Research and Development Administration and also done in part under the U. S. Army. Any conclusions or opinions expressed in this report represent solely those of the author and not necessarily those of the Lawrence Berkeley Laboratory nor of the U. S. Energy Research and Development Administration.

APPENDIX A. AN INTERPRETATION OF BATCH REACTOR DATA

In the work of Hagen and Somorjai;[92] Lang, Joyner and Somorjai[48] and unpublished data of Baron, Blakeley and Somorjai[49] catalytic reactions were run on single crystals at low pressures using a batch reactor configuration (see Section 2.4.1). The reactants were introduced to the reaction chamber with the catalyst well below the reaction temperature. To start the reaction, the catalyst was heated rapidly to the reaction temperature, and the pressure changes followed. The data followed the form shown in Fig. A-1.

Since the activity is very short lived, a few minutes, for all reactions on Pt except CH_4 formation, and since the reaction rate is measurable over a very narrow range of temperature with a definite maximum, it is questionable whether this is a true catalytic reaction (the catalyst returned to its original form after each cycle) or a Pt assisted thermal decomposition of the hydrocarbon which was adsorbed at low temperature. The Ir data may represent a true catalytic reaction. The following model explains the data based on the second proposal.

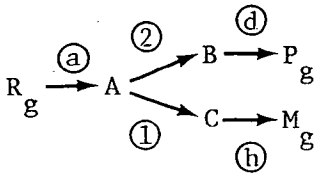

The gas phase reactant species, R_g, saturates the surface, probably dissociatively although not necessarily at the low temperatures of adsorption, to form the surface species A. The hydrocarbon reactant was generally put in the reaction chamber before the H_2 for ease of

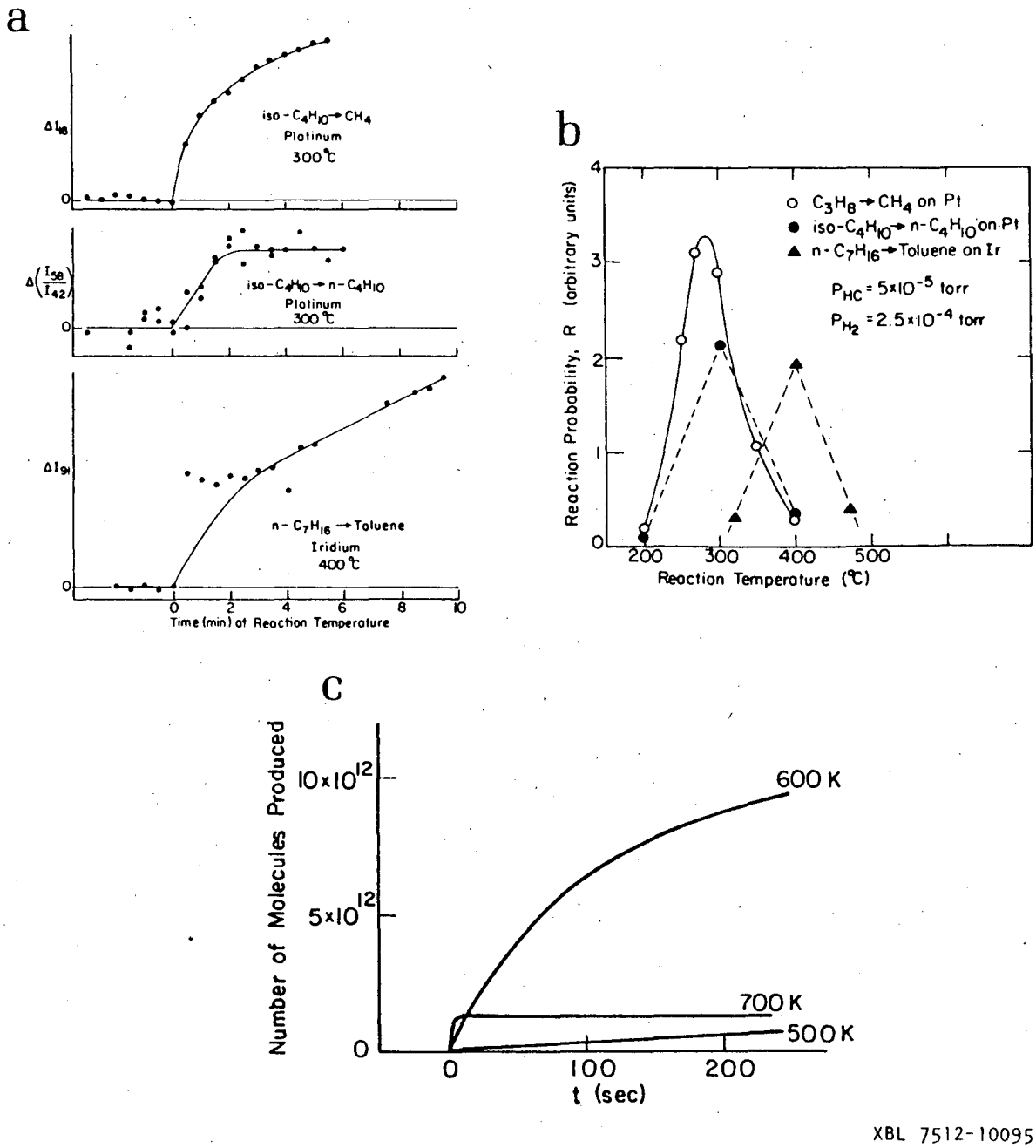

XBL 7512-10095

Fig. A-1. Data of Hagen and Somorjai[92] for studies of reactions at low pressure in a batch reactor, (a) rate of production with time and (b) rate of production with temperature. (c) Shows predicted rate of production using Eq. (A-4) as described in text.

pressure measurement in the work of Hagen and Somorjai.[92] This would completely saturate the surface with hydrocarbon (see Section 6.4.1.1). The amount of hydrocarbon removed by the introduction of H_2 at low temperature is not known, but is probably small. The surface species A have the potential of desorbing as isomeric or dehydrogenative products, P. There is also undoubtedly a small amount of hydrogen adsorbed on the surface, depending on the H_2 pressure and catalyst temperature. When the surface is heated to the reaction temperature, the adsorbed species, A, either decompose to a carbonaceous residue which can be hydrogenated to methane, or rearrange to form B which desorbs as product P. Possible rate equations for each step are:

$$r_a = k_a[1 - (\theta_A + \theta_B + \theta_R)]\, P_R$$

$$\left.\begin{aligned} r_1 &= k_1\theta_A(1 - \theta_H) \\ \text{or} \quad & \\ & \frac{k_1\theta_A}{1 + K_H\theta_H^2 + K\theta_A} \end{aligned}\right\} k_1\theta_A f(\theta_H)$$

$$r_2 = k_2\theta_A$$

$$r_3 = k_3\theta_B \quad \text{considered small for simplification}$$

$$r_d = k_d\theta_B$$

$$r_h = k_h\theta_R\theta_H$$

The peak temperature is usually around 600°K, peak rate approximately 10^{-4}/sec. A balance on species A yields

$$k_a P_R[1 - (\theta_A + \theta_B + \theta_R)] - [k_1\theta_A f(\theta_H) + k_2\theta_A] = \frac{d\theta_A}{dt} \quad . \quad (1)$$

If the desorption rate constant, k_d, can be written as $k_d = 10^{13} \exp(-25{,}000/kT)$, a reasonable pre-exponential factor and heat of desorption for a simple step, θ_B at 600°K is very small, $\theta_B = r_d/k_d \approx 10^{-8}$. At $>10^{-5}$ Torr, the bare metal area on the surface will rapidly readsorb another hydrocarbon so that the rate of adsorption is approximately equal to the rate of desorption of product $k_2\theta_A = k_d\theta_B$. Therefore Eq. (1) becomes

$$k_1\theta_A f(\theta_H) = \frac{d\theta_A}{dt}$$

which integrates to

$$\theta_A = \theta_{A_{initial}} e^{-k_1 f(+\theta_H)t} , \qquad (2)$$

assuming θ_H is constant and small. The rate of production of product P is

$$R_P = \frac{dP}{dt} = k_s S\theta_B = k_2 S\theta_A = k_2 S\theta_{A_{in}} e^{-k_1 f(\theta_H)\ t} \qquad (3)$$

where S is the total number of sites (10^{15} cm^{-2}). This gives

$$P - P_o = \frac{k_2}{k_1} \frac{S\theta_{A_{in}}}{f(\theta_H)} \left[1 - e^{-k_1 f(\theta_H)\ t}\right] \qquad (4)$$

From Eq. (3) it is seen at 600°K, $k_2 \approx 10^{-4}$ sec^{-1} from the initial reaction rate; Eq. (4) gives the time constant $k_1 f(\theta_H) \approx 10^{-2}$ sec^{-1} to match Fig. A-1. With an assumed E_a for the rearrangement of E_{a_2} = 20 kcal (reasonable for isomerization[225] or dehydrogenation[219]) and E_{a_1} = 40 kcal for residue formation (higher than E_{a2} from poisoning studies[226]), the pre-exponentials were calculated as $A_1 = 3\times10^{12}$ and

$A_2 = 1.5\times10^3$. Justification for the pre-exponentials cannot be given since their assumed values are dependent on the selected activation energies. The experimental results can now be readily explained. Table A-1 and Fig. A-1c give the models predictions at various temperatures. At the peak temperature (600°K), the pressure of P rises readily to about 5×10^{-8} Torr (10^{13} molecules/15 ℓ) within a few minutes, as this was a force fit of the data. At 500°K, 3×10^{14} molecules become product but the rate is slower by a factor of 33 which would be difficult to measure. At 700°K the rate of production is fast, but the rate to carbonaceous residues has become even faster, so only a 5×10^{-9} Torr (10^{12} molecules) pressure increase is observed. From 5×10^{-5} Torr reactant pressure, this is 1 part in 10^4 and probably not detectable. Methane production which comes from the residue increases with T and H_2 pressure.

For the steady state production of product in the flow reactor, the same reaction scheme would hold. However, the lower pressures used would affect the adsorption equilibria and cause less hydrocarbon buildup and more H_2 adsorption. The rate of hydrogenolysis of the residue to methane would be comparable to the rate of adsorption of hydrocarbon so the surface would be kept partially free of residues and be continually renewed as in a true catalytic reaction. More than one monolayer (10^{15} molecules) of product has been formed in the flow reactor configuration with the cyclohexane dehydrogenation reaction. In a batch reactor configuration the cyclohexane dehydrogenation had the same behavior as the other reactions and produced only a fraction of a monolayer of product, benzene.

Table A-1. Prediction of observed temperature dependence.

T°K	k_1	k_2	P
500	10^{-5}	3×10^{-6}	$\sim3\times10^{14}(1 - e^{-10^{-5}t})$
600	10^{-2}	10^{-4}	$\sim10^{13}(1 - e^{-10^{-2}t})$
700	1.2	10^{-3}	$\sim10^{12}(1 - e^{-t})$

This model explains the general trends of the batch reaction data and can justify the differences between the batch and flow experiment's deactivation of the catalyst. A more accurate fit of the data could readily be obtained by adding more parameters to the model, however, neither the data nor the model justify more accuracy. If this model is correct, in principal, then what has been measured in the batch experiments is not representative of a true catalytic reaction where the catalytic site is used many times. The deactivation of the catalyst occurs rapidly and will greatly effect the product distribution as well as the reaction rate. The product production rate is analogus to an isothermal desorption, an exponential decay in the rate of desorption, but the amount available for desorption decreases with increasing temperature. The poisoning or residue formation increases more rapidly with temperature than the conversion to the desired product, P, causing the maximum in the measured rate and the decrease in the number desorbed. Thus, the carbonaceous residue formation is the controlling factor throughout the measurable range instead of the product formation kinetics.

The Ir catalysts appear better under the batch experiment conditions because the residure formation kinetics are different and allow conversion to dominate. It is interesting that the Ir catalysts when heated in the batch reactor cause a rise in the reactant pressure, particularly with n-heptane. On the other hand when the Pt catalysts are heated under the same experimental conditions, the reactant pressure decreases rapidly without a concomitant increase in the desorbed products. Apparently the hydrocarbon fragments occupy less area on the

Pt surface than the relatively whole molecules, and upon heating more hydrocarbon molecules can be adsorbed and decomposed on the Pt catalysts. Iridium does not bond the hydrocarbon molecules in a similar manner to Pt and some of the reactant molecules can desorb before they decompose and leave bare metal surface. The bare metal can then adsorb H_2 and become an efficient catalyst, as discussed in Section 6.6.

In conclusion, the batch experiments performed with the Pt catalysts have been shown to not be truly representative of the catalytic reactions on Pt, but are representative of the ability of Pt to decompose organic molecules to stable residues.

APPENDIX B. DESIGN OF HIGH PRESSURE SYSTEMS FOR UHV STUDY

B.1. Design Criteria

There are several criteria which should be met to have a useful high pressure volume in a UHV system.

B.1.1. Essential Criteria

1. The most obvious is that the high pressure chamber must be vacuum compatable. The materials of construction and gaskets should not outgas, the pressurized volume should easily pump down to UHV conditions and not leak to UHV when pressurized.

2. The high pressure apparatus, when open to ultra-high vacuum, must not interfere with the UHV instruments. If the sample is to be sputter cleaned, no sample material should be deposited on the areas which are exposed to high pressure. These could and probably would become catalytically active and cause very high background rates.

3. The surface area exposed to high pressures and later pumped to UHV must be kept a minimum. There is slow reversible physical adsorption of most hydrocarbons on the stainless steel walls. These molecules will slowly desorb under UHV conditions causing a high ($\lesssim 10^{-8}$ Torr) level of hydrocarbons in the background for a considerable time. This could cause uncertainties with the UHV measurements. This was discussed in Section 2-4 with respect to low pressure reactions.

4. The gases and vapors in the high pressure reactor and the inlet lines must be well mixed and there must be provision for withdrawing a representative sample of the gas. Without mechanical mixing, diffusion can be a major problem, particularly with sampling.

5. A system is needed to measure gas compositions at both high and low pressures. A mass spectrometer is used at low pressures and a gas chromatograph at high pressures with a connection to the mass spectrometer to help in compound identification. A capillary column in the gas chromatograph allows complete separation and identification of all reaction products but requires small sample size. A larger sample (containing more product) can be used with a standard column which has less separation.

6. The ratio of high pressure volume to catalyst surface area should be kept as low as possible for ease in measuring the reaction rate. The product is produced at a rate in the range of 100 to 10^{-4} molecules, surface atom/sec, the more interesting reactions being in the range of 1 to 10^{-2}/sec. With 1.0 cm^2 of catalyst surface (typical for a single crystal slice is 0.7 to 1.0 cm^2) the rate is 10^{13} to 10^{15} molecules/sec. In one liter at atmospheric pressure there are approximately 3×10^{22} molecules; the hydrocarbon reactant compromising 0.1 to 0.01 of this. In the worst cast, the product is produced at a rate of 1 molecule per $3\times10^{+8}$ reactant molecules per second. The limit of sensitivity on a gas chromatograph with a flame ionization detector is $\gtrsim$1 ppm or 10^{-12} amp/sec, which ever is larger. Thus it requires 300 sec (5 min) before product can be detected (10^{-2} sec^{-1}, 1ℓ total volume, 0.5 ml sample size). If the volume is reduced by 90%, the time, before product can be detected, is dropped to 30 sec. This is because there is only 1/10 the dilution of the product in the reactant gases. (The sample size, the maximum possible for use with a capillary column, is 0.5% of the total volume, a

satisfactory level. A capillary column allows separation and identification of all reaction products.) The most satisfactory size appears to be 25 to 50 ml with a 0.1 ml sample size.

7. Heating of the catalyst sample is required at both low and high pressures. Resistively heating the single crystal samples is attractive if an inert support material can be found. Tantalum is inert catalytically but becomes embrittled by hydrogen at high pressures (200 Torr and 400°C). Most other catalytically inert metals have high vapor pressures and/or low surface tensions and would contaminate the catalyst. Radiation heating might provide insufficient power to a metallic sample at atmospheric pressure to overcome conduction losses to the gases. Heating the gas in the reactor and manifold to reaction temperature at high pressure is possible, but 450°C is too high for valves and the gas circulating device.

8. The temperature of the catalyst must be measurable. A thermocouple is of course the best way to measure the temperature of a metal sample; with a non-conductive sample the gas temperature can be measured.

B.1.2. Convient Criteria

Some features which are useful to incorporate into the design are:

1. The ability to pressurize quickly and return to ultra high vacuum fast is handy. A second or 10 min are both long on the molecular time scale of 10^{-12} sec, but the reversibly held ($\Delta E_{des} \approx$ 10 to 20 kcal/mole) molecules desorb for several minutes. They probably are measurable with a few second pump out time, but might be completely desorbed in 10 min. For the strongly held residues this is not a problem.

2. The reactor should be pressurizable to at least near the industrial conditions of the reaction being studied. This requires about 100 atm for NH_3 synthesis, Fischer-Tropsch synthesis and coal liquification, but only 1 to 5 atm is acceptable for hydrocarbon reforming on Pt metals.

3. The catalyst sample should be mobile at low pressure to facilitate analysis and assure the uniformity of the surface.

4. The entire gas manifold and reactor should be bakeable to a 100°C to allow condensable hydrocarbons to be used at pressures greater than their room temperature vapor pressures (20 Torr or lower). A small oven outside and probably electron bombardment in the vacuum are the easiest methods of accomplishing this.

5. Liquid phase work can be done if the system is designed for liquid drainage and N_2 gas flushing. This might be useful in coal liquification and dehydrosulfurization studies. Since liquid phase diffusivities are much lower than gas phase the circulating gas (H_2) should be bubbled up through the liquid to provide sufficient mixing.

6. It is also necessary to decide if the high pressure chamber should be inside the experimental area of the high vacuum chamber or attached as an appendage in order to not tie up the equipment. The first approach has been taken in this laboratory for the fundamental investigations undertaken. However, if actual catalysts were being studied where extended (several days) treatments are common or the machine is very expensive (i.e., an X-Ray Photoelectron Spectrometer) an appendage chamber would be advantageous.

B.2. Experimental High Pressure Systems

The systems used in this laboratory have progressed from a very simple add-on chamber to the recent additions of a custom built high-low pressure system and an adaptor for a Varian LEED chamber. They have also progressed in usefulness.

B.2.1. Early Models

The first chamber for atmospheric pressure work was a long bellows placed between the manipulator and a gate valve attached to the chamber. The crystal was moved up into the bellows and the gate valve shut. It is shown in Fig. B-1. Its purpose was to do adsorption studies of oxygen and fluorine at pressures near atmospheric. It had many disadvantages: high volume, high wall surface area, no provision for mixing gases; and several minutes to position the crystal in front of the LEED optics. It was, however, easy to build and readily attached to any of the LEED systems.

The second high pressure system was built around the high pressure cup. Its design has been described by Kahn[88] and Kahn, Petersen and Somorjai[221] and is shown in Fig. B-2. The 0.75ℓ cup encloses the crystal and support rods, but its placement makes it difficult to do Auger electron spectroscopy and impossible to do LEED. Auger Electron Spectroscopy is performed with a glancing incidence gun and a retarding potential analyzer which is centered at an angle of 40° to the surface normal and collect only $\pi/2$ steradian. The crystal is fixed but this is not a loss since LEED is not done. The surface area exposed to high pressure is low but the volume is still too high. The high pressure to UHV seal is a 4-1/2 in. diameter gold "O" ring

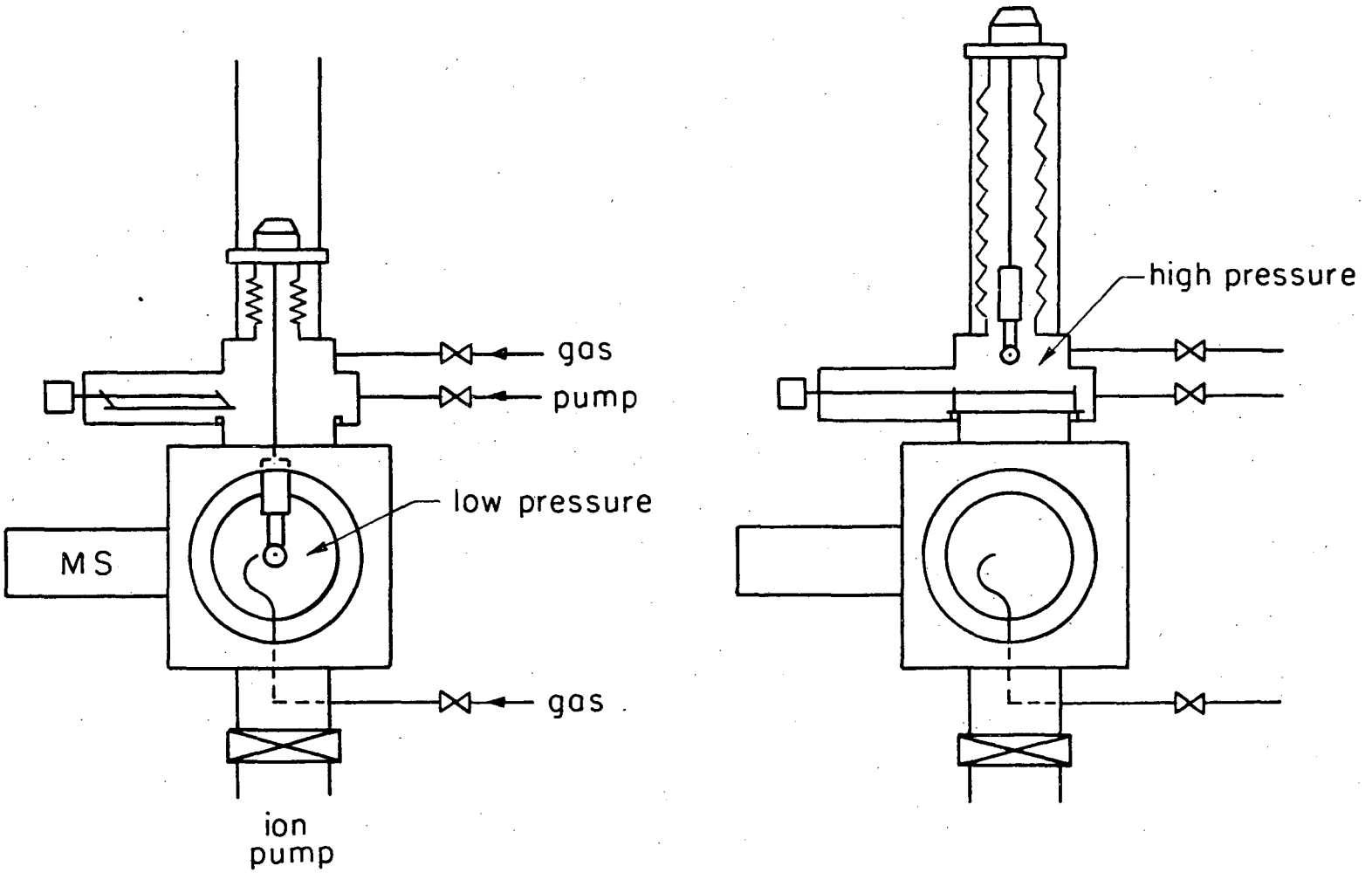

Fig. B-1. LEED chamber with manipulator on a long bellows. Sample could be retrieved above gate valve for high pressure treatment.

XBL 756-6429

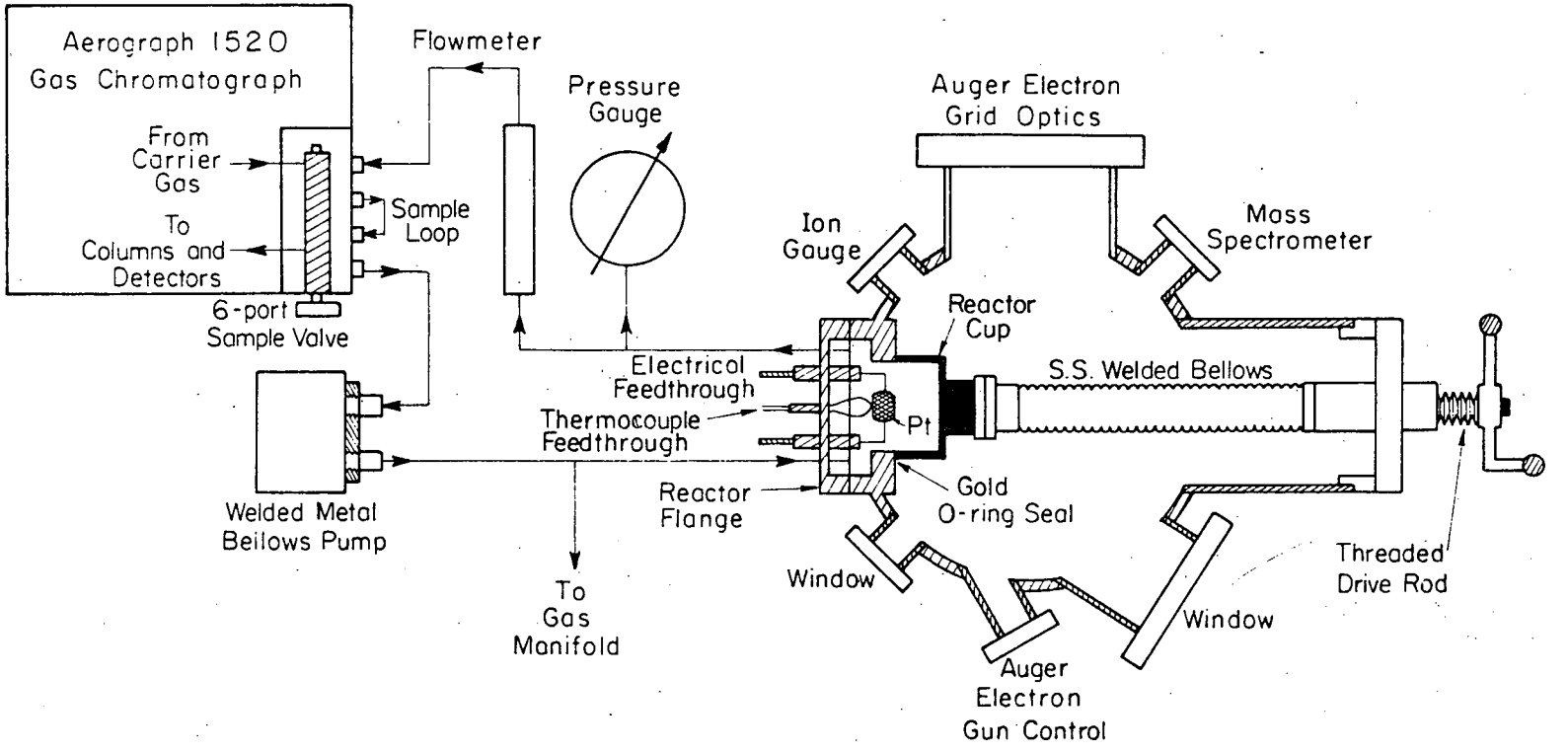

SCHEMATIC OF FLOW LOOP FOR HIGH PRESSURE (1 ATM.) CATALYSIS ON SINGLE CRYSTAL PLATINUM SURFACES

XBL 734-5969

Fig. B-2. Apparatus for atmospheric pressure studies designed by Kahn.[88] Immovable sample is encased in 0.75 ℓ cup.

which sets against "knife edges". If used carefully the O ring will seal over 100 times. Gas mixing and sampling are readily accomplished by a stainless steel welded bellows pumped and circulation loop. This reactor has been useful in studying high reactivity reactions, such as cyclopropane ring opening and cyclohexane dehydrogenation to benzene. It has also been used to study n-heptane dehydrocyclization on single crystals. A large sample volume was necessary which prevented the use of a capillary chromatographic column. Thus accurate determinations of all the reaction products are difficult. The catalyst sample is easily heated resistively by mounting on Ta rods.

B.2.2. Recent Designs

Recently, two more useful chambers have been designed and constructed. One which is a specially constructed vacuum chamber is used to study reactions which are run industrially at high pressures (greater than 50 atm). Typical reactions in this class are ammonia synthesis, Fischer-Tropsch synthesis and coal hydrogenation. The second newly designed reaction chamber will bolt into a Varian LEED chamber with no modifications to the chamber or instruments. Both these high pressure chambers have low volume (about 25 cm^3 total in high pressure gas loop) and low surface area exposed to high pressure, and when opened do not interfere with the surface characterization and cleaning instruments.

B.2.2.1. High Pressure System. The very high pressure apparatus has a hydraulic pressure mechanism, as shown in Fig. B-3, to seal the gasket. This also prevents over compression of the gasket from thermal expansion of the reactor. The gasket is a standard "mini" flange Cu gasket which was softened by annealing at 650°C in a hydrogen furnace.

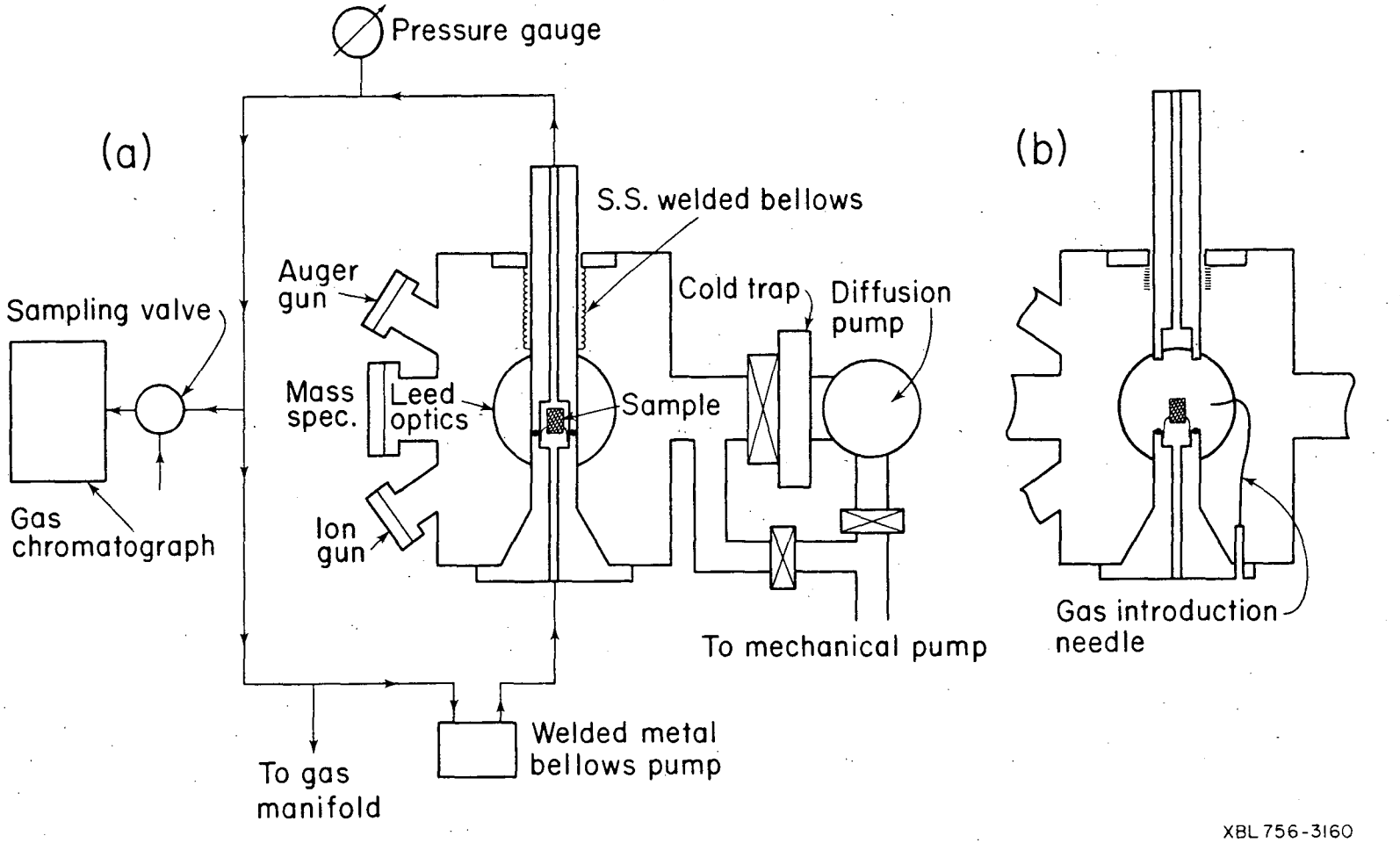

Fig. B-3. Apparatus for high pressure studies. Rotatable sample is encased in 25 ml gas system.

The present gasket has 10 closures and when pressurized with 100 atm of H_2 the background pressure is not raised. Copper was chosen because Au might flow at the 100 atm pressure and 450°C temperatures. The seal is made with two "knife-edges"; 100 atms hydraulic pressure of the cup is necessary to maintain the seal at 100 atm of H_2 internal pressure. There are two arrangments for heating the samples. If the sample is metallic, it is heated resistively and mounted as depicted in B-3 The rotary motion is a conventional high pressure teflon packing gland valve. This system allows about 180° rotation of the samples but no X-Y motion. For non-metallic samples, such as pieces of coal or the unreduced commercial synthesis catalysts, radiation heating is used in vacuo and the entire high pressure chamber is heated by external electron bombardment. If the inlet gas line is also heated, the sample temperature is very close to the wall temperature as determined on a metal sample with the gas circulating. The sample can be mounted on the rotary motion manipulator or mounted rigidly as shown in Fig. B-3; however, this device was conceived for the possibility of performing liquid-phase hydrogenation (liquification) of coal. It is designed for liquid to drain out the bottom with minimum hold-up and gas flushing required before opening to UHV. A liquid phase experiment has not been performed to test the design.

The chamber is pumped by a Ti sublimation pump and by an 8 in. oil diffusion pump (Octoil pump oil) equipped with an LN cooled cheveron baffled cold trap. This gives the system the very high pumping speed necessary for fast pump down from high pressure with the coal samples. The mass spectrometer shows no more hydrocarbon

contamination than is found in an ion pumped system after similar use. The system base pressure is 5×10^{-9} Torr. The pump down time from an atmospheric pressure mixture of CO and H_2 in the high pressure chamber to 1×10^{-8} Torr is about 2 min with a slow decrease (~1 to 2 hr) to the ultimate base pressure. With coal pyrolysis experiments the pump down time would be slower due to the high molecular weight hydrocarbons; however, experience with the 0.75ℓ cup indicates that the times will not more than double. With liquid phase experiments there would be a significant increase in the pump down time. The gases are mixed and circulated by a bellows pump enclosed in a pressurizable cylinder to allow its use above atmospheric pressure. The gases enter the high pressure cup from the bottom and leave at the top, stirring the liquid, if present, to remove diffusional limitations. The absence of diffusional limitation in the gas phase in an unstirred cup has been demonstrated by Kahn.[88] However, in the liquid phase the diffusivity is five orders of magnitude smaller and the rate would be severely limited by diffusion without the stirring provided by the gas bubbling through the liquid.

B.2.2.2. Atmospheric Pressure System. The atmospheric high pressure reaction chamber currently under construction will be used to study reaction of hydrocarbons on transition metals single crystals. The design is similar to that shown in Fig. B-3. The sample is mounted beneath the high pressure cup cap which is mounted on a normal sample manipulator. The X-Y motion of the manipulator is restricted to 2 cm by the yoke. The rotation of the manipulator is limited to 195° by the electrical feed-throughs mounted on the side of the cap. These are used for resistive

heating of the sample and thermocouple temperature measurement. In closing the cup, the cap and sample are raised by the manipulator about 7 mm into the centering yoke which supports the closure stress. The cup is then raised enclosing the sample and sealing to the cap. The seal is made by a two "knife-edge" and a gold "O-ring". The flexible gas inlet lines and cup walls are heatable to ~150°C by electron bombardment; the gas lines external to the chamber are in a 150°C oven. This heating allows atmospheric pressures of C_8 and smaller hydrocarbons to be used without condensation in the lines. Pump down time should be quite fast since the heated walls reduce physisorption of hydrocarbons.

The two recently designed and constructed high pressure chambers should prove to be very useful, versatile research tools. Practically all heterogeneous catalytic hydrocarbon reactions, hydrogenative or oxidative, may be studied at pressures up to 100 atm on well characterized surfaces. This will be very useful in understanding the effect of the surface structure and composition on the catalytic reaction rates; and the effect of industrially used high pressures and temperatures on surface structure and composition.

APPENDIX C. THE GLIDE SYMMETRY IN LEED PATTERNS

The phenomena of missing beams in LEED experiments has caused considerable difficulty in interpretation of the patterns. It has recently been observed that the general symmetry of the system affects the intensities of the beams and may cause come to vanish.[97] Lambert[227] has shown that the missing $\{1/2\ h^{odd},0\}$ beams from CO adsorbed on the (110) faces of Ni, Pd, Pt and Ir may be caused by the glide symmetry in the dimensional point group plgl. The position of the CO molecules is a zigzag pattern in the trough with one molecule per Pt atom in the top layer. The glide line is along the top of the ridges. It should be mentioned that Taylor and Erstrup[127] observed very dim $\{1/2\ h^{odd},0\}$ spots for CO on Ni(110). Ni(110) is the surface with the most steric hinderance for packing CO molecules in the required positions and apparently the symmetry breaks down, probably with out plane positions of some molecules.

Another recent work in which a set of missing diffraction beams caused a mis-interpretation of the pattern is the study of napthalene on a Pt(111) surface.[212] The diffraction pattern is shown in Fig. C-1a. It can be readily seen that this pattern is composed of three rectangular domains of $\begin{vmatrix} 6 & 3 \\ 0 & 3 \end{vmatrix}$ with the $\{h^{odd},0\}$ and $\{0,k^{odd}\}$ diffraction beams missing and other beams dimmer. This readily follows from a 4 molecular basis set with a plg2 point group glide symmetries are required along both the axes. The brighter beams occur where the 3 domains overlap and the dimmer beams are from 1 domain. If the molecules and the unit cell are put in the positions shown in Fig. C-1b the overlayer and first layer of Pt atoms have the correct general symmetry.

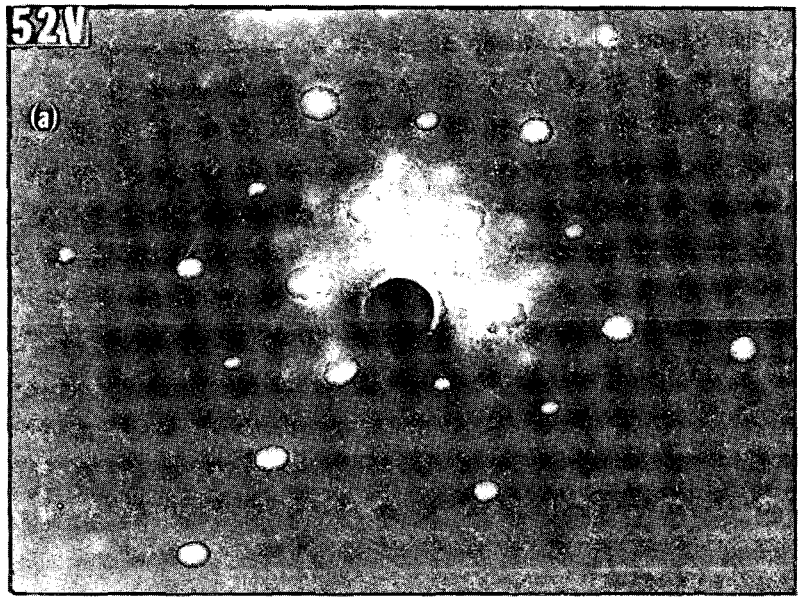

XBB 761-209

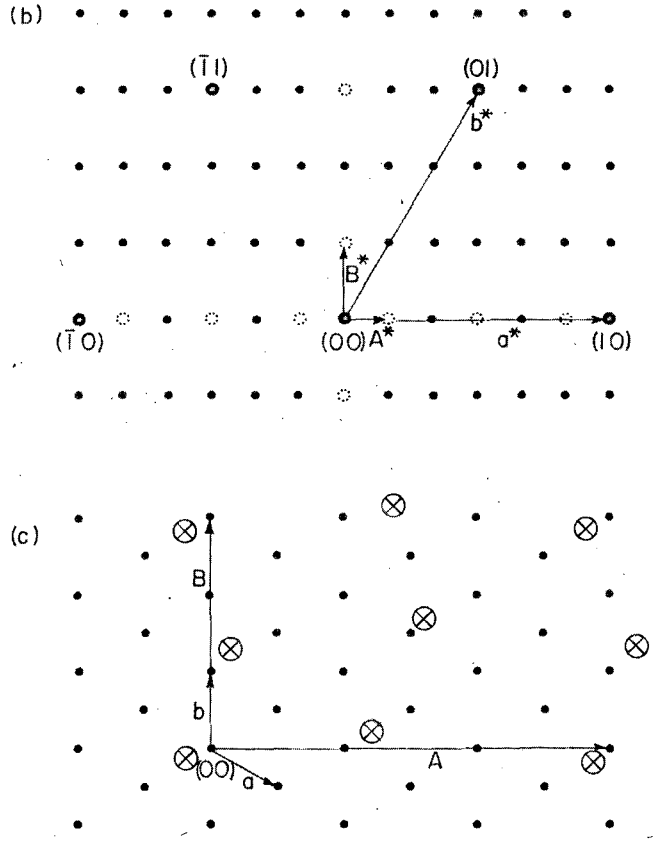

Fig. C-1. Photograph of LEED pattern of napthalene on Pt-(111)[212] is shown in (a). (b) is one domain of the diffraction indicating missing spots (☆) and (c) shows proposed interpretation of the diffraction pattern with two glide axes, one parallel to each unit cell vector.

The positions for the molecules are (-x,-y), (1/2+x, 1/2+y), (1/2-x,y) and (x,1/2-y) based on $(\vec{a},\vec{b})$ where x and y are arbitrary displacements. The molecular positions are almost identical with the (001) $(\vec{a},\vec{b})$ plane of crystalline nepthalene.[188] In solid napthalene (001) plane there is one glide axis and one screw axis. However, a screw axis in two dimensions appears as a glide axis and causes the same beams to vanish, therefore, the adsorbed layer of napthalene may have the same positions and symmetry as bulk napthalene.

APPENDIX D. THE SURFACE TENSION OF CRYSTAL SURFACES

D.1. Surface Free Energy

The atoms on a surface of a solid or liquid have an excess free energy, G^s, over atoms in the bulk.[129] It is this excess free energy or potential to do work which contracts liquid drops into balls and causes faceting on crystals. The work done in producing a surface of area A and orientation $\vec{n}$ at constant temperature and pressure is

$$\delta W_{T,P} \equiv \gamma(\vec{n})\ dA \quad , \tag{D-1}$$

which defines $\gamma(\vec{n})$, the surface tension of a material. For a liquid γ is independent of orientation, but in a crystalline solid γ is anisotropic. From the thermodynamics reversible work of producing surface is the change in free energy

$$\delta W_{T,P} = \left(\frac{\partial G}{\partial A}\right)_{T,P} da = \left[\frac{\partial (NG^\circ + G^s A)}{\partial A}\right]_{T,P} dA \tag{D-2}$$

where G° is the free energy of an atom in the bulk and N the number of atoms. Since NG°, the free energy if all the atoms were in the bulk, is independent of surface are A, Eq. (D-2) becomes

$$\delta W_{T,P} = \left[G^s + A\left(\frac{\partial G}{\partial A}\right)_{T,P}\right] dA \quad . \tag{D-3}$$

Since G^s is a function of n, $\left(\frac{\partial G^s}{\partial A}\right)_{TP}$ can be written as a tensor, which is called the surface stress tensor. In single component systems with particle size larger than $\sim 10^{-5}$ cm, the stress tensor generally becomes negligibly small. Therefore, equating Eqs. (D-1) and (D-3)

$$\gamma(\vec{n}) = G^s(\vec{n}) \tag{D-4}$$

defines surface tension for a macroscopic, single component system.

D.2. Stability of a Surface

Any system trys to minimize its free energy. At constant T and P, NG° is fixed and the total surface energy must be minimized to obtain the equilibrium configuration. Since γ is orientation dependent, this integral which must be minimized is of the form

$$\int \gamma(\vec{n})\, dA \quad . \tag{D-5}$$

On small particles, of the order of 1 to 10 microns in size, the sample can move enough atoms to obtain its ultimate equilibrium shape minimum total free energy. This geometric shape can be determined by the Wulff construction.[116,228] At each point on the polar plot of γ with crystallographic orientation, a perpendicular to the radius is constructed. The volume which does not cross any of these lines is geometrically similar to the ultimate equilibrium shape. This is demonstrated in Fig. D-1.

On large crystal, such as used in LEED experiments, the crystal does not obtain its equilibrium shape, but the surface may take on a microscopic hill and valley structure to lower its free energy, i.e., minimize Eq. (D-5). This hill and valley structure, or a faceted surface, will occur in preference to the plane surface if the rhs of Eq. (D-6) is smaller than the lhs. In Eq. (D-6)

$$\gamma_p A_p \gtrless \gamma_o A_o + \gamma_c A_c \tag{D-6}$$

γ_p, γ_o and γ_c and A_p, A_o and A_c are the surface tensions and areas of the plane surface, low Miller Index cusp and complex plane, respectively

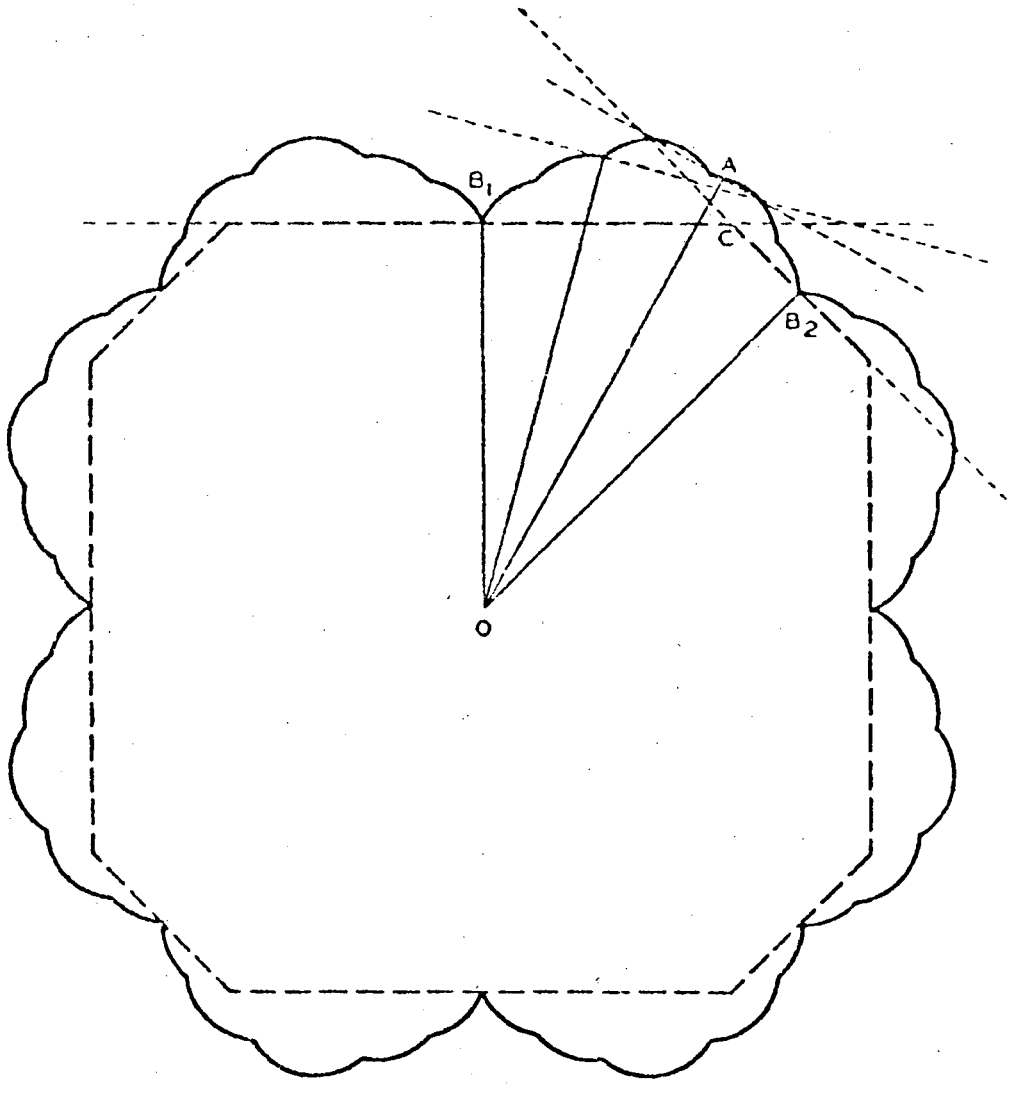

XBL 764-1603

Fig. D-1. Typical plot of surface free energy anisotropy with angular rotation showing construction of equilibrium polyhedron (from Ref. 116).

as shown in Fig. D-2. Given a γ plot such as Fig. D-1, the stability of a surface with respect to faceting may be readily determined. Herring[116] has shown that for a plane surface to be stable, it must lie on a portion of the Wulff construction which coincides with the γ-plot; in other words all surfaces in Fig. D-1 facet to a hill and valley structure. This also says unless the γ-plot is spherical, there is a region near the low index pole cusps in which the surface always facets. This has not been observed experimentally either by LEED or groove techniques to angles as small as 2° from the low index cusp.

It has been pointed out by Meijering[229] that it is easier to use the $1/\gamma$-plot to determine the stability of a surface. In Fig. D-2 a plane surface AB, with normal, $\vec{n}_p$, is shown with two possible facet planes, AC with normal $\vec{n}_o$ and BC with normal $\vec{n}$. An auxiliary line, AD, is constructed in Fig. D-2 such that $\angle CDA$ is equal to $\angle QSO$ in the $1/\gamma$-plot, Fig. D-3. Now ΔACD and ΔOSQ, and ΔBCD and ΔSRO are similar triangles, so that

$$\frac{AC}{OQ} = \frac{AD}{OS}$$

and (D-7)

$$\frac{BC}{RO} = \frac{BD}{OS}$$

The two equations in Eq. (D-7) are added to give Eq. (D-8)

$$\frac{AC}{OQ} + \frac{BC}{RO} = \frac{AD}{OS} + \frac{BD}{OS} = \frac{AB}{OS} \quad . \tag{D-8}$$

From the definitions of Figs. D-2 and D-3 , Eq. (D-8) is formally equivalent to Eq. (D-6). Since $1/\gamma$ must be maximized, the

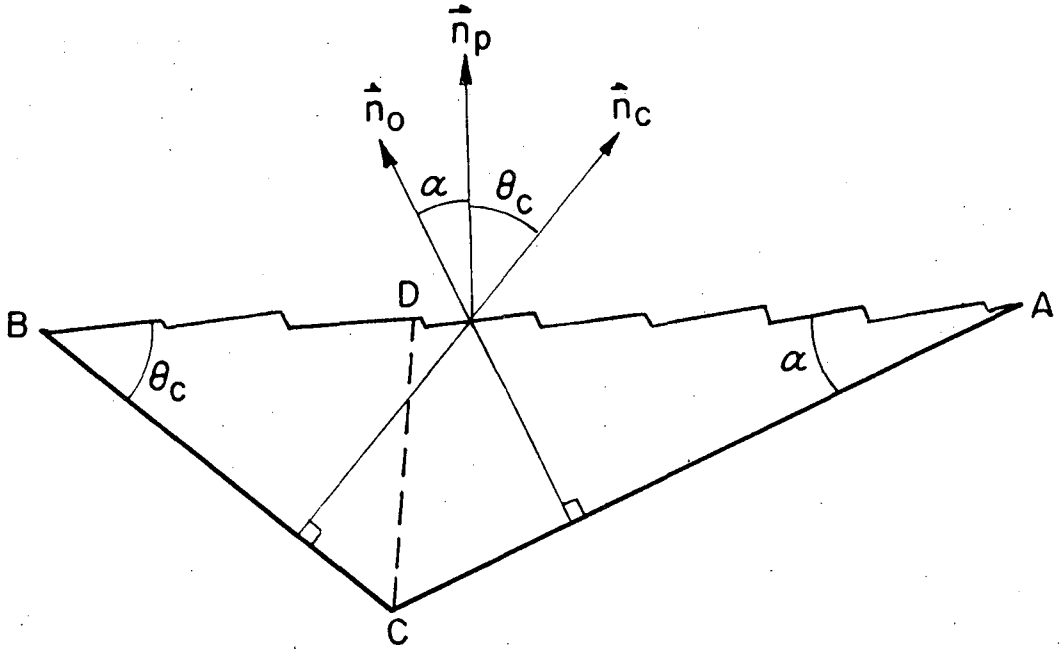

Fig. D-2. Possible faceting for a stepped surface defining the various surfaces.

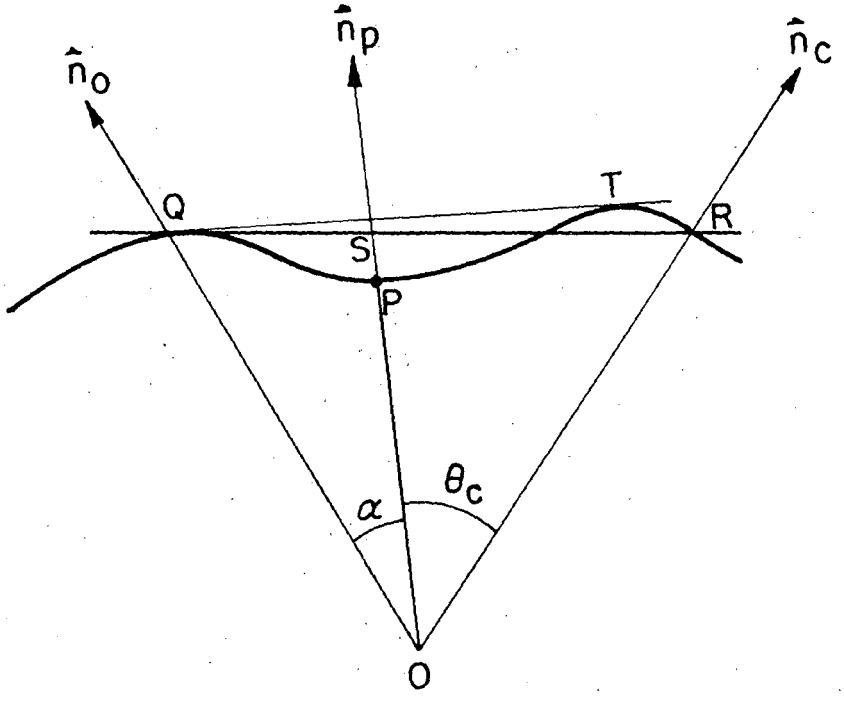

Fig. D-3. Reciprocal γ plot demonstrating determination of maximum extent of faceting (from Ref. 229).

surface will facet if OS, the reciprocal of the effective surface tension, γ_{eff}, of the hill and valley structure, is greater than OP, the reciprocal of the plane surface tension, γ_p. In the case shown in Fig. D-3, OS > OP ($\gamma_{eff} < \gamma_p$) and the surface would facet. However, it is obvious that a still larger $1/\gamma_{eff}$ can be produced by the orientations OQ and OT. As seen the double tangent line QT produces the largest $1/\gamma_{eff}$ not only at orientation OPS, but at all orientations between OT and OQ. Thus all orientations whose $1/\gamma$ plot lies inside a double tangent line (or touching at a cusp) are unstable with respect to a hill and valley structure consisting of planes whose orientation is at the tangent points. A concave $1/\gamma$ will always cause faceting while a convex $1/\gamma$ plot will not cause faceting. If a surface has a $1/\gamma$ plot composed of straight segments, it will be thermodynamically stable in any configuration; its ultimate shape will be controlled by kinetics.

D.3. The Twin Boundary Groove Method

This technique can be used to measure the relative surface tension of an annealing object. McLean and Mykura[121] have used the groove technique[117] to measure the surface free energy anistropy of Pt. In this technique the energy of a twin plane is used to roughen the surface of the sample with the local surface free energy acting to smooth the surface as shown in Fig. D-4. Since a metal always twins on the same plane, the energy of the twin boundary is constant. On different grains the twins will make different angles with the macroscopic normal, each having a different dihedral angle, θ. Therefore, using a large number of twin boundary groove angles for various orientations allows the surface free energy anisotropy to be plotted.

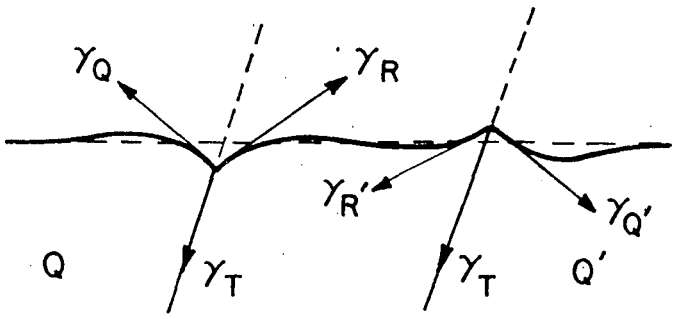

XBL 763-6615

Fig. D-4. The effect of a pair of twins on the smoothness of a macroscopic surface (from Ref. 117).

APPENDIX E. DETERMINATION OF HYDROGENOLYSIS STANDARD DEVIATION

Since there is a large measurement error associated with the determination of the rate of hydrogenolysis of CH to Hx, a statistical analysis was deamed appropriate. The test chosen was the F test. The F-statistic is the ratio of the standard deviation between means to the standard deviation of points within each mean. For a given number of points in each mean, the F-statistic must be larger than a number which can be looked up in a table,[210] if the two means compared are significantly different from each other at a given confidence level. The standard deviation of the means must be larger than can be explained by the random error in the individual points.

The data for hydrogenolysis rate with H_2 to hydrocarbon ratio was used. This allows an increased number of data points to be used to calculate the value of the rate at 300 to 1 H_2 to hydrocarbon ratio. The slope of the line is calculated with a zero rate at 20 to 1 ratio (determined from the equilibrium constant). The residual standard deviation from this procedure (linear regression) is used as the standard deviation of the individual points within the mean. The F-statistic is the calculated from the formula

$$F(m-1,\ (\Sigma n_i)-2) \approx \frac{\left(\frac{(\Sigma n_i)-1}{2}\right) \sum_1^m (\mu_i - \bar{\mu})^2}{\frac{\sum_1^2 (n_i - 1)\, S_i^2}{(\Sigma n_i) - 2}} \qquad \text{(E-1)}$$

where n_i is the number of individual data points in mean i, μ_i is the value of the mean at 300 to 1 ratio, $\bar{\mu}$ is the average of the means, S_i is the standard deviation of the individual mean i, and m is the number of means to be compared. The values of the F statistic calculated with Eq. (E-1) are given in Table E-1 along with the 95% confidence level value of F. As seen there is a significant difference between the values of hydrogenolysis rate for the various stepped surfaces.

Table E-1. F-statistic for hydrogenolysis rate.

Catalyst Compared	μ_i	S_i	F_{calc}	$F(1,n)_{table}$	n
7(111)×(310)	11.1	1.9	29.6	4.96	10
6(111)×(610)	5.6	0.53			
6(111)×(610)	5.6	0.53	9.3	5.1	9
6(111)×(100)	5.1	0.23			
6(111)×(100)	5.1	0.23	18	4.67	13
3(111)×(100)	6.6	0.79			

REFERENCES

1. J. H. Sinfelt, Adv. Chem. Engr. 5, 37 (1964).
2. H. F. Harnsberger, private communication.
3. V. Ponec, Cat. Rev.-Sci. Engr. 11, 1 (1975).
4. J. K. A. Clarke, Chem. Rev. 75, 291 (1975).
5. P. B. Weisz and E. W. Swegler, Science 126, 31 (1957).
6. S. M. Csicsery and R. L. Burnett, J. Cat. 8, 75 (1967).
7. S. M. Csicsery, J. Cat. 15, 111 (1969).
8. J. L. Carter, J. A. Cusamano and J. H. Sinfelt, J. Cat. 20, 223 (1971).
9. J. R. Anderson, Adv. Cat. 23, 1 (1973).
10. J. Newham, Chem. Rev. 63, 123 (1963).
11. Y. Barron, G. Marie, J. M. Muller and F. G. Gault, J. Cat. 5, 428 (1966).
12. Y. Barron, G. Marie, D. Cornet and F. G. Gault, J. Cat. 2, 152 (1963).
13. G. Marie and F. G. Gault, Bull. Soc. Chim. Fr., 894 (1967).
14. C. Corolaur, D. Tomanova and F. G. Gault, J. Cat. 24, 401 (1972).
15. F. M. Dautzenberg and J. C. Platteeuw, J. Cat. 19, 41 (1970).
16. J. R. Anderson and N. R. Avery, J. Cat. 8, 48 (1967).
17. J. R. Anderson and N. R. Avery, J. Cat. 5, 446 (1966).
18. J. R. Anderson and N. R. Avery, J. Cat. 7, 315 (1967).
19. M. Boudart, A. W. Aldag, L. D. Ptak and J. E. Benson, J. Cat. 11, 35 (1968).
20. J. M. Muller, Ph. D. Thesis, University of Caen, Caen, France (1969).
21. M. Boudart and L. D. Ptak, J. Cat. 16, 90 (1970).
22. M. Boudart, Adv. Cat. 20, 153 (1969).

23. M. Boudart, A. Aldag, J. E. Benson, N. A. Dougharty and C. Girvin-Harkins, J. Cat. 6, 92 (1966).

24. M. Boudart, AIChE J. 18, 465 (1972).

25. W. H. Manogue and J. R. Katzer, J. Cat. 32, 166 (1974).

26. D. W. Blakely and G. A. Somorjai, to be published, J. Cat.

27. A. N. Mitrofanova, V. S. Boronin and O. M. Poltorak, Zh. Fiz. Khim. 46, 32 (1972).

28. O. M. Poltorak and V. S. Boronin, Zh. Fiz. Khim. 40, 2671 (1966).

29. M. Kraft and H. Spindler in Proceedings of the 4th International Congress on Catalysis (Akademiai Kiado, Budapest, 1971), Vol. 2, p. 286.

30. J. A. Cusumano, G. W. Dembinski and J. H. Sinfelt, J. Cat. 5, 471 (1966).

31. R. W. Maatman, P. Mahaffy, P. Hoekstra and C. Addink, J. Cat. 23, 105 (1971).

32. P. C. Aben, J. C. Platteuw and B. Stouthames in Proceedings of the 4th International Congress on Catalysis (Akademiai Kiado, Budapest, 1971), Vol. 1.

33. T. A. Dorling and R. L. Moos, J. Cat. 5, 111 (1966).

34. R. Herz and D. Kahn, private communication.

35. P. N. Ross and P. Stonehart, presented at the ACS Meeting, Los Angeles, CA, April 2, 1974.

36. S. L. Bernasek and G. A. Somorjai, J. Chem. Phys. 62, 3149 (1975).

37. R. Van Hardeveld and F. Hartog in Proceedings of the 4th International Congress on Catalysis (Akademiai Kiado, Budapest, 1971), Vol. 2., p. 295.

38. K. Schrage and R. L. Burwell, J. Amer. Chem. Soc. 88, 4549 (1966).

39. H. J. Maat and L. Moscou, 3rd International Congress on Catalysis, Section II, paper 5 (1964).

40. J. L. Carter, J. A. Cusumano and J. H. Sinfelt, J. Phys. Chem. 70, 2257 (1966).

41. D. J. C. Yates and J. H. Sinfelt, J. Cat. 8, 348 (1967).

42. J. R. Anderson and Y. Shimoyama in Proceedings of the 5th International Congress on Catalysis, p. 696 (1973).

43. P. Pareja, A. Amariglio and H. Amariglio, J. Cat. 36, 379 (1975).

44. R. Maurel, G. Leclercq and J. Barbier, J. Cat. 37, 324 (1975).

45. G. A. Somorjai, J. Cat. 27, 453 (1972).

46. T. A. Dorling, M. J. Eastlake and R. L. Moss, J. Cat. 14, 23 (1969).

47. I. Yasumori, H. Shinohara and V. Inoue in Catalysis, J. Hightower, ed. (North Holland, Amsterdam, 1972).

48. B. Lang, R. W. Joyner and G. A. Somorjai, J. Cat. 27, 405 (1972).

49. K. Baron, D. W. Blakely and G. A. Somorjai, The Influence of Step Densities of the Reactivity of n-Heptane Dehydrocyclization and Isomerization on a Series of Low and High Miller Index Platinum Single Crystals, LBL-2796 (1974).

50. O. M. Poltorak and V. S. Boronin, Zh. Fiz. Khim. 40, 1436 (1966).

51. H. P. Bonzel and R. Ku, Surf. Sci. 33, 91 (1972).

52. J. Ostermaier, J. R. Katzer and W. H. Manogue, J. Cat. (to be published).

53. S. C. Dahlberg, G. A. Fisk and R. R. Rye, J. Cat. 36, 224 (1975).

54. G. R. Wilson and W. K. Hall, J. Cat. 17, 190 (1972); 24, 306 (1972).

55. M. A. Vannice, J. Cat. 40, 129 (1975).

56. J. Freel, J. Cat. 25, 149 (1972).

57. G. A. Somorjai and D. W. Blakely, Nature 258, 580 (1975).

58. N. Taylor, Varian LEED Manual, 1965.

59. H. B. Lyon, Jr., Low Energy Electron Diffraction Study of Low Index Platinum Single Crystal Surfaces (Ph. D. Thesis), UCRL-17549, June 1967.

60. M. A. Chesters and G. A. Somorjai, Ann. Rev. Mat. Sci., R. A. Higgins, ed., Annual Reviews Inc., 1975, p. 418.

61. H. H. Farrell and G. A. Somorjai, Adv. Chem. Phys. 20, 215 (1971).

62. L. L. Kesmodel and G. A. Somorjai, MTP International Review of Science (to be published).

63. R. C. A. Tube Manual (1960).

64. F. L. Szalkowski, Auger Electron Spectroscopy Analysis of Vanadium and Vanadium Compound Surfaces (Ph. D. Thesis), LBL-888, October 1973.

65. L. L. Kesmodel and G. A. Somorjai, Phys. Rev. B. 11, 630 (1975).

66. C. C. Chang, Surf. Sci. 25, 53 (1971).

67. F. L. Szalkowski and G. A. Somorjai, Adv. High Temp. Chem. 4, 137 (1971).

68. P. Palmberg, Auger Spectra (Physical Electronics Industries, Edina, MN, 1974).

69. LBL Print Numbers 7S1103, 7S1113, 7S1122, 7S1132, 7S1143, 7S1152 and 7S1161.

70. LBL Print Number 7S1422

71. B. Lang, R. Joyner and G. A. Somorjai, Surf. Sci. 30, 440 (1972); 30, 454 (1972).

72. R. H. Sille, W. A. Oates and R. B. McLellan, J. Less-Common Metals 16, 71 (1968).

73. G. O. Brink, Rev. Sci. Inst. 37, 857 (1966).

74. UTI Operators Manual; the optimum values vary from instrument to instrument and are determined at the factory.

75. G. J. Schulz, J. Appl. Phys. 28, 1149 (1957).

76. W. McGowan and L. Kerwin, Can. J. Phys. 38, 567 (1960).

77. G. Ehrlich, J. Appl. Phys. 32, 4 (1961).

78. B. Cobic, G. Carter and J. H. Peck, Vacuum 11, 247 (1961).

79. E. W. Rothe, J. Vac. Sci. Tech. 1, 66 (1966).

80. M. L. Shaw, Rev. Sci. Instrum. 37, 113 (1966).

81. N. G. Utterback and T. Griffith, Rev. Sci. Instrum 37, 866 (1966).

82. W. Hultzman (private communication to R. Holanda, J. Vac. Sci. Tech. 10, 1133 (1973)).

83. R. Holanda, NASA Report No. TN D-6815, 1972.

84. J. R. Young, J. Vac. Sci. Tech. 10, 212 (1973).

85. F. Williams, M. Boudart and A. Frennet, J. Vac. Sci. Tech. 9, 362 (1972).

86. Mass Spectral Data, American Petroleum Institute Research Project 44, contributed by Mass Spectrometer Laboratory, National Bureau of Standards, 1947. A Consolidated, #21-102 Mass Spectrometer was used (magnetic sector).

87. O. Levenspiel, Chemical Reaction Engineering (John Wiley and Sons, Inc., NY, 1962).

88. D. Kahn, The Hydrogenolysis of Cyclopropane on Platinum Stepped Single Crystals at Atmospheric Pressure (Ph. D. Thesis), LBL-1891, September 1973.

89. See any elementary chemical engineering text; e.g., Ref. 87 or D. M. Himmelblau, Basic Principles and Calculations in Chemical Engineering (Prentice Hall, Englewood, Cliffs, NJ, 1962).

90. F. Daniels and R. A. Alberty, Physical Chemistry (John Wiley and Sons, NY, 1966).

91. N. F. Ramsey, Molecular Beams (Clarendon Press, Oxford, 1966).

92. D. Hagen and G. A. Somorjai, J. Cat. 41, 466 (1976); D. Hagen, private communication.

93. P. Stair, private communication.

94. S. Csiscery, private communication.

95. M. Chesters and G. A. Somorjai, Surf. Sci. 52, 21 (1975).

96. A. Morgan and G. A. Somorjai, 12, 405 (1968).

97. See any book on diffraction, crystallography of elementary solid state physics; an example is C. Kittel, Introduction of Solid State Physics (John Wiley and Sons, Inc., NY, 1971), p. 78.

98. M. G. Lagally, T. C. Ngoc and M. B. Webb, Phys. Rev. Lett 26, 1557 (1971).

99. J. B. Pendry, J. Phys. C 5, 2567 (1972).

100. J. Buchholz, Ph. D. Thesis, University of Wisconsin, Madison, WI, 1974.

101. U. Landman and D. L. Adams, J. Vac. Sci. Tech. 11, 195 (1974).

102. M. Henzler, Surf. Sci. 19, 159 (1970); 22, 12 (1970).

103. W. P. Ellis, Surf. Sci. 45, 569 (1974).
W. P. Ellis and R. L. Schwoebel, Surface Science 11, 82 (1968).

104. J. Pedereau and G. Rhead, Surf. Sci. 24, 555 (1971).

105. R. L. Park, J. E. Houston and D. G. Schreiner, Rev. Sci. Instr. 42, 60 (1971).

106. J. L. Gland, Low Energy Electron Diffraction and Work Function Studies of Adsorbed Organic Layers on the (100) and (111) Crystal Surface of Platinum (Ph. D. Thesis), LBL-1816, September 1973.

107. R. L. Park in The Structure and Chemistry of Solid Surfaces, G. A. Somorjai, ed. (Wiley, NY, 1969).

108. J. E. Houston and R. L. Park. Surf. Sci. 21, 209 (1970).

109. R. L. Park and J. E. Houston, Surf. Sci. 18, 213 (1969).

110. J. E. Houston and R. L. Park. Surf. Sci. 26, 269 (1971).

111. A. Guinier, X-Ray Diffraction (W. H. Freeman and Co., San Francisco, CA, 1963).

112. T. L. Hill, Statistical Thermodynamics (Addison-Wesley, Reading, MA, 1960), p. 133.

113. H. P. Bonzel, Surf. Sci. 21, 45 (1970).

114. J. M. Blakely and H. Mykura, Acta Met. 10, 565 (1962).

115. A. J. Melmed, J. Appl. Phys. 38, 1885 (1967).

116. C. Herring, Phys. Rev. 82, 87 (1951).

117. H. Mykura, Acta Met. 9, 570 (1961); Acta Met. 5, 346 (1957).

118. B. Lang. Surf. Sci. 53, 317 (1975).

119. C. W. Tucker, Jr., J. Appl. Phys. 38, 2696 (1967); 35, 1897 (1964).

120. R. P. Merrill, private communication.

121. M. McLean and H. Mykura, Surf. Sci. 5, 466 (1966).

122. J. J. Burton, private communication.

123. E. E. Gruber and W. W. Mullins, J. Phys. Chem. Solids 28, 875 (1967).

124. W. L. Winterbottom in Surfaces and Interfaces I, J. J. Binke, N. L. Reed and V. Weiss, eds. (Syracuse University Press, 1967).

125. W. K. Burton, N. Cabrera and F. C. Frank, Phil. Trans. Roy. Soc. London, A243, 299 (1951).

126. L. C. Isett and J. M. Blakely, J. Vac. Sci. Tech. 12, 237 (1975).

127. T. N. Taylor, Ph. D. Thesis, Brown University, 1973.

128. G. E. Rhead and M. McLean, Acta Met. 12, 401 (1964).
N. A. Gjostein, Acta Met. 11, 957 (1963).
W. M. Robertson and P. G. Shewmon, J. Chem. Phys. 39, 2330 (1963).
G. E. Rhead and H. Mykura, Acta Met. 10, 843 (1962).

129. G. A. Somorjai, Principle of Surface Chemistry (Prentice Hall, 1972).

130. G. Ayrault and G. Ehrlich, J. Chem. Phys. 60, 281 (1974).

131. W. L. Winterbottom and N. A. Gjostein, Acta Met. 14, 1041 (1966).

132. R. Kumar and H. E. Grenga, Surf. Sci. 50, 399 (1975).

133. H. Mykura, Acta Met. 9, 570 (1961).

134. M. McLean, Acta. Met. 19, 387 (1971).

135. I. N. Stranski, Z. Physik. Chem. B11, 342 (1931).

136. J. Burton, Cat. Rev. 9, 209 (1974).

137. J. MacKenzie, A. Moore and J. F. Nicholas, J. Phys. Chem. Solids 23, 185 (1962).

138. W. M. Robertson and P. G. Shewmon, Trans. Am. Inst. Min. Metall. Engrs. 224, 804 (1962).

139. F. C. Frank, Metal Surfaces, Structure, Energetics and Kinetics ASM (1963).

140. J. F. Nicholas, Aust. J. Phys. 21, 21 (1968).

141. D. H. Dutton, B. N. Brockhouse and A. P. Miller, Can. J. Phys. 50, 2915 (1972).

142. S. K. Sinha and B. N. Harmon, Phys. Rev. Lett. 35, 1515 (1975).

143. T. T. Tsong, J. Chem. Phys. 54, 4205 (1971).

144. T. L. Eistein and J. R. Schreiffer, Phys. Rev. B7, 3629 (1973).

145. L. Kesmodel and L. Falicov, Solid State Comm. 16, 1201 (1975).

146. T. L. Hill, Statistical Mechanics (McGraw-Hill, NY, 1956).

147. R. L. Schwoebel and E. J. Shipsey, J. Appl. Phys. 37, 3682 (1966).

148. R. L. Schwoebel, J. Appl. Phys. 40, 614 (1969).

149. Anonymous, R. C. A. Review 23, 567 (1962).

150. R. W. McCabe, T. Pignet and L. D. Schmidt, J. Cat. 32, 114 (1974).

151. J. Oudar, private communication.

152. A. D. O. Cinneide and J. K. A. Clarke, Cat. Rev. 7, 213 (1972).

153. R. van Nordstrand, private communication.

154. J. J. Lander, Progress in Solid State Chemistry (MacMillan Co., NY, 1965), Vol. 2.

R. E. Schlier and H. E. Farnsworth, J. Chem. Phys. 30, 917 (1959).

155. T. French and G. A. Somorjai, J. Phys. Chem. 74, 2489 (1970).

156. S. Hagstrom. H. B. Lyon and G. A. Somorjai, Phys. Rev. Lett. 15, 491 (1965).

157. T. Rhodin, to be published, Phys. Rev. B (1976).

158. C. W. Tucker, J. Appl. Phys. 35, 1897 (1964).

159.

160. A. M. Mattera, R. M. Goodman and G. A. Somorjai, Surf. Sci. 7, 26 (1967).

161. D. G. Fedak and N. A. Gjostein, Phys. Rev. Lett. 16, 171 (1966).

162. J. T. Grant, Surf. Sci. 18, 228 (1969).

163. P. W. Palmberg and T. N. Rhodin, Phys. Rev. 161, 586 (1967).

164. A. Ignatiev, A. V. Jones and T. N. Rhodin, Surf. Sci. 30, 573 (1972).

165. D. G. Fedak and N. A. Gjostein, Surf. Sci. 8, 77 (1967).

166. D. W. Blakely and G. A. Somorjai, to be published.

167. P. W. Palmberg in Structure and Chemistry of Solid Surfaces, G. A. Somorjai, ed. (John Wiley & Sons, NY, 1969), article 29.

168. American Institute of Physics Handbook (McGraw-Hill, 1963).

169. An exact value could not be found, but similar high bulk modulus metals have lower

170. J. W. Matthews, J. Vac. Sci. Tech. 12, 126 (1975).

171. L. Brewer, Science 161, 115 (1968); in High Strength Materials, V. F. Zackay, ed. (Wiley, NY, 1965), pp. 12-103; in Phase Stability in Metals and Alloys, P. Rudman, J. Stringer and R. J. Jaffee, eds. (McGraw-Hill, NY, 1967), pp. 39-61.

172. F. C. Frank and J. H. van der Merwe, Proc. Roy. Soc. A 198, 205 (1949).

173. H. P. Bonzel, C. R. Helms and S. Kelemen, Phys. Rev. Lett. 35, 1237 (1975).

174. N. Cabrera, Surf. Sci. 2, 320 (1964).

175. C. Herring, The Physics of Powder Metallurgy, W. E. Kingston, ed. (McGraw-Hill, NY, 1951), p. 143.

176. T. A. Clarke, R. Mason and M. Tescari, Surf. Sci. 40, 1 (1973).

177. V. H. Baldwin and J. B. Hudson, J. Vac. Sci. Tech. 8, 49 (1971).

178. G. Kneringer and F. P. Netzer, Surf. Sci. 49, 125 (1975).

179. W. K. Huber and G. Rettinghaus, J. Vac. Sci. Tech. 7, 289 (1970).

181. H. P. Bonzel and R. Ku, J. Vac. Sci. Tech. 9, 663 (1972).

182. H. P. Bonzel and R. Ku, Surf. Sci. 33, 91 (1972).

183. P. R. Norton and P. J. Richards, Surf. Sci. 49, 567 (1975).

184. D. L. Adams, Surf. Sci. 42, 12 (1974).

185. W. L. Winterbottom, Surf. Sci. 37, 195 (1973).

186. G. Ehrlich, J. Appl. Phys. 32, 4 (1961).

187. P. Redhead, Vacuum 12, 203 (1962).

188. L. Firment, private communication.

189. A. E. Morgan and G. A. Somorjai, J. Chem. Phys. 51, 3309 (1969).

190. H. Conrad, G. Ertl and E. E. Latta, Surf. Sci. 41, 435 (1974).

191. H. Conrad, G. Erth, J. Koch and E. E. Latta, Surf. Sci 43, 462 (1974).

192. D. M. Collins, J. B. Lee and W. E. Spicer, submitted to Surf. Sci.

193. G. Doyen and G. Ertl, Surf. Sci. 43, 197 (1974).
C. G. Ballhausen and H. B. Gray, Molecular Orbital Theory (W. A. Benjamin, NY, 1964).

194. F. P. Netzer and G. Kneringer, Surf. Sci. 51, 526 (1975).

195. G. A. Somorjai, Proc. Roy Soc. A 331, 335 (1972).

196. H. Weinberg, Ph. D. Thesis, University of California, Berkeley, 1972.

197. J. C. Tracy, J. Phys. Chem. 56, 2736 (1972); 56, 2748 (1972).
J. C. Tracy and P. W. Palmberg, J. Phys. Chem. 51, 4852 (1969).

198. W. H. Weinberg and R. P. Merrill, Surf. Sci. 39, 206 (1973).

199. S. E. Tsang and L. F. Falicov, submitted to J. Phys. B.

200. H. S. Johnston, Gas Phase Reaction Rate Theory (Ronald Press Co., NY, 1966).

201. H. Weinberg and R. P. Merrill, Surf. Sci. 33, 493 (1972).

202. P. Emmett, private communication.

203. M. A. Vannice, J. Cat. 37, 449 (1975); 37, 462 (1975).

204. B. Sexton, Ph. D. Thesis, University of New South Wales (1975).

205. R. Joyner, private communication.

206. D. J. Darensbourg and R. P. Eischens, Proc. Int. Congr. Catal., 5th, 1972 1, 21 (1973).

207. P. B. Weisz and C. D. Prater, Adv. Cat. 9, 583 (1957).

208. D. R. Stull, E. F. Westrum and G. C. Sinke, Chemical Thermodynamics of Organic Compounds (J. Wiley, NY, 1969).

209. J. L. Gland, K. Baron and G. A. Somorjai, J. Cat. 36, 305 (1975).

210. T. H. Wonnacott and R. J. Wonnacott, Introductory Statistics (Wiley, NY, 1972).

211. C. Smith, private communication.

212. J. Gland and G. A. Somorjai, Surf. Sci. 38, 157 (1973).

213. K. Baron, D. W. Blakely and G. A. Somorjai, Surf. Sci. 44, 45 (1973).

214. J. W. May, Surf. Sci. 17, 267 (1969).

215. Z. Paál and P. Tétényi, J. Cat. 30, 350 (1973).

216. W. H. Weinberg, H. A. Deans and R. P. Merrill, Surf. Sci. 41, 312 (1974).

217. N. C. Gardner and R. S. Hansen, J. Phys. Chem. 74, 3298 (1970).

218. C. M. Holbrook and H. Wise, to be published.

219. J. H. Sinfelt, H. Hurwitz and R. A. Shulman, J. Phys. Chem. 64, 1559 (1960).

220. V. Haensel, G. R. Donaldson and F. J. Riedl, in Proc. Int. Congr. Catal., 3rd, 1964, Vol. 1, p. 294 (1965).

221. D. Kahn, E. E. Petersen and G. A. Somorjai, J. Cat. 34, 294 (1974).

222. J. Butt, Catalyst Deactivation in 1st Intern. Symp. of Chem. Reac. Engr., Washington, D.C. (1970).

223. A. Behnke, Ph. D. Thesis, University of California, Berkeley, 1976.

224. B. Nieuwenhuys, G. Rivoda, D. Hagen and G. A. Somorjai, to be published.

225. J. H. Sinfelt and J. C. Rohrer, J. Phys. Chem. 65, 978 (1961).

226. E. Wolf, Ph. D. Thesis, University of California, Berkeley, 1975.

227. R. M. Lambert, Surf. Sci. 49, 325 (1975).

228. G. W. Wulff, Z. Krist. 34, 449 (1901).

229. J. L. Meijering, Acta Met. 11, 847 (1963).

This report was done with support from the United States Energy Research and Development Administration. Any conclusions or opinions expressed in this report represent solely those of the author(s) and not necessarily those of The Regents of the University of California, the Lawrence Berkeley Laboratory or the United States Energy Research and Development Administration.

TECHNICAL INFORMATION DIVISION
LAWRENCE BERKELEY LABORATORY
UNIVERSITY OF CALIFORNIA
BERKELEY, CALIFORNIA 94720